ROYAUME DU MAROC
Université Mohammed V - RABAT -
جامعة محمد الخامس – الرباط –
Faculté des sciences
كلية العلوم
CENTRE D'ETUDES DOCTORALES - SCIENCES ET TECHNOLOGIES

N° d'ordre : *3175*

THESE

En vue de l'obtention du : ***DOCTORAT***

Structure de Recherche : Equipe *de Science de la* Matière *et du* Rayonnement.
Discipline : Physique.
Spécialité : Physique des hautes énergies.

Présentée et soutenue le 28/01/2019 par :

Salah-eddine DAHBI

Recherche de résonances dans le canal $WZ \rightarrow lvl'l'$ produits lors des collisions des proton-proton à $\sqrt{s}$=13 TeV auprès de LHC avec le détecteur ATLAS, et l'étude des performances de la granularité du sFCal qui est proposé comme une solution pour remplacer le calorimètre à l'avant d'ATLAS au HL-LHC

JURY

Karl JAKOBS	**P.E.S, Université Albert-Ludwigs, Fribourg.**	**Président**
Rajaâ. CHERKAOUI El MOURSLI	**P.E.S, *Université Mohammed V*, Faculté des Sciences, Rabat.**	**Rapporteur**
Abedelilah. MOUSSA	**P.E.S, *Université Mohammed I*, Faculté des Sciences, Oujda.**	**Rapporteur**
Yahya TAYALATI	**P.E.S, *Université Mohammed V*, Faculté des Sciences, Rabat.**	**Directeur**
Samira HASSANI	**P.E.S, IRFU du CEA, Saclay.**	**Examinateur**
Bengt LUND-JENSSON	**P.E.S, Institut Royal de Technologie, Stockholm.**	**Examinateur**
Mohamed GOUIGHRI	**P.H, Université Ibn Tofail, Faculté des Sciences Kenitra.**	**Examinateur**

Année Universitaire : 2018/2019

Mohammed V University in Rabat
Faculty of Science

Doctoral Thesis

Search for resonant $WZ \to \ell\nu\ell'\ell'$ production in Proton-Proton Collisions at $\sqrt{s} = 13$ TeV with the ATLAS Detector, and Performance studies of the sFCal granularity as a proposed replacement for the ATLAS Forward Calorimeter at HL-LHC

By

Salah-eddine DAHBI

Thesis submitted to obtain the degree of Ph.D. in:

"HIGH ENERGY PHYSICS"

Prof. Karl JAKOBS	ALU-Freiburg, DE	President
Prof. Rajaâ CHERKAOUI EL MOURSLI	FSR-UM5-Rabat, MA	Referee
Prof. Abdelilah MOUSSA	FS-UMP-Oujda, MA	Referee
Prof. Yahya TAYALATI	FSR-UM5-Rabat, MA	Supervisor
Prof. Samira HASSANI	IRFU-CEA-Saclay, FR	Examiner
Prof. Bengt LUND-JENSEN	KTH-Stockholm, SE	Examiner
Prof. Mohamed GOUIGHRI	FS-UIT-kenitra, MA	Examiner

Presented on January 28, 2019

Acknowledgements

I wish to express my gratitude, first and foremost, to my supervisor Prof. **Yahya TAYALATI** from the Faculty of Science at Mohammed V University of Rabat. Without his continuous support, ideas, enormous patience and valuable insight over the past three years, I would have never succeeded.

I express my sincere gratitude to Prof. **Karl Jakobs**, It is really a big honor for me to have the spokesperson of the collaboration as a president of jury in my thesis.

I am especially grateful to my rapporteur, Prof. **Rajaâ CHERKAOUI EL MOURSLI** from the Faculty of Science at Mohammed V University of Rabat, for the evaluation of this thesis and their useful comments.

I would like to thank my rapporteur, Prof. **Abdelilah MOUSSA** from the Faculty of Science at Mohammed I University of Oujda, for the evaluation of this thesis.

I would like to express my sincere gratitude to Prof. **Samira HASSANI** from the Institute of Research Into the Fundamental laws of the Universe (CEA/PAris-Saclay) for the sleepless nights we were working together before deadlines, for the continuous support of my Ph.D research, for her motivation, and immense knowledge. Her guidance helped me in all the time of research with her insightful comments and encouragement.

I would like to thank Prof. **Bengt LUND-JENSEN** from the KTH Royal Institute of Technology in Stockholm . I am grateful for his remarkable insight, unfailing support in all aspects of my ATLAS qualification task. I have benefited greatly from his immense knowledge, versatility, and experience.

I am grateful to Prof. **Mohamed GOUIGHRI** from the Faculty of Science at Ibn Tofail University of Kenitra, for going through my thesis and for accepting to be in my examining committee.

I would also like to particularly thank **Prof. Rachid.MAZINI** for going through my thesis, I really appreciate his detailed comments and interesting discussions.

My sincere thanks also goes to the ATLAS collaboration, that provided me with the opportunity to join their experiment and gave me access to the research facilities. I am also thankful to my colleagues in the **atlas-phys-exotics-vvres-run2-**$l\nu ll$ group, that took part in the realization of this research, namely **Joany Manjarres Ramos, Georges Azuelos, Benjamin Freund and Miaoran Lu**.

This work was supported by the **Swedish Research Council**, we are grateful for their generous funding. I also acknowledge the financial support by **Association Avenir pour la Sciences et le Savoir (AASS)** of Oujda.

I thank my fellow lab-mates in ESMaR laboratory and all my wonderful friends for the stimulating discussions and for all the fun we have had in the last three years.

Last but not the least, I would like to thank my family: my parents and sisters for supporting me and caring about my present and my future.

Abstract

A search for $WZ \to \ell\nu\ell'\ell'$ resonance has been performed with the ATLAS experiment at the CERN Large Hadron Collider. The search uses a data sample corresponding to an integrated luminosity of 36.1 fb^{-1}, which was recorded in 2015-2016 at the LHC from proton-proton collisions at a center-of-mass energy of 13 TeV.

No evidence for a resonance is found and upper limits are set on the production cross section times branching ratio of a heavy particle produced either in quark–anti-quark fusion ($q\bar{q}$) or via vector-boson fusion (VBF). Limits are derived as function of the mass of a charged member of a Heavy Vector Triplet or of the singly charged scalar in the Georgi-Machacek model.

This dissertation reports also on the performances, in term of energy and ϕ pointing resolutions of the finer readout granularity super forward calorimeter proposed as a replacement of the ATLAS forward calorimeter at the High luminosity LHC (HL-LHC).

CERN, LHC, ATLAS, UPGRADE, Forward Calorimeter, $WZ \to \ell\nu\ell'\ell'$, Resonance.

Résumé

Une recherche de résonnance $WZ \to \ell\nu\ell'\ell'$, où ℓ et ℓ' rèférent à un électron ou un muon, a été effectuée en utilisant 36.1 fb^{-1} de données collectées par le détecteur ATLAS durant 2015 et 2016 par la collision entre proton-proton à $s = \sqrt{13}$ de centre de masse énergie délivrée par le Large Collisionneur de Hadrons (LHC) au Centre Européen des Recherches Nucléaires (CERN).

Aucune preuve de résonance n'a été trouvée, des limites supérieures sur le produit de la section efficace et le rapport d'enbranchement d'une particule lourde produite sont extraites à 95% CL. Les limites sont déduites en fonction de la masse d'un membre chargé d'un triplet de vecteurs lourds ou du scalaire à charge unique du modèle de Georgi–Machacek.

Cette thèse présente également l'étude des performances du super calorimètre à l'avant simulé qui est proposé comme un remplacement du calorimètre à l'avant d'ATLAS à haute luminosité LHC (HL-LHC), pour évaluer l'impact d'une granularité extrêmement fine sur la résolution en position ϕ et en energie dans la région de hauts η du détecteur ATLAS.

CERN, LHC, ATLAS, UPGRADE, Forward Calorimeter, $WZ \to \ell\nu\ell'\ell'$, Resonance.

Contents

Acknowledgements iii

Abstract v

Résumé vii

Introduction 1

1 The Standard Model of particle physics 3
- 1.1 Introduction . . . 3
  - 1.1.1 The Standard Model . . . 4
- 1.2 The electroweak Interaction and symmetries . . . 5
  - 1.2.1 Gauge theory . . . 6
  - 1.2.2 Electroweak Lagrangian . . . 7
  - 1.2.3 Spontaneous Symmetry Breaking . . . 8
- 1.3 WZ production at the Large Hadron Collider . . . 10
- 1.4 WZ Beyond the Standard Model . . . 11
- 1.5 Conclusion . . . 12

2 ATLAS experiment at The Large Hadron Collider 13
- 2.1 Introduction . . . 13
- 2.2 The Large Hadron Collider . . . 13
  - 2.2.1 Operation . . . 14
  - 2.2.2 Luminosity . . . 14
  - 2.2.3 Pileup . . . 16
- 2.3 The ATLAS experiment . . . 17
  - 2.3.1 The ATLAS coordinate system . . . 17
  - 2.3.2 Inner detector . . . 19
    - 2.3.2.1 Transition radiation tracker . . . 19
    - 2.3.2.2 Pixel detector . . . 20
    - 2.3.2.3 Semiconductor tracker . . . 21
  - 2.3.3 ATLAS calorimeter system . . . 22
    - 2.3.3.1 Electromagnetic calorimeter . . . 22

2.3.3.2 Hadronic calorimeter . . . 23
2.3.4 The muon spectrometer . . . 24
2.3.5 ATLAS magnet system . . . 24
2.3.6 Trigger system . . . 25
2.3.7 ATLAS distributed computing . . . 27
2.3.7.1 The world wide LHC computing Grid . . . 28
2.3.8 ATLAS software distribution CVMFS . . . 31
2.3.9 Event Data Model . . . 32
2.3.10 ATLAS Dataset Nomenclature . . . 33
2.3.11 ATLAS Distributed Data Management (RUCIO) . . . 34
2.3.12 Conclusion . . . 34

3 Performance studies of the super Forward Calorimeter granularity 37
3.1 Introduction . . . 37
3.2 The ATLAS forward calorimeter . . . 37
3.3 Monte Carlo samples . . . 40
3.4 Electron Analysis . . . 43
3.4.1 Linearity and Energy resolution . . . 43
3.4.2 Pointing resolution . . . 45
3.4.2.1 Correction of the ϕ S-shape position in the FCal . . . 46
3.4.2.2 Logarithmic weighting . . . 47
3.5 Pion analysis . . . 49
3.5.1 Energy resolution . . . 49
3.5.2 Position resolution . . . 51
3.6 Conclusion . . . 53

4 Physics object reconstruction 55
4.1 Introduction . . . 55
4.2 Electron reconstruction . . . 55
4.3 Muon reconstruction . . . 59
4.4 Jet reconstruction . . . 63
4.5 Missing Transverse Energy reconstruction . . . 66
4.6 Overlap removal . . . 68

5 Resonant $WZ \to \ell\nu\ell'\ell'$ search at $\sqrt{s} = 13$ TeV 69
5.1 Introduction . . . 69
5.2 Data and Monte Carlo samples . . . 69
5.2.1 Data samples . . . 70
5.2.2 Monte Carlo samples . . . 71

5.2.3 Signal Monte Carlo samples . . . 72
5.2.4 Backgrounds Monte Carlo samples . . . 75
5.3 Event selection . . . 77
5.3.1 Event cleaning . . . 77
5.3.2 Triggers . . . 78
5.3.3 Primary vertex . . . 82
5.3.4 Lepton final selection . . . 82
5.3.5 Z candidate selection . . . 84
5.3.6 W candidate selection . . . 84
5.3.7 Event selection acceptance . . . 85
5.4 WZ Signal Optimization . . . 87
5.4.1 VBF category . . . 88
5.4.2 $q\bar{q}$ category . . . 91
5.5 Signal acceptance and acceptance times efficiency . . . 95
5.5.1 $q\bar{q}$ category acceptance . . . 95
5.5.2 VBF category acceptance . . . 97
5.6 Background Estimation . . . 98
5.6.1 Global Matrix Method . . . 99
5.6.2 Fake ratio estimation . . . 101
5.6.3 Backgrounds estimation for VBF category . . . 105
5.6.4 Backgrounds estimation for $q\bar{q}$ category . . . 108
5.7 Systematic uncertainties . . . 109
5.7.1 Theoretical systematic uncertainties . . . 109
5.7.1.1 Systematic uncertainties on the $q\bar{q}$ signal . . . 109
5.7.1.2 Systematic uncertainties on the VBF signal . . . 110
5.7.1.3 Parton shower uncertainties on the WZ background . . . 110
5.7.2 Experimental systematic uncertainties . . . 112
5.7.2.1 Integrated luminosity measurement . . . 112
5.7.2.2 Muons . . . 112
5.7.2.3 Electrons . . . 112
5.7.2.4 Jets . . . 113
5.7.2.5 Missing transverse energy . . . 113
5.7.2.6 Pile-up . . . 113
5.8 Statistics procedure . . . 114
5.8.1 Likelihood definition . . . 114
5.8.2 Statistical Treatment . . . 116
5.8.3 Background Modeling . . . 117
5.9 Results . . . 118

5.9.1 $q\bar{q}$ signal region . . . 118
5.9.2 VBF signal region . . . 118
5.10 Upper limit on signal cross section times branching fraction . . . 120
5.10.1 Exclusion limits for qq-analysis . . . 120
5.10.2 Exclusion limits for VBS-analysis . . . 121
5.11 Previous diboson resonance searches . . . 122
5.12 Combination of recent diboson resonance searches . . . 124
5.12.1 Combination of WW and WZ resonance . . . 124
5.12.2 Combination of ZZ and ZW resonance . . . 124
5.13 Conclusion . . . 125

Summary **127**

A Comparison between different WZ QCD MC samples generators **129**
A.1 WZ QCD PowhegPythia8/Sherpa2.2.2 comparison . . . 130
A.2 WZ QCD PowhegHerwig/Sherpa2.2.2 comparison . . . 132
A.3 WZ QCD PowhegPythia8/PowhegHerwig comparison . . . 136

B Comparison between different EW QCD MC samples generators **139**
B.1 WZ QCD PowhegPythia8/Sherpa2.2.2 comparison . . . 140

C Systematic uncertainties for the total background for $q\bar{q}$ SR **145**
C.1 Pileup Systematic uncertainties . . . 145
C.2 Muon Systematic uncertainties . . . 146
C.3 Electron Systematic uncertainties . . . 147
C.4 Jet Systematic uncertainties . . . 148
C.5 Missing transverse energy Systematic uncertainties . . . 149
C.6 B-tagging Systematic uncertainties . . . 150

Résumé détaillé **153**

Bibliography **157**

List of Figures

1.1 Elementary particles and their interaction in the Standard Model. The conserved quantum number (spin, electric charge, color charge) for each particle are shown. 5
1.2 The Higgs potential as a function of the complex scalar field [11]. 9
1.3 Leading order feyman diagrams for the WZ production at the Large Hadron Collider. From left to the right the s-channel (TGC), the t-channel, and the u-channel. 10
1.4 Feynman diagram showing the production of $WZjj$ via VBF process while predicting charged Higgs boson. 10

2.1 The CERN accelerator complex [30]. The protons are first accelerated in the LINAC-2, then in the booster, then in the PS, then in the SPS and finally in the LHC. 14
2.2 Integrated luminosity collected by the ATLAS detector from 2011 to 2018 [34]. 16
2.3 The ATLAS detector and subsystems view [35]. 17
2.4 ATLAS right-handed XYZ coordinates system. 18
2.5 Illustration of the cylindrical ATLAS coordinates (left). The pseudo-rapidity η values and corresponding polar angle θ (right). 18
2.6 A cut-away view of the ATLAS inner detector (left). The barrel part layers and end-cap disks is indicated, together with the radial and longitudinal coordinates [37]. 19
2.7 A schematic view of the ATLAS transition radiation tracker in the left. In the right a charged particle travels through the TRT's straws [39]. 20
2.8 (a) Schematic view of the ATLAS Pixel Detector.(b) Assembly view of an individual ATLAS Pixel Detector module [39]. 21
2.9 Cut-view of the ATLAS calorimeters systems [43]. 22
2.10 Sketch of a barrel module located at $\eta = 0$ of the ATLAS electromagnetic calorimeter [45]. 23
2.11 Sketch of the muon spectrometer in the $x-y$ (left) and $z-y$ (right) projections. The Monitored Drift Tubes, Cathode Strip Chambers, Thin Gap Chambers and Resistive Plate Chambers are shown. [49]. 24

2.12 Schematic view of the ATLAS magnetic system, it consists of eight barrel toroid coils in blue , end-caps coils in red and the solenoid in green. 25
2.13 A schematic view of the ATLAS trigger system level [54]. 26
2.14 ATLAS computing Grid model. 28
2.15 The left figure shows the CERN Data Center (Tier 0). On the right, servers at Tier 0 record a copy of primary LHC data, and distribute it to 13 Tier 1 centers around the world. 28
2.16 Schema of the IFIC Tier-3. 30
2.17 the Large Hadron Collider Optical Private Network (LHCOPN) map. 31
2.18 CernVM-FS content distribution network for the **cern.ch** domain: **Stratum1** replica servers are located in Europe, the U.S. and Asia. One protected read/write instance **Stratum 0** is feeding up the public. 32
2.19 Schema of the ATLAS Event Data Model (EDM). 33
2.20 The ATLAS Dataset Nomenclature. 34

3.1 *The left figure shows a schematic cutaway view of the ATLAS EndCap cryostat, showing the location of the forward calorimeter relative to the other EndCap calorimeters [66]. On the right, a cut-away view of the ATLAS forward calorimeter [67]. Particles from the interaction point traverse the electromagnetic FCal1 module (Cu/LAr), then the two hadronic FCal modules (W/LAr).* 38
3.2 *On the left, a transverse view of the forward calorimeter tube matrix [22]. On the right, a close-up views of an electrode in the FCal1* [67]. 38
3.3 *The forward calorimeter in a standalone Geant4 simulation. The three FCal modules and the Cryostat in grey are represented.* 39
3.4 *Readout chain of the ATLAS Forward calorimeter [22].* 40
3.5 *Hits in the different modules of FCal (Left), and sFCal (Right)* 41
3.6 *The response linearity for electrons taken from the first compartment of the FCal (left) and the sFCal1(right) standalone simulation.* 43
3.7 *Electron energy distribution in FCal (left) and sFCal (right), obtained using 8 cm radius cluster around the most energetic FCal1 (sFCal1) cells. Data is fitted with double Gaussian function.* 44
3.8 *Energy resolution of the FCal response to electrons as a function of the nominal electron energy, from analysis of FCal1 (sFCal1) standalone simulation, and fitted with the function in the Equation* (3.1)*. The uncertainties are estimated using the propagation of error.* 45
3.9 *Pointing ϕ resolution without S-Shape correction in the left for FCal (σ_ϕ= 18.99± 0.13 mrad) and for the sFCal in the right (σ_ϕ= 8.02± 0.13 mrad) for 100 GeV electrons fitted by double Gaussian.* 46

3.10 *ϕ_{true} as a function of $\phi_{Measured}$ measured in the FCal. It gives a S-shape distribution.* . . . 46
3.11 *ϕ_{true} as a function of $\phi_{Measured}$ after S-shape correction (left). A linear interpolation is computed to correct the S-Shape position. The pointing ϕ resolution for 100 GeV after S-shape correction (σ_ϕ= 10.02± 0.07 mrad) is shown in the right.* . . . 47
3.12 *The distribution of $(\phi_{e-} - \phi_{W.L})$ in the FCal1 (left) and sFCal1 (right) for 100 GeV e- fitted with a double Gaussian function.* . . . 48
3.13 *Position ϕ Resolution for electrons, as a function of electron energy, from analysis of FCal1 (sFcal) standalone simulation, fitted with the function in the Equation* (3.5)*. The uncertainties are estimated using the propagation of error from double gaussian fit.* . . . 48
3.14 *Pion energy distrubition, obtained using 16cm cylinder cluster around the most energetic FCal1, FCal2 and FCal3 readout cell (group or tile), fitted with sum of a double Gaussian.* . . . 50
3.15 *Energy resolution of the FCal response to pions, as a function of nominal pions energy, from analysis of FCal1 (sFCal1) standalone simulation, fitted with the function in the Equation* (3.1)*. The uncertainties are estimated using the propagation of error.* . . . 51
3.16 the distribution of $(\phi_{pion} - \phi_{cell})$ in the FCal1 (left) and sFCal1 (right) fitted with sum of a double Gaussian. . . . 52
3.17 *the distribution of $(\phi_{pion} - \phi_{L.P})$ in the FCal1 (left) and sFCal1 (right) fitted with sum of a double Gaussian.* . . . 52
3.18 *Position ϕ resolution of response to pions, as a function of nominal pions energy, from analysis of FCal1 (sFcal) standalone simulation, fitted with the function in the Equation* (3.5)*. The uncertainties are estimated using the propagation of error from the double gaussian fit.* . . . 53

4.1 Efficiency of electrons identification from $Z \to ee$ decays. The efficiency is obtained using Monte Carlo simulations, and is measured with respect to reconstructed electrons [76]. . . . 57
4.2 The efficiency to identify muons for medium working point from $Z \to \mu\mu$ and $J/\psi \to \mu\mu$ events. The error bars on the efficiencies indicate the statistical uncertainty [81]. . . . 62
4.3 Illustration of jets which are formed of partons, hadrons, or detector measurements [85]. . . . 63
4.4 The MV2c10 output for b-jets (blue line),c-jets (green line) and light-flavor jets (red line) in simulated $t\bar{t}$ events [90]. . . . 66

4.5 The resolution of the E_T^{miss} components E_x^{miss} and E_y^{miss} as a function of $< \mu >$ [93]. 68

5.1 The integrated luminosity as a function of time delivered by the LHC (green), and collected by ATLAS detector (yellow) during 2015 data-taking. The Blue shaded area shows all the good data quality passed the GRL criteria [112]. . 70
5.2 Muons Trigger Efficiency for 600,1300,2000 GeV HVT signal. 80
5.3 Electrons Trigger Efficiency for 600,1300,2000 GeV HVT signal. 80
5.4 Efficiency gain at the pre-selection level of adding other triggers to the nominal one using 600 GeV HVT signal sample for electrons (left) and muons (right). 81
5.5 Efficiency gain using current selection and nominal triggers per WZ channel for 2000 GeV HVT signal. 81
5.6 Efficiency gain using current selection and nominal triggers per WZ channel (left) and versus leptons momentum (right) for WZ-SM background. 81
5.7 A comparison between 7 GeV and 20 GeV ZZ veto cut for both ZZ (left) and VVV (right) events. 83
5.8 A comparison between 7 GeV and 20 GeV ZZ veto cut for WZ-SM. 83
5.9 The Z boson invariant mass is shown on the top left, the W boson transverse mass on the top right, the Z boson transverse momentum in the middle left, the W boson transverse momentum in the middle right, the $E_{\mathrm{T}}^{\mathrm{miss}}$ on the bottom left and the transverse mass of the WZ system on the bottom right. Backgrounds contribution include fake leptons are estimated from Monte Carlo and normalized to the data luminosity of 36.1 fb^{-1}. 86
5.10 The jet multiplicity and the total event yields in both data and MC are given for WZ events. Backgrounds contribution include fake leptons estimated from Monte Carlo and normalized to the data luminosity 36.1 fb^{-1}. 87
5.11 Distributions of m_{jj} and $\Delta\eta_{jj}$ for both signals modeling mass points, GM (top), HVT VBF (Bottom) models and the WZ SM backgrounds. 88
5.12 Two-dimensional (2-D) scan of the parameters m_{jj} and $|\Delta\eta_{jj}|$ for the mass point 200 GeV (top left), 300 GeV (top righ) for GM model and 250 GeV (bottom left), 300 (bottom right) for HVT signal. The z-axis represents the Poisson significance σ. 89
5.13 Distributions of the yield per channel, m_{jj}, $\Delta\eta_{jj}$, $\Delta\phi_{jj}$ missing energy and WZ transverse mass in the VBF signal region. 90
5.14 Distributions of $p_{\mathrm{T}}^{\mathrm{Z}}/\mathrm{m_{WZ}}$ (left) and $p_{\mathrm{T}}^{W}/\mathrm{m_{WZ}}$ (right) for the HVT signal mass points and the WZ-SM background normalized to the unit. 91
5.15 Distributions of $p_{\mathrm{T}}^{\mathrm{Z}}/\mathrm{m_{WZ}}$ (top left), $p_{\mathrm{T}}^{W}/\mathrm{m_{WZ}}$ (top right), $\Delta y(W,Z)$ the rapidity separation between W and Z bosons (bottom left), and $\Delta\phi(\ell^{\mathrm{W}}, E_{\mathrm{T}}^{\mathrm{miss}})$ which is $\Delta\phi$ (bottom right). 92

5.16 The expected limits on the cross section of several HVT model as a function of its invariant mass for different cuts on $p_{\mathrm{T}}^{\mathrm{Z}}/\mathrm{m_{WZ}}$ and $p_{\mathrm{T}}^{W}/\mathrm{m_{WZ}}$ and $\Delta y(W,Z) < 1.5$ and $\Delta\phi(\ell^{3\mathrm{rd}}, E_{\mathrm{T}}^{\mathrm{miss}}) < 1.5$ in the mass range between 500 GeV and 3 TeVGeV (top), zoom on the mass range below 1 TeV (middle), zoom on the mass range between 1 TeV to 3 TeV (bottom). 93
5.17 The total events yields in both data and MC for individual channel are given for WZ events after applying signal selection cuts : $p_{\mathrm{T}}^{\mathrm{Z}}/\mathrm{m_{WZ}} > 0.35$ and $p_{\mathrm{T}}^{W}/\mathrm{m_{WZ}} > 0.35$. The uncertainties are only statistical. 94
5.18 Distributions of the Z boson invariant (top left), the W boson transverse mass (top right), the E_T^{miss} (bottom left) and the transverse mass of the WZ system (bottom right) after applying signal selection cuts : $p_{\mathrm{T}}^{\mathrm{Z}}/\mathrm{m_{WZ}} > 0.35$ and $p_{\mathrm{T}}^{W}/\mathrm{m_{WZ}} > 0.35$. The uncertainties are only statistical. 95
5.19 The Acceptances times efficiency for different HVT mass per individual and inclusive WZ channels for the $q\bar{q}$ signal. Errors are statistical only. 97
5.20 The acceptance times efficiency of VBF HVT (left) and GM model (right) for different masses and for the individual and the inclusive WZ channels. Errors are statistical only. 98
5.21 Distribution of Z boson invariant mass in the Z+jets control region. On the left, the fake muon control region and on the right the fake electron control region. The statistical uncertainty is shown by shaded bands. 102
5.22 The transverse momentum distribution of the jet faking muons (left) and electrons (right) in the Z + jets loose region. The statistical uncertainty is shown by shaded bands. 103
5.23 The transverse momentum distribution of the jet faking muons (top), and electrons bottom after applying to the additional lepton the Z (right) and W (left) lepton requirements. The statistical uncertainty is shown by shaded bands. 103
5.24 Distributions of the muon fake rate as a function of p_T in the Z+jets control region, using the Z muon selection on the left. The muon fake rate using the W muon selection is shown on the right. 104
5.25 Distributions of the electron fake rate as a function of p_T in the Z+jets control region, using the Z electron selection on the left. The electron fake rate using the W electron selection is shown on the right. 104
5.26 Comparison of the data and MC WZ transverse mass (left) and the missing transverse energy distributions (right), the reducible backgrounds are estimated using the matrix method. The statistical and systematics uncertainties are shown by shaded bands. 105

5.27 The distributions m_{jj}, $\Delta\eta_{jj}$, missing transverse energy and WZ transverse mass in the WZ VBF validation region. 106
5.28 WZ transverse mass (left) and missing transverse energy (right) distributions in the VBF signal region, the reducible backgrounds are estimated using the matrix method. The statistical and systematics uncertainties are shown by shaded bands. 108
5.29 WZ transverse mass (left) and missing transverse energy (right) distributions in the $q\bar{q}$ signal region, the reducible backgrounds are estimated using the matrix method. The statistical and systematics uncertainties are shown by shaded bands. 109
5.30 Comparison of the M_{WZ} distribution between Sherpa2.2.2, Powheg+Herwig and Powheg+Pythia8 event generators in VBF SR on the left and $q\bar{q}$ SR in the right. The parton shower uncertainty is shown by shaded gray bands. . . 111
5.31 Comparison of the M_{WZ} distribution between Sherpa2.2.2 and MadGraph event generators in VBF SR on the left and $q\bar{q}$ SR in the right. The parton shower uncertainty is shown by shaded gray bands. 111
5.32 Average number of interactions per bunch crossing after pileup re-weighting for data and MC in the inclusive region after selection of the W and Z boson candidates. All MC expectations are scaled to the integrated luminosity of the data using the predicted MC cross sections of each sample. 114
5.33 Width of the resonance peak as a function of the resonance mass, for $q\bar{q}$. . . 116
5.34 Width of the resonance peak as a function of the resonance mass, for the VBF analyses. 116
5.35 The post-fit WZ invariant mass distribution in $q\bar{q}$ signal region. Pre-fit HVT signal expectation at m = 500 GeV is overlaid. The background expectation is shown after the profile likelihood fit to the data. The band denotes the statistical and systematic uncertainty on the background after the fit to the data. The lower panels show the ratio of the observed data to the SM background estimation. 118
5.36 The post-fit WZ invariant mass distribution in VBF signal region. Pre-fit HVT (left) and GM (right) signal expectation at $m = 450$ GeV are overlaid. The background expectation is shown after the profile likelihood fit to the data. The band denotes the statistical and systematic uncertainty on the background after the fit to the data. The lower panels show the ratio of the observed data to the SM background estimation. 119
5.37 Expected and observed 95% C.L. exclusion upper limits with an integrated luminosity of 36.1 fb^{-1} on the production cross section multiplied by the branching ration $\sigma \times \mathrm{BR}(HVT \to WZ)$ in the $q\bar{q}$-enriched category. 121

5.38 Expected and observed exclusion limits on $\sigma \times \mathrm{BR}(H_5^+ \to WZ)$ signal at 95% C.L confidence level and on the ratio of vacuum expectation values in the Georgi-Machacek Model as a function of $m_{H_5^+}$. 122
5.39 Expected and observed exclusion limits on $\sigma \times \mathrm{BR}(W' \to WZ)$ signal at 95% C.L confidence level in the HVT Model as a function of the mass heavy boson mass in the VBF phase space. 122
5.40 Combined 95% CL limit for diboson WZ with $\ell\nu\ell'\ell'$, $\ell\ell q\bar{q}$, $\ell\nu q\bar{q}$, JJfinal states. The green (yellow) bands representing the 1 σ (2σ) intervals of the expected limit including statistical and systematic uncertainties. 123
5.41 Combined 95% CL limit for diboson WZ with fully-leptonic, semi-leptonic, and all-hadronic final states at $\sqrt{s} = 8$ TeV and 13 TeV (2015) on HVT signal model-A (left) and model-B (right). The green (yellow) bands representing the 1 σ (2σ) intervals of the expected limit including statistical and systematic uncertainties. 123
5.42 The observed and expected cross-section upper limits at the 95% confidence level for WV production in the VBF category as a function of the resonance mass. The dots in the observed limit curve represent the generated resonance mass values for HVT W' (left) and heavy scalar signals H (right), produced via VBF are shown [141]. 124
5.43 The observed and expected cross-section upper limits at the 95% confidence level for ZV production in the VBF category as a function of the resonance mass. The dots in the observed limit curve represent the generated resonance mass values for HVT W' (left) and heavy scalar signals H (right), produced via VBF are shown [142]. 125

A.1 Comparison of the m_{WZ} distributions normalized to the cross section (top) and to the unit (bottom) in the $q\bar{q}$ SR and VBF SR of the WZ QCD MC samples. Powheg+Pythia8 (Blue) and Sherpa2.2.2 (Green). 130
A.2 Comparison of the m_{WZ} distributions normalized to the cross section (top) and to the unit (bottom) in the $q\bar{q}$ CR and VBF CR of the WZ QCD MC samples. Powheg+Pythia8 (Blue) and Sherpa2.2.2 (Green). 131
A.3 Comparison of the m_{WZ} distributions normalized to the cross section (top) and to the unit (bottom) in the $q\bar{q}$ SR and VBF SR of the WZ QCD MC samples. Powheg+Pythia8 (Blue) and Powheg+Herwig (Red). 132
A.4 Comparison of the m_{jj} and $\Delta\eta_{jj}$ distributions normalized to the cross section (top) and to the unit (bottom) in the VBF SR of the WZ QCD MC samples. Powheg+Pythia8 (Blue) and Powheg+Herwig (Red). 133

A.5 Comparison of the m_{WZ} distributions normalized to the cross section (top) and to the unit (bottom) in the $q\bar{q}$ CR and VBF CR of the WZ QCD MC samples. Powheg+Pythia8 (Blue) and Powheg+Herwig (Red). 134
A.6 Comparison of the m_{jj} and $\Delta\eta_{jj}$ distributions normalized to the cross section (top) and to the unit (bottom) in the VBF CR of the WZ QCD MC samples. Powheg+Pythia8 (Blue) and Powheg+Herwig (Red). 135
A.7 Comparison of the m_{WZ} distributions normalized to the cross section (top) and to the unit (bottom) in the $q\bar{q}$ SR and VBF SR of the WZ QCD MC samples. Powheg+Herwig (Red) and Sherpa2.2.2 (Green). 136
A.8 Comparison of the m_{WZ} distributions normalized to the cross section (top) and to the unit (bottom) in the $q\bar{q}$ SR and VBF SR of the WZ QCD MC samples. Powheg+Herwig (Red) and Sherpa2.2.2 (Green). 137

B.1 Comparison of the m_{WZ} distributions normalized to the cross section (top) and to the unit (bottom) in the $q\bar{q}$ SR and VBF SR of the WZ EW MC samples. MadGraph (Blue) and Sherpa2.2.2 (Green). 140
B.2 Comparison of the m_{jj} and $\Delta\eta_{jj}$ distributions normalized to the cross section (top) and to the unit (bottom) in the VBF SR of the WZ EW MC samples. MadGraph (Blue) and Sherpa2.2.2 (Green). 141
B.3 Comparison of the m_{WZ} distributions normalized to the cross section (top) and to the unit (bottom) in the $q\bar{q}$ CR and VBF CR of the WZ EW MC samples. MadGraph (Blue) and Sherpa2.2.2 (Green). 142
B.4 Comparison of the m_{jj} and $\Delta\eta_{jj}$ distributions normalized to the cross section (top) and to the unit (bottom) in the VBF CR of the WZ EW MC samples. MadGraph (Blue) and Sherpa2.2.2 (Green). 143

C.1 Pileup systematic uncertainties from the workspace for the total background for $q\bar{q}$ SR. 145
C.2 Muons systematic uncertainties from the workspace for the total background for $q\bar{q}$ SR. 146
C.3 Electrons systematic uncertainties from the workspace for the total background for $q\bar{q}$ SR. 147
C.4 Jets systematic uncertainties from the workspace for the total background for $q\bar{q}$ SR. 148
C.5 MET systematic uncertainties from the workspace for the total background for $q\bar{q}$ SR.. 149
C.6 b-tagging systematic uncertainties from the workspace for the total background for $q\bar{q}$ SR. 151

List of Tables

2.1 LHC beam's parameter for 2010, 2011, 2012, 2015 and 2016 data taking period [33]. . . . 15
2.2 LHC proton-proton performance during run-I (2010-2012), and run-II (2015-2017). Average $<\mu>$ refers to the pileup contamination. . . . 16
2.3 List of Tier 1 Grid sites. . . . 29
2.4 List of Spanish Tier 2 Grid sites. . . . 29

3.1 *General parameters for the Forward calorimeter modules [65].* . . . 39
3.2 *Standalone FCal/sFCal Samples used in the analysis.* . . . 42
3.3 *The fit parameters : $E_{deposit} = a.E_{e-}$ for both FCal and sFCal.* . . . 43
3.4 *Electron energy resolution fit results for FCal and sFCal. The uncertainties are estimated using the propagation of error.* . . . 45
3.5 *Electron pointing ϕ resolution fit results for FCal and sFCal. The uncertainties are estimated using the propagation of error.* . . . 49
3.6 *FCal and sFCal calibration parameters to pion for each module.* . . . 50
3.7 *Pion energy resolution fit results for FCal and sFCal. The uncertainties are estimated using the propagation of error.* . . . 51
3.8 *Pion pointing ϕ resolution fit results for FCal and sFCal. The uncertainties are estimated using the propagation of error.* . . . 53

4.1 Summary of seed-clusters size for the reconstruction of ATLAS electron in the barrel and end-cap regions of the EM calorimeter. . . . 56
4.2 Discriminating variables used for the identification of ATLAS electrons [75]. . . . 58
4.3 Electron isolation working points efficiency [75]. . . . 59
4.4 Baseline electron object selection used in the $WZ \to \ell\nu\ell'\ell'$ analysis. . . . 59
4.5 Quality selections used for the identification of ATLAS muons. . . . 61
4.6 Baseline muon object selection used in the $WZ \to \ell\nu\ell'\ell'$ analysis. . . . 62
4.7 Quality selections used for the identification of ATLAS jets. . . . 65
4.8 JVT cut values for the Loose, Medium and Tight working points [88]. . . . 65
4.9 The MV2c10 b-tagging algorithm Working points. b-jet efficiency, c-jet rejection and light-jet rate rejection are included in the table. . . . 66

4.10 Summary of algorithms used for the reconstruction of the missing transverse energy soft terme [91]. 67

5.1 The final GRLs used in the 2015 and 2016 data-taking by the ATLAS physics analysis. 71
5.2 HVT signal Monte Carlo samples Model-A used for the $q\bar{q}$ resonant search. . 73
5.3 HVT signal Monte Carlo samples for the VBF resonant search. 74
5.4 Georgi-Machacek signal MC simulations samples for the VBF resonant search. 74
5.5 List of background Monte Carlo samples. 76
5.6 Summary of the High Level Triggers for muon that are used during the 2015 and 2016 data taking periods. 78
5.7 Summary of the High Level Trigger for electrons that are used during the 2015 and 2016 data taking. 79
5.8 WZ cut-flow efficiency, using WZ-SM background. 85
5.9 Events yields in data and Monte Carlo passing the event selection before signal optimization per WZ channel, the uncertainties on the events yields are only statistical. The line gives the fraction between data and Monte-Carlo can be seen also in the table. 87
5.10 Yields of VBF selected events in 36.1 fb^{-1} of 2015 and 2016 data at 13 TeV, the uncertainties on the events yields are only statistical. 91
5.11 Summary of observed and expected yields for WZ events in each channel of the analysis and for inclusive channels after applying $p_{\mathrm{T}}^{\mathrm{Z}}/\mathrm{m_{WZ}} > 0.35$ and $p_{\mathrm{T}}^{W}/\mathrm{m_{WZ}} > 0.35$. The uncertainties are only statistical. 94
5.12 The acceptances $\mathcal{A}$ and the acceptance times efficiency $\mathcal{A}\times\epsilon$ for different HVT mass points per individual and inclusive WZ channels for the $q\bar{q}$ signal. Errors are statistical only. 96
5.13 The acceptances $\mathcal{A}$ and the acceptance times efficiency $\mathcal{A}\times\epsilon$ for GM H_5^+ model at different mass points per individual and inclusive WZ channels. Errors are statistical only. 97
5.14 The acceptances $\mathcal{A}$ and acceptance times efficiency $\mathcal{A}\times\epsilon$ for VBF HVT model at different mass points per individual and inclusive WZ channels. The error is statistical only. 98
5.15 Reducible Backgrounds estimation results before signal optimization using the Matrix Method in 36.1 fb^{-1} of 2015 and 2016 data.The statistical and systematics uncertainties are shown for matrix method data. 105
5.16 Yields of selected events in 36.1 fb^{-1} of 2015 and 2016 data compared to backgrounds yields from different processes in the VBF validation region. . . 107

5.17 Reducible Backgrounds estimation results after VBF signal optimization using the Matrix Method in 36.1 fb^{-1} of 2015 and 2016 data.The statistical and systematics uncertainties are shown for matrix method data. 107
5.18 Reducible Backgrounds estimation results after $q\bar{q}$ signal optimization using the Matrix Method in 36.1 fb^{-1} of 2015 and 2016 data.The statistical and systematics uncertainties are shown for matrix method data. 108
5.19 Expected and observed yields in the $q\bar{q}$ signal region. Yields and uncertainties are evaluated after a background-only fit to the data in the $q\bar{q}$ signal region. The uncertainty on the total background estimate can be smaller than the quadratic sum of the individual background contributions due to anti-correlations between the estimates of different background sources. . . . 119
5.20 Expected and observed yields in the VBF signal region. Yields and uncertainties are evaluated after a background-only fit to the data in the VBF signal region. The uncertainty on the total background estimate can be smaller than the quadratic sum of the individual background contributions due to anti-correlations between the estimates of different background sources. . . . 120

Introduction

The Large Hadron Collider (LHC) is the most powerful and complex system mankind has ever built to probe the fundamental forces of nature. After years of design and construction, LHC started to collide proton-on-proton at very high energy since 2009. Collected data allowed the ATLAS and CMS collaborations to achieve in 2012 a historical triumph. These two collaborations jointly announced the discovery of the Higgs boson at 125 GeV via its decays into photon, Z, and W pairs. This discovery completed the Standard Model of particle physics and justified the 2013 Nobel award to Peter Higgs and Francois Englert for the theoretical discovery of a mechanism that contributes to our understanding of the origin of mass of elementary particles.

Despite its enormous success, the Standard Model leaves several fundamental questions without reply. Among the questions left unanswered by this Model which is one of the most fundamental, that is the question of gravitational interaction, which the latter totally ignores in the description of fundamental interactions. The Standard Model is not a unified theory even for the three interactions it describes. Another major problem is related to the origin of dark matter and dark energy, constituting nearly 95% of the energy density of the Universe, remain totally unexplained and the Standard Model fails at providing a viable candidate for the observed abundance of Dark Matter in the Universe.

Many arguments suggest that this model is only an effective theory of a more fundamental model manifesting itself at higher energy. Faced with these shortcomings, many theories have been developed to extend the Standard Model and propose a theoretical explanation for these phenomena. Among these theories, many predict new particles vector resonances strongly coupled to WZ dibosons [1, 2, 3, 4]. Up to now, none of these theories have yet been confirmed. It is in this context that the LHC was conceived. By colliding protons at high energy and high luminosity, this powerful accelerator makes it possible to probe the matter on new scales and to thoroughly test the Standard Model.

The work presented in this thesis was carried out within the ATLAS collaboration and focuses on two main topics. The first one is related to a possible upgrade of the ATLAS Forward Calorimeter (FCal) at the High Luminosity projected for the HL-LHC. The second is fully dedicated to the search of the resonant WZ production in the ATLAS data as a strong evidence of new physics beyond the Standard Model. Concerning the first part, for the upgrade program a new Liquid Argon Forward Calorimeter (sFCal), with improved cooling, higher granularity and with smaller electrode gaps was studied, to reduce the impact of the

very high instantaneous luminosity at Phase-II LHC. Beam heating the FCal could lead to the formation of argon bubbles in the detector, the ionization rate will result in space-charge effects that will reduce the signal and the current draw will result in a voltage drop across the HV current limiting resistors. In collaboration with the particle physics group of the royal institute of technology of Stockholm, we performed the study of the super forward calorimeter (sFCal) as a proposed replacement of the FCal at High Luminosity LHC. Using a standalone simulation, the impact of a finer readout granularity on energy and pointing resolution in the high η region is evaluated for both electrons and pions.

The second part of this thesis is carried out in collaboration with the ATLAS group from CEA Saclay, and has faced the problem of defining a searching method for resonant WZ production using data collected by the ATLAS experiment during 2015 and 2016 period of LHC p-p collision at $s = \sqrt{13}\ TeV$ with 36.1 fb^{-1} integrated luminosity. From the null detection, upper limits on the production cross section times branching ratio of a heavy vector particle produced either in quark–anti-quark fusion ($q\bar{q}$) or through vector-boson fusion (VBF) have been derived. Constraints are also obtained on the mass and couplings of a singly charged Higgs boson, in the Georgi–Machacek model, produced through vector-boson fusion. These limits are competitive at lower masses with those from other di-bosons studies.

This thesis is made of five chapters. The first chapter deals on the Standard Model of Particle physics, specially the electroweak part focusing on the spontaneous breaking symmetry and the *Higgs* mechanism which generates the mass for both W and Z bosons which are involved in this analysis. The WZ production modes in the LHC as well as the models Beyond the Standard Model (BSM) used to interpret results are also exposed in this chapter. A brief description of the Large Hadron Collider, and the ATLAS experiment with its sub-detectors together with the ATLAS distributed computing facilities are given in the second chapter. The third chapter is dedicated to a simulation study of the super Forward Calorimeter ($sFCal$) performance as a proposal replacement of the actual ATLAS Forward Calorimeter (FCal) at High Luminosity, with investigating two different methods to correct the pointing resolution. The physic objects reconstruction involving in the WZ analysis are introduced in the fourth chapter, this include selection criteria and identification of electrons, muons, jets, and the transverse missing energy associated to the undetectable neutrinos. Finally, The WZ resonant analysis of data and the results are discussed in the chapter.

Chapter 1

The Standard Model of particle physics

1.1 Introduction

Particle physics describes the fundamental constituents of matter and their interaction. Until the beginning of the 20^{th} century, atom was considered as the fundamental constituent of matters, on which JOHN DALTON suggests that each chemical element is made up of indivisible atoms with different masses. In 1897, J.J. THOMPSON discovered the **electrons** [5] using a cathode ray tube and he proposed that electrons are embedded in a cloud of positive charge inside the atom. Fourteen years later, ERNEST RUTHERFORD [6] postulated using the gold-foil experience that positive charges are concentrated in the center of the atom on where electrons orbit. In 1905, A. EINSTEIN introduced the light-quantum in order to describe the Photoelectric Effect, he observed the creation of electric current when light incident on a metal surface and he suggested that kinetic energy of emitted photoelectrons is proportional to the incident light's frequency. Therefore, he proposed that light is transmitted in a discrete energy packets which is later called **Photon**. **Muon** was discovered by C.D. ANDERSON and S. NEDDERMEYER in 1936, while studying cosmic radiation. Afterwards, physicists started to develop a series of accelerators at high energies with very efficient detectors, these machines leads to the discovery of several elementary particles such as **Gluon**, $\mathbf{W}^{\pm}$, **Z** bosons as well **tau** lepton, and the **quarks**. In 2012, the last missing elementary particle of the SM is the **Higgs** boson predicted in 1964 by F. ENGLERT et R. BROUT and P. HIGGS is discovered at CERN with ATLAS and CMS detectors.

All known elementary particles and their interactions are gathered in a theory called the Standard Model (SM), which describes the dynamical propagation of particles in the space-time. This chapter will present the different blocks of this model as well as the mathematical description of particle interaction, specially for the electroweak interaction. The WZ production at the LHC which is of interest for this work will be discussed in term of the Standard Model and within some possible extensions of this model.

1.1.1 The Standard Model

Elementary particles in the Standard Model are classified based on their conserved quantum number, especially, the spin which is the angular momentum, the electric charge and the color charge that couple the electromagnetic field and the strong interaction. All particles are either fermions with half-integer spin (1/2), or bosons with integer spin (0 or 1). Furthermore, fermions are composed of two main types, namely Quarks and Leptons particles. Quarks comes in six flavors in pairs of three families, the first generation are Up and Down, second generation includes Charmed and Strange, the last generation is made of heavy top and bottom quarks. Leptons are divided on two categories, charged leptons (electron-like leptons) and neutral leptons called neutrinos. As for quarks, leptons are sorted in three generations, the first one is called electronic leptons, it comprises the electron and the electron neutrino (e^-, ν_e). The second generations is called muonic leptons, it includes muon and muon neutrino (μ^-, ν_μ). Tauonic leptons are forming the third generation, it consists of tau and it neutrino (τ^-, ν_τ).

On the other hand, bosons are divided on two categories, the vector bosons with spin 1 and scalar boson with spin 0. Vector bosons in the Standard Model are considered as the mediator of interaction between fermions. The first boson is called Photon which is the mediator of the electromagnetic force. W and Z vector bosons are the carriers of the weak interactions which responsible for the radioactive decay. Gluon vector bosons mediate the strong force, which binds protons and neutrons to form the atom's nucleus and it keeps the quarks together to form hadron particles such as proton and neutron. finally, the last discovered elementary particle is called Higgs scalar bosons, it gives mass to massive particles via the Higgs mechanism [7]. The list of elementary particles with their conserved quantum numbers, including spin, electrical and color charges as well as the different bosons with its carries forces can be seen in Figure 1.1.

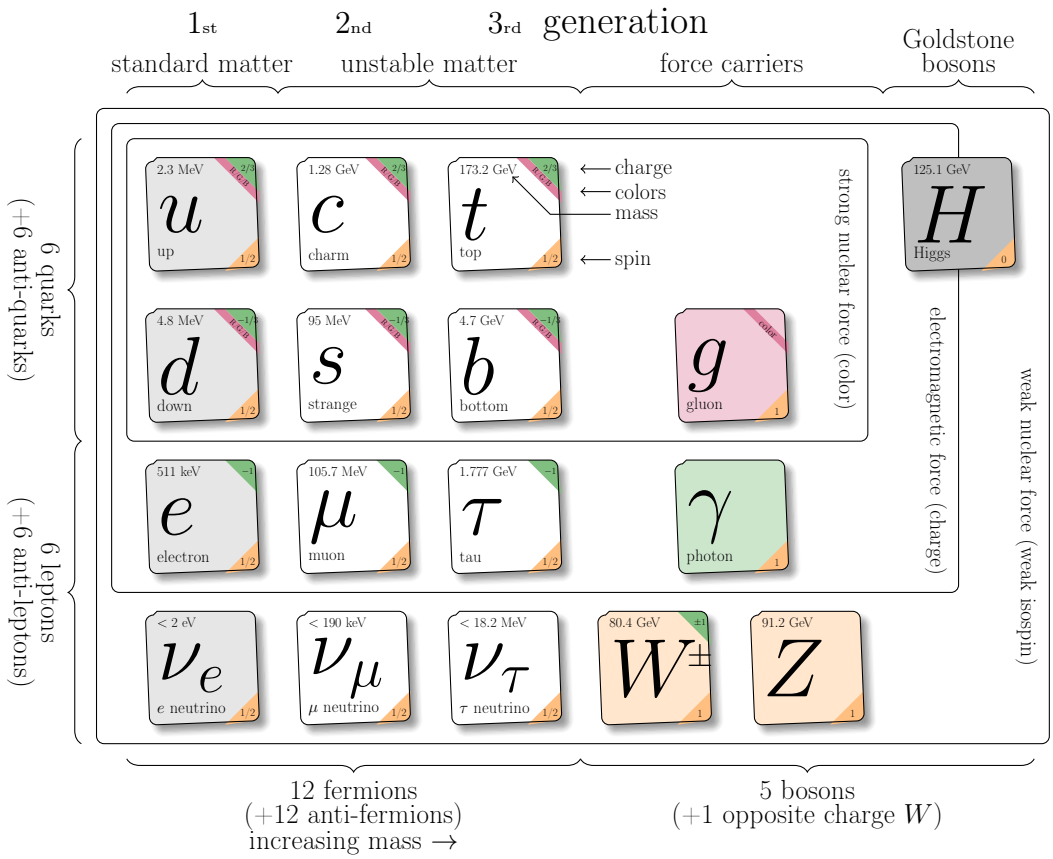


FIGURE 1.1: ***Elementary particles and their interaction in the Standard Model. The conserved quantum number (spin, electric charge, color charge) for each particle are shown.***

1.2 The electroweak Interaction and symmetries

The Standard Model of particle physics is developed based on quantum field theory, which study the invariance of the field's dynamics under certain symmetry transformations. The dynamics of the quantum field symmetry is often determined by the Lagrangian density in term of its conservative quantum components such as electrical and color charges. The SM is established from the gauge theory principles, by combining three symmetry groups $SU(3)_C \times SU(2)_L \times U(1)_Y$ according to the three forces described by the Standard Model. The $SU(3)_C$ symmetry for quantum chromodynamics (QCD) theory, to leaves invariant the Lagrangian in the color space (C). The $SU(2)_L \times U(1)_Y$ symmetry groups associated to the unified electromagnetic and weak forces in the Electroweak theory (EWK) grant the invariance of the relevant quantum numbers, namely the electrical charge (Q_{EM}) and the weak hyper-charge (Y). In what follow we will introduce the gauge theory and we will specially focus on the electroweak interaction symmetry.

1.2.1 Gauge theory

Symmetry principles and Gauge theories provides us with a comprehensive description of the fundamental particles and interactions.

The Standard Model of elementary particle physics is based on gauge theories, and the interaction between the elementary particles are governed by a symmetry principle, namely local gauge invariance, the dynamics of a free fermion field of mass "m" and electric charge "q" is described by the Dirac Lagrangian:

$$\mathcal{L} = \bar{\psi}(x)(i\gamma^{\mu}\partial_{\mu} - m)\psi(x). \tag{1.1}$$

This Lagrangian remains invariant under the following global gauge transformation:

$$\psi'(x) = e^{i\alpha q}\psi(x), \tag{1.2}$$

where, α is a constant phase. Therefore :

$$\mathcal{L}' = \bar{\psi}'(x)(i\gamma^{\mu}\partial_{\mu} - m)\psi'(x) = e^{-i\alpha q}\bar{\psi}(x)(i\gamma^{\mu}\partial_{\mu} - m)e^{i\alpha q}\psi(x) = \bar{\psi}(x)(i\gamma^{\mu}\partial_{\mu} - m)\psi(x) = \mathcal{L}. \tag{1.3}$$

We want to obtain a Lagrangian that can describe a local gauge of the form:

$$\psi'(x) = e^{i\alpha(x)q}\psi(x), \tag{1.4}$$

where $\alpha(x)$ now depends on the position, hence the local gauge transformation name. the local transformation leads to an additional term that leaves the Dirac equation invariant:

$$\mathcal{L}' = \mathcal{L} - q\bar{\psi}(x)\gamma^{\mu}\partial_{\mu}\alpha(x)\psi(x) = \mathcal{L} + \mathcal{L}_{int}. \tag{1.5}$$

As result, a vector field A_{μ} is introduced in the Dirac equation to ensure the invariance of the Lagrangian under local transformation, which $A'_{\mu} \rightarrow D_{\mu} = A_{\mu} - \partial_{\mu}\alpha(x)$. Then the additional term is given as:

$$\mathcal{L}_{int} = -q\bar{\psi}(x)\gamma^{\mu}A_{\mu}\psi(x). \tag{1.6}$$

The final Lagrangian for free fermion with wave function $\psi(x)$ and vector field A_{μ} can be written in the following form:

$$\mathcal{L}_{QED} = \bar{\psi}(x)(i\gamma^{\mu}\partial_{\mu} - m)\psi(x) - \frac{1}{4}F_{\mu\nu}F^{\mu\nu} - q\bar{\psi}(x)\gamma^{\mu}A_{\mu}\psi(x), \tag{1.7}$$

we can interpret the role of each of the terms in this Lagrangian. The first term corresponds to the Dirac field and thus describes the charged fermions. The second term describes particles without masses, so it corresponds to photons. The last term is the interaction

term. It is interesting to note that the interaction term could be obtained by replacing the derivative ∂_μ by the covariant derivative D_μ defines as:

$$D_\mu = iqA_\mu + \partial_\mu. \tag{1.8}$$

The Lagrangian in the Equation 1.7 leads to Quantum Electrodynamics theory (QED), it ensure the conservation of the charge via the U(1) symmetry. It describes the interaction of charged fermions by exchange of photon as mediator of the electromagnetic forces.

1.2.2 Electroweak Lagrangian

The Electroweak theory (EWK) [8] developed by S. Glashow, A. Salam, and S. Weinberg, represents the unified Weak interaction with the Quantum Electrodynamics in term of gauge theory with respect the $SU(2) \times U(1)$ symmetry groups. In general as for the QED theory, the Lagrangian symmetry is preserved under local gauge transformation "G", where the usual derivative ∂_ν is replaced with the covariant derivative D_ν:

$$D_\nu = \partial_\nu - igA^a_\nu T^a, \tag{1.9}$$

"g" is the gauge coupling, and T^a are the generators of the group "G". In the case of the electroweak symmetry, the covariant derivative is written as:

$$D_\nu = \partial_\nu - ig\vec{T}\vec{W}^a_\nu T^a - ig'\frac{Y}{2}B_\nu, \tag{1.10}$$

here, B_ν is a gauge field associated to $U(1)$ transformation with the coupling constant "g" and $(\vec{W}_\nu = (W^1_\nu, W^2_\nu, W^3_\nu)$ represents the three gauge fields for the $SU(2)$ transformation with the coupling constant "g'".

The kinematic terms related to the electroweak interaction is given by $-\frac{1}{4}W^i_{\nu\mu}W^{\nu\mu}_i - \frac{1}{4}B_{\nu\mu}B^{\nu\mu}$. The electroweak Lagrangian is expressed as:

$$\begin{aligned}\mathcal{L}_{EWK} = \mathcal{L}_{kin} + \mathcal{L}_{charged} + \mathcal{L}_{neutral} = &-\frac{1}{4}W^i_{\nu\mu}W^{\nu\mu}_i - \frac{1}{4}B_{\nu\mu}B^{\nu\mu} \\ &+ \bar{\psi}_L\gamma^\nu(\partial_\nu - ig\vec{T}^i\vec{W}^i_\nu - ig'\frac{Y}{2}B^i_\nu)\psi_L \\ &+ \bar{\psi}_R\gamma^\nu(\partial_\nu - ig'\frac{Y}{2}B_\nu)\psi_R.\end{aligned} \tag{1.11}$$

ψ_L and ψ_R represent the fermion fields in the chiral [9] left and right handed respectively.

A weak mixing angle [8] θ_W was introduced by WEINBERG-SALAM in order to form two neutral mediators: photon γ and the Z boson.

$$\begin{pmatrix} A_\nu \\ Z_\nu \end{pmatrix} = \begin{pmatrix} \cos\theta_W & \sin\theta_W \\ -\sin\theta_W & \cos\theta_W \end{pmatrix} \begin{pmatrix} B_\nu \\ W^3_\nu \end{pmatrix}. \tag{1.12}$$

As a results the neutral Lagrangian for the electroweak interaction can be written as:

$$\mathcal{L}_{neutral} = \bar{\psi}\gamma^\nu(g\sin\theta_W T_3 + \frac{Y}{2}g'\cos\theta_W)\psi A_\nu + \bar{\psi}\gamma^\nu(g\cos\theta_W T_3 - \frac{Y}{2}g'\sin\theta_W)\psi Z_\nu. \tag{1.13}$$

The unification between weak and electromagnetic forces represented by the Equation 1.14 which associates the electrical charge "e" to the coupling constants of the weak interaction isospin and hyper-charge using WEINBERG-SALAM angle, where:

$$e = g\sin\theta_W = g'\cos\theta_W. \tag{1.14}$$

The Electroweak theory elaborated by S. GLASHOW, A. SALAM, and S. WEINBERG predicts the existence of four massless gauge bosons, two electrically charged and two neutral that carrier the electroweak interaction. However, the experimental measurements shows that the interaction is carried by massive particles. To mitigate this disagreement, a spontaneous symmetry breaking mechanism is provided in order to generate the mass term while preserving the symmetry of the electroweak's Lagrangian.

In the case of the weak interaction it is found experimentally that the bosons of gauge are massive. We will therefore introduce a mechanism, called the Higgs mechanism, which allows to generate a mass for gauge bosons.

1.2.3 Spontaneous Symmetry Breaking

In order to have mass terms for the massless bosons predicted by EWK theory, an additional term should be added to its Lagrangian $\mathcal{L}_{EWK}$:

$$\mathcal{L}_{V_{Mass}} = -\frac{1}{4}V^\dagger_{\nu\mu}V^{\nu\mu} + m_V^2 V^\dagger_\nu V^\nu, \tag{1.15}$$

where V are the $W^\pm$ or Z bosons. However, the additional term $m_V^2 V^\dagger_\nu V^\nu$ will not preserve the invariant symmetries under $SU(2)_L \times U(1)_Y$ transformation groups.

Therefore, to generate the mass for the three weak gauge bosons while keeping the photon massless and respecting the gauge invariant, a spontaneous symmetry breaking is introduced based on the *Higgs* mechanism [10] defined by the following Lagrangian:

$$\mathcal{L}_H = (\partial_\mu\hat{\phi}^\dagger)(\partial^\mu\hat{\phi}) - V(\hat{\phi}), \qquad where \qquad V(\hat{\phi} = -\mu^2.\hat{\phi}^\dagger\hat{\phi} + \lambda(\hat{\phi}^\dagger\hat{\phi})^2. \tag{1.16}$$

The complex scalar ϕ can interact with massless vector bosons fields, to recover its masses depending on the sign of μ^2 parameter. At vacuum state, the ground state of *Higgs* field ϕ is defined as the field value ϕ_0 that corresponds to the minimum of the potential ($\frac{\partial V}{\partial \phi} = 0$). The *Higgs* potential does not have a minimum at zero field $< \phi >= 0$ for $\mu^2 < 0$ and $\lambda > 0$. As result, the minimum which known as the vacuum expectation value (vev) is given by:

$$\langle 0|\hat{\phi}|0\rangle = \begin{pmatrix} 0 \\ \frac{v}{\sqrt{2}} \end{pmatrix}, \qquad where \qquad v = \sqrt{\frac{-\mu^2}{\lambda}}. \tag{1.17}$$

An illustration of the potential is given in the Figure 1.2.3, at the vacuum expectation value corresponds to the *Higgs* potential minimum at $|\phi^2| = \frac{-\mu^2}{2\lambda}$, any points below the potential breaks spontaneously the symmetry.

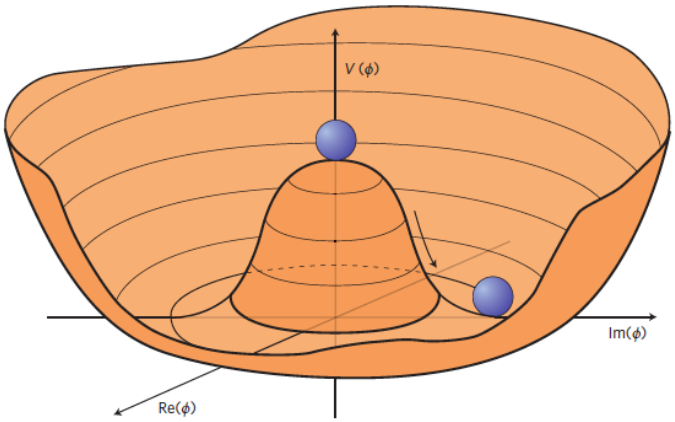


FIGURE 1.2: ***The Higgs potential as a function of the complex scalar field [11].***

The interaction between the *Higgs* field and the massless vector bosons predicts the existence of a new real scalar field called *Higgs* boson (H^0) and generates a mass for both $W^{\pm}$ and Z bosons, while the photon is kept massless.

The bosons mass are calculated using the following formula:

$$m_W^2 = \frac{1}{4}v^2g^2, \qquad m_Z^2 = \frac{1}{4}(g^2 + g'^2v^2), \qquad m_\gamma^2 = 0, \qquad m_{H^0}^2 = \mu^2. \tag{1.18}$$

In addition, the Z and W masses are related to the Weinberg θ_W as follow:

$$\frac{m_W}{m_Z} = \cos\theta_W. \tag{1.19}$$

Altogether, in 1983 the Z and $W^{\pm}$ bosons were discovered at CERN in the Super Proton Synchrotron. The measured values [12] of their masses are $m_W = 80.399 \pm 0.025(stat.)$ GeV and $m_Z = 91.1875 \pm 0.0021(stat.)$ GeV with $\sin^2\theta_W = 0.23140 \pm 0.00021(stat.)$, which is in agreement with the Equation 1.19. The *Higgs* bosons was detected at CERN with the

ATLAS [13] and CMS [14] experiments at a mass of 125.09 ± 0.21 (*stat.*) ± 0.11 (*syst.*) GeV.

1.3 WZ production at the Large Hadron Collider

The diboson production is sensitive to the self-coupling interaction between electroweak gauge bosons in Triple Gauge Coupling (TGC) or Quartic Gauge Coupling (QGC). Therefore, the WZ measurement in the present analysis, is sensitive to the WWZ coupling. At the Large Hadron Collider at CERN the WZ production is coming mainly from the quark anti-quark fusion in the s-,t,u-channels as shown in Figure 1.3.

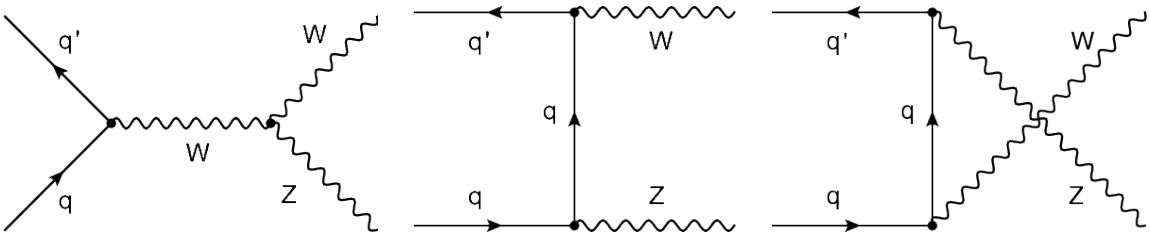


FIGURE 1.3: ***Leading order feyman diagrams for the WZ production at the Large Hadron Collider. From left to the right the s-channel (TGC), the t-channel, and the u-channel.***

In addition, the WZ production can originate at the LHC from Vector Boson Fusion (VBF). This process is characterized by the production of di-boson in association with two jets at the forward regions of the detector at final states ($WZjj$). At run-II the contribution from VBF is important due the the higher center of mass energy of the p-p collision. An example o Feynman diagram showing the production of $WZjj$ via VBF process while predicting a charged $Higgs$ bosons is illustrated in Figure 1.4.

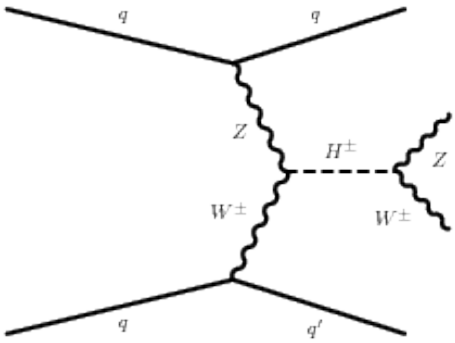


FIGURE 1.4: ***Feynman diagram showing the production of*** $WZjj$ ***via VBF process while predicting charged Higgs boson.***

The WZ production has been measured at the LHC in run-II (2015-2016 period) in both $ATLAS$ and CMS detectors. This section reports only the measurement of WZ production on the fully leptonic final state. The data analysis collected with the ATLAS detector in this period corresponds to an integrated luminosity of 36.1 fb^{-1}, the measured cross section [15] in the fiducial region of the detector in the leptonic decay is $\sigma^{fid}_{WZ\to l'\nu ll} = 63.7 \pm 1.0(stat.) \pm 2.3(sys.) \pm 1.5(lumi.)$ fb, which is in good agreement with the SM expectation $\sigma^{SM\ Expec}_{WZ\to l'\nu ll} = 61.7\ ^{+1.4}_{-1.3}$ fb.

The production of the WZ process is studied with CMS detector in the leptonic final state, using full 2016 data with a total integrated luminosity of $35.9fb - 1$. The WZ production cross section [16] collected by CMS is $\sigma^{Total}_{WZ\to l'\nu ll} = 48.09\ ^{+1.00}_{-0.96}(stat.)\ ^{+0.44}_{-0.37}(sys.) \pm 1.39(lumi.)$ fb, which is also in a good agreement with the predicted SM cross section $\sigma^{SM\ Expec}_{WZ\to l'\nu ll} = 49.98\ ^{+2.2\%}_{-2.0\%}$ fb.

1.4 WZ Beyond the Standard Model

Despite its success to describe the elementary particles, the Standard Model can not explain the full particle phenomenology of the universe. Therefore, a new extensions were developed to overcome the deficiencies of the SM. Physics beyond the Standard Model (BSM) deals with many open topics:

- The Gravity which is not considered in the SM, due to the difficulties arise when performing the instructions of the quantum theory to the gravity force via an hypothetical elementary particle called graviton bosons [17].

- The rotation of the galaxies indicates the exciting of massive neutral particles weakly interacting with the matters (WIMPs). It is expected to observe the $WIMPs$ at high energy colliders since their masses are in order of less than a TeV.

- Neutrinos in the SM are massless particles, but the oscillation between observed between its flavor is possible only with masses. Consequently, an extension of the SM with a model contains a massive right-handed, can solve this problem.

- The Higgs boson has left unanswered fundamental questions about the stability of the electroweak scale: why the Higgs boson mass is stabilized at 125 GeV while quantum corrections tend to pull it to a much higher energy scale. This is the so-called HIERARCHY PROBLEM of the SM. It is possible to recover the mass of the $Higgs$ boson by making adjustments to its proper value, but this is considered unnatural. Some models are introduced to solve this problem by predicting new particle at the oeder of TeV, such as LITTLE HIGGS MODEL[18]

Many theories have been developed to solve these riddles as best they can. Some of these theories are more seductive or popular than others, but all have one thing in common: they contain the Standard Model as an effective low energy theory.

In this context, search for diboson resonances provide an essential tool to test theories of electroweak symmetry breaking beyond the Standard Model (BSM). Vector and scalar resonances are predicted in various BSM scenarios, we will report on a search for a WZ resonance in the fully leptonic decay channel, produced either by quark-antiquark fusion or by vector boson fusion VBF. Two reference models are considered in this work:

- The HVT model that generalizes a large number of models that predict spin-1 resonances. With small number of parameters, this model describes the phenomenology of new spin-1 resonances (W' and Z') [19].

- The Georgi-Machacek (GM) model was proposed in 1985 [20], this model is used as a benchmark for a singly charged $Higgs$ boson resonance ($H_5^{\pm} \rightarrow WZ$) for the present WZ search in the VBF production.

1.5 Conclusion

Since 1967, the Standard Model has always guided researchers in the quest for the ultimate components of matter, all particles theoretically predicted by this model have been discovered experimentally.

Now, after the discovery of the Higgs boson in 2012, the Standard Model is complete and is more than ever a theoretical success. Nevertheless, many arguments suggest that this model is only an effective theory of more global one. As result, many theories have been developed beyond the Standard Model to address its weaknesses. Most of these theories predict new particles, new forces or even new dimensions to better understand our universe and how it evolve.

It is therefore, crucial to develop new tools and new technics to verify the predictions of these many theories. This is very challenging and could be performed via huge and innovative international collaboration. This is the case of the ATLAS experiment at the Large Hadron Collider (LHC), which will be discussed largely in the next chapter.

Chapter 2

ATLAS experiment at The Large Hadron Collider

2.1 Introduction

The ATLAS experiment is an international collaboration bringing together more than 3000 physicist and engineers, from 181 institutions in 38 countries from all world's populated continents. This experiment is installed at the LHC proton collider. The design and construction of the ATLAS detector was realized from the end of the 1980s to the mid-2000s. This chapter describe the main features of the LHC and give a simplified description of the ATLAS detector.

2.2 The Large Hadron Collider

The Large Hadron Collider [21] (LHC) is the most powerful circular accelerator and collider in the world, located at the European Organization for Nuclear Research (CERN). It has two long superconducting rings installed in a tunnel with a circumference of 26.7 kilometers and about 100 meters underground. It consists of 1232 of dipole magnets to curve protons accelerated with a superconducting cavity system via the Lorentz force. Inside the LHC, beams of protons travel in opposite direction and collide at four points along the ring, corresponding to the position of the four LHC experiments: ATLAS [22], ALICE [23], CMS [24] and LHCb [25].

Protons from the ionization of hydrogen atoms are accelerated to 50 MeV in a linear accelerator (LINAC-2) [26] before climbing to 1.4 GeV in a first proton synchrotron (the BOOSTER) [27]. they are then injected into another proton synchrotron (the PS) [28], the protons will get a total energy of 25 GeV. Finally, they enter the super proton synchrotron (SPS) [29], in which they acquire an energy of 450 GeV, which is the nominal energy injection in the LHC.

Since 2015, beam of protons are grouped in 2808 bunches per ring, each one contains 1.15×10^{11} protons in a beam size of 3.5 micrometers in diameter, which is reduced to 2.5

micrometers in 2016, in order to increase the number of collisions, resulting into increasing of the LHC luminosity (see section 2.2.2).

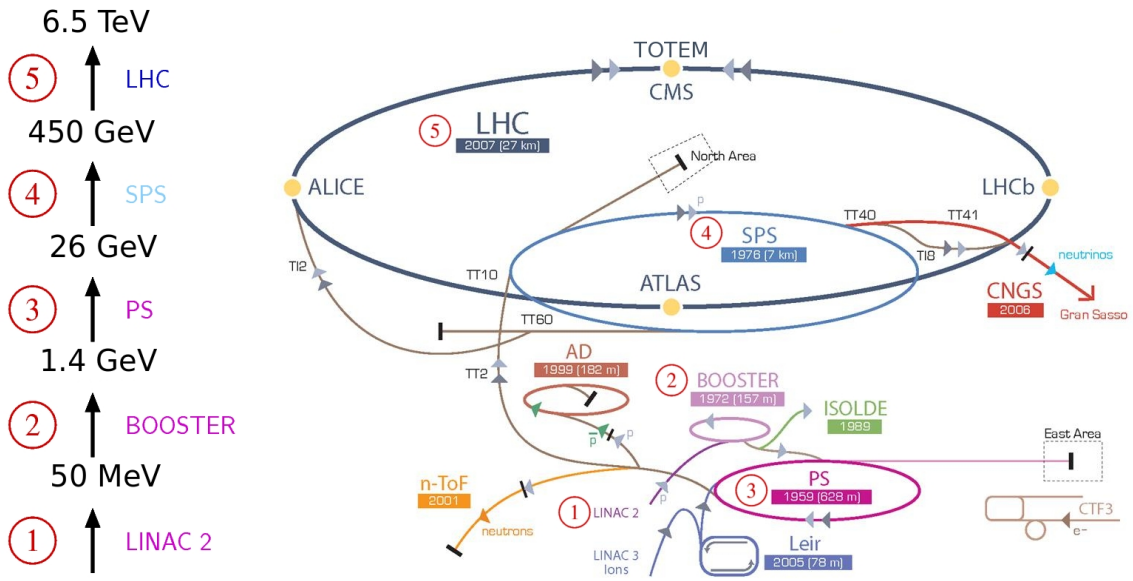


FIGURE 2.1: ***The CERN accelerator complex [30]. The protons are first accelerated in the LINAC-2, then in the booster, then in the PS, then in the SPS and finally in the LHC.***

2.2.1 Operation

The large hadron collider was designed to provide proton-proton collisions at a center of mass energy of 14 TeV, in September 2008 [31] during the first powering test an explosion caused by a failing connection between super-conductors damaged several magnets. After this incident, it was decided to decrease the energy from 7 TeV per beam to 3.5 TeV in the period between 2010 to 2011 producing proton-proton collisions at a center of mass energy of 7 TeV. This represents about 3.5 times more than the energies realized at TeVatron, the proton-antiproton collider built near Chicago in US. Later on, in 2012 the center of mass energy was increased to 8 TeV, before a long shut down in the period 2013-2014 for a series of repair in the LHC as well as for the upgrade of the performance of its four experiments, the large hadron collider restarted at 13 TeV center of mass energy in 2015.

2.2.2 Luminosity

Beside the center of mass energy of the proton-proton collision, the luminosity ($\mathcal{L}$) is another important feature of the LHC. It gives a measurement of the ability of the collider to produce a desired number of collisions in units of inverse cross section per second ($cm^{-2}\ s^{-1}$). The proportionality between the number of produced events (N_{event}) per time and the cross-section (σ_p) of the collision is given by the following formula:

$$\frac{dN_{event}}{dt} = \mathcal{L}\ \sigma_p. \tag{2.1}$$

For a Gaussian beam density distribution [32], the luminosity is defined as:

$$\mathcal{L} = \frac{N_b^2\ n_b\ f_{rev}\ \gamma_r}{4\pi\ \epsilon_n\ \beta^*}\ F, \tag{2.2}$$

where N_b is the number of particles per bunch, n_b, the number of bunch per beam, f_{rev}, the revolution frequency, γ_r, the relativistic gamma factor, ϵ_n is the normalized transverse beam emittance, β^*, the beta function at the collision point and "F" is the geometric luminosity reduction factor related to the crossing angle at the interaction point (IP).

LHC Beam parameter	**Design**	**2010**	**2011**	**2012**	**2015**	**2016**
Beam energy	7.0	3.5	3.5	4.0	6.5	6.5
Number of protons per bunch $N_b\ \times\ 10^{11}$	1.15	1.0	1.3	1.5	1.0	1.1
Number of bunch per beam n_b	2808	368	1380	1380	2244	2200
Normalized transverse beam emittance $\epsilon_n\ \mu m$	3.75	2.6	2.4	2.4	3.5	2.2
Peak luminosity $(10^{34}\ cm^{-2}\ s^{-1})$	1.0	0.021	0.35	0.77	0.47	1.45
β^* The beta function at the collision point (m)	0.55	3.5	1.0 - 1.5	0.6	0.8	0.4

TABLE 2.1: ***LHC beam's parameter for 2010, 2011, 2012, 2015 and 2016 data taking period [33].***

The integrated luminosity often used by the physicist gives an overview of the amount of collected data available for the analysis, it is defined as the time integral of the instantaneous luminosity over the relevant data-taking period "T" ($\int_0^T \mathcal{L}dt$). Figure 2.2 shows the variation of the integrated luminosity collected by the ATLAS detector in the periods between 2011 to 2017.

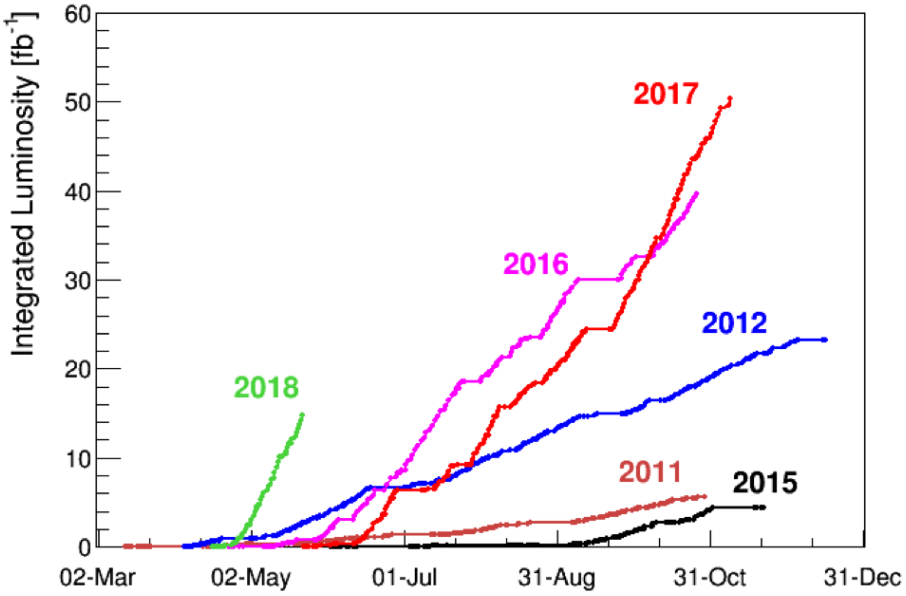


FIGURE 2.2: ***Integrated luminosity collected by the ATLAS detector from 2011 to 2018 [34].***

2.2.3 Pileup

Pileup is defined as the additional events hitting the detectors, coming mainly from additional proton proton collision during the same bunch-crossing or shortly before or after the collision. Particles produced in these pile-up events affects the reconstruction of physic objects, such as on lepton isolation, degrading the measurement of the transverse missing energy and jets. The contamination of pileup events has increased from an average of 9.1 in 2010 to 38.3 in 2017 with the luminosity rising (Table 2.2). To mitigate this issue, several algorithms were developed in order to reduce the pile-up contribution, for instance pileup coming from jets is removed using the jet vertex tagger (JVT) described in section 4.4.

Year	$\sqrt{s}$[TeV]	Peak $\mathcal{L}$	$\int_0^T \mathcal{L}dt$	Maximum bunches	Bunch spacing (ns)	Average $<\mu>$
2010	7 TeV	0.2^{33}	48.1 pb^{-1}	368	50 ns	9.1 for
2011	7 TeV	3.65^{33}	5.46 fb^{-1}	1380	50 ns	combined 7 TeV
2012	8 TeV	7.73^{33}	22.8 fb^{-1}	1380	50 ns	20.7
2013			Long shut dow			
2014			Long shut dow			
2015	13 TeV	5.0^{33}	4.2 fb^{-1}	224	25 ns	13.5
2016	13 TeV	13.8^{33}	38.5 fb^{-1}	2220	25 ns	24.9
2017	13 TeV	20.6^{33}	47.1 fb^{-1}	2556	25 ns	38.3

TABLE 2.2: ***LHC proton-proton performance during run-I (2010-2012), and run-II (2015-2017). Average $<\mu>$ refers to the pileup contamination.***

2.3 The ATLAS experiment

ATLAS (**A** **T**oroidal **L**HC **A**pparatu**S**) is one of the four detector installed around the LHC at CERN. A multipurpose particle physics system with a forward-backward symmetric cylindrical geometry. Equipped with three main components: a tracking system, a calorimeter, and a muon spectrometer. The inner detector is built in a few centimeters from the proton-proton interaction point,it is able to track charged particles and measure their momentum. The calorimeter system is consisting of a hadronic calorimeter and a liquid argon electromagnetic calorimeter. It is used to reconstruct the energy deposit for both charged and neutral particles. The outermost sub-detector is the muon spectrometer, it provides the trajectories and the momentum of muons.

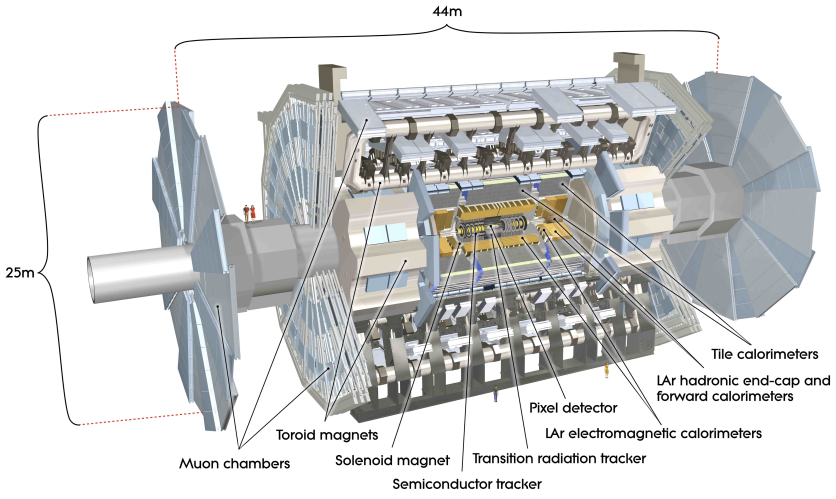


FIGURE 2.3: ***The ATLAS detector and subsystems view [35].***

2.3.1 The ATLAS coordinate system

The ATLAS coordinate system serve to describe the localization of its sub-detectors. A right-handed XYZ coordinates system 2.4 with its origin at the center of the ATLAS detector precisely in the nominal interaction point (IP) is introduced. The x-axis is oriented towards center of the LHC ring and the y-axis point upwards, both axis form the transversal plane of the ATLAS experiment, while the beam direction defines the z-axis.

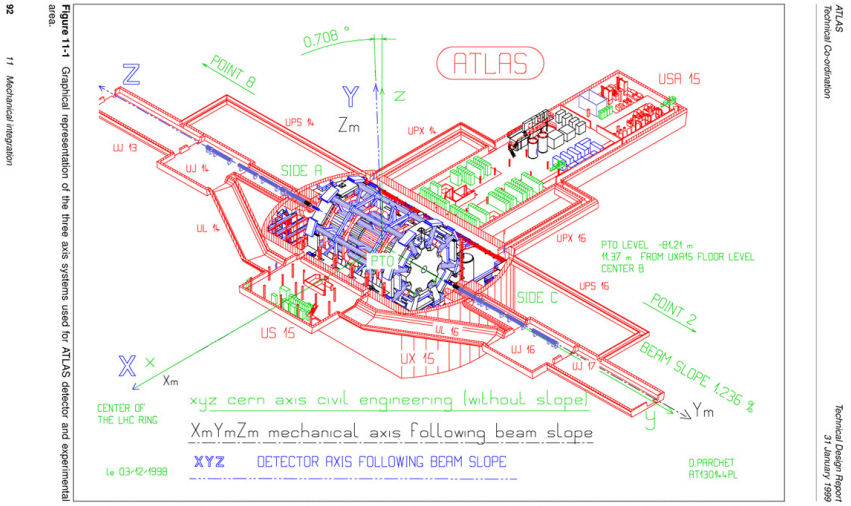


FIGURE 2.4: ***ATLAS right-handed XYZ coordinates system.***

Due to the cylindrical form of its sub-detectors, the employment of cylindrical coordinates 2.5 in the transverse plan of the ATLAS detector is more practical. The azimuthal angle ϕ is defined as the angle in the plane XY starting from the x-axis and increases clockwise around the beam line. The angle θ is defined as the angle around the positive z-axis. For massive particles, the rapidity y is often used instead of θ, where y is calculated as function of it energy and it longitudinal momentum p_z as follow:

$$y = \frac{1}{2} ln(\frac{E + p_z}{E - p_z}). \tag{2.3}$$

In case of particles traveling close to the speed of light ($m \ll p$), the rapidity converge to the pseudo-rapidity η(Figure 2.5):

$$\eta = -ln(\tan \frac{\theta}{2}). \tag{2.4}$$

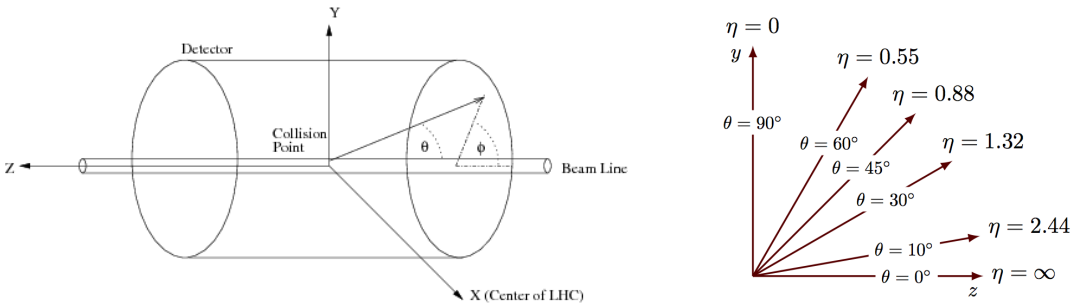


FIGURE 2.5: ***Illustration of the cylindrical ATLAS coordinates (left). The pseudo-rapidity η values and corresponding polar angle θ (right).***

The distance between two reconstructed physic objects in the transversal plane is given by:

$$\Delta R = \sqrt{\Delta\eta^2 + \Delta\phi^2}. \tag{2.5}$$

The transverse invariant mass (M_T) of a particle decaying into two particles 1 and 2, is expressed as function of its particles transverse energy E_T and momentum p_T as follow:

$$M_T = \sqrt{E_{T,1}E_{T,2} - \vec{p}_{T,1}.\vec{p}_{T,2}}. \tag{2.6}$$

2.3.2 Inner detector

The inner detector (ID) [36] is designed inside a solenoid magnet in the closest part to the beam. The ID is composed of three subcomponents, the transition radiation tracker (TRT) which cover the pseudo-rapidity region $|\eta| < 2$, the semiconductor tracker (SCT) and the pixel detector covering $|\eta| < 2.5$ region. The ID consists of a barrel part forming cylinders around the beam pipe and two end-caps of components assembled in a disks perpendicular to the beam axis.

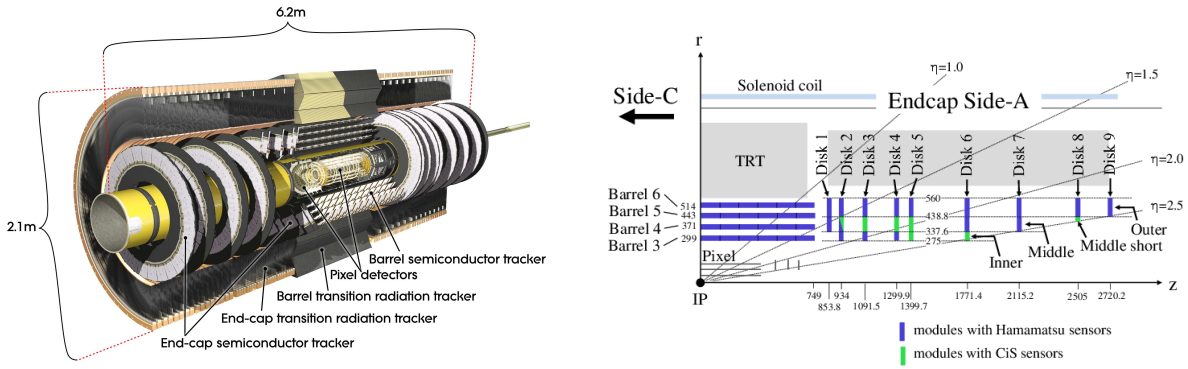


FIGURE 2.6: ***A cut-away view of the ATLAS inner detector (left). The barrel part layers and end-cap disks is indicated, together with the radial and longitudinal coordinates [37].***

2.3.2.1 Transition radiation tracker

The Transition radiation tracker (TRT) [38] is the outermost tracking systems of the ID, It is formed of ∼300000 straws of 4 mm diameter, on each a 31 μm diameter of gold plated tungsten anode filled with gas mixture of 70% Xe, 27% CO_2 and 3% of O_2. The geometry of the TRT allows charged particles to pass through 35 to 40 straws which provide a high efficiency of tracking. Charged particles crossing the TRT ionize the gas mixture inside the straws resulting in track points. Furthermore, the traversing charge particles can cause emission of transition radiation in the inter straw material. These transition radiation photons may be detected inside the straws. Since the energy emitted by the transition radiation is proportional to the relativistic factor $\gamma = E/m$, the TRT provide a significant separation

of charged particles. A schematic view of the ATLAS transition radiation tracker with its straws can be seen in Figure 2.7.

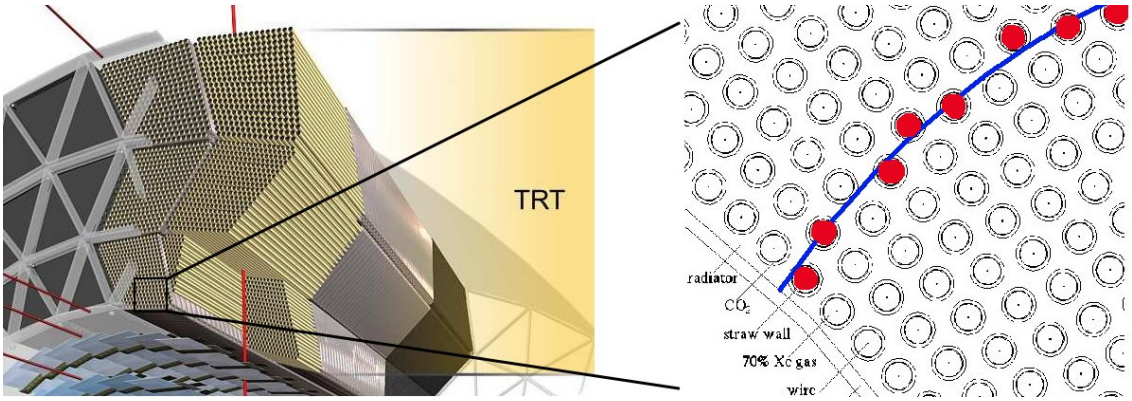
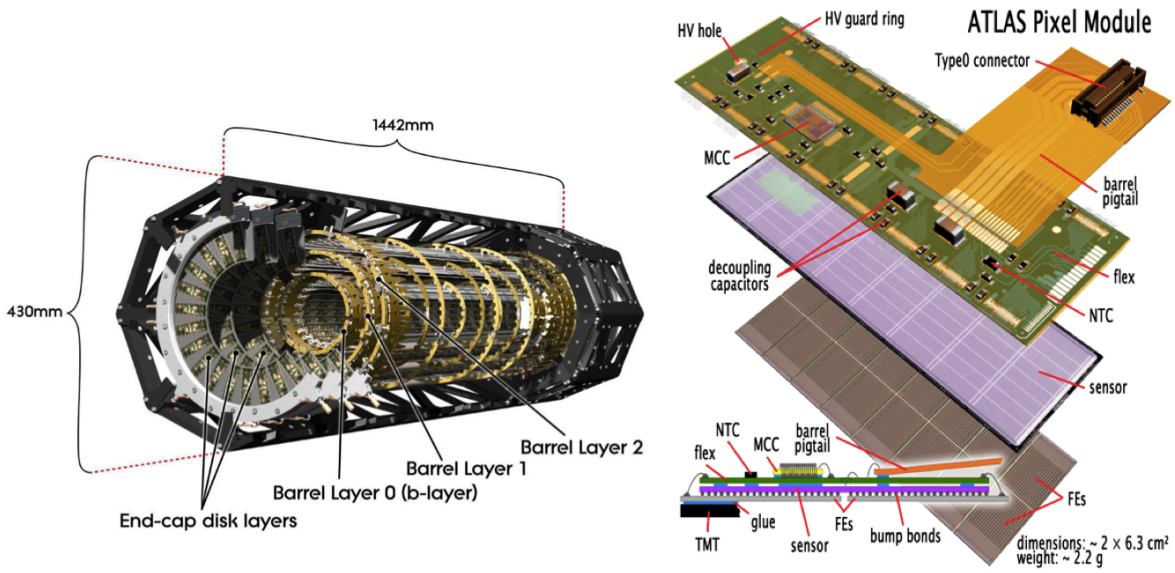


FIGURE 2.7: ***A schematic view of the ATLAS transition radiation tracker in the left. In the right a charged particle travels through the TRT's straws [39].***

2.3.2.2 Pixel detector

Pixel detector [40] is the innermost part of the ATLAS ID, It is made up of six end-cap disks with a three concentric cylindrical barrel layers around the beam pipe. Pixels in this detector are referring to 46080 readout channels of silicon sensor called pixel module with an area of $50 \times 400 \mu m^2$ in the plan $\phi \times z$. The three barrel layers contains 1456 modules and the six disks consist of 288. Profiting from its hight resolution with 10 μm and 115 μm receptively in ϕ and z direction, the pixel detector provides a precise measurement of the impact parameter and detect the short lived particles. A schematic view of the ATLAS Pixel detector with an assembly view of an individual ATLAS Pixel detector module are given in Figure 2.8.



(a) (b)

FIGURE 2.8: ***(a) Schematic view of the ATLAS Pixel Detector.(b) Assembly view of an individual ATLAS Pixel Detector module [39].***

During the first long shutdown (LS1) in 2014 an additional layer was added between the inner layer of the pixel detector and the beam-pipe, the new layer is called the Insertable B-Layer [41] (IBL) consists of 3D and planar silicon sensors. It covers the region $|\eta| < 3$ range and designed to improve the tracking and to minimize risks of high radiation damage at higher luminosity increasing.

2.3.2.3 Semiconductor tracker

The semiconductor tracker (SCT) [42] surrounds the pixel detector, It is a silicon micro-strip formed of four cylindrical barrels with nine disks in each two end-caps side. The four barrels are made up of 2112 modules of silicon-strip sensors, while an end-cap consists of 988 modules. In the barrel two parallel strips to the beam line are grouped in one layer back to back in a small stereo angle of 40 $mrad$ between each other leading to a two dimensional measurement in the $\phi - z$ direction. Strips in the end-cap disks have four radial geometries according to their position compared to the collision point. The geometry of both barrel and end-caps has been designed to allow charged particles to travel across at least four layers in the acceptance region ($|\eta| < 2.5$). The SCT provides eight precision measurement with a resolution of 17 μm and 580 μm respectively in $r - \phi$ and z directions. The signals from the sensors are read out by digital electronics and converted into optical signal directly on the module via optical links.

2.3.3 ATLAS calorimeter system

The calorimeter covers the region of $|\eta| < 3.2$ and $|\eta| < 4.9$ of the ATLAS experiment , it is made up of three main components: the electromagnetic (EM), the hadronic and the forward calorimeters. They are designed to measure the energy of all particles traveling the ATLAS detector except muons and neutrinos, as well as to identify the objects such as electrons, and jets. A Cut-view of the ATLAS calorimeters systems can be seen in Figure 2.9. An overview of the calorimeter systems is described in this section, specially the EM and hadronic calorimeter, while a detailed presentation of the forward calorimeter (FCal) is given in chapter 3, when a simulation study is performed for this calorimeter.

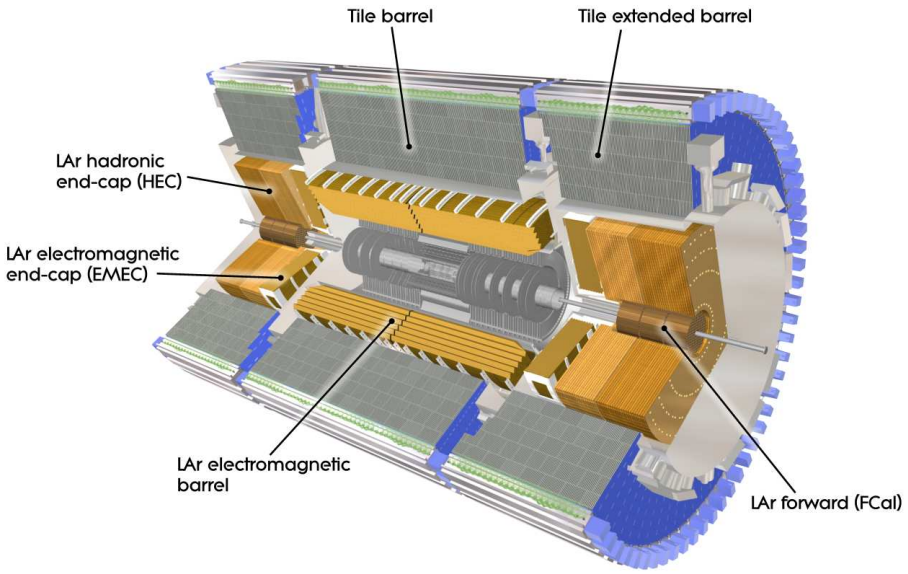


FIGURE 2.9: ***Cut-view of the ATLAS calorimeters systems [43].***

2.3.3.1 Electromagnetic calorimeter

The electromagnetic calorimeter [44] is a liquid-argon detector designed to measure the energies of particles that interact electromagnetically with matters, particularly photons and electrons. It is a lead-LAr detector with accordion shape using kapton as electrodes and lead plates as absorber. This geometry was chosen to provide a complete coverage in the ϕ direction with fast signal rise time. The EM calorimeter is divided in two parts: the electromagnetic barrel (EMB) which covers pseudo-rapidity $|\eta| < 1.475$, the electromagnet end-cap located in region $1.375 < \eta < 3.2$. In total, the EM calorimeter is made up of three layers, the first one had an η segmentation of $\Delta\eta < 0.0031$ allowing to reject π_0 and jet backgrounds. The second layer is located in $\eta < 2.47$, It has a fine granularity in $\eta - \phi$ direction with $\Delta\eta \times \Delta\phi = 0.025 \times 0.025$, this region of the ATLAS detector collects the largest fraction of electromagnetic shower on which both inner detector and the EM

calorimeter enable to identify photons and electrons with high precision. The last outer layer is dedicated to measure very energetic particles with a granularity of $\Delta\eta\times\Delta\phi = 0.050\times0.025$.

In front of the EM calorimeter, a presampler detector is installed to recover energy loss of electrons and photons in the inner detector and the cryostat, it consists of thin layer of LAr with no upstream absorber.

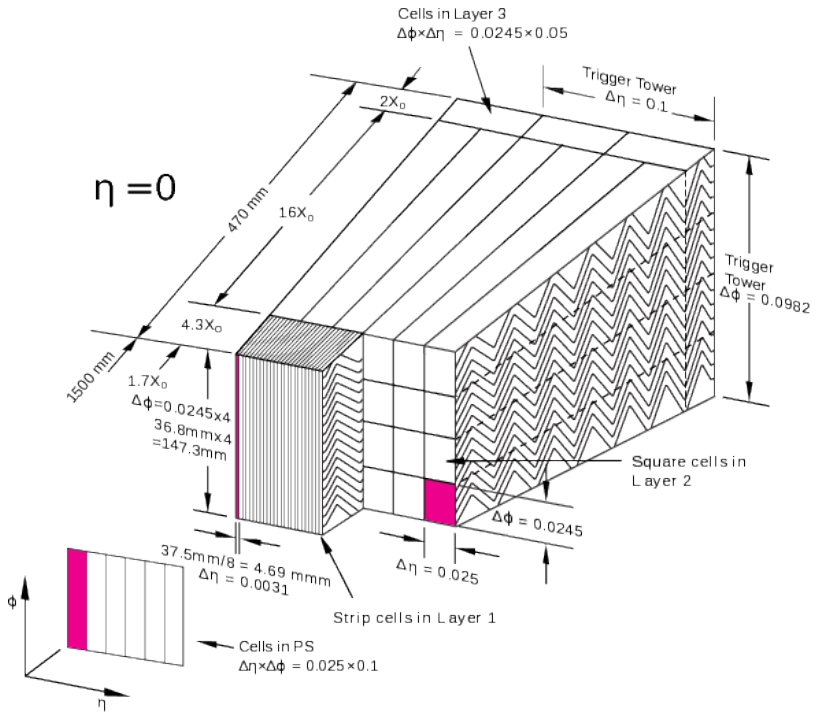


FIGURE 2.10: ***Sketch of a barrel module located at*** $\eta = 0$ ***of the ATLAS electromagnetic calorimeter [45].***

2.3.3.2 Hadronic calorimeter

The hadronic calorimeter surrounds the EMC, it is designed to measure the energy from hadronic showers using its main parts, namely the Tile calorimeter (TileCal) and the liquid argon hadronic end-cap (HCA). The TileCal is composed of a central barrel region with $|\eta| < 1$ and two extended barrel cover the region $0.8 < |\eta| < 1.7$. It made up of plastic scintillating tiles as the active material with steel absorbers. Light produced by charged particles in the scintillator is transmitted to photomultiplier (PMT) across wavelength shifting fibers, the signal from $PMTs$ is digitized every 25 ns before being transferred to off-detector data-acquisition systems.

The second part of the hadronic calorimeters which cover the pseudo-rapidity $1.5 < |\eta| < 3.2$ is the liquid argon hadronic end-cap. It is formed of two disks per end-cap, the central one is made of 25 mm of copper plates and the outer disk from 50 mm. The gaps between the plates are filled with the LAr as an active material.

2.3.4 The muon spectrometer

The muon spectrometer (MS) [46] surrounds the calorimeters systems, it is located in the outermost part of the ATLAS detector. It allows the measurement of the charge and the momenta of charged particles leaving the calorimeters. It is also used to identify muons. The muon tracker is made of three stations, the innermost one is located in $|\eta| < 2.0$ region consists of *Monitored Drift Tubes* [47] (MDTs) filled with 93% of argon and 7% of carbon dioxide with a tungsten-rhenium wire as anode. The outermost and the mid stations are located in the pseudo-rapidity $2.0 < |\eta| < 2.7$ where the backgrounds are expected to be largest, to overcome this problem, the physicist decide to use *Cathode Strip Chambers* (CSCs) [48] composed of multi-wire proportional chambers with cathode segmented into strips providing a fine spatial resolution with excellent counting.

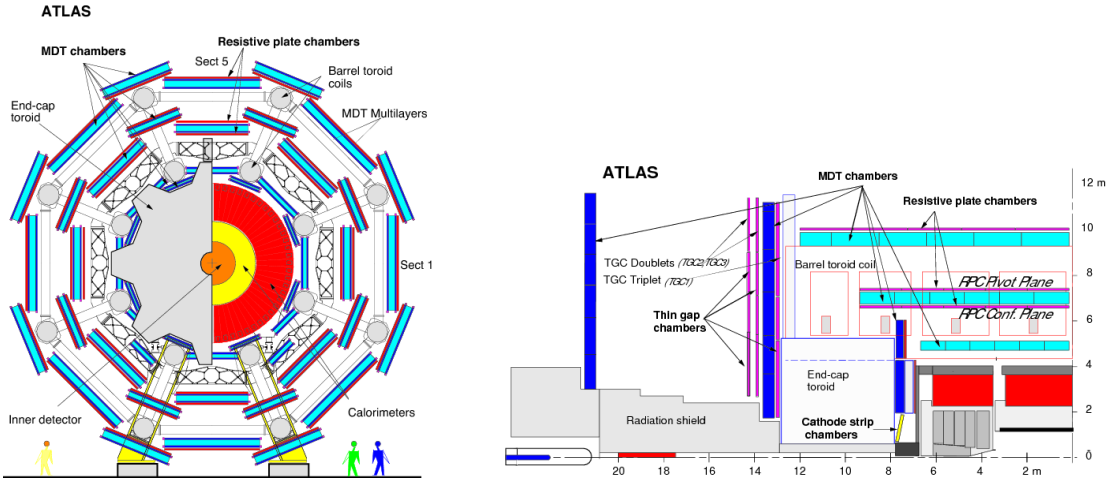


FIGURE 2.11: ***Sketch of the muon spectrometer in the $x-y$ (left) and $z-y$ (right) projections. The Monitored Drift Tubes, Cathode Strip Chambers, Thin Gap Chambers and Resistive Plate Chambers are shown. [49].***

In the central region where the muon spectrometer is close to the trigger system 2.3.6, the barrel is made up of *Resistive Plate Chambers* [50] (RPCs), while the end-cap consists of *Thin Gap Chambers* [51] (TGCs) and are used for the identification of the bunch crossing time of the muon and p_T thresholds.

Muons across the spectrometer ionize the gas mixture inside the MS chambers, creating a pairs of ion-electron. The electrons will drift to the anode and the positive ions moves to the cathode, measuring the charges drift time allows to determine the position of the muon and its momentum.

2.3.5 ATLAS magnet system

The Magnet system [52] in the ATLAS experiment include one central solenoid (CS), and three toroids (one barrel and two end-caps). The solenoid is located between the inner

detector and the EM calorimeter, It is built to produce an axial field of 2 *tesla* (T) inside the inner detector for tracking the charged particles. its axial length is 5.8 m, 0.1 m thick. The three toroids surrounds the calorimeters system, they serve for the identification and measurement of the muon proprieties. The toroid barrel produce approximately 0.5 T while the two end-caps generate 1 T. The size of the barrel toroid is 25.3 m with an inner and outer diameters of 9.4 m and 20.1 m respectively, on which eight coils are integrated. An end-cap toroid is formed of eight coils with a length of 5 m with inner and outer diameters of 1.65 m and 10.7 m.

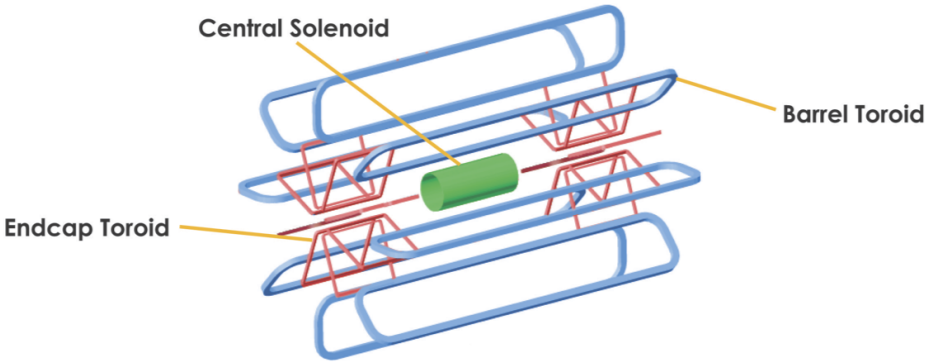


FIGURE 2.12: ***Schematic view of the ATLAS magnetic system, it consists of eight barrel toroid coils in blue , end-caps coils in red and the solenoid in green.***

2.3.6 Trigger system

Proton beams intersect at the heart of the ATLAS detector on the point-1 of the LHC ring every 25 nanoseconds, providing a maximum of 40 MHz event rate. The majority of these events are produced with low energy and have little interest in physics analysis. For that, the ATLAS collaboration has chosen to reduce the data storage rate by using an event filtering system called Trigger [53] . The reduction of data rates is realized in three levels as shown in Figure 2.13, the first being implemented electronically in hardware, while the second and the third levels are software:

- **Level 1 trigger (L1):** This level is responsible for reducing the information collected by the calorimeters and muon spectrometer to $100kHz$ event rate. The criteria that leads to this decreasing of data correspond to the threshold of the energy deposits in the calorimeters, in the case of the muon chambers the criterion is related to the transverse momentum threshold. These requirements define Regions Of Interest (ROI). Data passing the L1 are stored in pipeline memory.

- **Level 2 trigger (L2):** Data in the ROI from L1 trigger is forwarded to level 2 at this level the incoming data has 100 kHz event. The central computing farm runs a fast reconstruction algorithms with 40.000 processor cores, event rate in the second trigger

level is reduced to about 1 kHz which allows triggers to make more complete criteria based on the inner detector information.

- **Event filter (EF):** Considered as third level of the trigger, It ensures the separation between physic objects (electrons, muon, jets, ...) using an algorithm similar to the off-line analysis frameworks. It is designed to reduce the events rate to 400 Hz with about $\sim 1.3 Mbyte$ event size. The events passing specific EF are then used directly by the physics for any analysis.

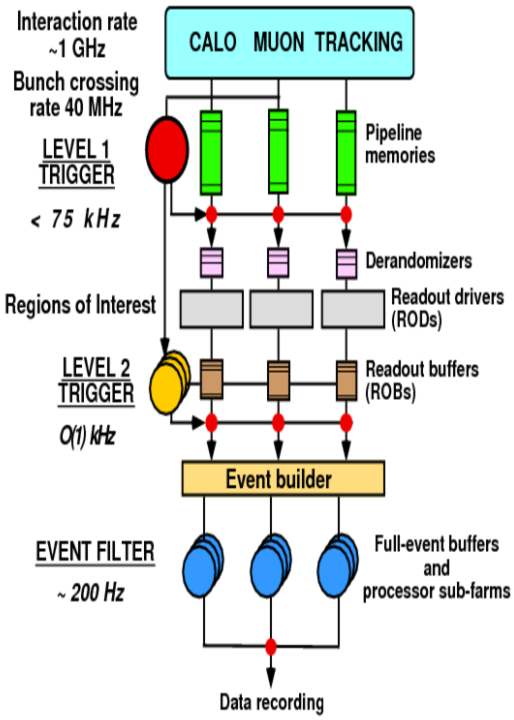


FIGURE 2.13: ***A schematic view of the ATLAS trigger system level [54].***

Level 2 and Event filter of the trigger system form the High Level Trigger (HLT) of the ATLAS detector. The nomenclature of the high-level trigger is given as follow:

$$[HLT]_[N][Type][Threshold][Info]_[Quality],$$

where:

- $[HLT]$: High Level Trigger (HLT).
- $[N]$: Number of particles, it is not noted for single particle.
- $[type]$: type of particles selected by the trigger (electron, muon ...).
- $[Threshold]$: particle's energy or transverse momentum recommendation.

- [$Info$]: refereed to specific requirements, "I" in case of isolation of the object, "V" means that the threshold can be varied and "H" when an isolation selection is applied to hadrons at Level 1.

- [$Quality$]: quality of particle identification (medium, loose, tight).

2.3.7 ATLAS distributed computing

The ATLAS experiment is meant to study proton-proton collisions at the LHC accelerator creating new particles that decay in complex ways as they move through layers of sub-detectors. The sub-detectors register each particle's passage and microprocessors convert the particle's paths and energies into electrical signals, combining the information to create a digital summary of the "collision event". The raw data per event is around one million bytes (1 Mb), produced at a rate of about 600 million events per second. In the first stage of the selection, the number of events is filtered from the 600 million per second picked up by detectors to 100.000 events per second for digital reconstruction. In a second stage, more specialized algorithms further process the data registering 200 events per second for approximately 50 thousands seconds per day, producing on the average around 16 TB of byte-stream data per day that will then be analyzed and made available to a very large community of physicists around the world. In order to cope with such amount of data the ATLAS Distributed Computing project [55] (ADC) was established to develop and operate a framework, following the ATLAS computing model, to enable data storage, processing and bookkeeping on top of the Worldwide LHC Computing Grid (WLCG) [56] distributed infrastructure. This section describes the main technologies used to optimize the usage of WLCG resources offered to ATLAS through Grid interfaces, including the Production and Distributed Analysis framework [57] (PanDA), and distributed data management [58] (DDM/Rucio).

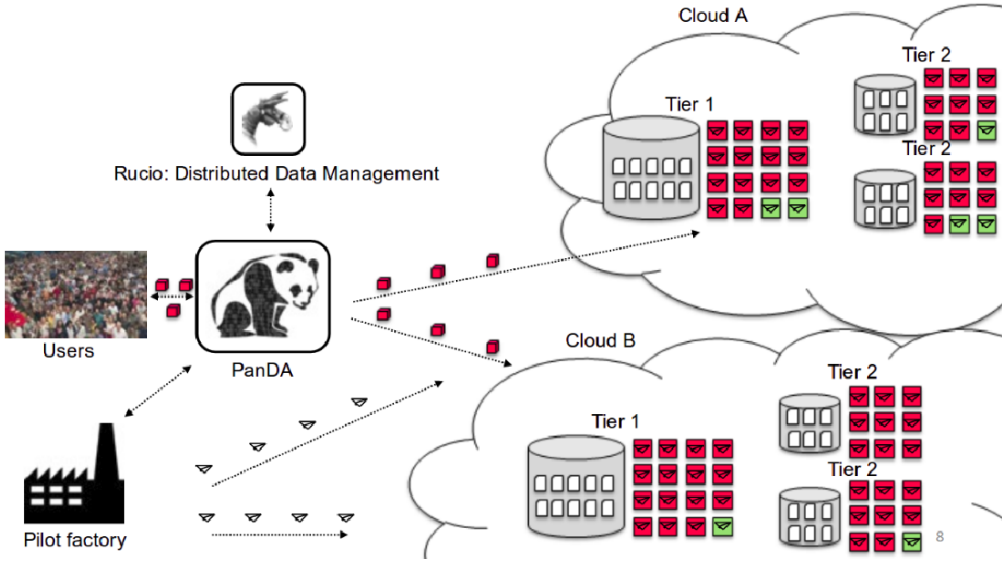


FIGURE 2.14: ***ATLAS computing Grid model.***

2.3.7.1 The world wide LHC computing Grid

The Worldwide LHC Computing Grid (WLCG) is a distributed infrastructure of computing resources used for production and analysis of data of the LHC experiments. It was designed to be organized in a hierarchy of computing centers of four tiers from Tier0 to Tier3 :

- **Tier 0:** the CERN computing center is the Only one Tier 0 site that exists in the $WLCG$. It was designed to perform prompt reconstruction of the raw data coming from the on-line data acquisition system and to distribute the raw data and the reconstructed output to Tier 1, and reprocesses data when the LHC is not running.



FIGURE 2.15: ***The left figure shows the CERN Data Center (Tier 0). On the right, servers at Tier 0 record a copy of primary LHC data, and distribute it to 13 Tier 1 centers around the world.***

- **Tier 1:** consists of 13 computer centers designed to store LHC data. They are responsible for storing a proportional share of raw and reconstructed data, as well as performing large-scale reprocessing and storing the corresponding output, distributing data to Tier 2; and storing a share of the simulated data that the Tier 2 produce.

CERN is connected to each of the 13 major Tier 1 centers around the world by Optical-fiber links at **10 gigabytes per second** of network. This dedicated high-bandwidth network is called the **LHC Optical Private Network (LHCOPN)**.

Country	Grid
Canada	TRIUMF
Germany	KIT
Spain	PIC
France	IN2P3
Italy	INFN
Nordic countries	Nordic Datagrid Facility
Netherlands	NIKHEF / SARA
Republic of Korea	GSDC at KISTI
Russian Federation	RRC-KI and JINR
Taipei	ASGC
United Kingdom	GridPP
US	Fermilab-CMS
US	BNL ATLAS

TABLE 2.3: ***List of Tier 1 Grid sites.***

- **Tier 2:** These sites are typically dedicated clusters run by Universities and scientific institutes. They can store enough data to perform individual analysis tasks, and do their share of simulation data production and data reconstruction. There are around 155 Tier 2 sites around the world.

Federation Name	Federation Accounting Name	Site(s)	Infrastructure	Institute Name
ATLAS Federation	ES-ATLAS-T2	IFIC-LCG2	EGI	IFIC, Valencia
ATLAS Federation	ES-ATLAS-T2	UAM-LCG2	EGI	UAM, Madrid
ATLAS Federation	ES-ATLAS-T2	ifae	EGI	IFAE, Barcelona
CMS Federation	ES-CMS-T2	CIEMAT-LCG2	EGI	CIEMAT, Madrid
CMS Federation	ES-CMS-T2	IFCA-LCG2	EGI	IFCA, Santander
LHCb Federation	ES-LHCb-T2	UB-LCG2	EGI	UB, Barcelona
LHCb Federation	ES-LHCb-T2	USC-LCG2	EGI	USC, Santiago

TABLE 2.4: ***List of Spanish Tier 2 Grid sites.***

- **Tier 3:** Tier-3 resources can be individual nodes or shared university clusters without any formal engagement to the WLCG. IFIC Tier-3 is attached to IFIC Tier-2. It currently has around 100 TB (60 TB under ATLAS Distributed Data Management (DDM tool) control plus 40 TB under IFIC control).

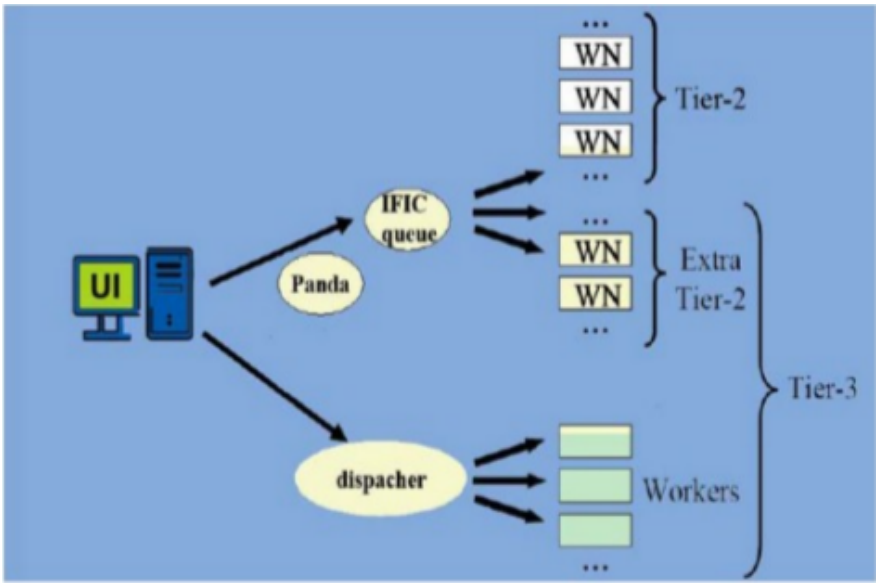


FIGURE 2.16: ***Schema of the IFIC Tier-3.***

The main components of the Worldwide LHC Computing Grid are :

- **Hardware:** Each Grid center combines the computing resources of more than 100,000 processors from 140 institutions in 33 countries, producing a massive collection of distributed supercomputer and storage systems.

- **Middleware:** Grid middleware stacks are used for Grid Computing and Storage Elements. For Storage Elements, the middleware defines a set of protocols and authentication methods which allow jobs to reference and access the data from the local or shared file system of a storage cluster. On Compute Elements, the middleware provides a common interface for running and managing jobs on different clusters by handling user authentication, accepting jobs and forwarding them to the Local Resource Management System (LRMS) of the cluster. The most important middleware stacks in the WLCG are : **EGI** (European Grid Infrastructure), **NDGF** (Nordic Data Grid Facility), **OSG** (Open Science Grid) and other partners.

- **Physics analysis software:** The physics software on the Grid includes programs such as **ROOT** [59], a set of object-oriented core libraries used by all the LHC experiments. **POOL** [60], a framework that provides storage for event data, and other software for modeling the generation, propagation and interactions of elementary particles. Grid projects supply much of the software that manages distribution and access, as well as job submission, user authentication and authorization. They also supply software known collectively as "middleware".

- **Networking :** CERN is connected to each of the Tier 1s around the world on a dedicated, private, high-bandwidth network called the Large Hadron Collider Optical Private Network [61] (LHCOPN). It consists of optical-fiber links working at 10 gigabytes per second, spanning oceans and continents.

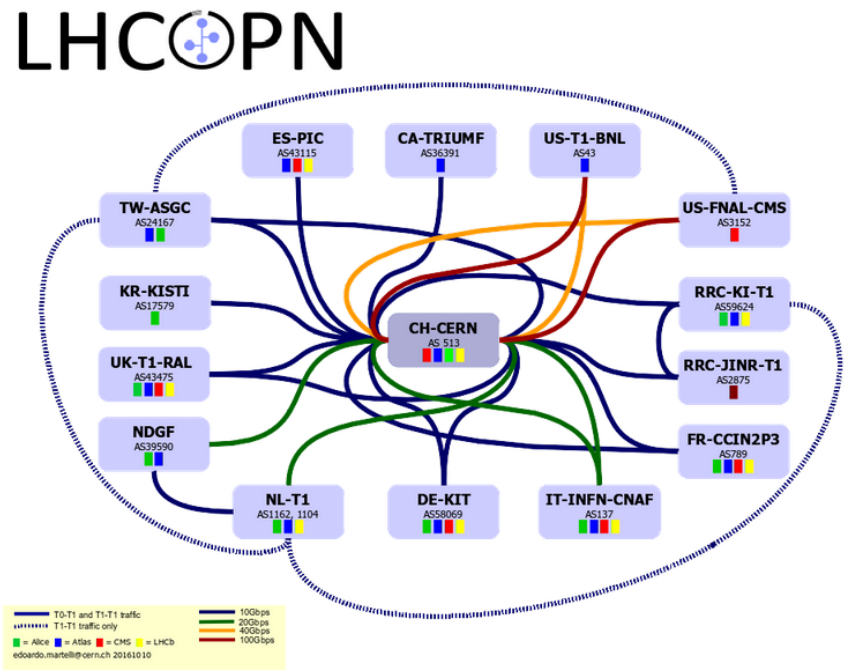


FIGURE 2.17: ***the Large Hadron Collider Optical Private Network (LHCOPN) map.***

2.3.8 ATLAS software distribution CVMFS

The CernVM File System [62] (CernVM-FS) is a network file system based on HTTP and designed to deliver scientific software onto virtual machines and physical worker nodes in a fast, scalable, and reliable way. The CernVM-FS repositories are located under /**cvmfs**, each repository is identified by a *fully qualified repository*. For the ATLAS experiment software, the fully qualified repository name is *atlas.cern.ch* although the hosting web servers are spread around the world.

Repository data can be replicated to multiple web servers and cached by standard web proxies such as Squid. In a typical setup, repositories are replicated to a handful of web servers in different locations. These replicas form the CernVM-FS Stratum 1 service, whereas the replication source server is the CernVM-FS Stratum 0 server. In every cluster of client machines, there should be two or more web proxy servers that CernVM-FS can use. These site-local web proxies reduce the network latency for the CernVM-FS clients and they reduce the load for the Stratum 1 service.

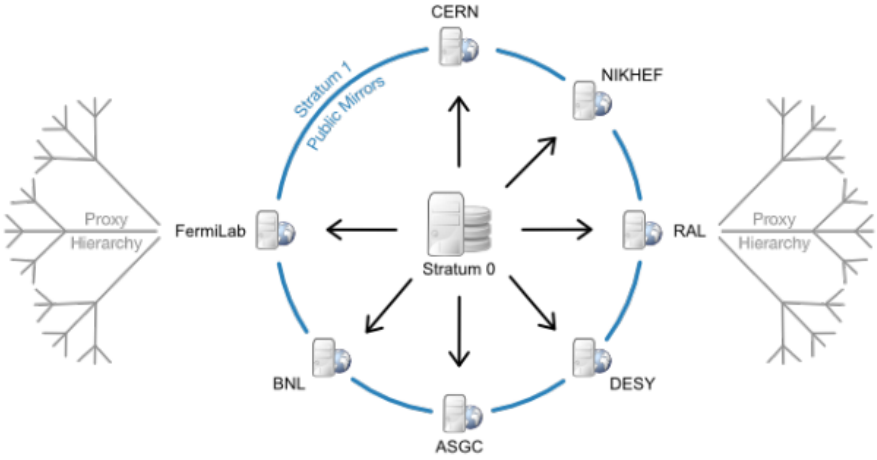


FIGURE 2.18: ***CernVM-FS content distribution network for the cern.ch domain: Stratum1 replica servers are located in Europe, the U.S. and Asia. One protected read/write instance Stratum 0 is feeding up the public.***

2.3.9 Event Data Model

The ATLAS Event Data Model [63] (EDM) refers to the content and format of the ATLAS data. EDM is a collection of classes, interface and concrete objects which together provide a representation of the physics Objects (electrons, muons, jets, etc) detected by ATLAS. The output of the simulation (MC) is stored as Raw Data Objects **(RDO)** and contains information similar to detected RAW of real data and the information about the generated event. The next level is the Event Summary Data **(ESD)** wich refers to event data written as the output of the reconstruction process. ESD is intermediate in size between RAW and the new Analysis Object Data **(xAOD)**. The xAOD is a reduced event representation, derived from ESD, suitable for analysis. It contains all of the necessary information for reconstruction of physics objects (missing energy transverse, jets,electrons, muons, etc) and other elements of interested analysis. Some users who work with xAOD files apply some additional analysis selection to produce Derived Analysis Object Data **(DAOD)**, this format is created by applying specific selection cuts to reduce the size of the file. The figure below presents the official supported set of the ATLAS data format.

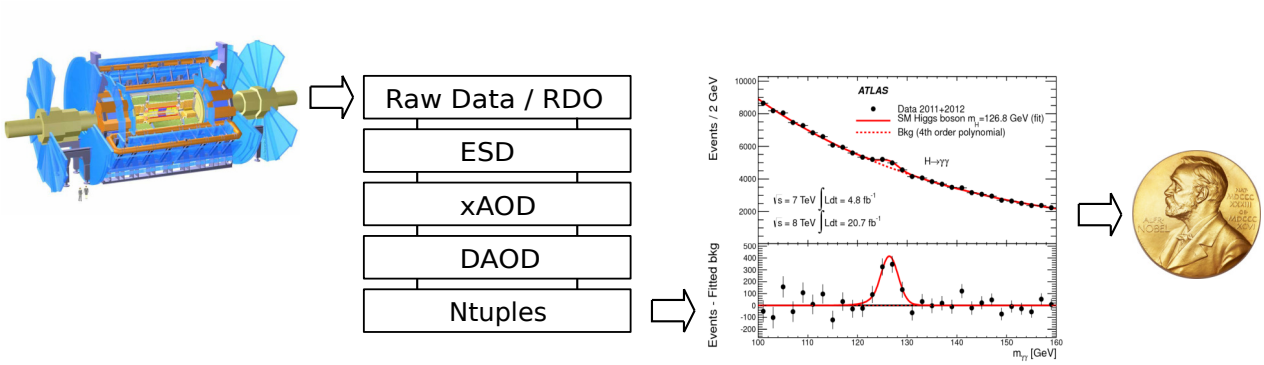


FIGURE 2.19: ***Schema of the ATLAS Event Data Model (EDM).***

2.3.10 ATLAS Dataset Nomenclature

Because of the large size of data in ATLAS It is not possible to put all the data from one run into one file. As result of this ATLAS uses a collections of files containing events and form the fundamental unit of ATLAS data and MC. These collections of files are called datasets. This section defines the nomenclature of physics datasets for ATLAS. Official datasets are real data or files generated (MC) using the production system they should be registered in both the Distributed Data Management **(DDM)** catalogs and in ATLAS Metadata Interface **(AMI)** in a general format :

Real Data Datasets: *Project.datasetNumber.physicsShort.prodStep.dataType.Version.*

Monte-Carlo datasets: *Project.runNumber.streamName.prodStep.dataType.Version.*

Where:

- Project: This field is a string which identifies the center of mass **(CM)** energy of proton-proton collision and the year of DAQ recording for data and the year of the production for MC dataset. For example the project in the whole year 2015 in a CM of 13GeV collisions are named data15_13TeV, mc15_13TeV.
- DatasetNumber: The dataset number is currently a 6 digit decimal number. It must be registered in the *datasetNumber broker* by the production manager or by a physics group before being used.
- RunNumber: The DAQ run number is a 31 digit number which is incremented for each run.
- PhysicsShort: This field is a text description of the physics channel.
- StreamName: This field is a string identifying the data stream, which is part of the file names, and is assigned by the Trigger and DAQ configuration.

- ProdStep: This is a string which gives the production step which was used to create the data. Although this field is not needed to define the dataset, since all the production steps are encoded in the version field
- DataType: This field is a string which identifies the format EDM of data in the dataset.
- Version: The version field is an encoding of the configuration used for each of the production steps which were passed by the data in the dataset.

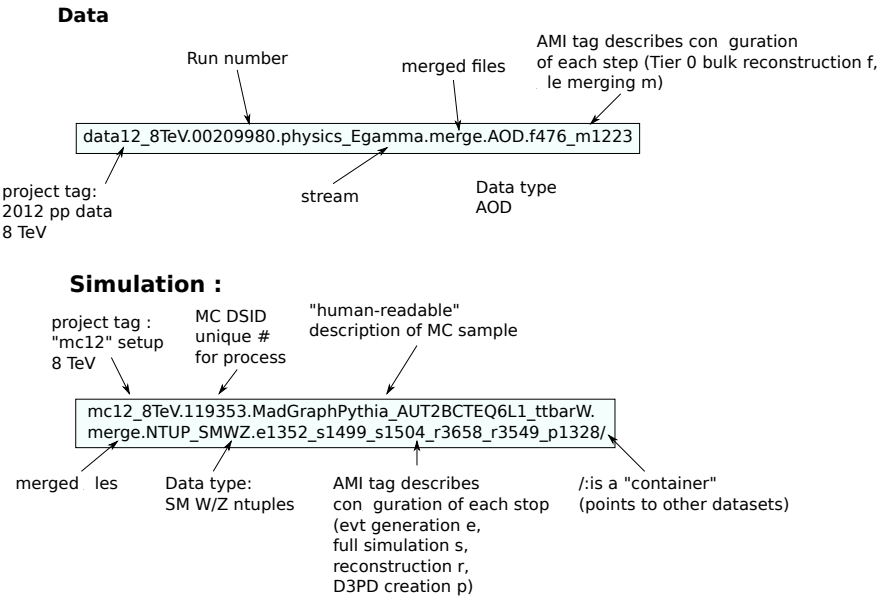


FIGURE 2.20: ***The ATLAS Dataset Nomenclature.***

2.3.11 ATLAS Distributed Data Management (RUCIO)

RUCIO is the ATLAS Distributed Data Management [58] (DDM) project that manages ATLAS data on the grid in order to help the collaboration store, manage and process LHC data in a heterogeneous distributed environment. DDM manages more than 160PB of physics data across more than 130 sites globally. Rucio organizes not only the RAW data from the detector, but also handles all data inputs and outputs from the collaborations users.

2.3.12 Conclusion

This chapter showed the important part of the experimental device in high energy physics. The large hadron collider and its four experiments played a crucial role in detecting and understanding of several phenomena predicted by theoretical physics. The high LHC Luminosity is the next phase of the LHC, where the ATLAS system will collect most of data and in that sense it is the phase of our exploration that we let us to search for new physics beyond the Standard Model. Proton beams will be so intense that pileup in the machine

will be five to then times greater than the actual one. Therefore, an upgrade of the detector is extremely needed to follow this huge LHC progress.

Our group in Rabat participated in collaboration of KTH group to the Forward calorimeter upgrade study. In the next chapter we will discuss the main simulation technics we have developed for this concern.

Later on, we return to the physics analysis analysis part of this thesis which is dedicated to the search for new physics beyond Standard Model in the WZ resonants fully leptonic decays.

Chapter 3

Performance studies of the super Forward Calorimeter granularity

3.1 Introduction

The ATLAS forward calorimeter is located in the environment near the LHC beam-line where the particle density and the radiation dose are highest. At HL-LHC, the performance of the FCal will be degraded [64] because of the high ionization rate which will result in space charge effects. The resistors used in the FCal anode high voltage chain were designed to limit currents from the supplies in case of arcing and protect the sensitive electronics from large pulses. These resistors are too large for currents at HL-LHC and a significant voltage drop across resistors inside cryostat may occur.

Two solutions for reducing the degradation have been under study, the first option is a complete replacement of the actual FCal system. The new FCal called super-FCal (sFCal) would have similar design as the existing FCal, with smaller liquid argon ionization gaps, and lower high voltage protection resistors values. The second proposed solution is the installation of a small calorimeter named Mini-FCal in front of the FCal, which would reduce the flux of radiation in the first compartment of the FCal. This work focuses on the simulation studies of the FCal (sFCal) in collaboration with the KTH ATLAS group of Sweden, in order to evaluate the impact of a finer readout granularity on the position resolution. Results of this study will help the author's group to decide on the final upgrade choice for the FCal.

3.2 The ATLAS forward calorimeter

The liquid argon Forward Calorimeter (FCal), which covers the pseudo-rapidity of about $3.2< |\eta| <4.9$ [65], consists of three LAr calorimeter modules named FCal1, FCal2 and FCal3. The particles produced at the interaction point travel 4.7 m before hitting the front of the FCal.

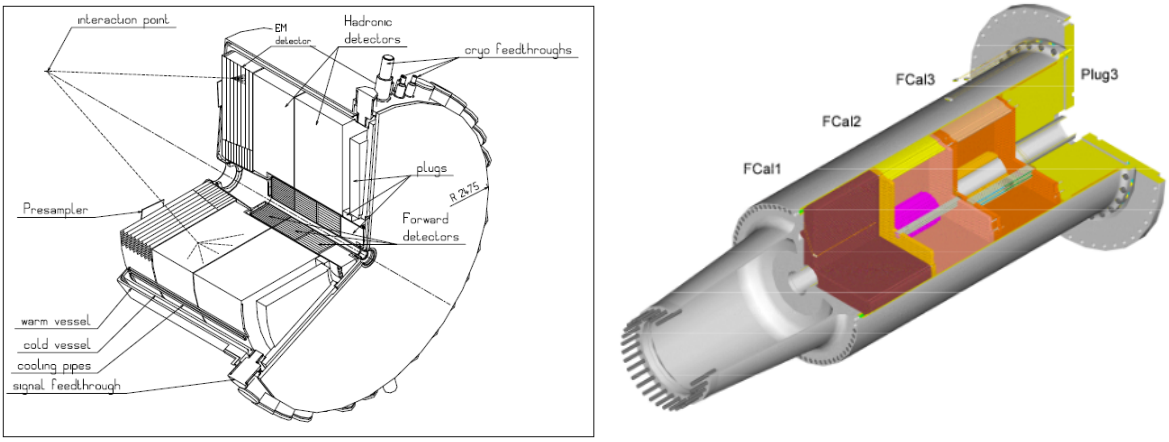


FIGURE 3.1: ***The left figure shows a schematic cutaway view of the ATLAS EndCap cryostat, showing the location of the forward calorimeter relative to the other EndCap calorimeters [66]. On the right, a cut-away view of the ATLAS forward calorimeter [67]. Particles from the interaction point traverse the electromagnetic FCal1 module (Cu/LAr), then the two hadronic FCal modules (W/LAr).***

The first module is made of a copper absorber matrix in which copper tubes (cathodes) and copper rods (anodes) with 270 μm of liquid-argon gaps in between which are maintained by PEEK fibers (Figure 3.2). The cathode is grounded with a high positive voltage of about +250 V applied to the anode to drift ionization electrons by the electric field. The second and the third modules, FCal2 and FCal3 respectively are hadronic LAr calorimeters with high density tungsten absorber to obtain a short particle mean free path. The anode and the cathode are separated with liquid argon gaps of 380 μm and 500 μm respectively in FCal2 and FCal3. Detailed information about the design and the construction of the FCal are summarized Table 3.1.

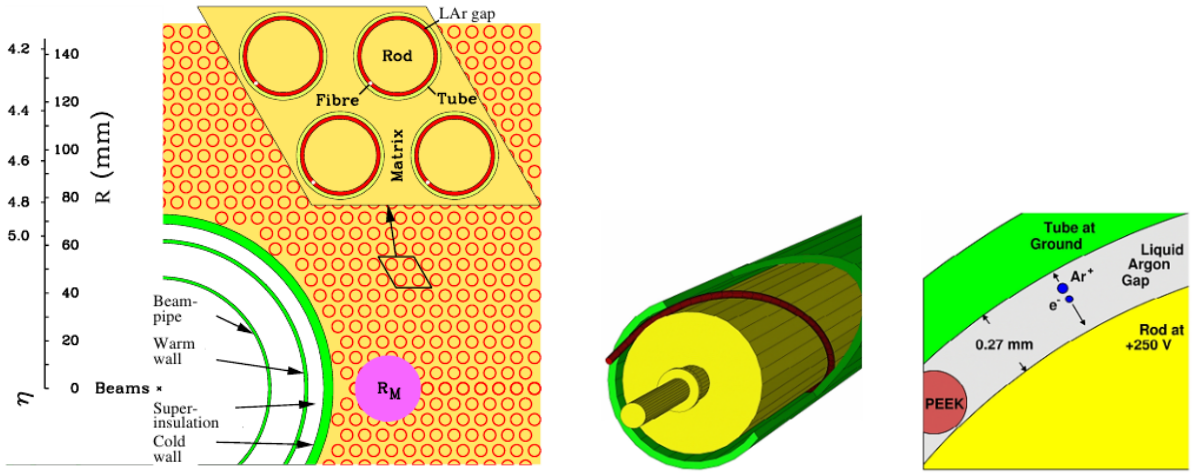


FIGURE 3.2: ***On the left, a transverse view of the forward calorimeter tube matrix [22]. On the right, a close-up views of an electrode in the FCal1 [67].***

	FCal1	FCal2	FCal3
Module	Electromagnetic	Hadronic	Hadronic
Absorber material	Copper	Tungsten	Tungsten
LAr gap (mm)	0.27	0.38	0.5
Radiation length	27.6	91.3	89.2
High-Voltage Cathode	+250	+375	+500
Number of tubes	12260	10200	8224
Mass (kg)	2119	3826	3695

TABLE 3.1: ***General parameters for the Forward calorimeter modules [65].***

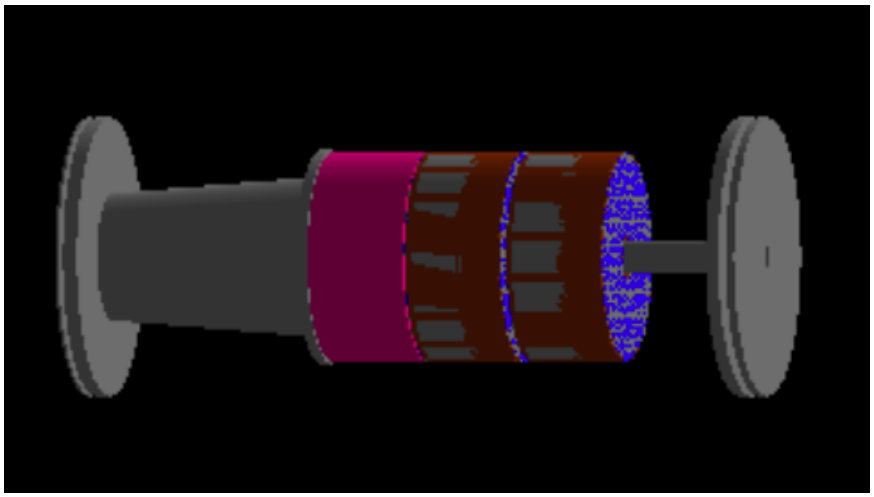


FIGURE 3.3: ***The forward calorimeter in a standalone Geant4 simulation. The three FCal modules and the Cryostat in grey are represented.***

The readout channels are divided into two categories namely: summed channels which are made of 4 tiles of 4 gaps in the FCal1 module (6 gaps in the FCal2 and 9 gaps in the FCal3 respectively) and unsummed tiles which covers the inner and outer edges of the FCal modules consisting of a single n-tube group (Figure 3.4).

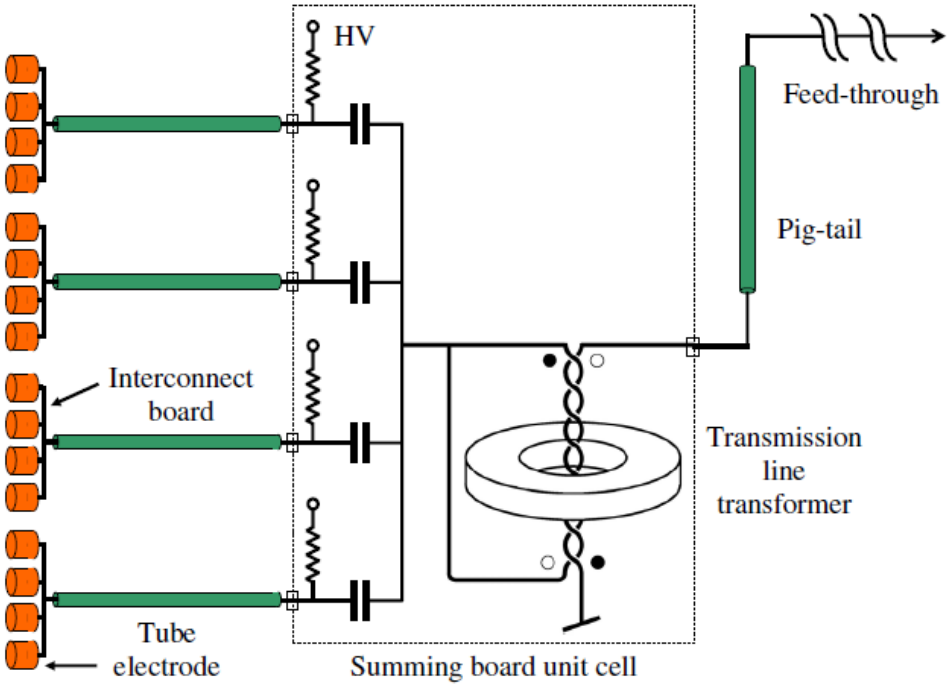


FIGURE 3.4: ***Readout chain of the ATLAS Forward calorimeter [22].***

3.3 Monte Carlo samples

This study uses Monte Carlo samples from standalone GEANT4 [68] simulations of the forward calorimeter (FCal) and super forward calorimeter (sFCal). The FCal consists of three modules with the same nominal outer dimensions, an electromagnetic module made of copper followed by two hadronic ones made of tungsten alloy. The corresponding parameters of these modules are defined inside the parameter files that contain details about the dimensions and the positions as well as FCal modules. Data files describing the gap position and cabling as in ATLAS FCal were used to obtain the correct gap position and gap grouping into readout cells. In FCal1 4 electrodes are connected together in tiles on the front face. Except at the inner and outer radius 4 such tiles are grouped into one readout cell, in FCal2 and FCal3 the tiles consist of 6 and 9 electrodes respectively, while in the sFCal the tiles will be readout individually. The readout granularity is visible in Figure 3.5.

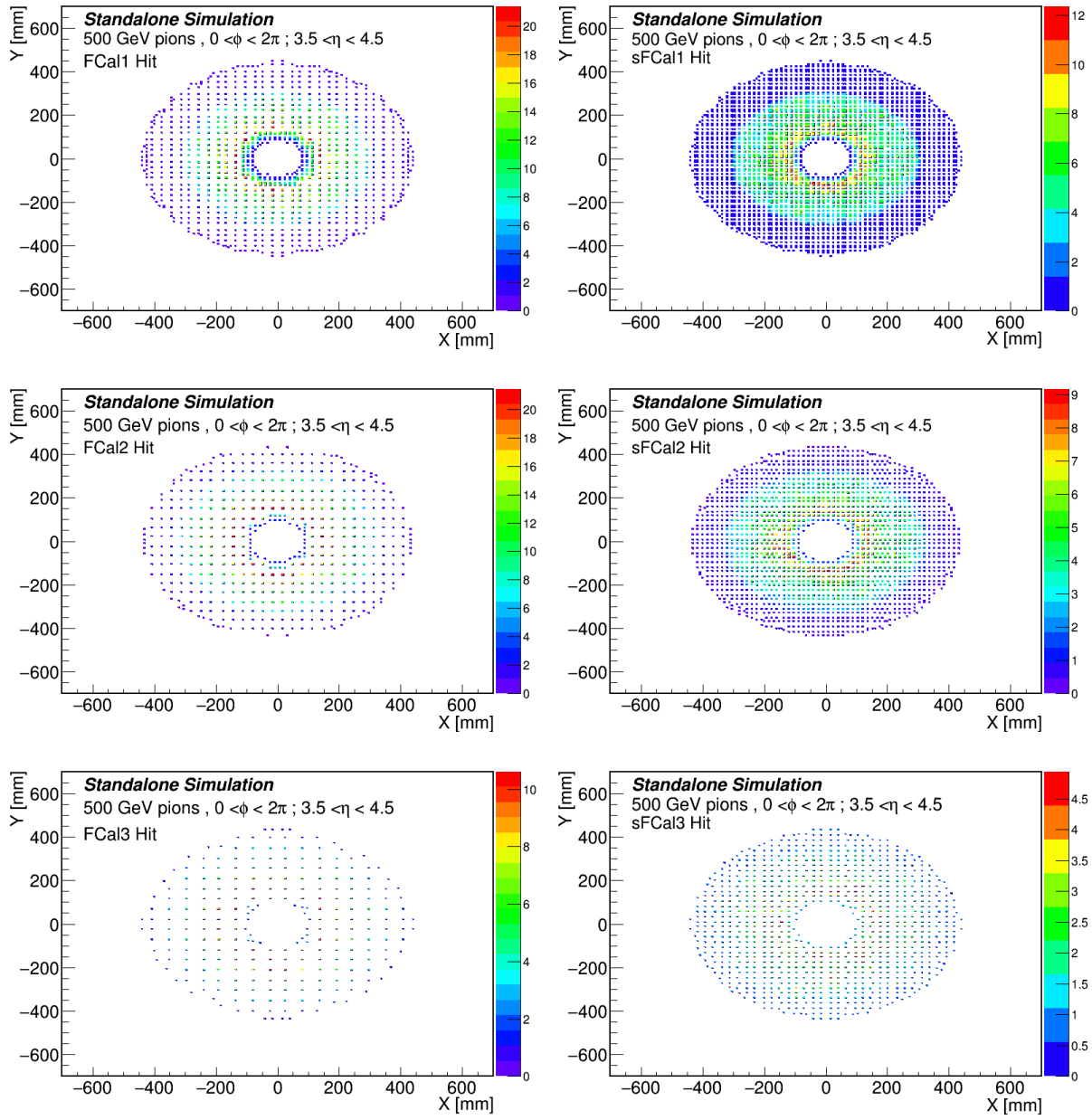


FIGURE 3.5: ***Hits in the different modules of FCal (Left), and sFCal (Right) .***

The analysis is performed using a collection of Ntuples provided by the FCal/sFCal standalone simulation and saved in separated root files [69] which contain the relevant information. This work focuses on the response and the position resolution for electrons and pions with energies of 5,10, 20, 50, 100, 200, 300 and 500 GeV in η between 3.5 and 4.5 where the shower energy containment is maximaum. The MC samples used in this analysis are listed in Table 3.2:

Particle	MC Samples	Number of events
e^-	fcal_e_5GeV.root	20000
	fcal_e_10GeV.root	20000
	fcal_e_20GeV.root	20000
	fcal_e_50GeV.root	20000
	fcal_e_100GeV.root	10000
	fcal_e_200GeV.root	10000
	fcal_e_300GeV.root	10000
	fcal_e_500GeV.root	10000
	sfcal_e_5GeV.root	20000
	sfcal_e_10GeV.root	20000
	sfcal_e_20GeV.root	20000
	sfcal_e_50GeV.root	20000
	sfcal_e_100GeV.root	10000
	sfcal_e_200GeV.root	10000
	sfcal_e_300GeV.root	10000
	sfcal_e_500GeV.root	10000
π^-	fcal_pi_5GeV.root	20000
	fcal_pi_10GeV.root	20000
	fcal_pi_20GeV.root	20000
	fcal_pi_50GeV.root	20000
	fcal_pi_100GeV.root	10000
	fcal_pi_200GeV.root	10000
	fcal_pi_300GeV.root	10000
	fcal_pi_500GeV.root	10000
	sfcal_pi_5GeV.root	20000
	sfcal_pi_10GeV.root	20000
	sfcal_pi_20GeV.root	20000
	sfcal_pi_50GeV.root	20000
	sfcal_pi_100GeV.root	10000
	sfcal_pi_200GeV.root	10000
	sfcal_pi_300GeV.root	10000
	sfcal_pi_500GeV.root	10000

TABLE 3.2: ***Standalone FCal/sFCal Samples used in the analysis.***

3.4 Electron Analysis

The electrons deposit their energy mainly in the first part of the FCal/sFCal. In order to contain as much of the shower as possible, the analysis used a cylindrical cluster with 8 cm radius around the most energetic cells in FCal1/sFCal1 [70]. The response calibration of the FCal1(sFCal1) to electrons was obtained from the linearity between the nominal electron energy and the energy deposited in the FCal1/sFCal1 cluster. The ratio is in agreement with earlier [**studiesGillberg_2011**]. The aims of this analysis were to establish the FCal (sFCal) energy resolution, to study the performance of the FCal versus the sFCal and to measure the position resolution using both S-Shape [71] and logarithmic weighting [72] corrections. A comparison of the results between FCal and sFCal will be discussed in the section.

3.4.1 Linearity and Energy resolution

The energy response of the sFCal/FCal is illustrated in Figure 3.6, where the Y axis presents the average energy deposited in the LAr gaps of the cluster while the X axis presents the nominal electron energy. The energy distributions were fitted by a linear function of the form: $E_{deposit} = aE_{e^-}$. The fit parameters for both FCal and sFCal are shown in Table 3.3.

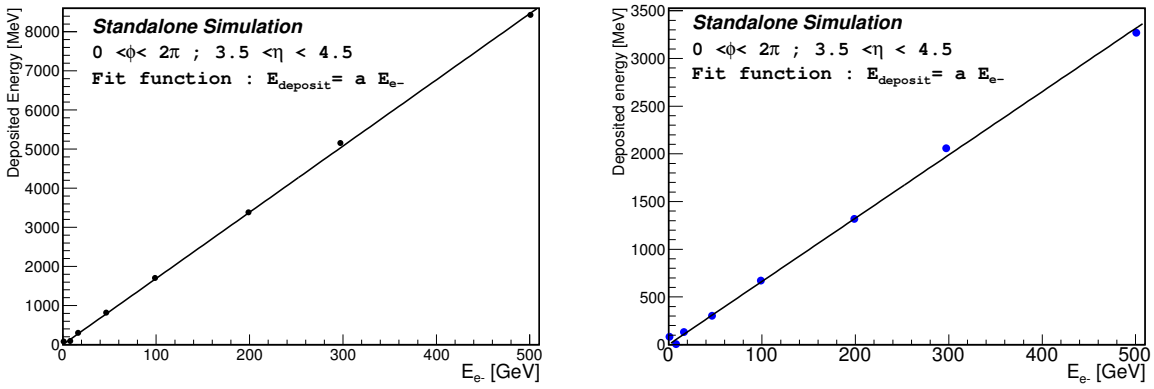


FIGURE 3.6: ***The response linearity for electrons taken from the first compartment of the FCal (left) and the sFCal1(right) standalone simulation.***

Detector	a [MeV/GeV]	χ^2/NDF
FCal	16.93±0.045	0.7/7
sFCal	6.63±0.036	0.5/7

TABLE 3.3: ***The fit parameters :*** $E_{deposit} = a.E_{e^-}$ ***for both FCal and sFCal.***

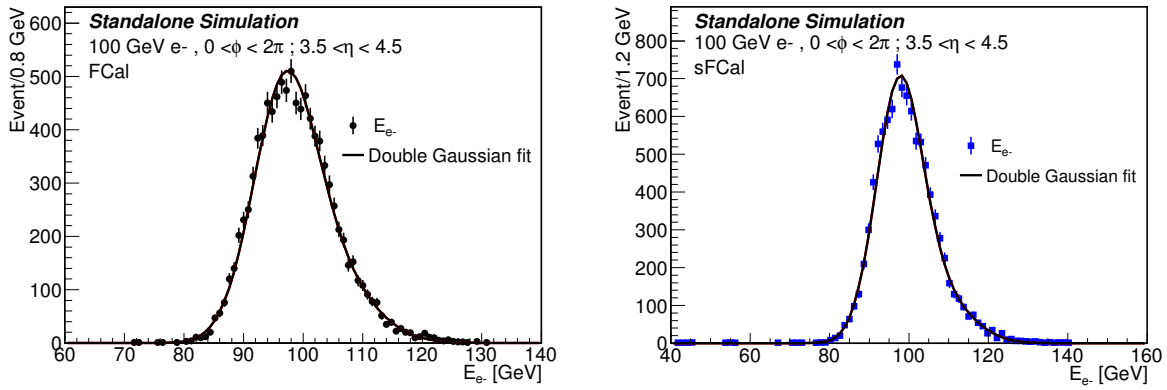


FIGURE 3.7: ***Electron energy distribution in FCal (left) and sFCal (right), obtained using 8 cm radius cluster around the most energetic FCal1 (sFCal1) cells. Data is fitted with double Gaussian function.***

The relative energy resolution $\frac{\sigma_E}{E_{particle}}$ for a given calorimeter system varies with the particle energy $E_{particle}$ and can be written in a more general way as:

$$\frac{\sigma_E}{E_{particle}} = \frac{a}{\sqrt{E_{particle}}} \oplus b, \tag{3.1}$$

where σ_E is the standard deviation of the deposited energy distribution in the FCal/sFCal in [GeV], "a" is the Stochastic term which includes the fluctuations related to the physical development of the shower, and "b" is the constant term that includes contributions which are rnergy independent. No electronics noise is included in these simulations.

A degradation in the sFCal resolution due to lower sampling fraction gives an increase of the stochastic term 28.5±0.40 [$\%\sqrt{GeV}$] in the sFCal compared to 25.4±0.47 [$\%\sqrt{GeV}$] in FCal . The fitted constant term is slightly smaller in FCal 6.12±0.10 [%] than sFCal 6.73±0.08 [%] (Figure 3.8 and Table 3.4).

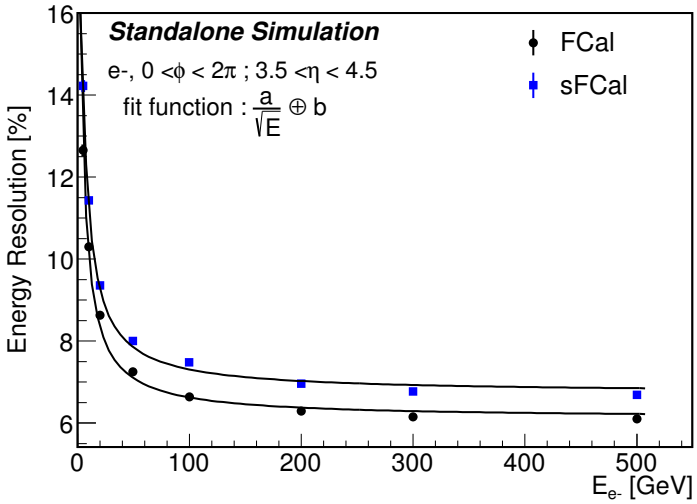


FIGURE 3.8: ***Energy resolution of the FCal response to electrons as a function of the nominal electron energy, from analysis of FCal1 (sFCal1) standalone simulation, and fitted with the function in the Equation*** (3.1)***. The uncertainties are estimated using the propagation of error.***

Detector	Stochastic term ($\%\sqrt{GeV}$)	Constant term (%)
FCal	25.4±0.47	6.12±0.10
sFCal	28.5±0.40	6.73±0.08

TABLE 3.4: ***Electron energy resolution fit results for FCal and sFCal. The uncertainties are estimated using the propagation of error.***

3.4.2 Pointing resolution

A study of the ϕ position resolution of the first module in FCal/sFCal was performed. The measured ϕ coordinate is defined using the barycenter within the energy cluster. The measured ϕ is given as follows:

$$\phi_{Measured} = \frac{\sum_{i=1}^{N} E_i.\phi_i}{\sum_{i=1}^{N} E_i}, \tag{3.2}$$

where E_i is the energy deposited in the i^{th} cell (group for FCal or tile for sFCal) and ϕ_i in [rad] is the azumith angle of its center, and N refers to the number of cells in the FCal or sFCal cluster.

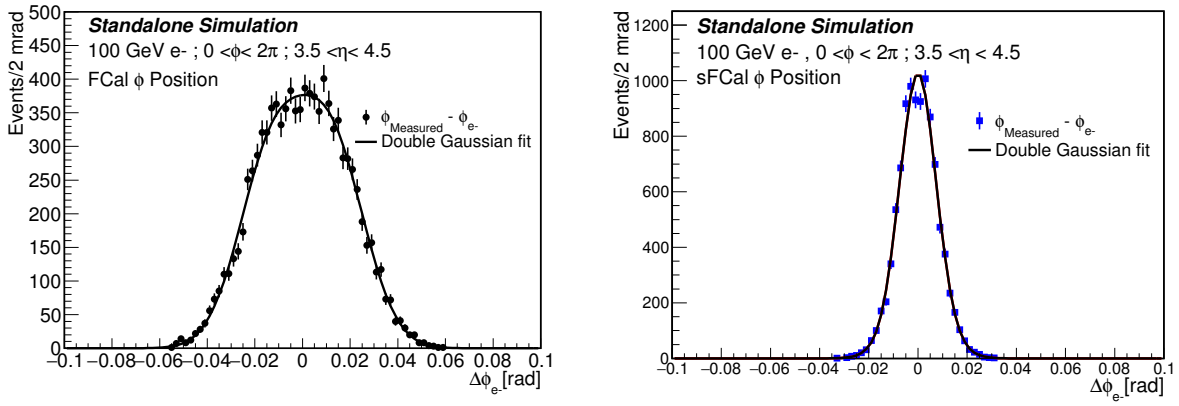


FIGURE 3.9: ***Pointing ϕ resolution without S-Shape correction in the left for FCal (σ_ϕ= 18.99± 0.13 mrad) and for the sFCal in the right (σ_ϕ= 8.02± 0.13 mrad) for 100 GeV electrons fitted by double Gaussian.***

In order to have a better resolution in the ϕ pointing measurement, two methods were used. The first one is based on the correction of the S-shape ϕ using a look-up-table interpolation, the second uses logarithmic weighting. The measured $\Phi_{Measured}$ position versus the true Φ_{True} position before correction in a window $\Delta\phi \times \Delta\eta = 0.4{\times}0.1$ is presented in the fig 3.10.

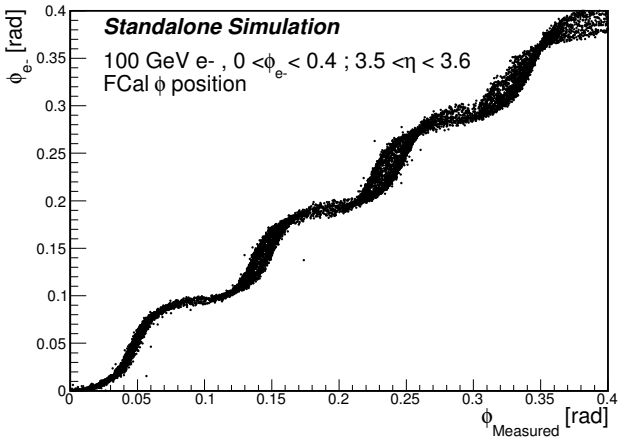


FIGURE 3.10: ϕ_{true} ***as a function of*** $\phi_{Measured}$ ***measured in the FCal. It gives a S-shape distribution.***

3.4.2.1 Correction of the ϕ S-shape position in the FCal

Due to the finite size of the cells of the FCal, the energy weighted barycenter of a cluster is shifted to the center of a cell in ϕ direction, leading to an S-shape in the ϕ measurement of the electron position. In order to improve the pointing resolution of the detector, a look-up-table was created using 100000 simulated events of electrons at 100 GeV. Since the phi correction is η and ϕ dependent an individual S-shape correction for each 0.1 η range was obtained for the full η range from 3.5 up to 4.5. Furthermore the correction of S-Shape was assumed

to be independent of the energy, due to the fact that the Moliere radius has a negligible energy dependence. Thus, we are applying a 100 GeV corrected ϕ to correct the S-shape for all energies. The true position (Φ_{True}) position versus the corrected $\Phi_{corrected}$ position in a window $\Delta\phi x\Delta\eta$ = 0.4x0.1 and the ϕ pointing resolution of the FCal are presented in Figure 3.11.

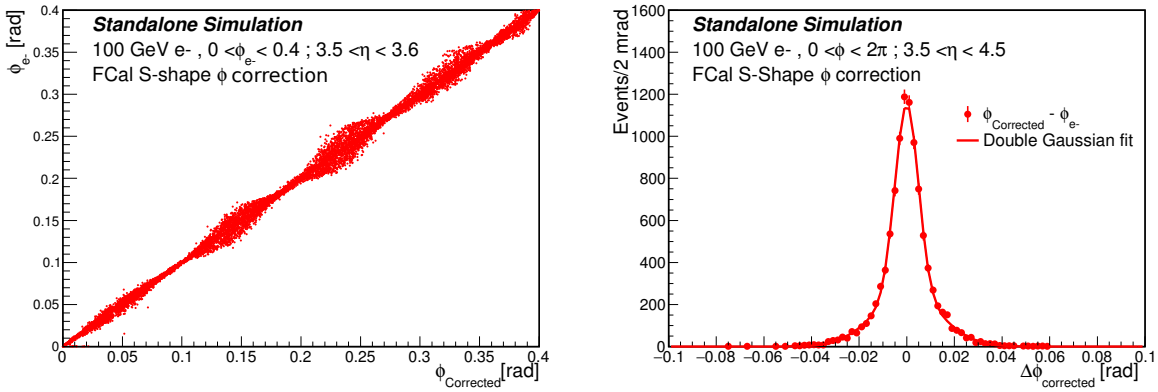


FIGURE 3.11: ϕ_{true} ***as a function of*** $\phi_{Measured}$ ***after S-shape correction (left). A linear interpolation is computed to correct the S-Shape position. The pointing*** ϕ ***resolution for 100 GeV after S-shape correction (***σ_ϕ***= 10.02± 0.07 mrad) is shown in the right.***

3.4.2.2 Logarithmic weighting

A measurement of ϕ_{e-} for both FCal and sFCal was computed to take the lateral spread of the shower by using the Logarithmic Weighting (L.P), to improve the pointing resolution of a calorimeter $\phi_{L.P}$ is defined as :

$$\phi_{L.P} = \frac{\sum_{i=1}^{N} w_i.\phi_i}{\sum_{i=1}^{N} w_i}, \tag{3.3}$$

the weights w_i were calculated with the following formula :

$$w_i = w_{offset} + \log\left(\frac{E_i}{E_{Cluster}}\right), \tag{3.4}$$

where the w_{offset} is a tunable offset (set to 4.7 by the ATLAS collaboration). It has been chosen to take in to account only cells with fractional energy below 1% of the cluster energy. E_i is the cell redout (group/tile) energy and $E_{Cluster}$ is the total energy in a cluster of 8 cm radius around the most energetic cell.

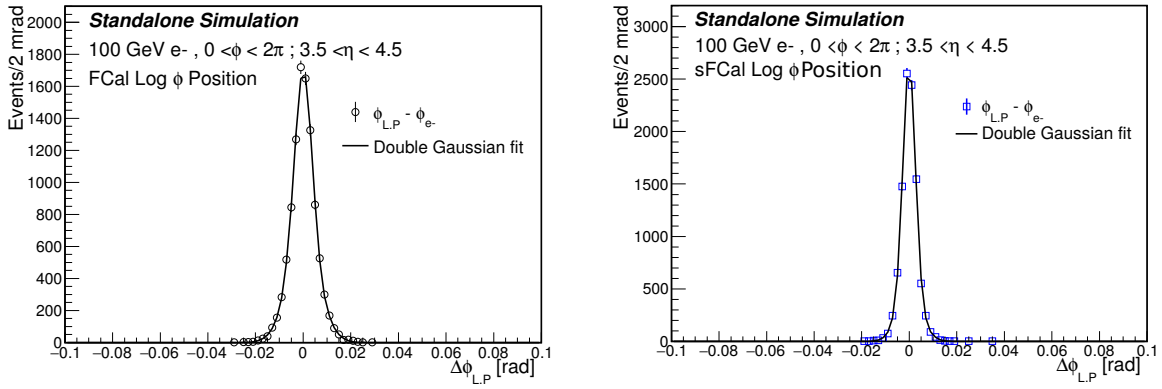


FIGURE 3.12: ***The distribution of*** $(\phi_{e-} - \phi_{W.L})$ ***in the FCal1 (left) and sFCal1 (right) for 100 GeV e- fitted with a double Gaussian function.***

The distributions of the ϕ pointing resolution as a function of particle energy were fitted with functions of the form:

$$\sigma_\phi = \frac{c}{\sqrt{E_{particle}}} \oplus d, \tag{3.5}$$

where "c" $[mrad\sqrt{GeV}]$ is the stochastic term and "d" $[mrad]$ present the constant term.

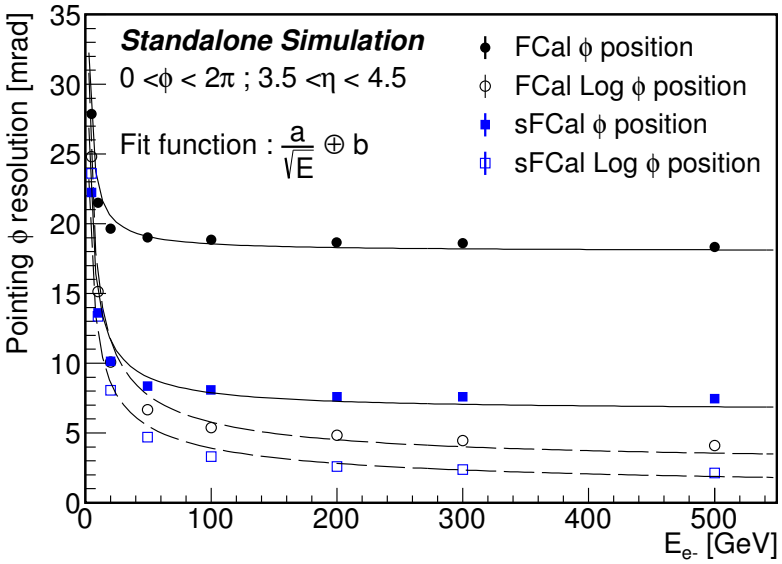


FIGURE 3.13: ***Position*** ϕ ***Resolution for electrons, as a function of electron energy, from analysis of FCal1 (sFcal) standalone simulation, fitted with the function in the Equation*** (3.5)***. The uncertainties are estimated using the propagation of error from double gaussian fit.***

Detector	Stochastic term ($mrad\sqrt{GeV}$)	Constant term (mrad)
FCal	44.4±2.45	18±0.38
sFCal	43.21±2.5	6.60±0.6
FCal log ϕ position	50.9±2.23	2.73±0.96
sFCal log ϕ position	38±0.10	0.75±0.032

TABLE 3.5: ***Electron pointing ϕ resolution fit results for FCal and sFCal. The uncertainties are estimated using the propagation of error.***

It has been found that the ϕ pointing resolution for electrons is clearly better in sFCal than FCal (Figure 3.13) both with and without correction. In the case of logarithmic weighting the FCal1 Stochastic term "c" (50.9±2.23 $mrad\sqrt{GeV}$) decreases by 25% for sFCal1 (38±0.10 $mrad\sqrt{GeV}$), while the constant term decreases by a factor of 3.4 . The low position resolution for uncorrected FCal is recovered by the logarithmic weighting.

3.5 Pion analysis

The FCal and the sFCal response to pions was studied in pseudo-rapdity 3.5< $|\eta|$ <4.5, since the shower containment in this region is at maximum. The deposited energy in the LAr gaps within a cylindrical cluster of 16 cm radius for both FCal and sFCal are converted to the total reconstructed energy using the calibration parameters obtained by normalizing to the pion energy. The larger cluster radius is motivated by the size of the hadronic showers. Since the S-shape in the ϕ measurement of the pion position was not present, only logarithmic weighting method was taken into account to measure the pointing resolution in ϕ for both FCal and sFCal. Further details are described in the following sections.

3.5.1 Energy resolution

The energy of pion is reconstructed by summing the deposited energy in the three FCal/sFCal compartments within 16 cm radius around the most energetic cells [70]:

$$E_{pion} = \alpha_1 E_{FCal1} + \alpha_2 E_{FCal2} + \alpha_3 E_{FCal3}, \tag{3.6}$$

each FCal modules is characterized by its own calibration parameters, α_1, α_2, α_3 respectively for FCal1, FCal2 and FCal3 respectively (Equation (3.6)). These parameters are chosen by optimizing the energy resolution and setting deposited energy in the cluster to the nominal beam particle energy. The estimation of these parameters is calculated by minimizing the difference (χ^2) between the nominal beam energy (200 GeV pions) and the deposited

energy, where χ^2 is calculated using the following formula:

$$\chi^2 = \sum_{0}^{N} (\alpha_1 E_{FCal1} + \alpha_2 E_{FCal2} + \alpha_3 E_{FCal3} - 200)^2, \tag{3.7}$$

where $E_{FCal1}, E_{FCal2}, E_{FCal3}$ are the deposited energy in each FCal (sFCal) compartment. The following table presents the FCal and sFCal calibration parameters to the pions response.

Detector	α_1 [GeV/MeV]	α_2 [GeV/MeV]	α_3 [GeV/MeV]
FCal	0.065	0.082	0.083
sFCal	0.17	0.16	0.13

TABLE 3.6: ***FCal and sFCal calibration parameters to pion for each module.***

For both FCal and sFCal the energy distribution for 100 GeV pions obtained using a cylindrical cluster of 16 cm radius around the most energetic cells which presents a Gaussian-like shape as shown in Figure 3.14. The mean value is centrated around 100 GeV and the energy resolution is equal to 8.17±0.32 % and 8.89±0.24 % for both FCal and sFCal respectively.

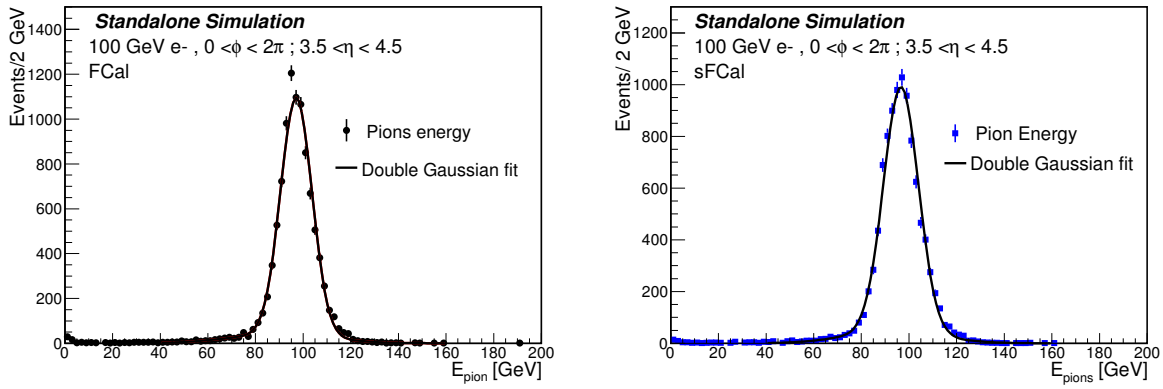


FIGURE 3.14: ***Pion energy distrubition, obtained using 16cm cylinder cluster around the most energetic FCal1, FCal2 and FCal3 readout cell (group or tile), fitted with sum of a double Gaussian.***

The energy resolution of pion as a function of nominal energy (Figure 3.15) for both FCal and sFCal is fitted with the Equation (3.1). For pions below 100 GeV the FCal has slightly better resolution than sFCal, although FCal and sFCal present the same energy response to pions. The best parameters of fit are listed in (Table 3.7).

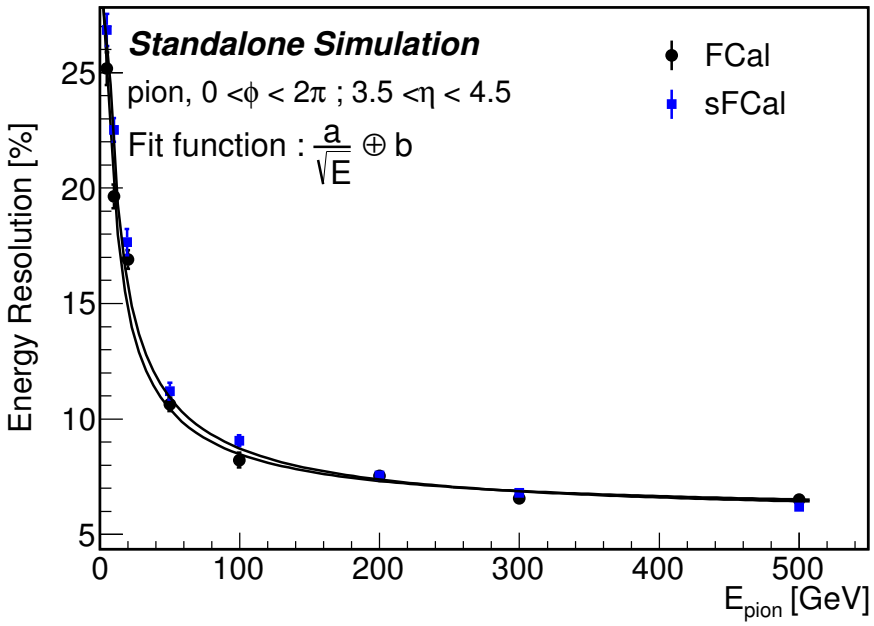


FIGURE 3.15: ***Energy resolution of the FCal response to pions, as a function of nominal pions energy, from analysis of FCal1 (sFCal1) standalone simulation, fitted with the function in the Equation*** (3.1)***. The uncertainties are estimated using the propagation of error.***

Detector	Stochastic term ($\%\sqrt{GeV}$)	Canstant term (%)
FCal	65.80±1.05	5.72±0.12
sFCal	60.60±1.00	5.93±0.13

TABLE 3.7: ***Pion energy resolution fit results for FCal and sFCal. The uncertainties are estimated using the propagation of error.***

3.5.2 Position resolution

The pointing ϕ resolution for pions was studied using two methods. The first one is based on the center of gravity technique (Equation 3.2) and the second one was computed to take into account the lateral spread of the shower by using the logarithmic weighting technique (Equation 3.3).

The distributions of $(\phi_{pion} - \phi_{measured})$ using the center of gravity method for 100 GeV pion are gaussian-like in both FCal and sFCal, and are fitted with a double Gaussian function. The pointing resolution in ϕ for 100 GeV pions is better in sFCal (22.06±0.27 mrad) than FCal (30.73±0.36 mrad) because of the small size of sFCal's readout cells.

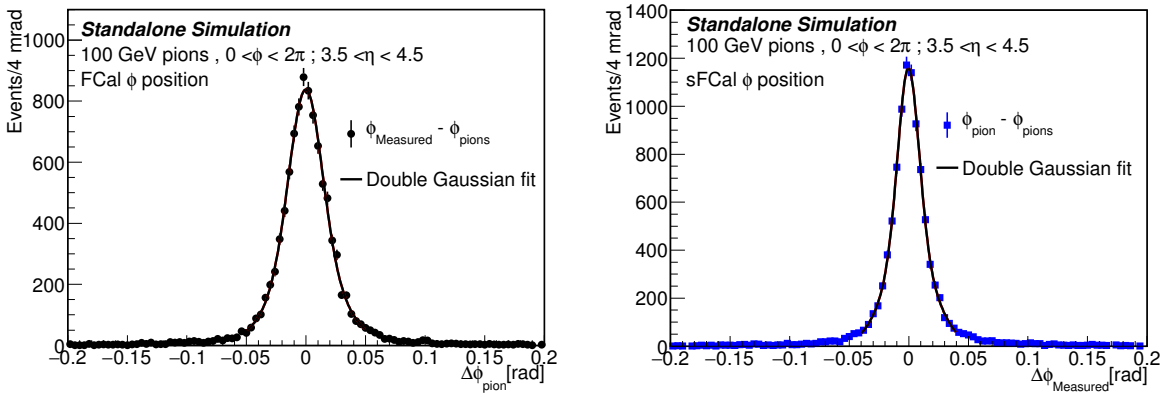


FIGURE 3.16: ***the distribution of*** $(\phi_{pion} - \phi_{cell})$ ***in the FCal1 (left) and sFCal1 (right) fitted with sum of a double Gaussian.***

After applying the logarithmic weighting correction as described in section 3.4.2.2, the ϕ pointing resolution was improved by a factor of 1.40 and 1.23 in the FCal and sFCal respectivly (Figure 3.17).

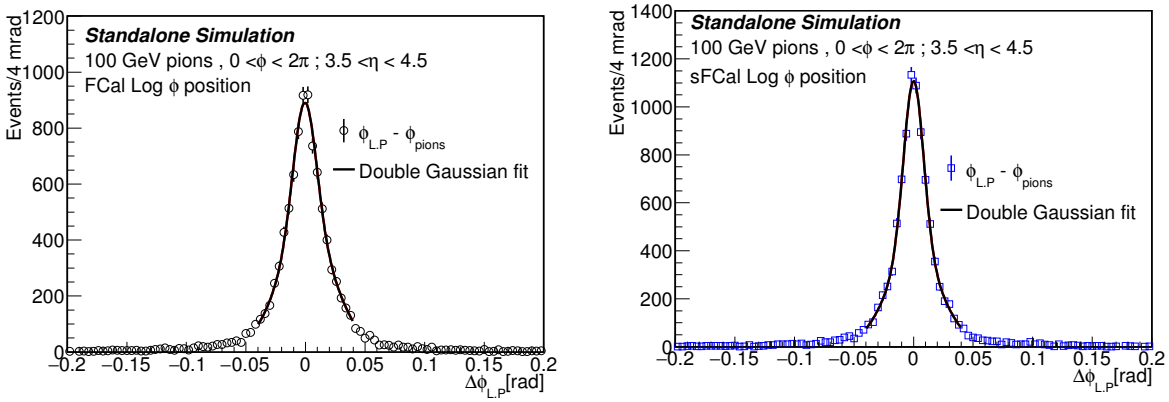


FIGURE 3.17: ***the distribution of*** $(\phi_{pion} - \phi_{L.P})$ ***in the FCal1 (left) and sFCal1 (right) fitted with sum of a double Gaussian.***

From the Figure 3.18 which shows the position resolution in response to pions as a function of nominal energy one can clearly notice how the better is the position resolution in the sFCal compared to the FCal. The fit parameters using Equation (3.5) are summarized in Table 3.8.

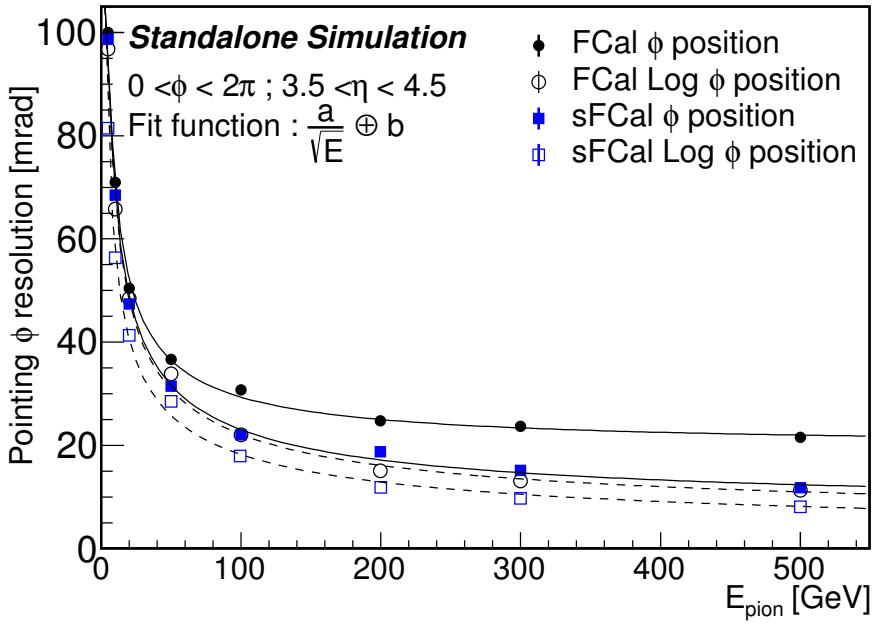


FIGURE 3.18: ***Position ϕ resolution of response to pions, as a function of nominal pions energy, from analysis of FCal1 (sFcal) standalone simulation, fitted with the function in the Equation*** (3.5)***. The uncertainties are estimated using the propagation of error from the double gaussian fit.***

Detector	Stochastic term ($mrad\sqrt{GeV}$)	Constant term (mrad)
FCal	217±2.07	19.7±0.69
sFCal	217±2.15	7.65±1.28
FCal log ϕ position	214±2.04	4.97±1.71
sFCal log ϕ position	182±1.85	3.50±1.84

TABLE 3.8: ***Pion pointing ϕ resolution fit results for FCal and sFCal. The uncertainties are estimated using the propagation of error.***

3.6 Conclusion

A standalone simulation study of the super forward calorimeter (sFCal) as a proposed replacement for the ATLAS forward calorimeter (FCal) at High Luminosity LHC was performed for both FCal and sFCal with electrons and pions in the energy region between 5 GeV to 500 GeV in order to evaluate the impact of a finer readout granularity in the high η region.

The results obtained show that the energy resolution for electrons and pions is slightly worst in the sFCal compared to the FCal due to lower sampling fraction that gives an increase of the constant term in the sFCal by a factor of 1.12 for electrons and 1.03 for pions. Furthermore, the pointing resolution in ϕ for electrons was estimated using three methods.

The logarithmic weighting is the best method as it improves the pointing resolution compared to the two other methods. Moreover, the study showed that the sFCal is more performant than FCal in terms of pointing resolution. For pions the logarithmic weighting method is better as well and also proves that sFCal has a higher performance.

After a careful analysis of the potential physics gains and associated risks, the ATLAS collaboration decided not to replace the current $FCal$ with an upgraded $sFCal$ during Phase-II. Focus will instead be placed on correcting for any potential degradation in the FCal signals.

Chapter 4

Physics object reconstruction

4.1 Introduction

The purpose of the reconstruction is to interpret the signals provided by the detector in terms of energy deposits from particles. We seek to identify the different types of particles, to determine their trajectory, their energy and thier momentum.

This chapter presents the reconstruction and the identification of the main physics object involved in the $WZ \to \ell\nu\ell'\ell'$ analysis, namely Electrons, Muons, Jets and B-jet respectively in sections 4.2, 4.3 and 4.4 . While, section 4.5 discusses the missing transverse energy reconstruction referred to the undetected neutrino. After the reconstruction of the particles, an overlap-removal process is performed in section 4.6 in order to avoid duplicate counting of physics object.

4.2 Electron reconstruction

The main inputs for the reconstruction of high p_T Electrons candidates in the central region $|\eta| < 2.47$ of the ATLAS detector are clusters of energy deposits in the EM Calorimeter associated with a good tracks from the Inner Detector. Clusters in the EM Calorimeter are computed using sliding-window algorithm [73] which is based on assembling cells within a fixed rectangular size and it is chosen to maximizes the energy inside the cluster.

The electron deposits its energy in different calorimeter cells, the sliding-window algorithm starts by regrouping the EM Calorimeter cells in a grid of $N_\eta^{tower} \times N_\phi^{tower} = 200 \times 256$ towers of size $\Delta\eta \times \Delta\phi = 0.025 \times 0.025$ according to the EM Calorimeter granularity. After that the algorithm scans over the tower grid in a rectangular window of fixed size $\Delta\eta^{window} \times \Delta\phi^{window} = 0.075 \times 0.125$ searching for window clusters with transverse energy [1] E_T^{window} above 2.5 GeV to form seed-clusters.

Tracks from the ID are extrapolated to the EM calorimeter and to form ATLAS electron, at least one track matches the seed-cluster within $\Delta\eta < 0.05$ and $\Delta\phi < 0.1$ between the

[1] E_T^{window} is defined as the sum of the transverse energy of the towers inside the window.

center of the seed-cluster and the extrapolated tracks is required. In case of multiple tracks matching, the one in a closest cone $\Delta R = \sqrt{\Delta\eta^2 + \Delta\phi^2}$ is chosen. Furthermore, all tracks associated with electromagnetic clusters are refitted using a Gaussian-sum Filter (GSF) [74], which accounts for bremsstrahlung energy losses. After track-cluster matching, seed-clusters are resized to take into consideration the nature of the reconstructed particle and the region of the calorimeter. For instance, EM shower generated by an electron is larger than that from photon, and may produce bremsstrahlung photons.

In the barrel the electron path is curved by the magnetic field in the ϕ direction, as a result the $\Delta\phi$ size of seed-clusters are extended to $\Delta\eta^{window} \times \Delta\phi^{window} = 0.075 \times 0.175$ in order to recover a maximum of the electron energy. While in the end-caps the $\Delta\eta$ size of seed-clusters is increased to $\Delta\eta^{window} \times \Delta\phi^{window} = 0.125 \times 0.125$ because of the low magnetic field effect and the small physical cells size in η direction in this region compared to the barrel.

EM Calorimeter region	Barrel	End-cap
$\lvert\eta\rvert <$	2.47	2.47
$N_{\eta}^{tower} \times N_{\phi}^{tower}$	3×7	5×5
$\Delta\eta^{window} \times \Delta\phi^{window}$	0.075×0.175	0.125×0.125
$E_T^{window} >$	2.5 GeV	2.5 GeV

TABLE 4.1: ***Summary of seed-clusters size for the reconstruction of ATLAS electron in the barrel and end-cap regions of the EM calorimeter.***

Moreover, the reconstructed electrons have to satisfy a set of identification quality requirements to decide whether the physics object are a pure electrons or a fake objects such as hadrons misidentification or photon conversions. The identification algorithms are based on the discriminating variables (Table 4.2) related to the track-cluster matching, taking in the account showers-shape in the calorimeter, track measurements from several ID component (IBL, pixel detector,SCT, TRT) and variables describing the bremsstrahlung process. In order to increase the background rejection, three operating points (OP) based on these discriminating variables cuts are defined. The first one is named *Loose*, which uses variables related to electron showers defined in the middle layer of the EM calorimeter as before the hadronic leakage selection is applied. A supplementary cut on the track quality ($|\Delta\eta| < 0.015$) is used to improve the identification efficiency by the rejection of hadronic backgrounds. The second operating point is *Medium*, on which the cut on $|\Delta\eta|$ is reduced to 0.005 and it adds to *Likelihood Loose* selection cuts on variables that describe showers in the strip layer of the EM calorimeter, cuts from TRT informations and transverse impact parameter ($d_0 < 5$ mm) to reject charged hadron. The last operating point is *Likelihood Tight* which includes

Likelihood Medium criteria and track-cluster matching such as the ratio of the cluster energy to the track momentum (E/p), and $\Delta\phi_2$ between the cluster position in the middle layer of EM calorimeter and the extrapolated track. The efficiency to identify electrons from $Z \to ee$ decays can be seen in Figure 4.1

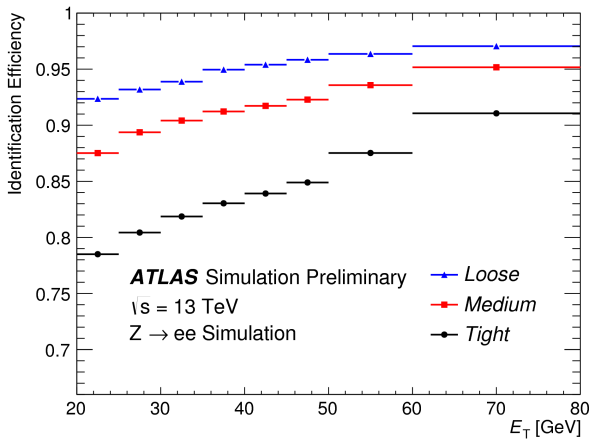


FIGURE 4.1: ***Efficiency of electrons identification from $Z \to ee$ decays. The efficiency is obtained using Monte Carlo simulations, and is measured with respect to reconstructed electrons [76].***

After the identification, ATLAS analyses requires electrons to pass isolation criteria to substrat prompt electrons from non-isolated candidates. Two dedicated variables have been introduced for this purpose [77]:

- **Calorimetric isolation $E_T^{cone\Delta R}$:** Defined as the sum of the transverse energy deposited in the EM calorimeter in a cone of ΔR around electron cluster.
- **track isolation $p_T^{cone\Delta R}$:** Defined as the scalar sum of the transverse momentum of ID tracks originating from the primary vertex in a cone of ΔR around electron.

Five isolation working points (WK) are defined by combining both calorimeter and track isolation variables (Table 4.3).

In $WZ \to \ell\nu\ell'\ell'$ analysis using Run-2 data, the baseline electrons are required to pass *Likelihood Loose* identification criteria with $E_T > 25GeV$ and $|\eta| < 2.47$. Electron object quality is also applied with cuts on $d_0/\sigma_{d_0} < 5$ and longitudinal impact parameter $z_0|\sin(\theta)|$ < 0.5 mm to select only tracks

originate from the primary vertex. Prompt Baseline electrons are reconstructed in this analysis using *LooseTrackOnly* because of the high isolation efficiency of this working point. The baseline Electron criteria used in the analysis are summarized in Table 4.4.

Type	Description	Name
Hadronic leakage	Ratio of E_T in the first layer of the hadronic calorimeter to E_T of the EM cluster. (used over the range $\|\eta\| < 0.8$ or $\|\eta\| > 1.37$)	R_{had1}
	Ratio of E_T in the hadronic calorimeter to E_T of the EM cluster. (used over the range $0.8 < \|\eta\| < 1.37$)	R_{had}
Back layer of EM calorimeter	Ratio of the energy in the back layer to the total energy in the EM accordion calorimeter. This variable is only used below 100 GeV because it is known to be inefficient at high energies.	f_3
Middle layer of EM calorimeter	$\sqrt{(\Sigma E_i \eta_i^2)/(\Sigma E_i) - ((\Sigma E_i \eta_i)/(\Sigma E_i))^2}$, where E_i is the energy and η_i is the pseudo-rapidity of cell i and the sum is calculated within a window of 3 × 5 cells (Lateral shower width),	W_{η^2}
	Ratio of the energy in 3 × 3 cells over the energy in 3 × 7 cells centered at the electron cluster position	R_ϕ
	Ratio of the energy in 3 × 7 cells over the energy in 7 × 7 cells centered at the Strip layer of electron cluster position	R_η
Strip layer of EM calorimeter	Shower width, $\sqrt{(\Sigma E^2_{i-i_{max}})/(\Sigma E_i)}$, where i runs over all strips in a window of $\Delta\eta \times \Delta\phi \approx 0.0625 \times 0.2$, corresponding typically to 20 strips in η, and i_{max} is the index of the highest-energy strip	W_{stot}
	Ratio of the energy difference between the largest and second largest energy deposits in the cluster over the sum of these energies	E_{ratio}
	Ratio of the energy in the strip layer to the total energy in the EM accordion	f_1
Track conditions	Number of hits in the innermost pixel layer; discriminates against photon conversions	n_{Blayer}
	Number of hits in the pixel detector	n_{Pixel}
	Number of total hits in the pixel and SCT detectors	n_{Si}
	Transverse impact parameter with respect to the beam-line	d_0
	Significance of transverse impact parameter defined as the ratio of d_0 and its uncertainty	d_0/σ_{d_0}
	Momentum lost by the track between the perigee and the last measurement point divided by the original momentum	$\Delta p/p$
TRT	Likelihood probability based on transition radiation in the TRT	eProbabilityHT
Track-cluster matching	$\Delta\eta$ between the cluster position in the strip layer and the extrapolated track	$\Delta\eta_1$
	$\Delta\phi_2$ between the cluster position in the middle layer and the track extrapolated from the perigee	$\Delta\phi_2$
	Defined as $\Delta\phi_2$, but the track momentum is rescaled to the cluster energy before extrapolating the track from the perigee to the middle layer of the calorimeter	$\Delta\phi_{res}$
	Ratio of the cluster energy to the track momentum	E/p

TABLE 4.2: ***Discriminating variables used for the identification of ATLAS electrons [75].***

	Efficiency		
Working points	Calorimeter isolation	track isolation	Total efficiency
LooseTrackOnly	-	99 %	99 %
Loose	99 %	99 %	∼98 %
Tight	96 %	99 %	∼95 %
Gradient	$0.1143\ \% \times E_T + 92.14\ \%$	$0.1143\ \% \times E_T + 92.14\ \%$	90-99 % at 25/60 GeV
GradientLoose	$0.057\ \% \times E_T + 95.57\ \%$	$0.057\ \% \times E_T + 95.57\ \%$	95-99 % at 25/60 GeV

TABLE 4.3: ***Electron isolation working points efficiency [75].***

Baseline electron object selection		
Selection	Z selection	W selection
$E_T > 25$ GeV	✓	✓
Electron object quality	✓	✓
$\lvert\eta^{\text{cluster}}\rvert < 2.47$	✓	✓
LooseLH+BLayer identification	✓	✓
$\lvert d_0/\sigma(d_0)\rvert < 5$	✓	✓
$\lvert\Delta z_0 \sin\theta\rvert < 0.5$ mm	✓	✓
LooseTrackOnly isolation	✓	✓

TABLE 4.4: ***Baseline electron object selection used in the*** $WZ \to \ell\nu\ell'\ell'$ ***analysis.***

4.3 Muon reconstruction

Muon reconstruction algorithms use the track informations from the muon spectrometer, the inner detector and the calorimeter. Tracks in the MS are reconstructed firstly on each muon chamber independently to build segments by making a straight line fit to hits in the same layer. Later, the segments are combined from different chambers to produce the entire MS tracks. Based on which ATLAS sub-detectors are employed, muons can be reconstructed in four types:

- **Combined (CB):** Inside the inner detector coverage $|\Delta\eta| < 2.5$, muons are reconstructed by matching MS and ID track. Two algorithms are used to combine track parameters, they are called *STACO* [78] and *Muid* [79]. The first one performs a statistical combination between ID and MS parameters to calculate muon track variables, the second algorithm is based on a track refit using hit in both ID and MS detectors.

- **Standalone (SA):** In the ATLAS pseudo-rapidity region up to $|\Delta\eta| = 2.7$ which is not covered by the inner detector, muons are reconstructed using tracks from the MS alone. Then afterwards, the tracks are projected backward to the interaction point where the muon parameters are defined with respect to the energy loss in the calorimeters.

- **Segment-tagged (ST):** Muons with low transverse momentum p_T are reconstructed using *Mutag* [80] software, it tags ID track as a muon if it is associated with a segment in the inner stations of MS.

- **Calorimeter-tagged (CT):** CaloMuonTag and CaloMuonLH [79] algorithms are dedicated to reconstruct muons by matching an ID track with a deposited energy in the last calorimeter layer with minimum ionization.

In addition, the algorithms use a hierarchy of control that avoid overlaps between muon categories, e.g. when muons share the same inner Detector or muon Spectrometer track, CB muons have the higher priority than ST muons and then came CT muons with less priority. Overlaps with standalone muons are resolved by selecting track with good fit quality and large number of hits in the MS.

In the next step, a muon identification is performed based on the number of hits in the ID and MS to select prompt muons with high efficiency and reject backgrounds mainly from pion and kaon decay. For instance, ID quality selections ask for a track with at least 1 Pixel hit, at least 5 SCT hits, less than 3 Pixel or SCT [2]holes, and that up to 10% of TRT hits are involved in the track final fit. For **CB** muons the discriminating variables used for the identification are:

- χ^2: An observable parameter for the combined track fit quality, defined as the square of the track-to-hit distance divided by the hit resolution. A small value of the χ^2 correspond to good track quality.

- q/p significance: defined as the absolute value of the difference between the ratio of the muon charge and momentum measured in the ID and MS divided by the sum in quadrature of the corresponding uncertainties.

- $\rho\prime$: defined as the absolute value of the difference between the transverse momentum p_T measured in the ID and MS divided by the p_T of the combined track.

ATLAS analyses provide four muon identification qualities which are *Medium, Loose, Tight*, and *High-p_T*, a description of these qualities selection are summarized in Table 4.5. The efficiency to identify muons for medium working point used in the present analysis is shown in Figure 4.2.

[2]A hole is defined as an active sensor traversed by the track but containing no hits.

Identification quality	Description
Medium	• Only CB and SA tracks are used. • Up to two hits in at least two MDT layers are required, • for $\|\eta\| > 0.1$ region, tracks with at least one MDT layer and at maximum of one hole layer are selected. • In $2.5 < \|\eta\| < 2.7$ region at least three MDT/CSC layers are considered. • The q/p significance is required to be less than seven to reject fake muons due to the hadrons misidentification.
Loose	• Medium muons are included in the Loose selection. • CT and ST muons are restricted to the $\|\eta\| < 0.1$ region.
Tight	• Only CB muons with hits in at least two MS stations passing the Medium selection are used. • χ^2 of the tracks fit is required to be less than eight to select a good track quality. • CB muons with momenta lower than 20 GeV. • A cut in the q/p significance and $\rho\prime$ as a function of the muons p_T is applied.
High-p_T	• In order to improve the momentum resolution for track with p_T up to 100 GeV a High-p_T selection is used. • CB muons satisfying the Medium selection with at least 3 hits in 3 MS stations are required.

TABLE 4.5: ***Quality selections used for the identification of ATLAS muons.***

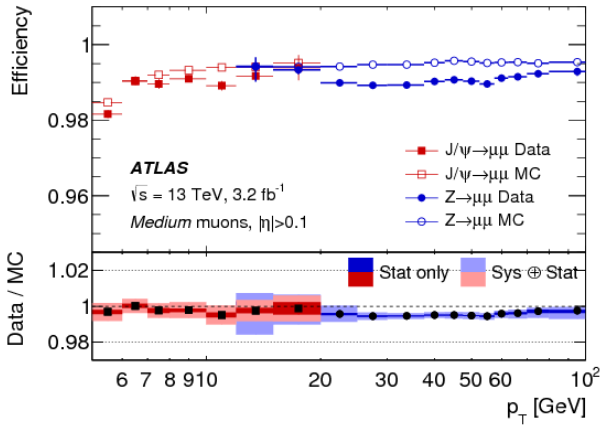


FIGURE 4.2: ***The efficiency to identify muons for medium working point from $Z \to \mu\mu$ and $J/\psi \to \mu\mu$ events. The error bars on the efficiencies indicate the statistical uncertainty [81].***

In the same way as for electron isolation (Table 4.3), five isolation working points are introduced to select prompt ATLAS muons and increase the background rejection. For muon isolation track-based a p_T^{cone30} variable which defined as a scalar sum of transverse momenta of the tracks with $p_T > 1$ GeV in a cone of size $\Delta R = \min(0.3, 10\text{GeV}\ /p_T^{\mu})$, for the calorimeter-based a E_T^{cone20} variable is used and it is defined as the sum of transverse energy in a cone of size $\Delta R < 0.2$ around the muon [82].

The baseline muons used in this analysis are required to pass *Medium* quality selection that are recommended by the ATLAS Combined Performance group (CP). Furthermore, muons are required to have $p_T > 25$ GeV and $\eta > 2.7$ whit $d_0 < 1mm$ to avoid cosmic events. To select only muons that originate from the primary vertex, the d_0 significance $d_0/\sigma_{d_0} < 3$ and the longitudinal impact parameter $z_0|\sin(\theta)| < 0.5$ mm are applied. As for electrons, *LooseTrackOnly* isolation is also used to select good muons. The baseline Electron criteria used in the analysis are summarized in Table 4.6.

Baseline muon object selection		
Selection	Z selection	W selection
$p_T > 25$ GeV	✓	✓
$\lvert\eta\rvert > 2.7$	✓	✓
Medium quality	✓	✓
$\lvert d_0/\sigma(d_0)\rvert < 3$	✓	✓
$\lvert\Delta z_0 \sin\theta\rvert < 0.5$ mm	✓	✓
LooseTrackOnly isolation	✓	✓

TABLE 4.6: ***Baseline muon object selection used in the $WZ \to \ell\nu\ell'\ell'$ analysis.***

4.4 Jet reconstruction

The color charged particles such as quarks and gluon can not be isolated and observed individually because of the quantum chromodynamics confinement law which permits for colorless particles in the final states. In the ATLAS detector, quarks and gluon are combined to form a cone of colorless objects called a jet (Figure 4.3). The main tool used in the present analysis for the reconstruction of jets is the anti-k_t algorithm [83], based on a three-dimensional topological clusters [84] of calorimeter cells with a significant seed signal compared to noise.

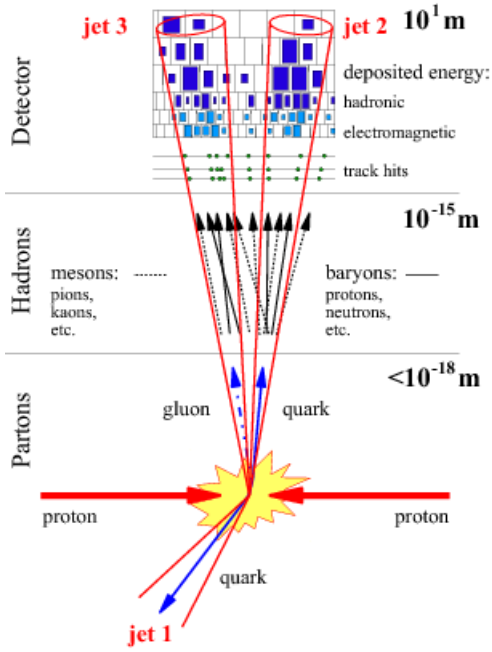


FIGURE 4.3: ***Illustration of jets which are formed of partons, hadrons, or detector measurements [85].***

Two basic observables are used by the anti-k_t algorithm which are the distance d_{ij} measures between two i and j objects and the momentum space distance d_{iB} between the beam axis and the detected particle i. d_{ij} and d_{iB} are defined as follow:

$$d_{ij} = \min\left(\frac{1}{p_{Ti}^2}, \frac{1}{p_{Tj}^2}\right) \frac{(\eta_i - \eta_j)^2 + (\phi_i - \phi_j)^2}{R^2}, \tag{4.1}$$

$$d_{iB} = \frac{1}{p_{Ti}^2}, \tag{4.2}$$

where p_{Ti}, η_i and ϕ_i are the transverse momentum of the i_{th} particle, its rapidity and azimuthal angle respectively. The jet cone size is defined by the radius parameter $R = 0.4$ which is chosen to reduce the contributions from pileup and underlying event (UE) that are not coming from the primary hard scattering. The algorithm proceeds by defining the

minimum distance d_{min} at each cluster between all objects. Particles i and j with the smallest distance are combined and tagged as a jet if the distance d_{ij} is below d_{iB}. Thus, if $d_{iB} < d_{ij}$ for all j objects, the particle i is considered as jet. The operation is repeated until all jets are selected.

After the selection of jets, a cleaning procedure is applied to reject bad jets that are not associated with a cluster of energy deposits in the calorimeters and they are coming mainly from hardware noise and cosmic-ray showers. To reduce these sources of backgrounds, the following discriminating variables [86] are useful:

- **emf:** defined as the energy fraction in the electromagnetic calorimeter.
- **fmax:** referred to the maximum energy fraction in one calorimeter layer.
- **HECf:** the energy fraction in the Hadronic End-Cap.
- **NegativeE:** is the negative energy in the jet
- **t:** the jet time is computed as the energy squared cells mean time.
- **AverageLArQF:** the jet quality computed as the energy squared cells mean quality.
- **n90:** defined as the minimum number of cells containing at least 90% of the jet energy.
- $\boldsymbol{\eta_{NoCorr}}$: is the jet's $\boldsymbol{\eta}$ without corrections.
- **chf:** the jet charged fraction is the ratio of the $\boldsymbol{p_T}$ sum of tracks associated to the jets divided by the CALIBRATED jet $\boldsymbol{p_T}$.
- **LArQmean:** normalized jet quality computed as the energy squared of the LAr cells.
- **LArQ:** The jet quality is the fraction of energy corresponding to LAr cells with a cell $\boldsymbol{Q-factor}$ [3] greater than 4000.
- **HECq:** same as the **LArQ** except calculated only with the Hadronic End-Cap.

Here also, four working points are introduced for the jet identification based on the previous discriminating variables. *Looser, Loose, Medium* and *Tight* criteria are provided to increase the efficiency of selection of the good jet and to reject the bad one. More details on the jets identification working points are summarized in Table 4.7.

To reduce the contamination of pileup jets a new discriminant parameter named Jet-vertex-tagger (JVT) [87] is defined using the corrected jet-vertex-fraction (corrJVF) [87]

[3] The cell Q-factor is defined as the sum of the square difference between the measured pulse shape ($\boldsymbol{a_i^{meas}}$) and the predicted one ($\boldsymbol{a_i^{pred}}$) that is computed to estimate the cell energy: $\boldsymbol{Q-factor = \sum_{i=1}^{samples}(a_i^{meas}-a_i^{pred})^2}$.

Target	Looser	Loose	Medium	Tight
HEC spikes	$HECf > 0.5$ && $\|HECQ\| > 0.5$ && $LArQmean > 0.8$ *or* $\|neg.E\| > 60GeV$	$HECf > 0.55$ && $\|HECQ\| > 0.5$	$HECf > 1 - \|HECQ\|$	
EM coherent noise	$EMf > 0.95$ && $\|LArQ\| > 0.8$ && $LArQmean > 0.8$ && $\|\eta_{NoCorr}\| < 2.8$	$EMf > 0.95$ && $\|LArQ\| > 0.8$ && $\|\eta_{NoCorr}\| < 2.8$	$EMf > 0.9$ && $\|LArQ\| > 0.8$ && $\|\eta_{NoCorr}\| < 2.8$	$EMf > 0.98$ && $\|LArQ\| > 0.05$ *or* $\|LArQ\| > 0.95$
cosmic-ray showers	$EMf > 0.05$ && $Chf < 0.05$ && $\|\eta_{NoCorr}\| < 2$ *or* $EMf < 0.05$ && $\|\eta_{NoCorr}\| \neq 2$ *or* $FMax > 0.99$ && $\|\eta_{NoCorr}\| < 2$	$\|t\| > 25\ ns$	$\|t\| > 10\ ns$ *or* $EMf > 0.05$ && $Chf < 0.1$ && $\|\eta_{NoCorr}\| < 2$ *or* $EMf > 0.95$ && $Chf < 0.05$ && $\|\eta_{NoCorr}\| < 2$	$EMf > 0.1$ && $Chf < 0.2$ && $\|\eta_{NoCorr}\| < 2.5$ *or* $EMf > 0.9$ && $Chf < 0.1$ && $\|\eta_{NoCorr}\| < 2.5$ *or* $Chf < 0.01$ && $\|\eta_{NoCorr}\| < 2.5$ *or* $EMf > 0.1$ && $\|\eta_{NoCorr}\| < 2.5$

TABLE 4.7: ***Quality selections used for the identification of ATLAS jets.***

and the R_{pT} [87] variable which is the ratio of the scalar p_T sum of tracks that are associated with the hard-scatter vertex jet to the jet p_T. CorrJVT and R_{pT} are used as a 2-dimensional likelihood to define the best JVT working points with high pileup rejection. Three JVT working point have been considered in the run-2 for the central regions of the detector with $|\eta| < 2.4$ and $20 < p_T^{jet} < 60$ using a Monte Carlo sample of Z boson decaying into muons with at lest one jet. The different JVT working points are summarized in Table 4.8.

Working Point Topo	JVT Cut	Average efficiency
Loose	0.11	97%
Medium	0.59	92%
Tight	0.91	85%

TABLE 4.8: ***JVT cut values for the Loose, Medium and Tight working points [88].***

Furthermore, an algorithm of jet flavor tagging called MV2c10 is evaluated to suppress backgrounds enriched with light-flavor jets (u-, d-, s-quark or gluon fragmentation) and c-jets in the signal region. Based on a Boosted Decisions Tree (BDT) studies [89], four working points for the MV2c10 b-tagging algorithm are performed using a $t\bar{t}$ MC sample. The BDT distribution are shown in Figure 4.4 and the working points are listed in Table 4.9.

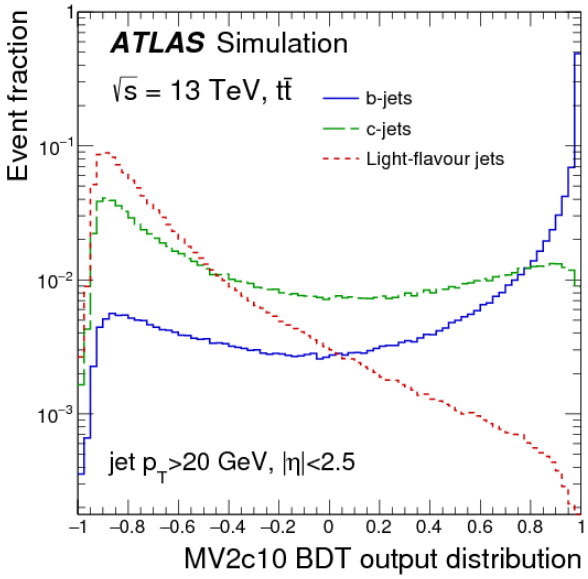


FIGURE 4.4: ***The MV2c10 output for b-jets (blue line),c-jets (green line) and light-flavor jets (red line) in simulated $t\bar{t}$ events [90].***

MV2c10 Working Point	b-jet efficiency [%]	c-jet rejection	light-jet rejection
0.8244	70	12	381
0.6459	77	6	134
0.1758	85	3.1	33

TABLE 4.9: ***The MV2c10 b-tagging algorithm Working points. b-jet efficiency, c-jet rejection and light-jet rate rejection are included in the table.***

4.5 Missing Transverse Energy reconstruction

the missing transverse energy $\vec{E}_t^{miss}$ referred to the unobserved particles that travel through the ATLAS detector without leaving any measurable energy or tracks. Based on the momentum conservation law, the $\vec{E}_t^{miss}$ is reconstructed as the negative vector sum of transverse momenta of the all visible physics objects (electrons, muons, photons, tau, jets) and the reconstructed momenta which not associated to any particle objects. The $\vec{E}_t^{miss}$ is calculated then as the sum shown below:

$$E_{x(y)}^{miss} = E_{x(y)}^{miss,hard\ terms} + E_{x(y)}^{miss,soft\ term}, \tag{4.3}$$

where $E_{x(y)}^{miss,hard\ terms}$ represents the negative vectorial sum of the transverse momenta of electrons, muons, photons, tau and jets. It is computed as the formula below:

$$E_{x(y)}^{miss,hard\ terms} = -E_{x(y)}^{electons,} - E_{x(y)}^{muons} - E_{x(y)}^{photons} - E_{x(y)}^{jets}. \tag{4.4}$$

The $E_{x(y)}^{miss,soft\ term}$ includes all the observed information by the ATLAS detector that not matched to any particle objects involved in the hard term. Four algorithms are dedicated for the reconstruction of the soft term and are described in the Table 4.10.

Soft term Algorithm	Description
Calorimeter Soft Term (CST)	Its soft term is computed from energy deposited in the calorimeter which are not associated to high-p_T physics objects. As well, fake signals are reduced by applying noise suppression procedure, no more pileup reduction is requested.
Track Soft Term (TST)	Its soft term is performed from the inner detector tracks that are not matched to high-p_T physics objects. The JVT selection criteria is applied to jets.
Extrapolated Jet Area with Filter (EJAF)	Algorithms applies pileup suppression to the Calorimeter Soft Term.The JVT selection criteria is applied to jets.
Soft-Term Vertex-Fraction (STVF)	Algorithm suppress pileup events in the CST by scaling the soft term by a multiplicative factor calculated based on the fraction of scalar-summed track p_T not associated with high-p_T physics objects that can be associated to the primary vertex. The JVT selection criteria is applied to jets.
Track E_T^{miss}	Reconstructed only from tracks to avoid pileup contribution that affects the other algorithms.

TABLE 4.10: ***Summary of algorithms used for the reconstruction of the missing transverse energy soft terme [91].***

The missing transverse energy in this analysis is reconstructed using the *METMakerTool* [92] which takes as inputs the calibrated muons and electrons satisfying the baseline selection and the full jet container information without any selection. According to the recommendations, The $E_{x(y)}^{miss,soft\ term}$ is reconstructed using the Track Soft Term algorithms (Table 4.10) in the ID acceptance ($|\eta| < 2.5$), benefiting from the good vertex matching for the soft term and it guarantees an excellent pileup subtraction. The resolution of the E_T^{miss} components E_x^{miss} and E_y^{miss} as a function of The average number of proton-proton interactions per bunch crossing $< \mu >$ is presented in Figure 4.5.

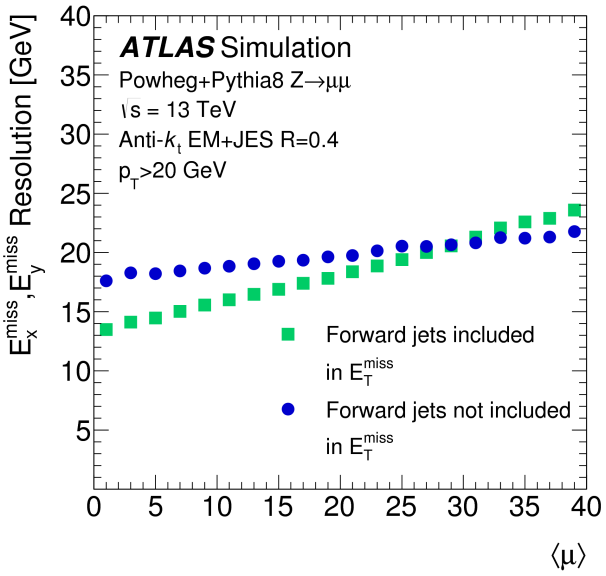


FIGURE 4.5: ***The resolution of the*** E_T^{miss} ***components*** E_x^{miss} ***and*** E_y^{miss} ***as a function of*** $< \mu >$ ***[93].***

4.6 Overlap removal

After the selection of the physics objects involved in the analysis, an overlapping objects treatment called Overlap removal (OR) is performed as it is discussed by the harmonization group (HG) [94]. The OR is applied to avoid duplication of physics object definition, where a particle can be identified as two different physical objects. In this analysis the Overlap removal is evaluated between electrons, muons and jets according the following criteria [94]:

- **Electron-jet overlap removal:** it is recommended to remove jet that can reconstructed as a prompt electron within a cone of $\Delta R(e, j) < 0.2$ from the baseline electron, and to reject electron or the full event for events with $0.2 < \Delta R(e, j) < 0.4$.

- **Muon-jet overlap removal:** to avoid duplication between muon and jet, it is requested to apply a muon-jet overlap removal in a cone region of $\Delta R(\mu, j) < 0.4$ where the muon is removed if the number of jet tracks $N_{tracks}^{Jet} > 2$.

- **Electron-muon overlap removal:** it is required to reject electron sharing the same track with a baseline muon.

- **Electron-electron overlap removal:** an overlap removal is applied to electrons if they share the same ID track. The electron with the highest E_T cluster is considered in the analysis.

Chapter 5

Resonant $WZ \to \ell\nu\ell'\ell'$ search at $\sqrt{s} = 13\ TeV$

5.1 Introduction

The production of WZ pairs at the Large Hadron Collider (LHC) with proton-proton collisions open a great opportunity for the physicists to learn and understand more about the electroweak symmetry breaking (EWSB) of the Standard Model, as well as to search for a new physics beyond the SM. Such as Grand Unified theories [95], and theories of dynamical EWSB [96], Little *Higgs* models [97], Technicolor [98, 99, 100, 101], or more generic Composite *Higgs* models [102, 103], and theories with extra dimensions [104, 105, 106]. This chapter presents a search for WZ resonances in the fully leptonic final state

A detailed description of the procedure used in this physics analysis is presented in this chapter. Section 5.2 presents the data samples as well as Monte Carlo ones, for both signal and background processes used in the analysis. In section 5.2.4, the selection procedure of WZ events identification is shown. Section 5.4 is dedicated to optimize both VBF and $q\bar{q}$ contamination while reducing as much as possible the backgrounds contribution. Then the backgrounds estimation are described in section 5.6, where the irreducible backgrounds are estimated directly from the Monte-Carlo normalized to data luminosity, while the reducible one are estimated using a data-driven method. The deferent source of systematic uncertainties affecting the results are listed in section 5.7.

5.2 Data and Monte Carlo samples

The analysis is performed using data collected by the ATLAS detector in the 2015-2016 data-taking period at a center of mass energy of $\sqrt{s} = 13TeV$ with an integrated luminosity of about 36.1 fb^{-1} (section 5.2.1). Backgrounds and signal contamination are estimated using Monte Carlo (MC) ATLAS detector simulation [107] based on **GEANT4** [68] (GEometry ANd Tracking) platform, the different MC samples used in this analysis are listed in section 5.2.2.

5.2.1 Data samples

Data used in the present $WZ \to \ell\nu\ell'\ell'$ resonant search is stored in luminosity blocks (LBs) corresponding to 1-2 minutes of data collection. A Good Run List (GRL) [108], is built from all runs satisfying a set of data quality condition that exclude bad luminosity blocks affected by potential problems with trigger, luminosity, detector calibration or data acquisition. The luminosity calculation for a specific GRL are determined by the **atlas-lumicalc tool** [109] which provides the integrate luminosity per run. the systematic uncertainties related to the cumulative luminosity calculation are detailed in the reference [110] and it is estimated to be equal to 2.1% for the inclusive 2015 and 2016 data. The integrated 2015 luminosity delivered by the LHC, collected by ATLAS detector and selected for physics analysis with GRL good data quality are presented in Figure 5.1. The 2015-2016 data events used in this analysis are collected using the $L1_EM$ or $L1_MU$ triggers [111] then pre-selected with the "$DAOD_HIGGS2D1$" di-lepton filter in order to contain at least two charged leptons (electrons or muons) with a transverse momentum of the leading (sub-leading) lepton larger than 15 GeV (5 GeV).

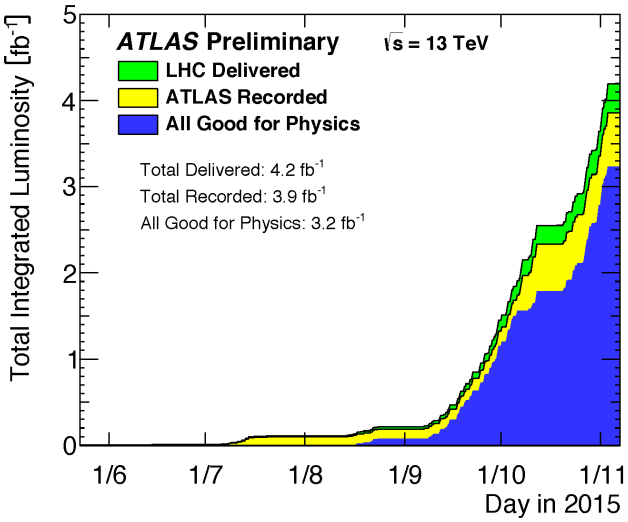


Figure 5.1: ***The integrated luminosity as a function of time delivered by the LHC (green), and collected by ATLAS detector (yellow) during 2015 data-taking. The Blue shaded area shows all the good data quality passed the GRL criteria [112].***

GRL XML file	Run number	integrated luminosity
data15_13TeV.periodAllYear_DetStatus-v79-repro20-02_DQDefects-00-02-02_PHYS_StandardGRL_All_Good_25ns	276262, 276329, 276336, 276416, 276511, 276689, 276778, 276790, 276952, 276954, 278880, 278912, 278968, 279169, 279259, 279279, 279284, 279345, 279515, 279598, 279685, 279813, 279867, 279928, 279932, 279984, 280231, 280273, 280319, 280368, 280423, 280464, 280500, 280520, 280614, 280673, 280753, 280853, 280862, 280950, 280977, 281070, 281074, 281075, 281317, 281385, 281411, 282625, 282631, 282712, 282784, 282992, 283074, 283155, 283270, 283429, 283608, 283780, 284006, 284154, 284213, 284285, 284420, 284427, 284484.	3.22 fb^{-1}
data16_13TeV.periodAllYear_DetStatus-v88-pro20-21_DQDefects-00-02-04_PHYS_StandardGRL_All_Good_25ns	297730, 298595, 298609, 298633, 298687, 298690, 298771, 298773, 298862, 298967, 299055, 299144, 299147, 299184, 299243, 299584, 300279, 300345, 300415, 300418, 300487, 300540, 300571, 300600, 300655, 300687, 300784, 300800, 300863, 300908, 301912, 301918, 301932, 301973, 302053, 302137, 302265, 302269, 302300, 302347, 302380, 302391, 302393, 302737, 302831, 302872, 302919, 302925, 302956, 303007, 303079, 303201, 303208, 303264, 303266, 303291, 303304, 303338, 303421, 303499, 303560, 303638, 303832, 303846, 303892, 303943, 304006, 304008, 304128, 304178, 304198, 304211, 304243, 304308, 304337, 304409, 304431, 304494, 305380, 305543, 305571, 305618, 305671, 305674, 305723, 305727, 305735, 305777, 305811, 305920, 306269, 306278, 306310, 306384, 306419, 306442, 306448, 306451, 307126, 307195, 307259, 307306, 307354, 307358, 307394, 307454, 307514, 307539, 307569, 307601, 307619, 307656, 307710, 307716, 307732, 307861, 307935, 308047, 308084, 309375, 309390, 309440, 309516, 309640, 309674, 309759, 310015, 310247, 310249, 310341, 310370, 310405, 310468, 310473, 310634, 310691, 310738, 310809, 310863, 310872, 310969, 311071, 311170, 311244, 311287, 311321, 311365, 311402, 311473, 311481.	32.86 fb^{-1}

TABLE 5.1: ***The final GRLs used in the 2015 and 2016 data-taking by the ATLAS physics analysis.***

5.2.2 Monte Carlo samples

The production of Monte Carlo samples used in this analysis is done with several event generators within The ATLAS detector simulation framework. This includes the simulation of the additional pp interaction (i.e. pile-up),the detector response and the trigger decision. These samples are used to confirm the validity of theoretical models, to reject and/or estimate

the backgrounds contribution as well as to optimize the kinematic selection cuts in order to maximize the signal significance.

The ATLAS Monte Carlo samples are produced essentially in three steps:

- **Event generation:** This step is dedicated to the generation of MC event based on the parton density function (PDF) by creating four-momenta associated to particle objects. Particles with shortest lifetime as they decay quickly without hitting the ATLAS detector are produced in the generation level, while stable particles with longer lifetime are transmitted to the next step for the ATLAS simulation.

- **Simulation:** The ATLAS detector simulation is based on the Geant4 toolkit. This framework simulates the interactions of stable particles with all material layers of the ATLAS detector. This step provides a fit file output containing energy deposition, position and time for all particle-material interactions. The result is used as input to the digitization step.

- **Digitization:** It is the final stage of the ATLAS sample production that converts the detector simulation hits to readable data to be used in the reconstruction and physics analysis. The digitalization applies the ATLAS detector response to hit files by including readout electronic signals, pulse shaping, trigger hardware, pileup events.

Several event generators are used to produce Monte Carlo samples for the ATLAS experiment as well as to simulate backgrounds and signal modeling,

5.2.3 Signal Monte Carlo samples

For the $q\bar{q} \to W' \to WZ$ resonant search, a Heavy Vector Triplet (HVT) signal samples are generated using MadGraph [113] (**MA**trix element **D**iagram and **Graph**) interfaced to Pythia-8 [114] for hadronization. The analysis is carried out for WZ resonance masses ranging from 250 GeV to 3 TeV.

In fact, the production of events is conducted in two ways: in the so called HVT Model-A, the vector-boson interaction parameter is set to $g_v = 1$ (see Table 5.2), while in the Model-B, the heavy vector triplet is produced in a strongly coupled scenario with $g_v = 3$ as in a composite Higgs model [113] without fermionic couplings. Since the width of the resonance remains well below the experimental resolution and the angular distributions are the same in the Model-A as well as in the Model-B, the interpretation of resonant search in the last one is done by scaling the Model-A cross sections.

DSID	Mass	Events	Filter eff.	Cross-section [fb]	k-factor
302263	250	30000	1.00	4103	1.00
302264	300	30000	1.00	2258	1.00
302265	400	30000	1.00	716.3	1.00
302266	500	30000	1.00	283.9	1.00
302267	600	30000	1.00	132.2	1.00
302268	700	18000	1.00	69.23	1.00
302269	800	25000	1.00	39.41	1.00
302270	900	30000	1.00	23.80	1.00
302271	1000	45000	1.00	15.09	1.00
302272	1100	18000	1.00	9.921	1.00
302273	1200	30000	1.00	6.751	1.00
302274	1300	10000	1.00	4.676	1.00
302275	1400	30000	1.00	3.313	1.00
302276	1500	29000	1.00	2.391	1.00
302277	1600	30000	1.00	1.749	1.00
302278	1700	28000	1.00	1.298	1.00
302279	1800	30000	1.00	0.9720	1.00
302280	1900	30000	1.00	0.7350	1.00
302281	2000	18000	1.00	0.5610	1.00
302282	2200	35000	1.00	0.3334	1.00
302283	2400	45000	1.00	0.2028	1.00
302284	2600	30000	1.00	0.1258	1.00
302285	2800	29000	1.00	0.07925	1.00
302286	3000	20000	1.00	0.05036	1.00

TABLE 5.2: ***HVT signal Monte Carlo samples Model-A used for the $q\bar{q}$ resonant search.***

The VBF signal search is performed in term of two different models. The first one is interpreted using HVT samples with masses ranging from 250 GeV to 2 TeV with $g_v = 1$, the coupling parameter $c_H = 1$ and all other HVT coupling parameters are set to 0 in order to maximize the VBF signal contribution. Thus, the dijet invariant mass m_{jj} is required to be higher than 150 GeV in these samples at generation level. Further details about HVT VBF samples are given in Table 5.3.

The second signal model is called Georgi-Machacek (GM) and it used to predict the charged higgs $H_5^{\pm}$ sector ($pp \rightarrow H_5 \rightarrow WZ$). Samples for this model are produced with MADGRAPH using GMCALC [115] for masses between 200 and 900 GeV with $\sin(\theta_H) = 0.5$

as defined in reference [116], the cross sections and widths, which scale as $\sin^2\theta_H$, are given in reference [117]. These samples are produced with p_T higher than 15 GeV (10 GeV) for the jets (leptons), $|\eta| < 5$ for jets and $|\eta| < 2.7$ for leptons at event generation level. More details about GM VBF samples are given in Table 5.4.

DSID	Mass	Events	Filter eff.	Cross-section [fb]	k-factor
307730	250	49000	1.00	24.196	1.00
307731	300	50000	1.00	10.54	1.00
307732	400	49000	1.00	2.30	1.00
307733	500	49000	1.00	0.7975	1.00
307734	600	47000	1.00	0.3408	1.00
307735	700	50000	1.00	0.1663	1.00
307736	800	50000	1.00	0.088	1.00
307737	900	47000	1.00	0.04986	1.00
307738	1000	49000	1.00	0.02961	1.00
307739	1100	48000	1.00	0.01814	1.00
307740	1200	48000	1.00	0.01171	1.00
307741	1300	50000	1.00	0.007622	1.00
307742	1400	49000	1.00	0.005076	1.00
307743	1500	49000	1.00	0.003449	1.00
307744	1600	50000	1.00	0.002391	1.00
307745	1700	50000	1.00	0.001673	1.00
307746	1800	50000	1.00	0.001192	1.00
307747	1900	50000	1.00	0.0008536	1.00
307748	2000	50000	1.00	0.0006183	1.00

TABLE 5.3: ***HVT signal Monte Carlo samples for the VBF resonant search.***

DSID	Mass	Events	Filter eff.	Cross-section [fb]	k-factor
305028	200	40000	1.00	7.0596	1.00
305029	300	40000	1.00	3.9238	1.00
305030	400	40000	1.00	2.4428	1.00
305031	500	40000	1.00	1.6113	1.00
305032	600	40000	1.00	1.1005	1.00
305033	700	40000	1.00	0.77398	1.00
305034	800	40000	1.00	0.55433	1.00
305035	900	40000	1.00	0.40394	1.00

TABLE 5.4: ***Georgi-Machacek signal MC simulations samples for the VBF resonant search.***

5.2.4 Backgrounds Monte Carlo samples

Backgrounds contribution comes mainly from processes with two or three electroweak gauge bosons, such as WZ, ZZ, WW and VVV (V= W or Z), from processes associated to top quark pair as $t\bar{t}$ and $t\bar{t}V$, as well as single top process and tZ. Finally, $Z\gamma$ and jet Zj processes are also accounted in the analysis (Table 5.5).

The QCD WZ Standard Model is the dominant background in this analysis and it is modeled using SHERPA 2.2.2 [118] (**S**imulation of **H**igh-**E**nergy **R**eactions with **PA**rticles) at the next-to-leading order (NLO) corrections. The background includes primary hard-scattering, parton shower, hadronization and the underlying events. which are not coming from the primary hard scattering. Further simulated WZ final states associated with at least two jets ($WZjj \rightarrow \ell\nu\ell'\ell'jj$) labeled $WZjj$ electroweak are produced using SHERPA 2.2.2 at LO for the strong coupling constant a_s.

The ZZ processes $q\bar{q} \rightarrow ZZ \rightarrow \ell\ell\ell'\ell'$ and $q\bar{q} \rightarrow ZZ \rightarrow \ell\ell\nu\nu$ samples are produced with POWHEG-BOX V2 [119] interfaced to PYTHIA-8 and a next-to-next-to-leading order (NNLO) factor (K-factor) is applied for the cross-section normalization as described in reference [120]. The processes $gg \rightarrow ZZ \rightarrow \ell\ell\ell'\ell'$ and VVV backgrounds are simulated by SHERPA 2.1.1 with CT10 PDFs [121]. The $t\bar{t}V$ and tZ samples are generated with MADGRAPH at leading order (LO) term, the first one is combined with PYTHIA-8 and normalized to NLO prediction, the second process is interfaced with PYTHIA-6 [122].

Events with at least one misidentified and fake leptons arise from $Z\gamma$, $W\gamma$, Drell–Yan $Z \rightarrow \ell\ell$, $W \rightarrow \ell\nu$, top-pair and single-top processes. They are estimated using data-driven techniques [123], where the Drell–Yan $Z \rightarrow \ell\ell$, $W \rightarrow \ell\nu$, top-pair and single-top are simulated with POWHEG-BOX V2 and hadronized with PYTHIA-8. Thus, Z events in the Drell-Yan backgrounds with a photon in the final-state with $p_T > 10\ GeV$ are removed to aviod duplicated events with $Z\gamma$.

DSID	Process	Generators	PDF	Events	Filter eff.	Cross-section [pb]	k-factor
361601	$WZ \to \ell\nu\ell\ell$	Powheg+Pythia8	NLO CT10	4890000	1.00	4.5023	1.00
364253	$WZ \to \ell\nu\ell\ell$	Sherpa	NNPDF30NNLO	5485580	1.00	4.583	1.00
361071	WZ VBF EW: $WZ \to \ell\nu\ell\ell$	Sherpa	CT10	1009000	1.00	0.042287	0.91
361603	$q\bar{q} \to ZZ \to \ell\ell\ell\ell$	Powheg+Pythia8	NLO CT10	3920000	1.00	1.2673	1.08
361604	$q\bar{q} \to ZZ \to \ell\ell\nu\nu$	Powheg+Pythia8	NLO CT10	981000	1.00	0.92498	1.08
361073	$gg \to \ell\ell\ell\ell$	Sherpa	CT10	502000	1.00	0.020931	$1.67 \cdot 0.91$
361106	$Z \to ee$	Powheg+Pythia8	CTEQ6L1	19916520	1.00	1901.2	1.026
361107	$Z \to \mu\mu$	Powheg+Pythia8	CTEQ6L1	19916520	1.00	1901.2	1.026
361108	$Z \to \tau\tau$	Powheg+Pythia8	CTEQ6L1	19197457	1.00	1901.2	1.026
361100	$W^+ \to e\nu$	Powheg+Pythia8	CTEQ6L1	29878800	1.00	11278.0	1.0198
361101	$W^+ \to \mu\nu$	Powheg+Pythia8	CTEQ6L1	29892400	1.00	11299.0	1.0179
361102	$W^+ \to \tau\nu$	Powheg+Pythia8	CTEQ6L1	29837800	1.00	11306.0	1.0172
361103	$W^- \to e\nu$	Powheg+Pythia8	CTEQ6L1	19902600	1.00	8290.8	1.0348
361104	$W^- \to \mu\nu$	Powheg+Pythia8	CTEQ6L1	19948400	1.00	8287.1	1.0352
361105	$W^- \to \tau\nu$	Powheg+Pythia8	CTEQ6L1	19951400	1.00	8282.6	1.0358
301535	$Z\gamma \to ee\gamma$ $(10 < p_T^\gamma < 35)$	Sherpa	CT10	4957800	1.00	52.706	1.00
301899	$Z\gamma \to ee\gamma$ $(35 < p_T^\gamma < 70)$	Sherpa	CT10	500000	1.00	5.242	1.00
301900	$Z\gamma \to ee\gamma$ $(70 < p_T^\gamma < 140)$	Sherpa	CT10	246400	1.00	0.38455	1.00
301901	$Z\gamma \to ee\gamma$ $(p_T^\gamma > 140)$	Sherpa	CT10	250000	1.00	0.047209	1.00
301536	$Z\gamma \to \mu\mu\gamma$ $(10 < p_T^\gamma < 35)$	Sherpa	CT10	4981400	1.00	52.708	1.00
301902	$Z\gamma \to \mu\mu\gamma$ $(35 < p_T^\gamma < 70)$	Sherpa	CT10	498600	1.00	5.2455	1.00
301903	$Z\gamma \to \mu\mu\gamma$ $(70 < p_T^\gamma < 140)$	Sherpa	CT10	249800	1.00	0.38548	1.00
301904	$Z\gamma \to \mu\mu\gamma$ $(p_T^\gamma > 140)$	Sherpa	CT10	249200	1.00	0.04724	1.00
301905	$Z\gamma \to \tau\tau\gamma$ $(35 < p_T^\gamma < 70)$	Sherpa	CT10	499000	1.00	5.249	1.00
301906	$Z\gamma \to \tau\tau\gamma$ $(70 < p_T^\gamma < 140)$	Sherpa	CT10	249800	1.00	0.38482	1.00
301907	$Z\gamma \to \tau\tau\gamma$ $(p_T^\gamma > 140)$	Sherpa	CT10	249000	1.00	0.047025	1.00
301908	$Z\gamma \to \nu\nu\gamma$ $(35 < p_T^\gamma < 70)$	Sherpa	CT10	498400	1.00	4.0365	1.00
301909	$Z\gamma \to \nu\nu\gamma$ $(70 < p_T^\gamma < 140)$	Sherpa	CT10	249000	1.00	0.97151	1.00
301910	$Z\gamma \to \nu\nu\gamma$ $(p_T^\gamma > 140)$	Sherpa	CT10	248600	1.00	0.17115	1.00
410000	$t\bar{t}$ $(\geq 1\ell)$	Powheg+Pythia6	NLO CT10	19958779	0.543	696.11	1.1949
410066	$t\bar{t}W + 0p$	Madgraph+Pythia8	NNPDF23LO	1992400	1.00	0.17656	1.25
410067	$t\bar{t}W + 1p$	Madgraph+Pythia8	NNPDF23LO	1943800	1.00	0.14062	1.25
410068	$t\bar{t}W + 2p$	Madgraph+Pythia8	NNPDF23LO	999200	1.00	0.13680	1.25
410111	$t\bar{t}ee + 0p$	Madgraph+Pythia8	NNPDF23LO	299600	1.00	0.0096235	1.35
410112	$t\bar{t}ee + 1p$	Madgraph+Pythia8	NNPDF23LO	299700	1.00	0.017344	1.35
410113	$t\bar{t}\mu\mu + 0p$	Madgraph+Pythia8	NNPDF23LO	300000	1.00	0.0096462	1.35
410114	$t\bar{t}\mu\mu + 1p$	Madgraph+Pythia8	NNPDF23LO	300000	1.00	0.017361	1.35
410115	$t\bar{t}\tau\tau + 0p$	Madgraph+Pythia8	NNPDF23LO	299700	1.00	0.0098874	1.35
410116	$t\bar{t}\tau\tau + 1p$	Madgraph+Pythia8	NNPDF23LO	299200	1.00	0.017790	1.35
410049	tZ (3ℓ)	Madgraph+Pythia6		995000	1.0	0.0090636	1.0
410011	t (t-channel)	Powheg+Pythia6	NLO CT10	4988200	1.0	43.739	1.0094
410012	$\bar{t}$ (t-channel)	Powheg+Pythia6	NLO CT10	4989800	1.0	25.778	1.0193
410015	Wt (2ℓ)	Powheg+Pythia6	NLO CT10	997200	1.0	3.5835	1.054
410016	$W\bar{t}$ (2ℓ)	Powheg+Pythia6	NLO CT10	997600	1.0	3.5814	1.054
410025	t (s-channel) $(\geq 1\ell)$	Powheg+Pythia6	NLO CT10	997800	1.0	2.0517	1.6806
410026	$\bar{t}$ (s-channel) $(\geq 1\ell)$	Powheg+Pythia6	NLO CT10	997400	1.0	1.2615	1.7088
361620	$WWW \to 3\ell 3\nu$	Sherpa	CT10	59800	1.00	0.008343	1.00
361621	$WWZ \to 4\ell 2\nu$	Sherpa	CT10	59600	1.00	0.001734	1.00
361622	$WWZ \to 2\ell 4\nu$	Sherpa	CT10	59800	1.00	0.0034299	1.00
361623	$WZZ \to 5\ell 1\nu$	Sherpa	CT10	49800	1.00	0.00021783	1.00
361624	$WZZ \to 3\ell 3\nu$	Sherpa	CT10	49800	0.44444	0.0019248	1.00
361625	$ZZZ \to 6\ell 0\nu$	Sherpa	CT10	35000	1.00	1.7059e-05	1.00
361626	$ZZZ \to 4\ell 2\nu$	Sherpa	CT10	34600	0.22542	0.00044125	1.00
361627	$ZZZ \to 2\ell 4\nu$	Sherpa	CT10	35000	0.44815	0.0004453	1.00

TABLE 5.5: ***List of background Monte Carlo samples.***

5.3 Event selection

This section describes the event selection criteria chosen for the reconstruction of the three WZ leptonic decays final states with electrons and muons i.e. $\mu^+\mu^-\mu^\pm, \mu^+\mu^- e^\pm, e^+e^-\mu^\pm$ and $e^+e^-e^\pm$, where the two first leptons are originated from Z bosons decay and the third one which is associated with a neutrino from W bosons decay. Event are collected using single muon or electron triggers. Then Good Run Lists described in 5.2.1 is applied in order to keep only event with high quality data. Finally only event with three lepton emerging from the primary vertex are used in this analysis.

5.3.1 Event cleaning

Following the recommendations provided by the ATLAS data quality group, an additional events cleaning is applied to candidates passing the requested GRL (section 5.2.1) to discard corrupted events and ensure that candidate's informations are completely measured by the whole ATLAS sub-detectors. The different sources of bad event measurements are described as follow:

- **Tile calorimeter corrupted events:** Since run-I TileCal has suffered from the photomultiplier tubes (PMTs) that are not properly powered in some consecutive trip modules. In case of one unpowered module, trips issue is signed as tolerable defect by the data quality group and the events are recovered by extrapolating information from its neighbouring modules. On the other hand, if the problem exists in several consecutive modules, the issue is signed-off as intolerable defect and the events are rejected [124].

- **LAr calorimeter's noise bursts:** The LAr calorimeter is affected by the large noise bursts due to the high instantaneous luminosity delivered by the LHC. This noise is observed for a short time of about 0.5 s with about 90% found to be less than 5 μs. This issue is treated by applying a *time-window veto* [125] procedures. Once the noise burst is identified data in a time window (1 ms) around the burst is vetoed. In case of many noise events the entire LB is rejected.

- **Semiconductor Tracker corrupted events:** The high energetic particles that pass through the SCT's junction creates electron-hole pairs by interacting with the atom of silicon. Some of those pairs are recombined forming a short current pulse leading to *soft errors* called *single event upset* (SEU) [126] producing a bit flip where data with 1 bit becoming 0 bit or vice versa in the memory. To mitigate this defect the data quality group reset the event counters automatically once the error is detected in a SCT module. In this analysis, the affected candidates by single event upsets are rejected.

5.3.2 Triggers

Events in this analysis are required to pass single muon or electron triggers listed in Tables 5.7 and 5.6 with a total efficiency of about 99%. Where the trigger efficiency ϵ_{trig} is defined as the ratio of the number of events passing the selection N_{trig} over the total number of events N_{total} that passing the selection without any trigger requirement as shown in the following equation:

$$\epsilon_{trig} = \frac{N_{trig}}{N_{total}}. \tag{5.1}$$

The errors on the trigger efficiency are calculated using binomial distribution:

$$\Delta\epsilon_{trig} = \sqrt{\frac{\epsilon_{trig}(1-\epsilon_{trig})}{N_{total}}}. \tag{5.2}$$

Particle type	Muon trigger	Period
	HLT_mu20_iloose_L1MU15=	2015
	HLT_mu60_0eta105_msonly=	2015 D-J periods
	HLT_mu20_ivarloose_L1MU15=	2016 A period
	HLT_mu24_iloose_L1MU15=	2016 A period
	HLT_mu24_ivarloose_L1MU15=	2016 A period
	HLT_mu20_iloose= (_L1MU15 MC=)	
	HLT_mu20_ivarloose=	2016 A period
μ	HLT_mu24_iloose=	2016 A period
	HLT_mu24_ivarloose=	2016 A period
	HLT_mu24_imedium=	2016 B-D3 periods
	HLT_mu24_ivarmedium=	2016 B-D3 periods
	HLT_mu26_imedium=	2016 D4- periods
	HLT_mu26_ivarmedium=	2016 D4- periods
	HLT_mu40=	2015-2016
	HLT_mu50=	2015-2016

TABLE 5.6: ***Summary of the High Level Triggers for muon that are used during the 2015 and 2016 data taking periods.***

Particle type	electons trigger	Period
	HLT_e24_lhtight_nod0_ivarloose=	2016 A-D3 periods
	HLT_e24_lhmedium_nod0_L1EM20VH=	2016
	HLT_e60_lhmedium_nod0=	2016 A-D3 periods
	HLT_e60_lhmedium=	2015-2016 A-D3 periods
	HLT_e60_medium=	2016 A-D3 periods
	HLT_e26_lhtight_ivarloose=	2016 D4- periods
	HLT_e26_lhtight_nod0_ivarloose=	2016 D4- periods
e	HLT_e26_lhtight_smooth_ivarloose=	2016 D4- periods
	HLT_e26_lhmedium_nod0_ivarloose=	2016 D4- periods
	HLT_e300_etcut=	2016 A-D3 periods
	HLT_e140_lhloose_nod0=	2016 A-D4 periods
	HLT_e140_lhloose=	2016 A-D4 periods
	HLT_e120_lhloose=	2015
	HLT_e24_lhmedium_L1EM18VH=	2015 MC
	HLT_e24_lhmedium_L1EM20VH=	2015 data

TABLE 5.7: ***Summary of the High Level Trigger for electrons that are used during the 2015 and 2016 data taking.***

The study of efficiency of individual triggers is performed using HVT signal MC samples (Table 5.2) with 600,1300, 2000 GeV WZ mass points and justifies the choice of the single lepton triggers which provides the highest efficiency (Figures 5.2 and 5.3).

We explored additional triggers to increase the efficiency. The missing transverse energy, di-leptons, tri-leptons or combined triggers have been tested using a $q\bar{q}$ HVT signal sample with a WZ mass point of 600 GeV. We found that adding MET triggers to the single lepton offers less than 1% gain in term of efficiency for muon channel and about 1% for electron channel (Figure 5.5).

However, MET triggers brings about 2.63% efficiency for the $\mu\mu\mu$ channel in the high WZ resonant mass region (2 TeV). In fact, after selecting W and Z candidates, the single lepton trigger is 100% efficient for $e\mu\mu$, μee, and eee channels, while the observed drop in the $\mu\mu\mu$ efficiency is recovered by adding MET triggers (Figure 5.5).

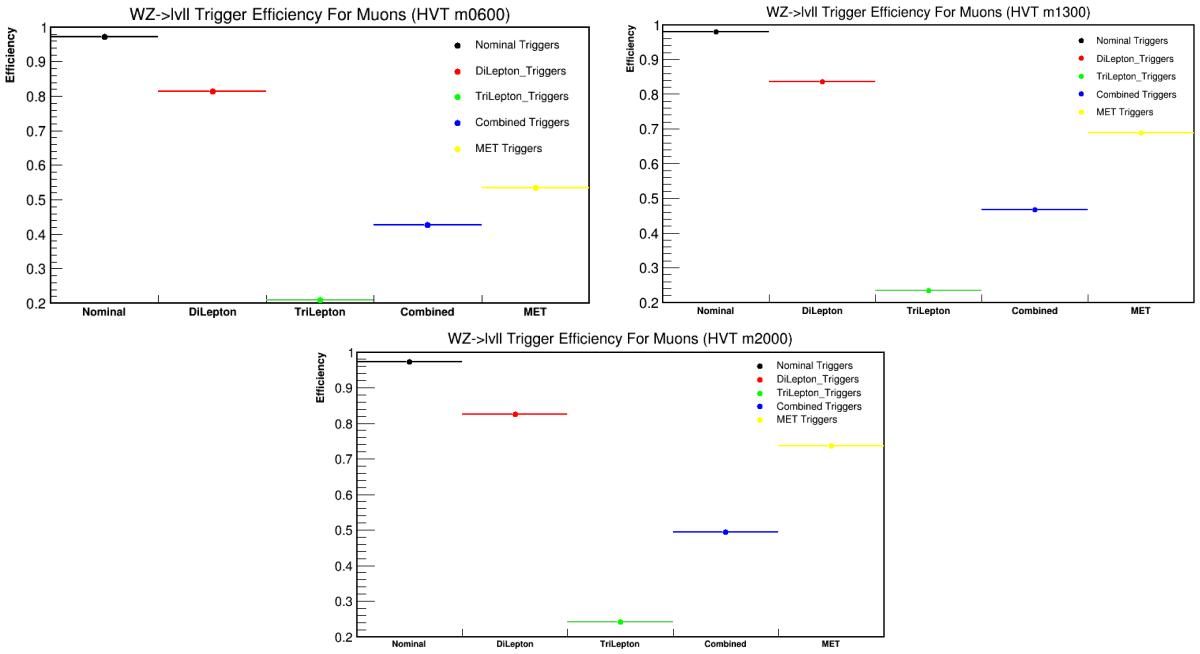


FIGURE 5.2: ***Muons Trigger Efficiency for 600,1300,2000 GeV HVT signal.***

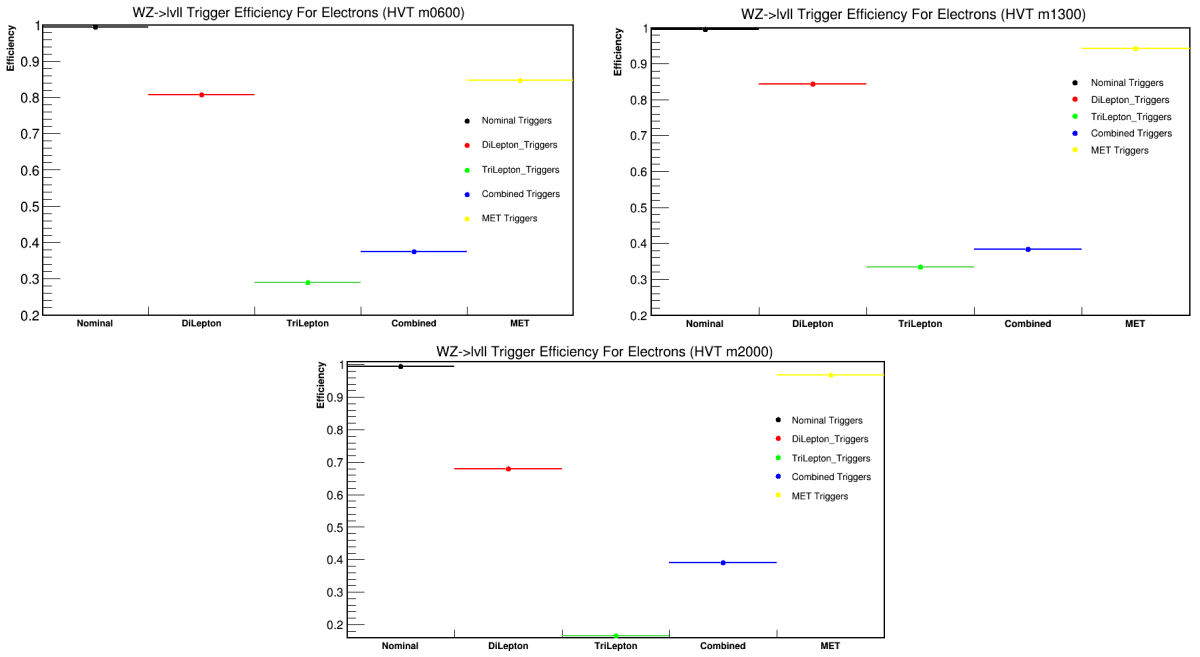


FIGURE 5.3: ***Electrons Trigger Efficiency for 600,1300,2000 GeV HVT signal.***

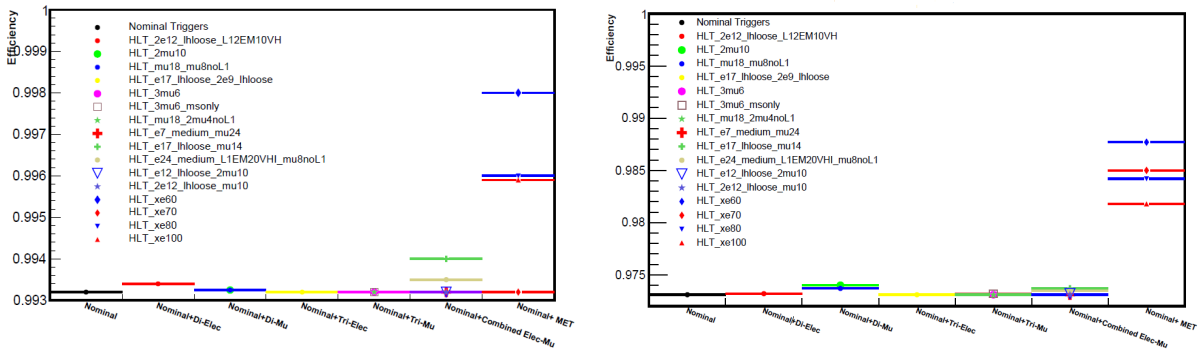


FIGURE 5.4: ***Efficiency gain at the pre-selection level of adding other triggers to the nominal one using 600 GeV HVT signal sample for electrons (left) and muons (right).***

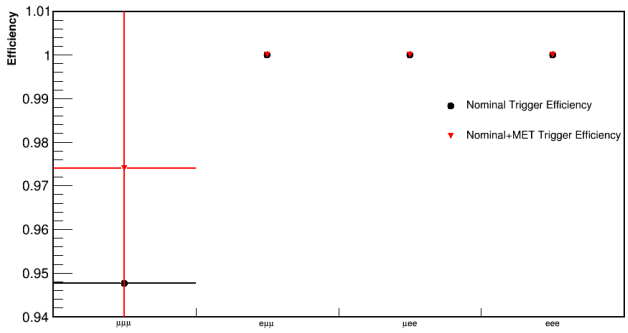


FIGURE 5.5: ***Efficiency gain using current selection and nominal triggers per WZ channel for 2000 GeV HVT signal.***

The trigger efficiency for backgrounds after WZ candidates selection is evaluated using WZ-SM backgrounds sample as it is the dominant one. Results show that the single lepton efficiency is more than 99% for all WZ channels with 100% at high leptons p_T and no gain by adding MET triggers (figure 5.6).

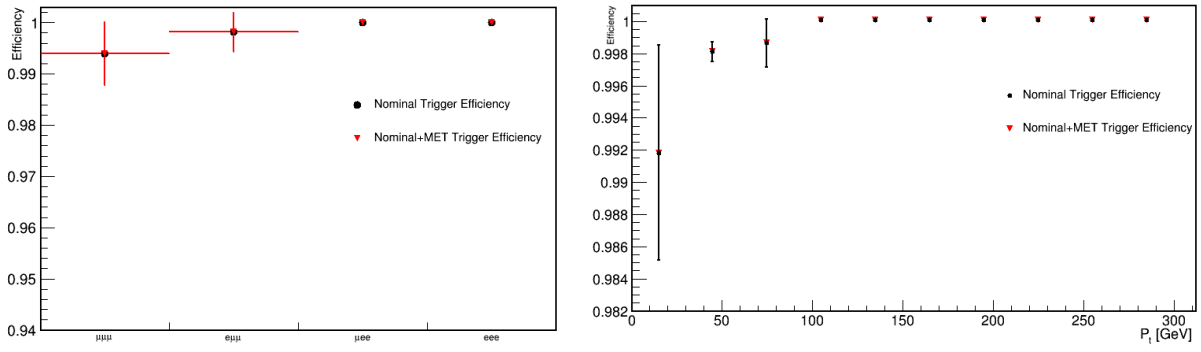


FIGURE 5.6: ***Efficiency gain using current selection and nominal triggers per WZ channel (left) and versus leptons momentum (right) for WZ-SM background.***

Furthermore, there is no evident gain in HVT signal or the SM WZ by including MET triggers. That is why, only single muon and electron triggers are used in this analysis.

5.3.3 Primary vertex

Primary vertex selection requests a set of criteria on the event's track parameters such as P_T, d_0, z_0, numbers of hits or holes in the SCT, Pixel and IBL detectors according to following cuts [127]:

- $p_T^{Track} > 0.4\ GeV$, $|\sigma(d_0)| < 4\ mm$, $\sigma(z_0) < 10\ mm$.
- At least 4 hits in the SCT detector, more than 8 silicon hits in the SCT or pixel with no holes.
- In case of $|\eta| \geq 1.65$, events should have more than 11 silicon hits with at maximum one hole.
- The sum of hits in both IBL and B-layer should be more than one.
- A maximum 1 shared pixel hit or 2 shared SCT hits.

Due to the harder transverse momentum of the charged particles in the proton proton collision compared to the pileup collision, the primary vertex selection in this analysis is realized by asking for the vertex with the highest sum of the squared transverse momenta $\sum(p_T^{Track})^2$ of the vertex with at least two associated tracks satisfying all the previous criteria.

5.3.4 Lepton final selection

The final lepton selection used for the reconstruction of WZ candidates starts by requesting events with exactly three high-p_T leptons with $p_T > 25GeV$ originating from the primary vertex and passing trigger requirement. Two of them which are associated with Z boson must fulfill the medium quality criteria for muons and electrons as described in sections 4.3 and 4.2. At least one lepton must be in the trigger plateau with $p_T^{leading} > 27GeV$. The third lepton in the events which is expected to originate from W decays, is required to pass the tight quality criteria since it is the one used, with the missing transverse energy E_T^{miss}, to reconstruct the W boson's invariant mass.

Furthermore, events with additional leptons passing looser criteria, coming mainly from ZZ and VVV backgrounds are rejected by a ZZ *veto* which requires a minimum lepton p_T. An optimization study was performed with 20 GeV and 7 GeV transverse momentum threshold, and has shown that $ZZ(VVV)$ backgrounds was reduced by more than 25 % (\$13%) (Figure 5.7). However, the dominant WZ-SM background is not affected as can be seen in Figure 5.8.

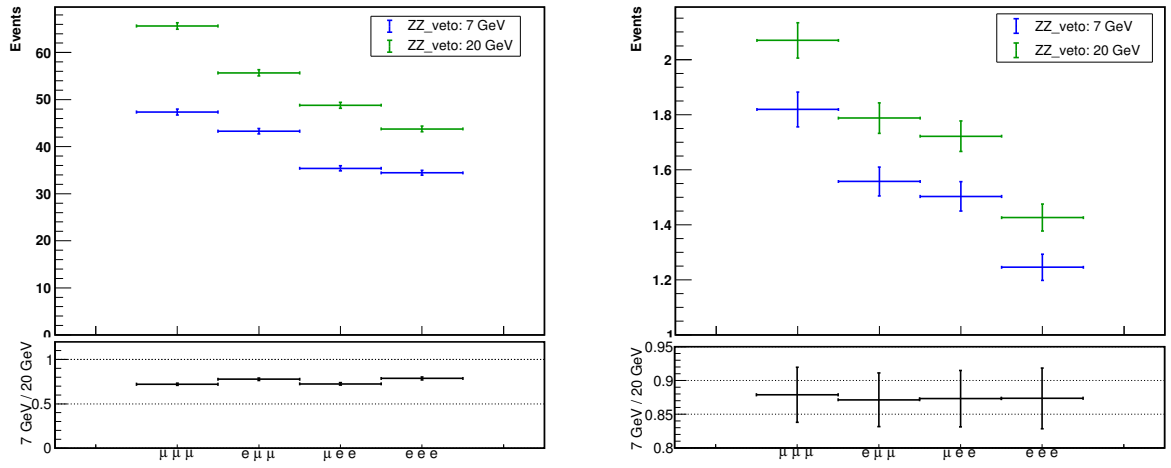


FIGURE 5.7: ***A comparison between 7 GeV and 20 GeV ZZ veto cut for both ZZ (left) and VVV (right) events.***

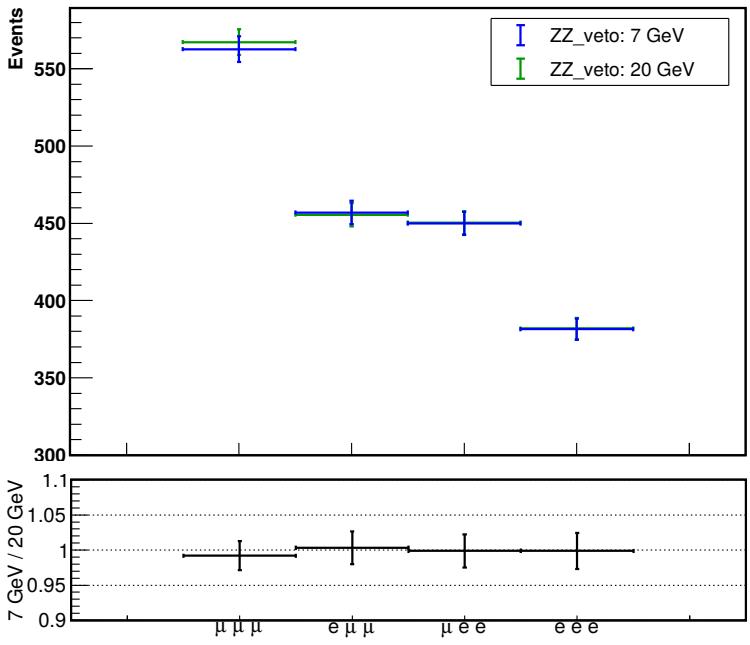


FIGURE 5.8: ***A comparison between 7 GeV and 20 GeV ZZ veto cut for WZ-SM.***

5.3.5 Z candidate selection

Z bosons candidates at $Z \to \mu^+\mu^-$ or $Z \to e^+e^-$ channels are reconstructed by selecting event passing the previous selection with two leptons (dileptons) of the same flavor and opposite charge, where dileptons pairing must have an invariant mass close to the Z mass $m_Z = 91.1876$ within a windows of 20 GeV. For events with three same flavor leptons, such as in $e^+e^-e^\pm$ and $\mu^+\mu^-\mu^\pm$, the pair with closest invariant mass to m_Z is chosen.

5.3.6 W candidate selection

This section presents the identification of different $W^\pm$ boson decays from the combination of third leptons kinematic variables and the missing transverse energy E_T^{miss} related to the non-interacting neutrinos. The third lepton is required to pass tight identification quality, while the missing transverse energy must be larger than 25 GeV ($E_T^{miss} > 25GeV$).

To reconstruct the W boson and its kinematic features, we consider the four-momentum conservation law:

$$p_W^\mu = p_l^\mu + p_\nu^\mu, \tag{5.3}$$

where, $p_W^\mu = (E_W, \vec{P}_W)$, $p_l^\mu = (E_l, \vec{P}_W)$, $p_\nu^\mu = (E_\nu, \vec{P}_W)$ are the momentum-energy four-vector of W boson, lepton and neutrino respectively with index μ. Taking square on both side and using the relativistic energy-momentum relation $E^2 = \vec{P}^2 + m_0^2$, where m_0 represents the particle rest mass, then the Equation 5.3 can be written as:

$$(m_0^W)^2 = (E_l + E_\nu)^2 - (\vec{P_l} + \vec{P_\nu})^2. \tag{5.4}$$

For massless particle as neutrino $(m_0^\nu)^2 \simeq 0$, the Equation 5.3 can be reduced to the following form:

$$\frac{(m_0^W)^2 - (m_0^l)^2}{2} = E_l E_\nu - \vec{P_l}\vec{P_\nu}, \tag{5.5}$$

where:

$$\vec{P_l}\vec{P_\nu} = p_l^x p_\nu^x + p_l^y p_\nu^y + p_l^z p_\nu^z. \tag{5.6}$$

$$E_l E_\nu = E_l \sqrt{(p_T^\nu)^2 - (p_z^\nu)^2} = \frac{(m_0^W)^2 - (m_0^l)^2}{2} + p_l^x p_\nu^x + p_l^y p_\nu^y + p_l^z p_\nu^z. \tag{5.7}$$

Considering $\Omega = \frac{(m_0^W)^2 - (m_0^l)^2}{2} + p_l^x p_\nu^x + p_l^y p_\nu^y$, the Equation 5.7 became:

$$((p_l^z)^2 - E_l^2)\ (p_\nu^z)^2 + 2\Omega p_l^z\ p_\nu^z + (\Omega^2 - E_l^2 (p_\nu^T)^2) = 0. \tag{5.8}$$

where p_ν^z represents the unknown variable, one can get the neutrino longitudinal momentum p_ν^z is written as follows roots:

$$p_\nu^z = \frac{-\Omega p_l^z \pm \sqrt{(\Omega p_l^z)^2 - ((p_l^z)^2 - E_l^2)(\Omega^2 - E_l^2(p_\nu^T)^2)}}{2((p_l^z)^2 - E_l^2)}. \tag{5.9}$$

The measured E_T^{miss} is assumed to be the transverse momentum of the neutrino p_ν^T, then p_ν^z is finally calculated using the following formula:

$$p_\nu^z = \frac{-\Omega p_l^z \pm \sqrt{(\Omega p_l^z)^2 - ((p_l^z)^2 - E_l^2)(\Omega^2 - E_l^2(E_T^{miss})^2)}}{2((p_l^z)^2 - E_l^2)}, \tag{5.10}$$

Equation 5.10 leads to two possible roots, if they are real the solution with smaller absolute value $|p_\nu^z|$ is chosen. While in case of negative discriminant the real part is kept as p_ν^z value. Then, the WZ invariant mass (m_{WZ}) is reconstructed using the selected three leptons and neutrinos four-momentum of the events passing all the previous events selection.

5.3.7 Event selection acceptance

The relative acceptance for each cut is shown in Table 5.8 using a WZ-SM subset sample with 4731 events. The acceptance is calculated cut by cut with respect to the residual events after the previous selection.

MC Sample		
mc15_13TeV.361601.PowhegPy8EG_CT10nloME_AZNLOCTEQ6L1_WZlvll_mll4		
Event selection	**Number of events per cut**	**Acceptance [%]**
Good Run List (GRL)	4731	100
Event cleaning	4731	100
Primary vertex	4731	100
Trigger	3493	74
Exactly three leptons	305	8.73
ZZ veto	305	100
Z candidate	276	90.50
W candidate	241	87.32
$E_T^{miss} > 25GeV$	186	77.20
Leading lepton $p_T > 27GeV$	186	100

TABLE 5.8: ***WZ cut-flow efficiency, using WZ-SM background.***

Selected event are then normalized to the corresponding data luminosity (36.1 fb^{-1}) using the event generator cross-sections listed in Table 5.5. The agreement between data and Monte Carlo is presented in Figure 5.9 for the Z boson invariant mass, W boson transverse mass, missing transverse energy and the WZ transverse mass distributions. The jet multiplicity and the total events yield per WZ channel agreement can be seen in Figure 5.10. For all distributions, backgrounds contributions include fake leptons estimated from Monte Carlo.

A reasonable agreement between data and Monte Carlo is obtained. The total event yields passing the selection before signal optimization for both data and simulated backgrounds is listed in Table 5.9, the uncertainties on the events yields are only statistical. Data to Monte Carlo ratio can also be seen in the table, and confirms the good agreement.

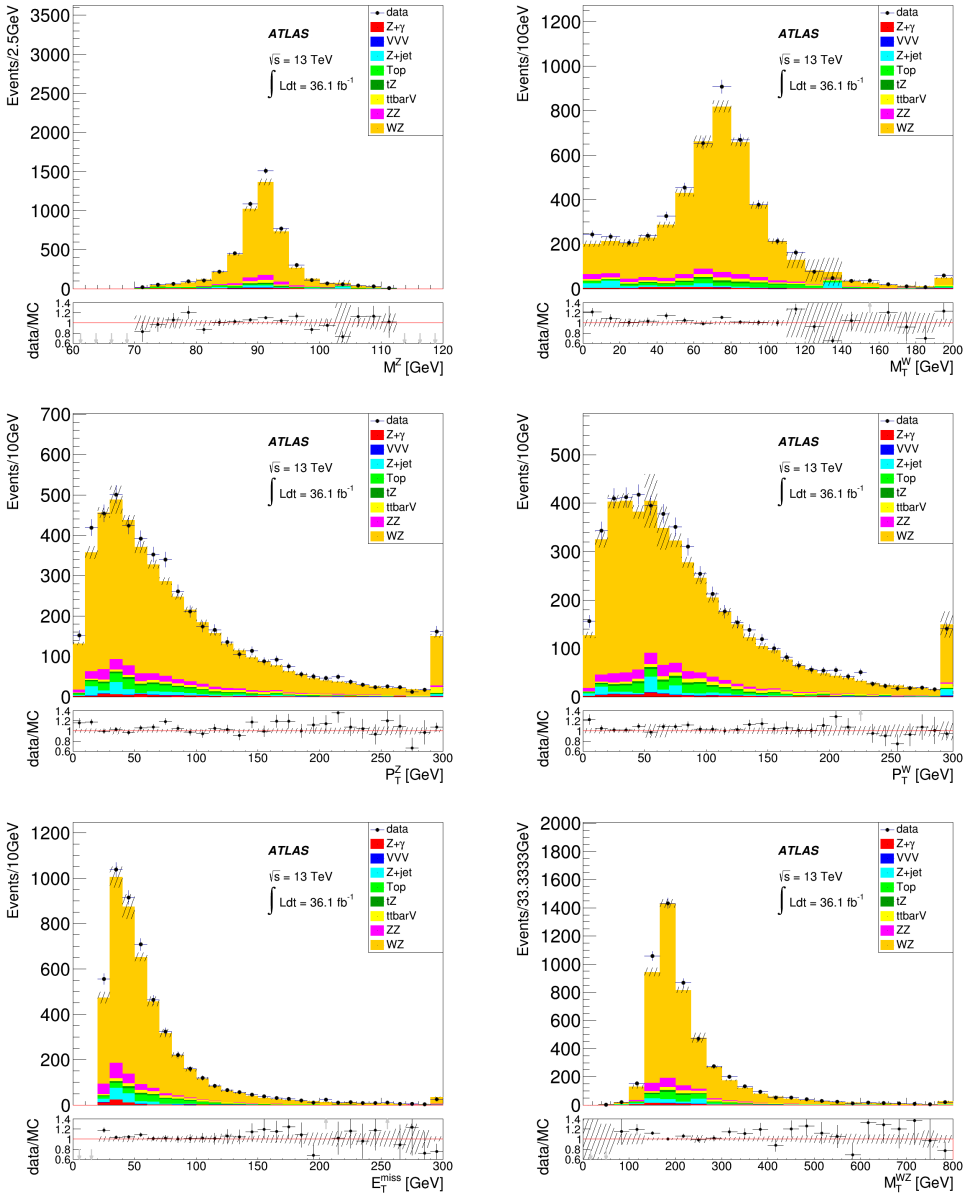


FIGURE 5.9: ***The Z boson invariant mass is shown on the top left, the W boson transverse mass on the top right, the Z boson transverse momentum in the middle left, the W boson transverse momentum in the middle right, the $E_{\mathrm{T}}^{\mathrm{miss}}$ on the bottom left and the transverse mass of the WZ system on the bottom right. Backgrounds contribution include fake leptons are estimated from Monte Carlo and normalized to the data luminosity of 36.1 fb^{-1}.***

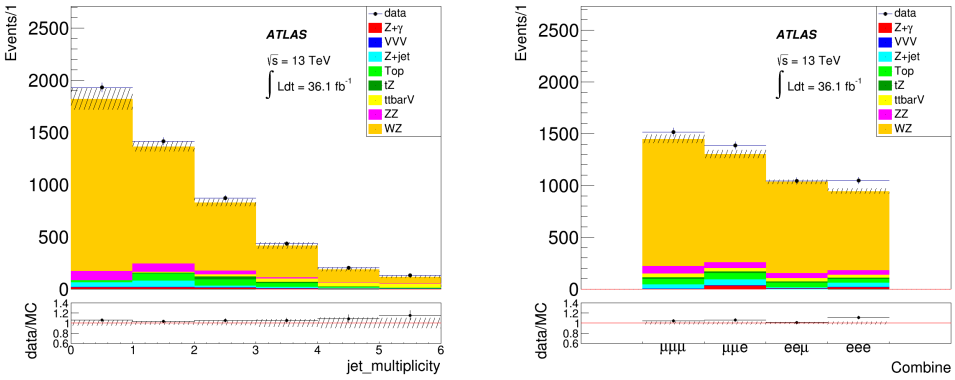


FIGURE 5.10: ***The jet multiplicity and the total event yields in both data and MC are given for WZ events. Backgrounds contribution include fake leptons estimated from Monte Carlo and normalized to the data luminosity 36.1 fb^{-1}.***

Process	$\mu\mu\mu$	$e\mu\mu$	μee	eee	Total events
data	1561±39.5	1341±36.6	954±30.9	927±30.4	4783±69.2
total MC	1504.6±13.8	1360.6±16.0	1088.3±27.8	1029.5±47.1	4982.9±58.7
WZ	1263.2±8.4	1061.7±7.8	914.2±7.3	815.6±8.5	4054.5±16.0
ZZ	87.0±1.2	80.8±1.1	57.5±1.0	57.9±1.0	283.1±2.1
VVV	1.9±0.05	1.7±0.04	1.5±0.04	1.3±0.04	6.4±0.09
Z+gamma	1.3±0.7	58.5±4.8	1.6±1.4	24.9±2.4	86.4±5.6
Z+jets	35.6±9.1	53.1±12.2	30.6±26.4	65.8±46.2	185.1±55.3
ttbar	58.7±5.9	56.3±4.6	36.9±4.7	24.4±3.5	176.3±9.5
ttbarV	38.3±0.4	33.1±0.34	32.3±0.3	28.1±0.3	131.9±0.7
tZ	18.6±0.09	15.5±0.08	13.6±0.08	11.5±0.07	59.3±0.2
Data/MC	1.04±0.026	0.99±0.027	0.88±0.028	0.90±0.029	0.96±0.026

TABLE 5.9: ***Events yields in data and Monte Carlo passing the event selection before signal optimization per WZ channel, the uncertainties on the events yields are only statistical. The line gives the fraction between data and Monte-Carlo can be seen also in the table.***

5.4 WZ Signal Optimization

After the selection of the WZ candidates, a procedure to optimize background rejection and conserve events enriched with signal is performed. Two different event selections are used to discriminate $q\bar{q}$ and VBF categories and hence define two different signal regions. The selection starts by applying cuts related to VBF signature as it will be described in section 5.4.1, then events which are not accepted by VBF selection are considered for $q\bar{q}$ one.

5.4.1 VBF category

VBF events are produced with two forward jets in association with the reconstructed WZ leptons candidates. The identification of VBF category begins with requiring at least two jets with $p_T > 30GeV$ passing B-tagging criteria using 0.1758 $MV2c10$ working point with a n-jet efficiency of 85% as described in section 4.4. Furthermore, a cut on both dijet mass m_{jj} and the pseudo-rapidity separation $\Delta\eta_{jj}$ of the two leading jets produces a clear separation between VBF signal region and backgrounds as shown in Figures 5.11.

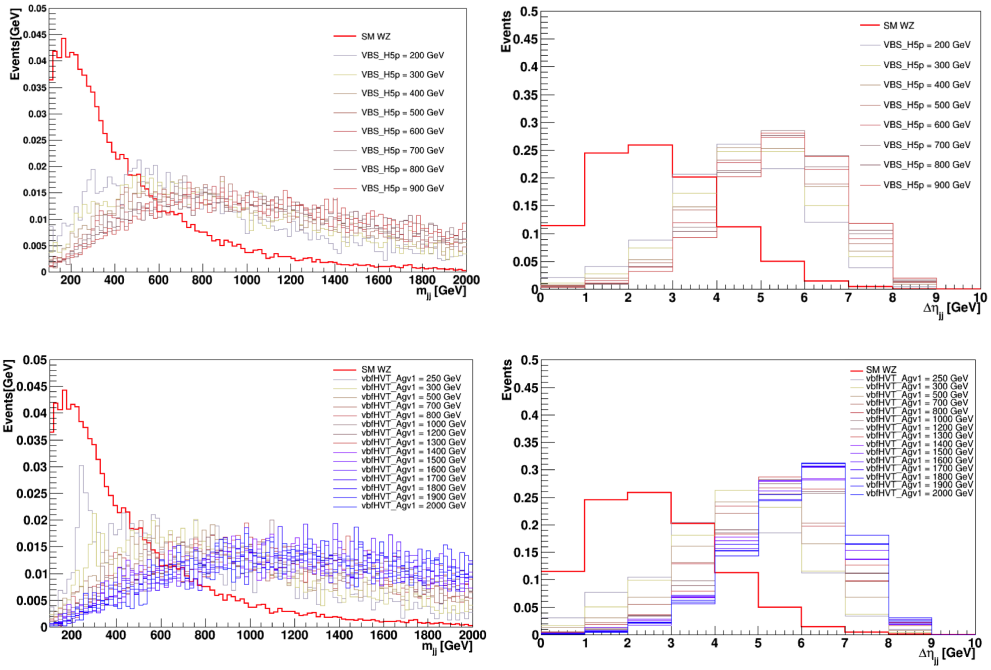


FIGURE 5.11: ***Distributions of m_{jj} and $\Delta\eta_{jj}$ for both signals modeling mass points, GM (top), HVT VBF (Bottom) models and the WZ SM backgrounds.***

From Figures 5.11 one can look for a cut on m_{jj} and $|\Delta\eta_{jj}|$ in the intervals $3 < |\Delta\eta_{jj}| < 4$ and 400 GeV $< m_{jj} <$ 600 GeV. The best signal-background isolation point is evaluated by using the Poisson significance σ given by the following formula:

$$\sigma = \sqrt{\sum_i 2\left((S_i + B_i)\log\left(1 + \frac{S_i}{B_i}\right) - S_i\right)}, \tag{5.11}$$

where S_i and B_i are respectively the number of events of signal and backgrounds in bin i of $\Delta\eta_{jj}$ and m_{jj} distributions. Figure 5.12 shows a two-dimensional (2-D) scan on the $|\Delta\eta_{jj}|$ and m_{jj} variable for the different WZ signal mass points, the z-axis of the figure corresponds to the Poisson significance σ value for each cut scan. The optimal cut values with highest binned significance is found for $|\Delta\eta_{jj}| > 3.5$ and $m_{jj} > 500$ GeV.

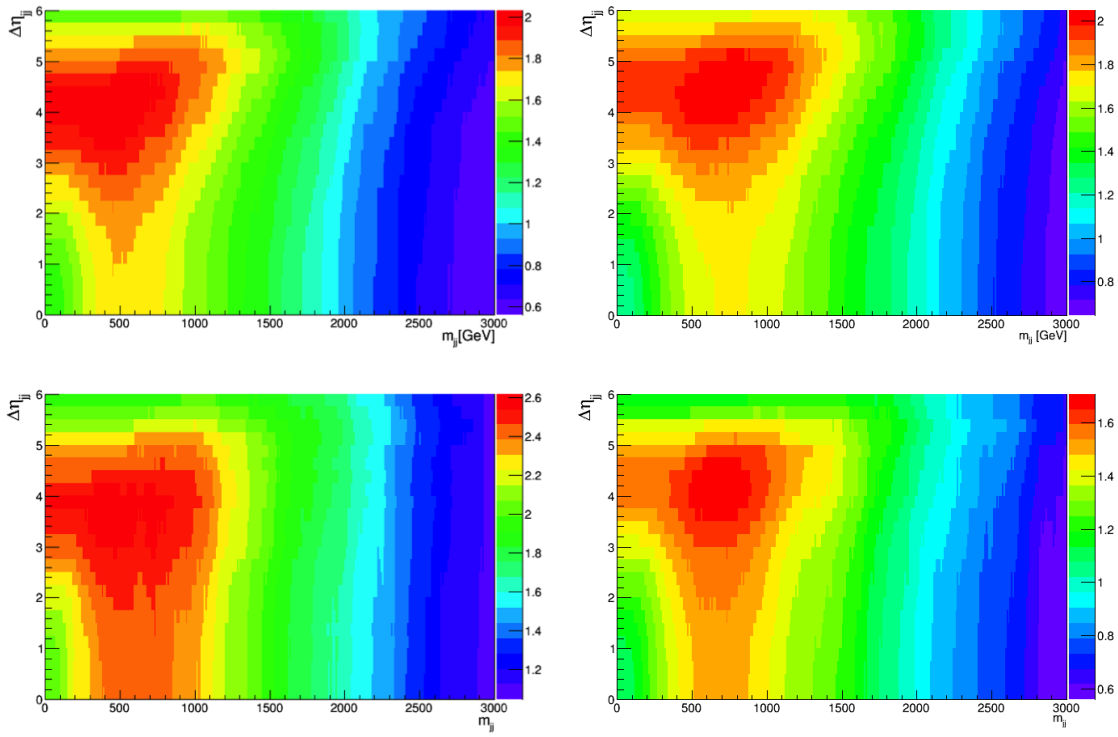


FIGURE 5.12: ***Two-dimensional (2-D) scan of the parameters*** m_{jj} ***and*** $|\Delta\eta_{jj}|$ ***for the mass point 200 GeV (top left), 300 GeV (top righ) for GM model and 250 GeV (bottom left), 300 (bottom right) for HVT signal. The z-axis represents the Poisson significance*** σ***.***

The total event yields in both data and MC can be seen in Table 5.10 after applying the fully VBF signal events selection including cut optimization. thus, a data-Monte-Carlo comparison is shown in Figure 5.13 for distributions of the yield per channel as well as some kinematic variables related with the di-jets system (m_{jj}, $\Delta\eta_{jj}$, $\Delta\phi_{jj}$), the missing energy and WZ transverse mass, the backgrounds are estimated from Monte Carlo.

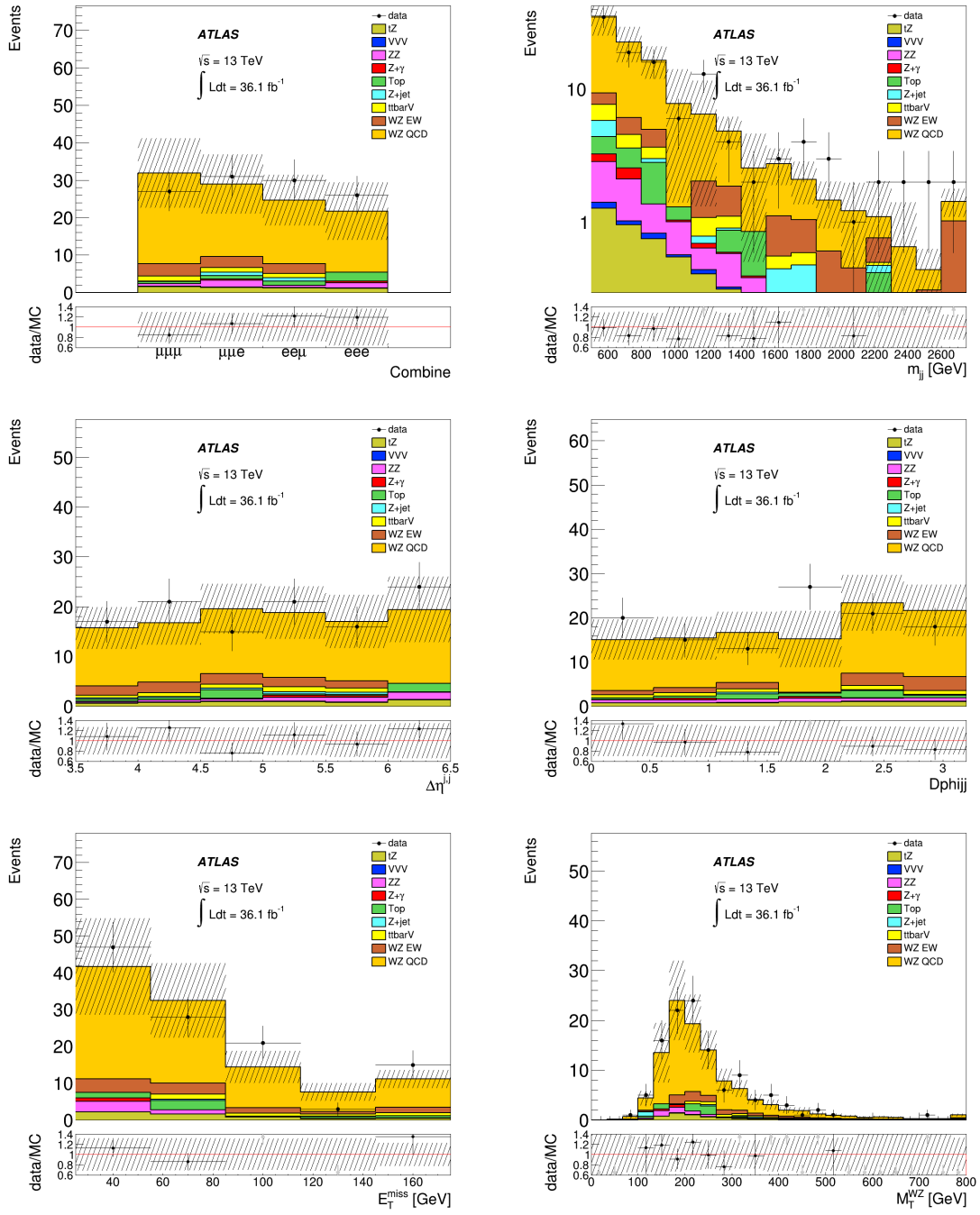


FIGURE 5.13: ***Distributions of the yield per channel, m_{jj}, $\Delta\eta_{jj}$, $\Delta\phi_{jj}$ missing energy and WZ transverse mass in the VBF signal region.***

Process	all lepton final states combined
data	114±10.68
total MC	99.54±13.68
VVV	0.37±0.05
tZ	5.20±0.51
$Z\gamma$	0.96±1.27
Top	4.94±2.75
$t\bar{t}V$	4.98±0.47
ZZ	4.40±1.46
Zjets	1.72±6.62
WZ	76.97±11.47
Data/MC	1.15±0.19

TABLE 5.10: ***Yields of VBF selected events in 36.1 fb^{-1} of 2015 and 2016 data at 13 TeV, the uncertainties on the events yields are only statistical.***

5.4.2 $q\bar{q}$ category

The residual of WZ events failing the VBF selection are considered for $q\bar{q}$ signal region. As for VBF category, an optimized selection is applied to this events in order to reduce backgrounds contribution. To achieve this, a cut on $p_{\mathrm{T}}^{\mathrm{Z}}/\mathrm{m_{WZ}}$ and $p_{\mathrm{T}}^{W}/\mathrm{m_{WZ}}$ parameters is requested, since the W and Z bosons pair produced in term of HVT model in the s-channel with m_{WZ} highest than 250 GeV have transverse momenta close to 50 % of its mass. From Figure 5.14 showing the distributions of $p_{\mathrm{T}}^{\mathrm{Z}}/\mathrm{m_{WZ}}$ and $p_{\mathrm{T}}^{W}/\mathrm{m_{WZ}}$, one can see that the cut point providing the best background-signal separation for both parameters is close to 0.35 value.

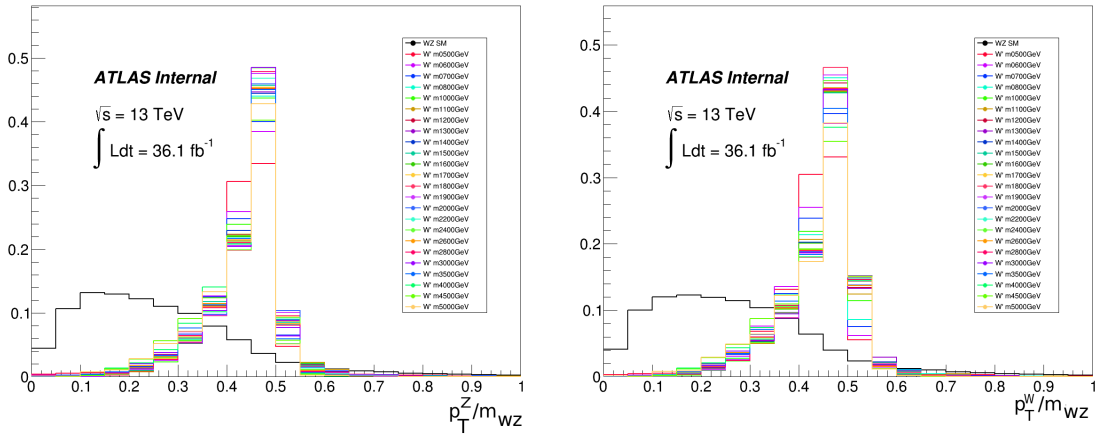


FIGURE 5.14: ***Distributions of $p_{\mathrm{T}}^{\mathrm{Z}}/\mathrm{m_{WZ}}$ (left) and $p_{\mathrm{T}}^{W}/\mathrm{m_{WZ}}$ (right) for the HVT signal mass points and the WZ-SM background normalized to the unit.***

The optimal value of the $p_{\mathrm{T}}^{\mathrm{Z}}/\mathrm{m_{WZ}}$ and $p_{\mathrm{T}}^{W}/\mathrm{m_{WZ}}$ cut is confirmed by minimizing the expected limits on the cross section of several HVT model's mass points using a statistical framework called ResonanceFinder. The procedure is performed by varying $p_{\mathrm{T}}^{\mathrm{Z}}/\mathrm{m_{WZ}}$ and $p_{\mathrm{T}}^{W}/\mathrm{m_{WZ}}$ between 0.2 to 0.45 with 0.5 step, while extracting the number of events passing each cut scan from the total sum of all Monte-Carlo backgrounds, the WZ invariant mass was used for the limits calculation as an observable without including systematic uncertainties.

More optimized cuts from previous ATLAS WZ analysis at 8 TeV [128] were tested, specifically the W and Z bosons pair rapidity separation $\Delta y(W,Z) < 1.5$, the azimuthal angle between the third lepton and the transverse missing energy coming from W boson decay $\Delta\phi(\ell^{\mathrm{W}}, E_{\mathrm{T}}^{\mathrm{miss}}) < 1.5$, as well as the combination of all cuts. The distribution of different parameters tested for the optimization of $q\bar{q}$ are given in Figure 5.15.

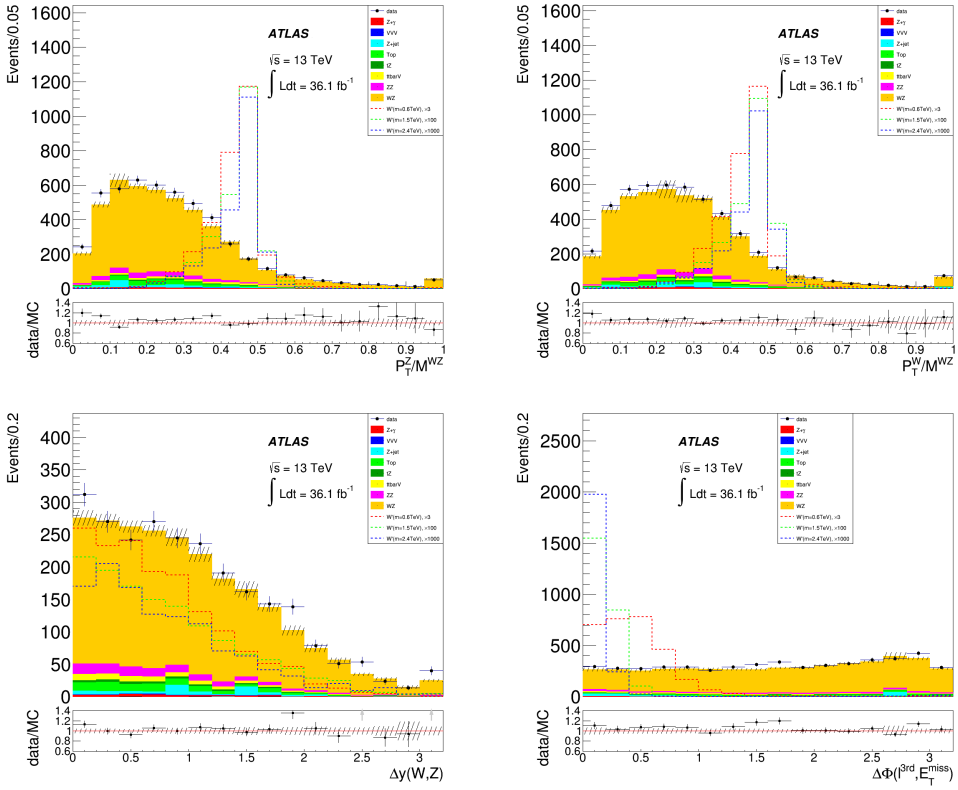


Figure 5.15: ***Distributions of*** $p_{\mathrm{T}}^{\mathrm{Z}}/\mathrm{m_{WZ}}$ ***(top left),*** $p_{\mathrm{T}}^{W}/\mathrm{m_{WZ}}$ ***(top right),*** $\Delta y(W,Z)$ ***the rapidity separation between*** W ***and*** Z ***bosons (bottom left), and*** $\Delta\phi(\ell^{\mathrm{W}}, E_{\mathrm{T}}^{\mathrm{miss}})$ ***which is*** $\Delta\phi$ ***(bottom right).***

The results on the expected limits presented in Figure 5.16 for different HVT mass points from 500 GeV to 3 TeV, show that the best cut is obtained for $p_{\mathrm{T}}^{\mathrm{Z}}/\mathrm{m_{WZ}}$ and $p_{\mathrm{T}}^{W}/\mathrm{m_{WZ}}$ with value of 0.35, while there is no gain by applying the cuts on $\Delta y(W,Z)$, $\Delta\phi(\ell^{3\mathrm{rd}}, E_{\mathrm{T}}^{\mathrm{miss}})$ or the combined one.

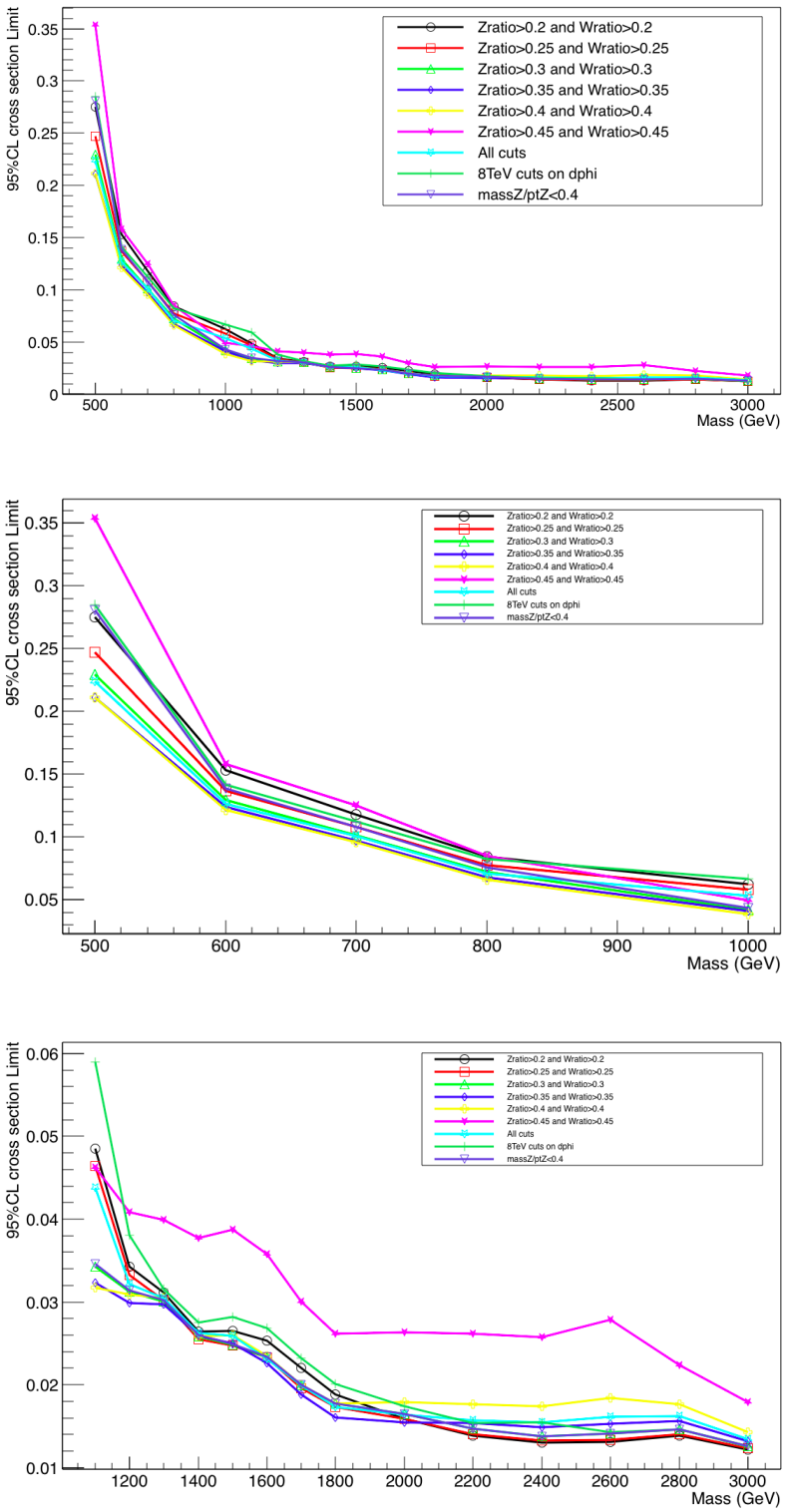


FIGURE 5.16: ***The expected limits on the cross section of several HVT model as a function of its invariant mass for different cuts on*** $p_{\mathrm{T}}^{\mathrm{Z}}/\mathrm{m_{WZ}}$ ***and*** $p_{\mathrm{T}}^{W}/\mathrm{m_{WZ}}$ ***and*** $\Delta y(W,Z) < 1.5$ ***and*** $\Delta\phi(\ell^{3\mathrm{rd}}, E_{\mathrm{T}}^{\mathrm{miss}}) < 1.5$ ***in the mass range between 500 GeV and 3 TeVGeV (top), zoom on the mass range below 1 TeV (middle), zoom on the mass range between 1 TeV to 3 TeV (bottom).***

The events yields for data and backgrounds passing the whole $q\bar{q}$ selection including cuts $p_{\mathrm{T}}^{\mathrm{Z}}/\mathrm{m_{WZ}} < 0.35$ and $p_{\mathrm{T}}^{W}/\mathrm{m_{WZ}} < 0.35$ are listed in Table 5.11 and represented in Figure 5.17 per WZ channel, the numbers show a good agreement between data and Monte-Carlo. Furthermore, the data-Monte-Carlo agreement is commfirmed in Figure 5.18 for the distributions of W boson transverse mass, WZ transverse mass, transverse missing energy as well as for Z boson invariant mass.

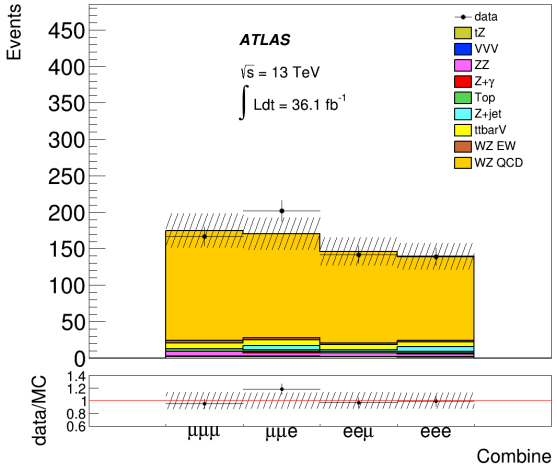


FIGURE 5.17: ***The total events yields in both data and MC for individual channel are given for WZ events after applying signal selection cuts :*** $p_{\mathrm{T}}^{\mathrm{Z}}/\mathrm{m_{WZ}} > 0.35$ ***and*** $p_{\mathrm{T}}^{W}/\mathrm{m_{WZ}} > 0.35$***. The uncertainties are only statistical.***

Process	$\mu\mu\mu$	$e\mu\mu$	μee	eee	Total events
data	167±12.92	202±14.21	142±11.92	139±11.79	650±25.50
total MC	174.52±23.65	170.27±22.13	145.88±19.25	139.39±18.16	630.06±81.58
WZ QCD	150.68±23.50	142.59±21.84	125.10±19.17	114.99±17.77	533.35±81.23
WZ EW	2.98±0.47	2.89±0.45	2.45±0.39	2.41±0.38	10.74±1.66
ZZ	6.36±0.81	4.42±0.61	4.66±0.57	3.48±0.55	18.91±2.17
VVV	0.67±0.08	0.61±0.07	0.55±0.06	0.54±0.06	2.37±0.24
Z+gamma	0.00±0.00	2.25±1.35	0.00±0.00	1.51±0.59	3.76±1.48
Z+jet	0.14±1.02	6.05±1.91	2.11±0.79	5.77±1.89	14.08±3.01
Top	3.93±2.09	2.24±2.50	1.97±1.14	2.43±3.04	10.57±5.43
ttbarV	7.84±0.75	7.43±0.69	7.36±0.70	6.73±0.65	29.36±2.66
Zt	1.94±0.30	1.79±0.28	1.68±0.26	1.53±0.23	6.93±1.06
Data/MC	0.96±0.15	1.19±0.18	0.97±0.15	1.00±0.16	1.03±0.14

TABLE 5.11: ***Summary of observed and expected yields for*** WZ ***events in each channel of the analysis and for inclusive channels after applying*** $p_{\mathrm{T}}^{\mathrm{Z}}/\mathrm{m_{WZ}} > 0.35$ ***and*** $p_{\mathrm{T}}^{W}/\mathrm{m_{WZ}} > 0.35$***. The uncertainties are only statistical.***

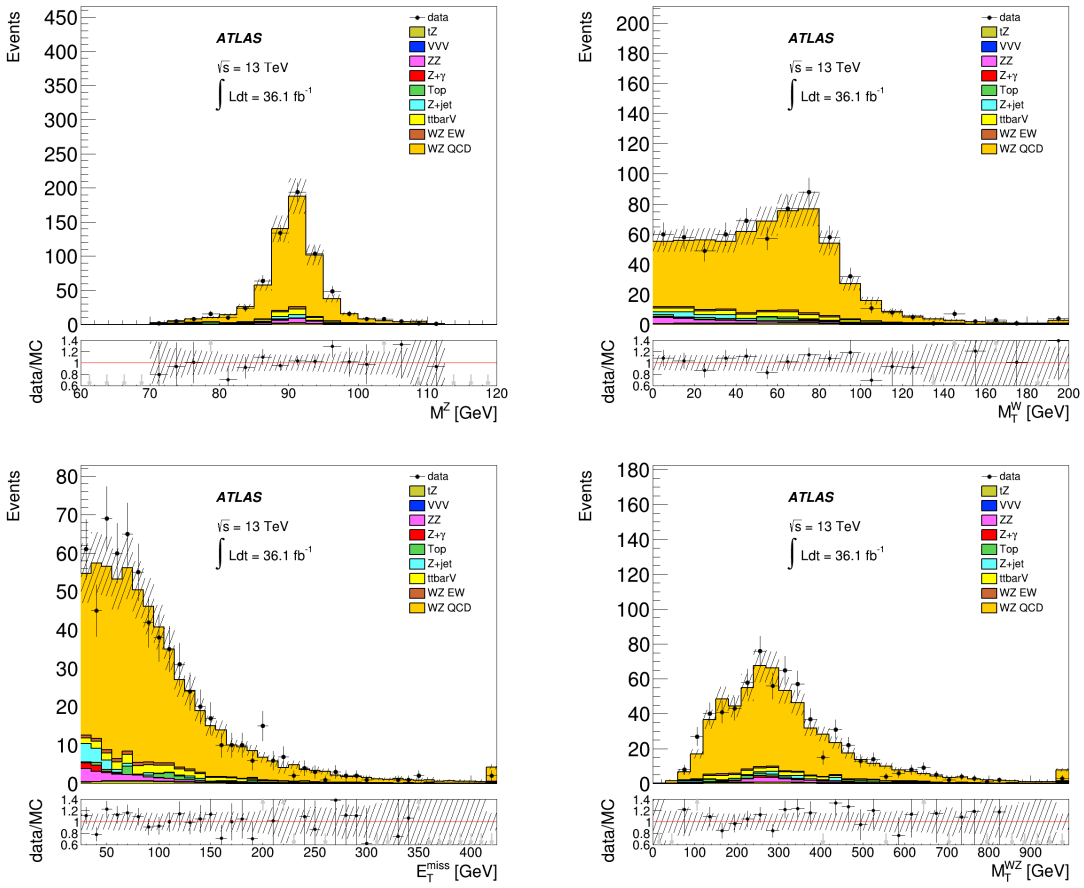


FIGURE 5.18: ***Distributions of the Z boson invariant (top left), the W boson transverse mass (top right), the E_T^{miss} (bottom left) and the transverse mass of the WZ system (bottom right) after applying signal selection cuts :*** $p_{\mathrm{T}}^{\mathrm{Z}}/\mathrm{m_{WZ}} > 0.35$ ***and*** $p_{\mathrm{T}}^{W}/\mathrm{m_{WZ}} > 0.35$***. The uncertainties are only statistical.***

5.5 Signal acceptance and acceptance times efficiency

The acceptance $\mathcal{A}$ and the acceptance times efficiency $\mathcal{A}\times\epsilon$ play an important role for the determination of the inclusive signal production cross-section, where the acceptance $\mathcal{A}$ is calculated form MC and defined as the ratio of the number of events passing the truth level cuts over the total number of events in MC signal. The $\mathcal{A}\times\epsilon$ is calculated by dividing the number of signal events passing the analysis selection cuts by the total number of event at the generation level. The acceptance and acceptance times efficiency for both $q\bar{q}$ and VBF categories are calculated in this section.

5.5.1 $q\bar{q}$ category acceptance

The acceptance $\mathcal{A}$ for this category was evaluated by applying the fully $q\bar{q}$ selection to the HVT Monte-Carlo signal at the truth level except the isolation criteria. While the acceptance

times efficiency is calculated by dividing the final signal yield passing the whole $q\bar{q}$ selection by the total number of events at generation level. The results for each HVT mass are gathered in Table 5.12.

mass (GeV)	$\mu\mu\mu$ (in %)	$e\mu\mu$ (in %)	$ee\mu$(in %)	eee (in %)	$\mathcal{A}\times\epsilon$ Inclusive (in %)	$\mathcal{A}$ (in %)
250	0.27 ± 0.05	0.34 ± 0.06	0.29 ± 0.05	0.26 ± 0.04	1.16 ± 0.12	3.22 ±0.25
300	1.17 ± 0.10	1.34 ± 0.10	1.22 ± 0.10	1.08 ± 0.09	4.81 ± 0.21	10.06 ±0.43
400	3.13 ± 0.17	3.30 ± 0.17	2.88 ± 0.16	2.64 ± 0.15	11.94 ± 0.39	19.88 ±0.56
500	4.25 ± 0.19	4.23 ± 0.20	3.38 ± 0.17	3.16 ± 0.16	15.02 ± 0.43	23.70 ±0.60
600	4.59 ± 0.20	4.97 ± 0.22	4.76 ± 0.21	4.65 ± 0.20	18.97 ± 0.53	27.88 ±0.63
700	4.84 ± 0.27	5.19 ± 0.28	4.97 ± 0.27	4.92 ± 0.26	19.92 ± 0.66	29.50 ±0.64
800	5.37 ± 0.26	5.43 ± 0.26	5.62 ± 0.27	5.46 ± 0.26	21.88 ± 0.75	31.50 ±0.66
900	5.85 ± 0.28	6.05 ± 0.28	5.61 ± 0.27	5.82 ± 0.27	23.34 ± 0.85	32.74 ±0.66
1000	6.70 ± 0.29	6.66 ± 0.28	5.91 ± 0.25	6.25 ± 0.27	25.51 ± 0.90	35.62 ±0.68
1100	6.47 ± 0.39	6.47 ± 0.39	6.49 ± 0.39	6.46 ± 0.39	25.88 ± 1.22	35.84 ±0.68
1200	6.85 ± 0.40	6.99 ± 0.38	6.66 ± 0.35	6.74 ± 0.35	27.25 ± 1.23	36.93 ±0.28
1300	6.75 ± 0.49	6.64 ± 0.48	6.08 ± 0.47	6.95 ± 0.50	26.42 ± 1.45	35.94 ±0.68
1400	6.93 ± 0.42	7.36 ± 0.43	6.46 ± 0.37	7.03 ± 0.40	27.78 ± 1.40	36.62 ±0.68
1500	6.60 ± 0.38	7.26 ± 0.40	7.05 ± 0.38	6.61 ± 0.35	27.52 ± 1.28	36.92 ±0.28
1600	6.99 ± 0.45	7.03 ± 0.43	6.72 ± 0.41	7.23 ± 0.42	27.97 ± 1.51	38.42 ±0.69
1700	6.68 ± 0.40	7.04 ± 0.43	6.87 ± 0.38	7.56 ± 0.40	28.15 ± 1.35	37.24 ±0.68
1800	6.58 ± 0.40	6.74 ± 0.42	7.68 ± 0.43	7.80 ± 0.44	28.80 ± 1.48	38.42 ±0.69
1900	6.30 ± 0.42	6.81 ± 0.43	7.35 ± 0.44	7.94 ± 0.46	28.40 ± 1.54	38.82 ±0.69
2000	6.87 ± 0.51	6.35 ± 0.50	7.17 ± 0.46	7.81 ± 0.47	28.19 ± 1.59	37.76 ±0.69
2200	6.77 ± 0.49	6.56 ± 0.47	7.28 ± 0.44	8.11 ± 0.47	28.72 ± 1.66	39.28 ±0.69
2400	6.90 ± 0.56	7.06 ± 0.52	7.32 ± 0.44	7.57 ± 0.44	28.85 ± 1.74	39.14 ±0.69
2600	6.44 ± 0.54	6.58 ± 0.51	6.72 ± 0.41	7.07 ± 0.43	26.81 ± 1.64	38.78 ±0.69
2800	6.01 ± 0.49	6.51 ± 0.56	6.08 ± 0.38	6.80 ± 0.42	25.40 ± 1.58	38.76 ±0.69
3000	5.79 ± 0.50	6.93 ± 0.68	5.37 ± 0.36	5.78 ± 0.38	23.86 ± 1.56	40.26 ±0.69

TABLE 5.12: ***The acceptances $\mathcal{A}$ and the acceptance times efficiency $\mathcal{A}\times\epsilon$ for different HVT mass points per individual and inclusive WZ channels for the $q\bar{q}$ signal. Errors are statistical only.***

The acceptance times efficiency $\mathcal{A}\times\epsilon$ for HVT quark anti-quark fusion category increases with increasing WZ mass in 250 GeV to 2400 GeV range before dropping at higher mass. The drop can be explained with the high boost of the Z boson in the HVT models. Hence, its decay products are very close and difficult to resolve in the detector. This is specially the case for the $e^+e^-e^\pm$ decay channel because of the limited spatial resolution of the ATLAS calorimeter. The acceptances times efficiency variation with HVT mass per individual and inclusive WZ channels for the $q\bar{q}$ signal is represented in Figure 5.19.

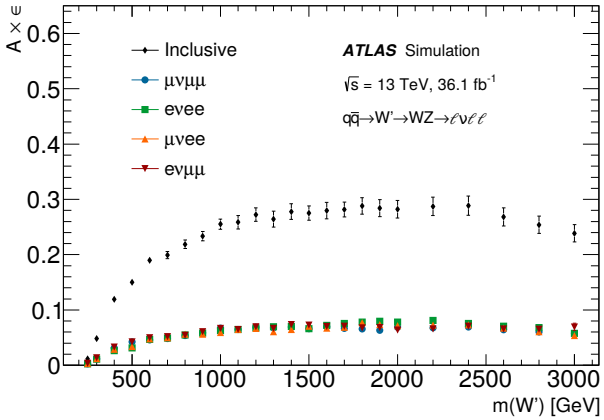


FIGURE 5.19: ***The Acceptances times efficiency for different HVT mass per individual and inclusive WZ channels for the $q\bar{q}$ signal. Errors are statistical only.***

5.5.2 VBF category acceptance

The acceptance and the acceptance times efficiency for the VBF category were determined for both GM and HVT models using the same procedure as in $q\bar{q}$ models while applying the full VBF selection. The value of $\mathcal{A}\times\epsilon$ and $\mathcal{A}$ are given for GM and VBF HVT models in Table 5.13 and Table 5.14 respectively. The results show that both acceptance and acceptance times efficiency for GM model are higher than HVT VBF signal. This is explained by the kinematics selection required at generator level for GM model that are not applied for HVT VBF. Also, the GM samples are not including W and Z events decaying to $\tau\tau$ leptons present in the HVT VBF samples. Furthermore, the difference may be due to the kinematics and angular distributions of the final products.

mass (GeV)	$\mu\mu\mu$ (in %)	$e\mu\mu$ (in %)	$ee\mu$ (in %)	eee (in %)	$\mathcal{A}\times\epsilon$ Inclusive (in %)	$\mathcal{A}$ (in %)
200	1.01 ± 0.08	0.96 ± 0.09	0.85 ± 0.07	0.75 ± 0.06	3.58 ± 0.24	6.08±0.26
250	1.41 ± 0.11	1.33 ± 0.09	1.18 ± 0.10	1.13 ± 0.08	5.05 ± 0.29	7.35±0.35
300	1.71 ± 0.11	1.60 ± 0.12	1.46 ± 0.09	1.31 ± 0.09	6.08 ± 0.32	9.52±0.30
350	2.10 ± 0.12	1.89 ± 0.10	1.78 ± 0.11	1.71 ± 0.10	7.49 ± 0.32	10.64±0.39
400	2.17 ± 0.12	2.17 ± 0.13	1.92 ± 0.13	1.95 ± 0.11	8.22 ± 0.41	11.76±0.31
450	2.36 ± 0.12	2.54 ± 0.13	2.20 ± 0.11	2.19 ± 0.14	9.30 ± 0.37	12.67±0.41
500	2.56 ± 0.15	2.65 ± 0.14	2.33 ± 0.13	2.30 ± 0.13	9.84 ± 0.46	13.68±0.33
600	2.65 ± 0.14	2.84 ± 0.17	2.62 ± 0.16	2.61 ± 0.14	10.72 ± 0.54	14.91±0.34
700	2.95 ± 0.17	3.01 ± 0.16	2.92 ± 0.17	2.81 ± 0.17	11.69 ± 0.60	15.33±0.34
800	2.98 ± 0.19	3.10 ± 0.17	3.07 ± 0.18	3.10 ± 0.21	12.26 ± 0.67	16.63±0.19
900	2.91 ± 0.19	3.00 ± 0.18	2.86 ± 0.18	2.96 ± 0.18	11.74 ± 0.65	16.56±0.35

TABLE 5.13: ***The acceptances $\mathcal{A}$ and the acceptance times efficiency $\mathcal{A}\times\epsilon$ for GM H_5^+ model at different mass points per individual and inclusive WZ channels. Errors are statistical only.***

mass (GeV)	$\mu\mu\mu$ (in %)	$e\mu\mu$ (in %)	$ee\mu$ (in %)	eee (in %)	$\mathcal{A}\times\epsilon$ Inclusive (in %)	$\mathcal{A}$ in (%)
250	0.76 ± 0.07	0.64 ± 0.07	0.72 ± 0.10	0.60 ± 0.07	2.71 ± 0.19	4.80 ±0.30
300	1.18 ± 0.10	0.91 ± 0.07	0.94 ± 0.10	0.80 ± 0.08	3.83 ± 0.27	6.20 ±0.34
350	1.13 ± 0.11	1.06 ± 0.09	1.03 ± 0.10	0.77 ± 0.08	3.99 ± 0.25	6.86 ±0.36
400	1.31 ± 0.09	1.13 ± 0.11	0.96 ± 0.09	1.09 ± 0.09	4.48 ± 0.25	7.40 ±0.37
450	1.49 ± 0.14	1.28 ± 0.11	1.26 ± 0.11	1.21 ± 0.12	5.24 ± 0.35	8.94 ±0.00
500	1.45 ± 0.11	1.56 ± 0.12	1.36 ± 0.11	1.29 ± 0.12	5.66 ± 0.33	9.64 ±0.42
600	1.71 ± 0.12	1.61 ± 0.11	1.59 ± 0.10	1.48 ± 0.10	6.39 ± 0.29	10.28 ±0.43
700	1.64 ± 0.15	1.98 ± 0.15	1.53 ± 0.11	1.48 ± 0.11	6.63 ± 0.40	10.82 ±0.44
800	1.92 ± 0.12	2.09 ± 0.14	1.65 ± 0.11	1.67 ± 0.13	7.33 ± 0.38	11.80 ±0.46
900	2.07 ± 0.14	2.01 ± 0.19	1.99 ± 0.16	1.82 ± 0.13	7.88 ± 0.43	13.24±0.48

TABLE 5.14: ***The acceptances $\mathcal{A}$ and acceptance times efficiency $\mathcal{A}\times\epsilon$ for VBF HVT model at different mass points per individual and inclusive WZ channels. The error is statistical only.***

The distribution of the acceptance times efficiency $\mathcal{A}\times\epsilon$ for GM and HVT models are illustrated in Figure 5.20 for different masses and for the individual channels $\mu^+\mu^-\mu^\pm$, $\mu^+\mu^-e^\pm$, $e^+e^-\mu^\pm$, $e^+e^-e^\pm$ and for the sum of all channels.

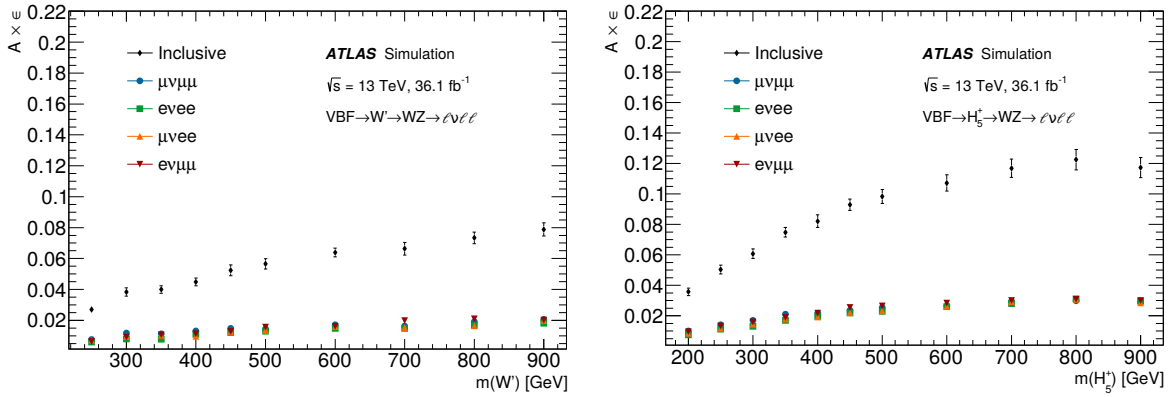


FIGURE 5.20: ***The acceptance times efficiency of VBF HVT (left) and GM model (right) for different masses and for the individual and the inclusive WZ channels. Errors are statistical only.***

5.6 Background Estimation

Backgrounds in this analysis are classified in two categories, the first one includes Standard Model processes with three real leptons from W and Z bosons decays, especially the dominant WZ, ZZ, $t\bar{t}+V$ and $t+V$ which are called irreducible backgrounds since they have the same signature as the signal. These backgrounds are well modelled and are estimated from Monte-Carlo simulation with large statistics samples. The second category is called reducible backgrounds, it consists of processes with at least one fake leptons originating either from pion, kaon or heavy-quark decay, or from jets misidentified as lepton. In addition, fake electrons can also come from photon conversion. These Fake and non prompt leptons are

mainly originated from $Z+jets$, $t\bar{t}$, single top, $Z+\gamma$ or QCD multi-jet where one or two jets are mis-identified as leptons. These backgrounds are insufficiently simulated by the ATLAS Monte-Carlo and must be estimated using data-driven such as global Matrix Method [129]. A detailed description of the method is presented in the following section.

5.6.1 Global Matrix Method

The matrix method allows to determine the contribution of the reducible backgrounds $Z+jets$, $t\bar{t}$, single top, $Z+\gamma$ directly from data by exploiting the classification of real leptons (R) as Loose (L) or Tight (T) and the probability that a fake lepton (F) is mis-identified as tight or loose lepton. In this analysis, loose leptons are the ones passing the overlap removal requirements while relaxing the isolation criteria. Tight leptons are those passing the signal selection.

In the present analysis, the three leptons candidates at final states are classified into eight number of events (N_{ijk}) categories, where the index (i, j, k) refers respectively to W lepton, Z leading and sub-leading leptons ($p_{T,lead} > p_{T,Sub-lead}$), each index can be a T or L whether is a Tight or Loose lepton. Moreover, these eight number of event type can be decomposed according to WZ lepton feature as real or fake leptons to the following categories:

- N_{RRR} : the number of events with three real, mainly coming from the WZ signal events and backgrounds with three prompt leptons, namely the dominant WZ, ZZ, $t\bar{t}+V$ and $t+V$ denoted irreducible background.

- N_{FRR} : the number of events with one fake lepton associated to the W decay plus two prompt real leptons associated to the Z boson. This category mostly consists of Z+jets, $Z+\gamma$ and $t\bar{t}$.

- N_{RRF} and N_{RFR} : the number of events where one fake lepton is entering the Z selection. Here the Z+jets, $Z+\gamma$ are contributing when one of the two Z leptons is miss-paired with a fake lepton to form the Z. The $t\bar{t}$ background can also contribute to this category.

- N_{FFR}, N_{FRF}, N_{RFF}, N_{FFF} : the number of events with two or three fake leptons. In this case, the W+jets, Z+jets, $t\bar{t}$ events and QCD are contributing. However, the number of events with three fakes is very small and can be neglected.

The number of events $N_{ijk=T,L}$ is related to $N_{ijk=R,F}$ by 8×8 matrix reflecting the probability that a real lepton is identified as tight (loose) lepton, denoted " e " ($\bar{e} = 1 - e$), and the probability that a fake lepton is mis-identified as a tight (loose), denoted " f " ($\bar{f} = 1 - f$). The matrix can be reduced to 7×7 since the number of events with three fakes is very small and can be neglected. thus, its corresponding N_{LLL} was not considered in

the calculation. Then, the number of events with at most two fake and non prompt leptons can be written as function of events with one or two loose leptons according to the following equation:

$$\begin{pmatrix} N_{TTT} \\ N_{TTL} \\ N_{TLT} \\ N_{LTT} \\ N_{TLL} \\ N_{LTL} \\ N_{LLT} \end{pmatrix} = \begin{pmatrix} e_1e_2e_3 & e_1e_2f_3 & e_1f_2e_3 & f_1e_2e_3 & e_1f_2f_3 & f_1e_2f_3 & f_1f_2e_3 \\ e_1e_2\bar{e}_3 & e_1e_2\bar{f}_3 & e_1f_2\bar{e}_3 & f_1e_2\bar{e}_3 & e_1f_2\bar{f}_3 & f_1e_2\bar{f}_3 & f_1f_2\bar{e}_3 \\ e_1\bar{e}_2e_3 & e_1\bar{e}_2f_3 & e_1\bar{f}_2e_3 & f_1\bar{e}_2e_3 & e_1\bar{f}_2f_3 & f_1\bar{e}_2f_3 & f_1\bar{f}_2e_3 \\ \bar{e}_1e_2e_3 & \bar{e}_1e_2f_3 & \bar{e}_1f_2e_3 & \bar{f}_1e_2e_3 & \bar{e}_1f_2f_3 & \bar{f}_1e_2f_3 & \bar{f}_1f_2e_3 \\ e_1\bar{e}_2\bar{e}_3 & e_1\bar{e}_2\bar{f}_3 & e_1\bar{f}_2\bar{e}_3 & f_1\bar{e}_2\bar{e}_3 & e_1\bar{f}_2\bar{f}_3 & f_1\bar{e}_2\bar{f}_3 & f_1\bar{f}_2\bar{e}_3 \\ \bar{e}_1e_2\bar{e}_3 & \bar{e}_1e_2\bar{f}_3 & \bar{e}_1f_2\bar{e}_3 & \bar{f}_1e_2\bar{e}_3 & \bar{e}_1f_2\bar{f}_3 & \bar{f}_1e_2\bar{f}_3 & \bar{f}_1f_2\bar{e}_3 \\ \bar{e}_1\bar{e}_2e_3 & \bar{e}_1\bar{e}_2f_3 & \bar{e}_1\bar{f}_2e_3 & \bar{f}_1\bar{e}_2e_3 & \bar{e}_1\bar{f}_2f_3 & \bar{f}_1\bar{e}_2f_3 & \bar{f}_1\bar{f}_2e_3 \end{pmatrix} \begin{pmatrix} N_{RRR} \\ N_{RRF} \\ N_{RFR} \\ N_{FRR} \\ N_{RFF} \\ N_{FRF} \\ N_{FFR} \end{pmatrix}. \quad (5.12)$$

Multiplying each side of the equation with the same term of interest as shown below:

$$\begin{pmatrix} N_{TTT} \\ -N_{TTL}\frac{f_3}{\bar{f}_3} \\ -N_{TLT}\frac{f_2}{\bar{f}_2} \\ -N_{LTT}\frac{f_1}{\bar{f}_1} \\ N_{TLL}\frac{f_2}{\bar{f}_2}\frac{f_3}{\bar{f}_3} \\ N_{LTL}\frac{f_1}{\bar{f}_1}\frac{f_3}{\bar{f}_3} \\ N_{LLT}\frac{f_1}{\bar{f}_1}\frac{f_2}{\bar{f}_2} \end{pmatrix} = \begin{pmatrix} e_1e_2e_3 & e_1e_2f_3 & e_1f_2e_3 & f_1e_2e_3 & e_1f_2f_3 & f_1e_2f_3 & f_1f_2e_3 \\ -e_1e_2\bar{e}_3\frac{f_3}{\bar{f}_3} & -e_1e_2f_3 & -e_1f_2\bar{e}_3\frac{f_3}{\bar{f}_3} & -f_1e_2\bar{e}_3\frac{f_3}{\bar{f}_3} & -e_1f_2f_3 & -f_1e_2f_3 & -f_1f_2\bar{e}_3\frac{f_3}{\bar{f}_3} \\ -e_1\bar{e}_2e_3\frac{f_2}{\bar{f}_2} & -e_1\bar{e}_2f_3\frac{f_2}{\bar{f}_2} & -e_1f_2e_3 & -f_1\bar{e}_2e_3\frac{f_2}{\bar{f}_2} & -e_1f_2f_3 & -f_1\bar{e}_2f_3\frac{f_2}{\bar{f}_2} & -f_1f_2e_3 \\ -\bar{e}_1e_2e_3\frac{f_1}{\bar{f}_1} & -\bar{e}_1e_2f_3\frac{f_1}{\bar{f}_1} & -\bar{e}_1f_2e_3\frac{f_1}{\bar{f}_1} & -f_1e_2e_3 & -\bar{e}_1f_2f_3\frac{f_1}{\bar{f}_1} & -f_1e_2f_3 & -f_1f_2e_3 \\ e_1\bar{e}_2\bar{e}_3\frac{f_2}{\bar{f}_2}\frac{f_3}{\bar{f}_3} & e_1\bar{e}_2f_3\frac{f_2}{\bar{f}_2} & e_1f_2\bar{e}_3\frac{f_3}{\bar{f}_3} & f_1\bar{e}_2\bar{e}_3\frac{f_2}{\bar{f}_2}\frac{f_3}{\bar{f}_3} & e_1f_2f_3 & f_1\bar{e}_2f_3\frac{f_2}{\bar{f}_2} & f_1f_2\bar{e}_3\frac{f_3}{\bar{f}_3} \\ \bar{e}_1e_2\bar{e}_3\frac{f_1}{\bar{f}_1}\frac{f_3}{\bar{f}_3} & \bar{e}_1e_2f_3\frac{f_1}{\bar{f}_1} & \bar{e}_1f_2\bar{e}_3\frac{f_1}{\bar{f}_1}\frac{f_3}{\bar{f}_3} & f_1e_2\bar{e}_3\frac{f_3}{\bar{f}_3} & \bar{e}_1f_2f_3\frac{f_1}{\bar{f}_1} & f_1e_2f_3 & f_1f_2\bar{e}_3\frac{f_3}{\bar{f}_3} \\ \bar{e}_1\bar{e}_2e_3\frac{f_1}{\bar{f}_1}\frac{f_2}{\bar{f}_2} & \bar{e}_1\bar{e}_2f_3\frac{f_1}{\bar{f}_1}\frac{f_2}{\bar{f}_2} & \bar{e}_1f_2e_3\frac{f_1}{\bar{f}_1} & f_1\bar{e}_2e_3\frac{f_2}{\bar{f}_2} & \bar{e}_1f_2f_3\frac{f_1}{\bar{f}_1} & f_1\bar{e}_2f_3\frac{f_2}{\bar{f}_2} & f_1f_2e_3 \end{pmatrix} \begin{pmatrix} N_{RRR} \\ N_{RRF} \\ N_{RFR} \\ N_{FRR} \\ N_{RFF} \\ N_{FRF} \\ N_{FFR} \end{pmatrix}. \quad (5.13)$$

Adding rows in both sides leads to the following equation:

$$N_{TTT} - N_{TTL}\frac{f_3}{\bar{f}_3} - N_{TLT}\frac{f_2}{\bar{f}_2} - N_{LTT}\frac{f_1}{\bar{f}_1} + N_{TLL}\frac{f_2}{\bar{f}_2}\frac{f_3}{\bar{f}_3} + N_{LTL}\frac{f_1}{\bar{f}_1}\frac{f_3}{\bar{f}_3} + N_{LLT}\frac{f_1}{\bar{f}_1}\frac{f_2}{\bar{f}_2} = \quad (5.14)$$

$$\left(e_1e_2e_3 - e_1e_2\bar{e}_3\frac{f_3}{\bar{f}_3} - e_1\bar{e}_2e_3\frac{f_2}{\bar{f}_2} - \bar{e}_1e_2e_3\frac{f_1}{\bar{f}_1} + e_1\bar{e}_2\bar{e}_3\frac{f_2}{\bar{f}_2}\frac{f_3}{\bar{f}_3} + \bar{e}_1e_2\bar{e}_3\frac{f_1}{\bar{f}_1}\frac{f_3}{\bar{f}_3} + \bar{e}_1\bar{e}_2e_3\frac{f_1}{\bar{f}_1}\frac{f_2}{\bar{f}_2}\right) N_{RRR} + \mathcal{O}(f^3),$$

where $\mathcal{O}(f^3)$ represents the high order terms of " f " and can be neglected, then the equation can be written as follows:

$$N_{TTT} - e_1e_2e_3N_{RRR} = [N_{TTL} - e_1e_2\bar{e}_3N_{RRR}]\frac{f_3}{\bar{f}_3} + [N_{TLT} - e_1\bar{e}_2e_3N_{RRR}]\frac{f_2}{\bar{f}_2} + [N_{LTT} - \bar{e}_1e_2e_3N_{RRR}]\frac{f_1}{\bar{f}_1} \quad (5.15)$$

$$-[N_{TLL} - e_1\bar{e}_2\bar{e}_3N_{RRR}]\frac{f_2}{\bar{f}_2}\frac{f_3}{\bar{f}_3} - [N_{LTL} - \bar{e}_1e_2\bar{e}_3N_{RRR}]\frac{f_1}{\bar{f}_1}\frac{f_3}{\bar{f}_3} - [N_{LLT} - \bar{e}_1\bar{e}_2e_3N_{RRR}]\frac{f_1}{\bar{f}_1}\frac{f_2}{\bar{f}_2}.$$

The terms N_{TTL}, N_{TLT}, N_{LTT}, N_{TLL}, N_{LTL} and N_{LTL} are independent of N_{TTT}, they can be taken from data either by applying all the WZ selection requirements or reverting the tight requirements, while the MC simulation can be used to estimate the contribution from irreducible background (N^{irr}_{ijk}).

Therefore, the amount of reducible backgrounds is calculated using the formula below:

$$N_{reducible} = N_{TTT} - e_1e_2e_3N_{RRR} = [N_{TTL} - N^{irr}_{TTL}]\frac{f_3}{\bar{f}_3} + [N_{TLT} - N^{irr}_{TLT}]\frac{f_2}{\bar{f}_2} + [N_{LTT} - N^{irr}_{LTT}]\frac{f_1}{\bar{f}_1} \quad (5.16)$$

$$-[N_{TLL} - N^{irr}_{TLL}]\frac{f_2}{f_2}\frac{f_3}{f_3} - [N_{LTL} - N^{irr}_{LTL}]\frac{f_1}{f_1}\frac{f_3}{f_3} - [N_{LLT} - N^{irr}_{LLT}]\frac{f_1}{f_1}\frac{f_2}{f_2}.$$

In order to simplify the equation, a *fake ratio* $F_i = \frac{f_i}{f_i}$ is introduced in the Equation 5.16

$$N_{reducible} = N^{red}_{TTL}F_3 + N^{red}_{TLT}F_2 + N^{red}_{LTT}F_1 - N^{red}_{TLL}F_2F_3 - N^{red}_{LTL}F_1F_3 - N^{red}_{LLT}F_1F_2, \quad (5.17)$$

$N^{red}_{ijk} = N_{ijk} - N^{irr}_{ijk}$, F_1, F_2 and F_3 represent the *fake ratio* of the W lepton, Z leading and sub-leading respectively, and are measured in a bins of lepton's transverse momentum p_T using $Z + jet$ control region. Since Z leptons are passing the same selection F_2 and F_3 are equal. As result, the number of reducible events taking in the account the leptons p_T bins is given by the equation below:

$$N_{reducible} = \sum_i N^{red^i}{}_{TTL}F^i_2 + \sum_i N^{red^i}{}_{TLT}F^i_2 + \sum_i N^{red^i}{}_{LTT}F^i_1 - \sum_i\sum_j N^{red^{ij}}{}_{TLL}F^i_2F^j_2 - \quad (5.18)$$

$$- \sum_i\sum_j N^{red^{ij}}{}_{LTL}F^i_1F^j_2 - \sum_i\sum_j N^{red^{ij}}{}_{LLT}F^i_1F^j_2.$$

5.6.2 Fake ratio estimation

The *fake ratio* F_i in this analysis is estimated from data in a dedicated $Z + jet$ control region composed of events with mis-identified leptons from heavy jets and from photon conversion. Moreover, two different fake factors are calculated depending on the lepton flavor since the isolation and identification criteria are not the same for electrons and muons. A $Z + jets$ control region is constructed by requiring event passing all Z candidates selection listed in section 5.3.5 with applying further cuts according to the additional lepton flavor (see Figure 5.21):

- Control region Z + "fake" e (CRZj$_e$): The missing transverse energy and the transverse mass of the W boson are requested to be higher than 25 GeV and 30 GeV respectively. The isolation and d_0 significance cuts on the additional electron are relaxed, and only $loose + BL$ identification requirement is applied. The mass $m_{\mu\mu}$ is required to be between 81 GeV and 106 GeV.

- Control region Z + "fake" μ (CRZj$_\mu$): the d_0 significance cut for additional muon is inverted (d_0 significance > 3.0) and no isolation is required.

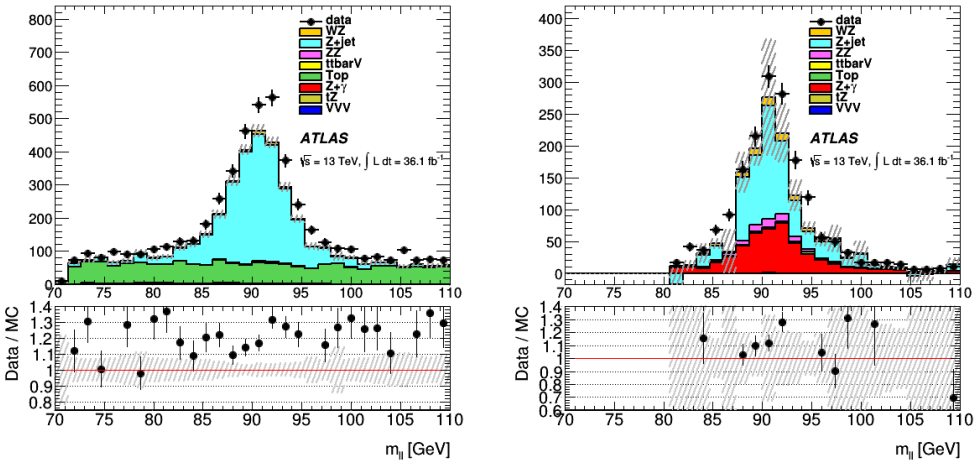


FIGURE 5.21: ***Distribution of Z boson invariant mass in the Z+jets control region. On the left, the fake muon control region and on the right the fake electron control region. The statistical uncertainty is shown by shaded bands.***

After defining Z + "fake" e and Z + "fake" μ loose control region, the probability f_i involved in the measurement of the fake factor F_i is estimated using a tight control region that is reconstructed by applying lepton isolation and identification cuts requested for Z and W bosons in this analysis. Then, the probability f_i for each lepton flavor coming either from W or Z decay is calculated by dividing the numbers of events per transverse momentum distribution's bin in the tight control region by its corresponding number of events in the control loose region using the following formula:

$$f_i^{Z,\ l} = \frac{N_{i,\ tightCR}^{Z,\ l}}{N_{i,\ looseCR}^{Z,\ l}} \qquad \text{and} \qquad f_i^{W,\ l} = \frac{N_{i,\ tightCR}^{W,\ l}}{N_{i,\ looseCR}^{W,\ l}}, \tag{5.19}$$

$(N_{i,\ tightCR})$, $(N_{i,\ looseCR})$ are the number of events subtracted from data in the bins of leptons p_T within tight and loose control region respectively, and " l " refers to the lepton flavor. The transverse momentum distribution of the jet faking electron in the $Z+jets$ loose region are given in the Figure 5.22, while the distribution of p_T electrons and muons after applying to the additional lepton the Z and W requirements are shown in Figure 5.23.

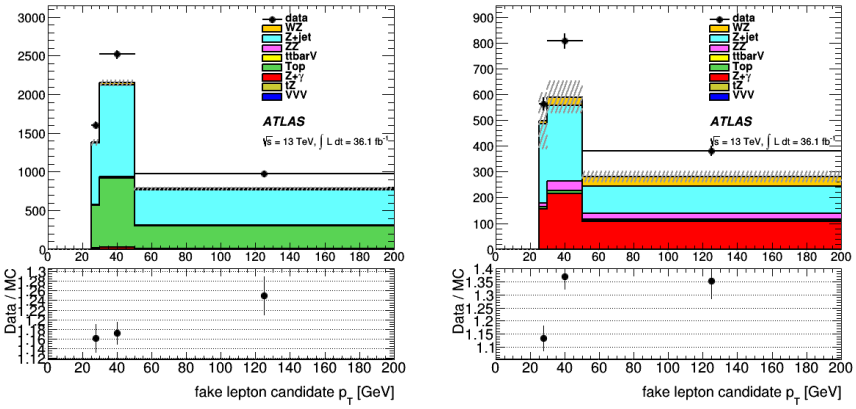


FIGURE 5.22: *The transverse momentum distribution of the jet faking muons (left) and electrons (right) in the Z + jets loose region. The statistical uncertainty is shown by shaded bands.*

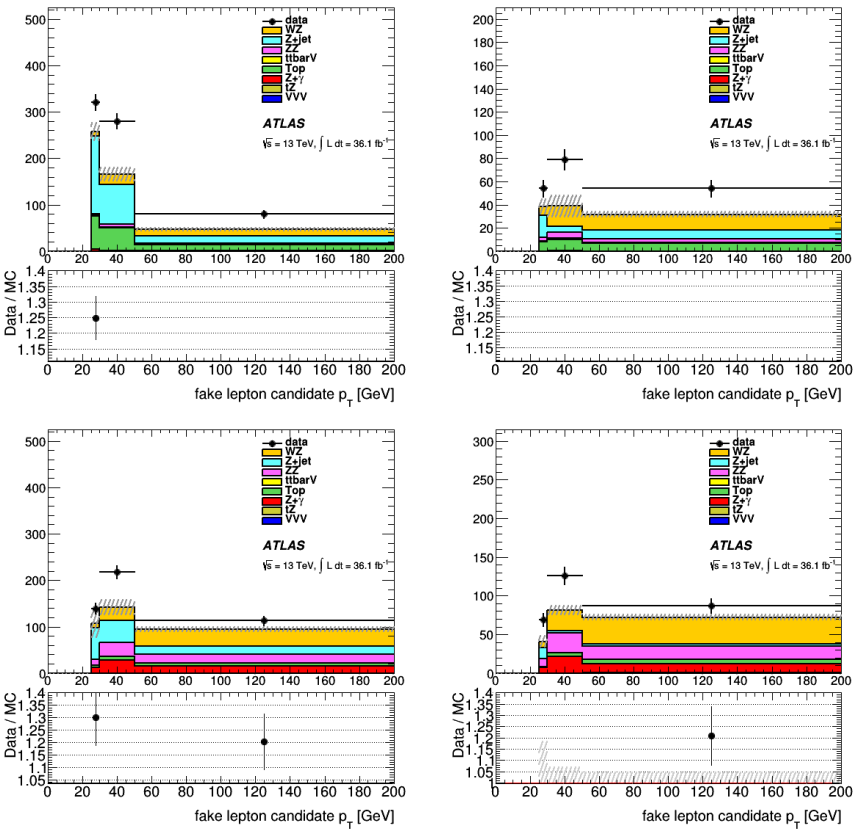


FIGURE 5.23: *The transverse momentum distribution of the jet faking muons (top), and electrons bottom after applying to the additional lepton the Z (right) and W (left) lepton requirements. The statistical uncertainty is shown by shaded bands.*

Finally, the fake factor for different leptons flavor originating from Z or W bosons are calculated using the Equation 5.19 and the ratio $F_i = \frac{f_i}{1-f_i}$ in a three bins of leptons p_T.

Afterward, the fake factors for muons and electrons can been taken from Figures 5.24 and 5.25 respectively.

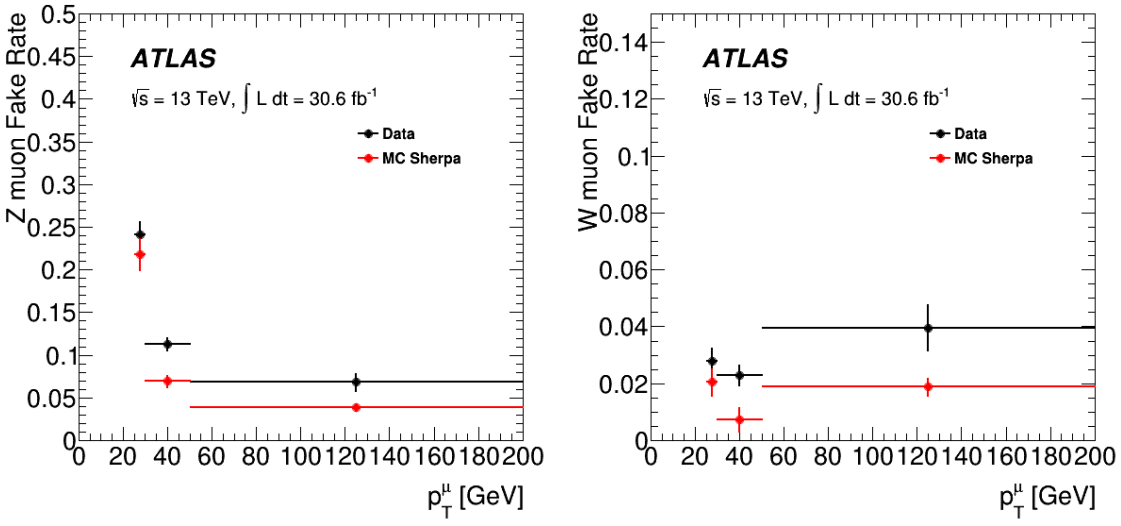


FIGURE 5.24: ***Distributions of the muon fake rate as a function of*** p_T ***in the*** Z***+jets control region, using the*** Z ***muon selection on the left. The muon fake rate using the*** W ***muon selection is shown on the right.***

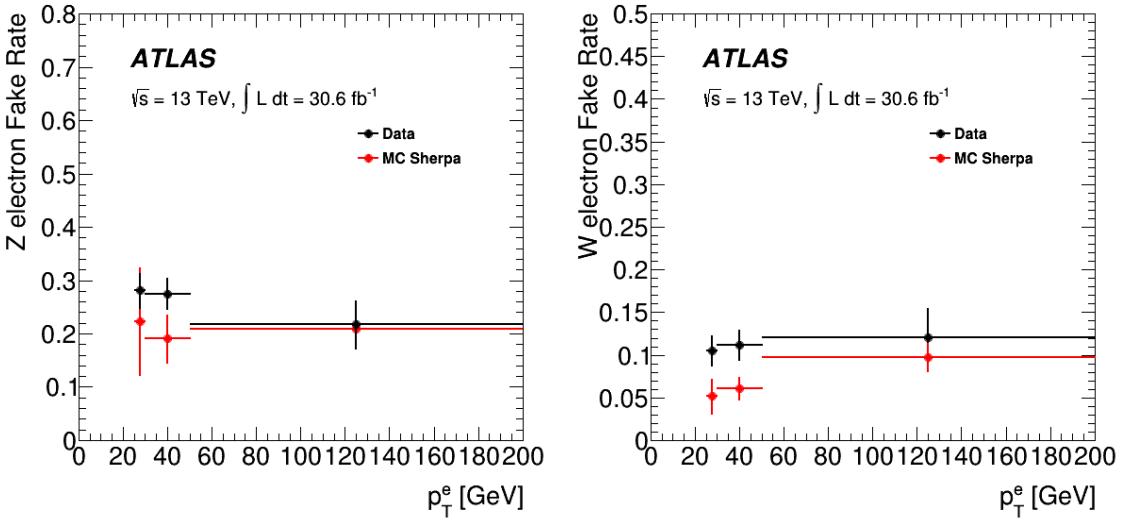


FIGURE 5.25: ***Distributions of the electron fake rate as a function of*** p_T ***in the*** Z***+jets control region, using the*** Z ***electron selection on the left. The electron fake rate using the*** W ***electron selection is shown on the right.***

The final yield of measured reducible background is derived, once calculated the fake rates F_1 and F_2. The N_{TTL}, N_{TLT}, N_{LTT}, N_{TLL}, N_{LTL} and N_{LTL} taken from the signal region. The statistical uncertainties are determined from the N_{TTL}, N_{TLT}, N_{LTT}, N_{TLL}, N_{LTL} and N_{LTL}

ones. The systematics in the background measurement contains the uncertainties affecting the fake rates from cuts used to built the different control regions 5.15.

Channels	$\mu\mu\mu$	$e\mu\mu$	μee	eee
Z+γ	1.1±0.6	35.7±3.3	1.5±1.2	26.6±2.6
Z+jets	41.4±11.4	57.9±25.0	8.8±7.0	43.0±15.5
$t\bar{t}$	58.0±5.6	51.2±4.6	35.8±4.4	23.9±3.2
Total MC fake Background	101.5±12.7	150.9±25.7	46.1±8.4	93.5±16.0
Matrix method data	88.8±2.8±6.2	228.8±5.7±41.1	83.2±5.2±6.2	174.4±6.6±26.0

TABLE 5.15: ***Reducible Backgrounds estimation results before signal optimization using the Matrix Method in 36.1 fb^{-1} of 2015 and 2016 data.The statistical and systematics uncertainties are shown for matrix method data.***

For the inclusive WZ signal, Figure 5.26 compare the simulated WZ transverse mass and the missing transverse energy distributions to the experimental ones. Overall, one can see that the profiles are in good agreement. This prove the robustness of the matrix method data-driven technique in the evaluation of reducible backgrounds.

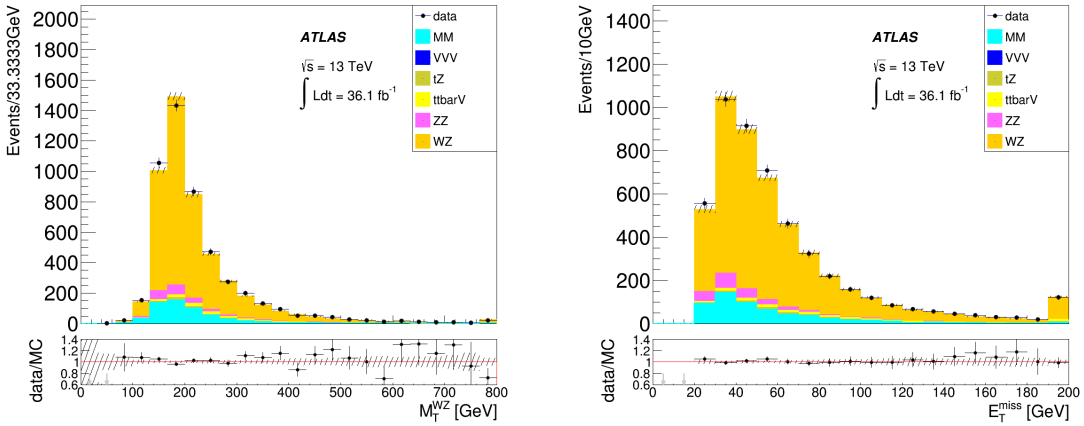


FIGURE 5.26: ***Comparison of the data and MC WZ transverse mass (left) and the missing transverse energy distributions (right), the reducible backgrounds are estimated using the matrix method. The statistical and systematics uncertainties are shown by shaded bands.***

5.6.3 Backgrounds estimation for VBF category

Irreducible backgrounds for both $q\bar{q}$ and VBF categories are estimated from the simulated Monte-Carlo. A validation region for both categories are then defined to verify the backgrounds normalization particularly for the dominant SM-WZ. The validation region for VBF is built by inverting cuts on the pseudo-rapidity separation $\Delta\eta_{jj} < 3.5$ and the dijet mass

$100GeV < m_{jj} < 500\ GeV$. The total data yields and backgrounds contamination for different processes in the VBF validation region is given in Table 5.16. In addition, the distributions of the kinematic variables m_{jj}, $\Delta\eta_{jj}$, the missing transverse energy and WZ transverse mass are showen in the Figure 5.27.

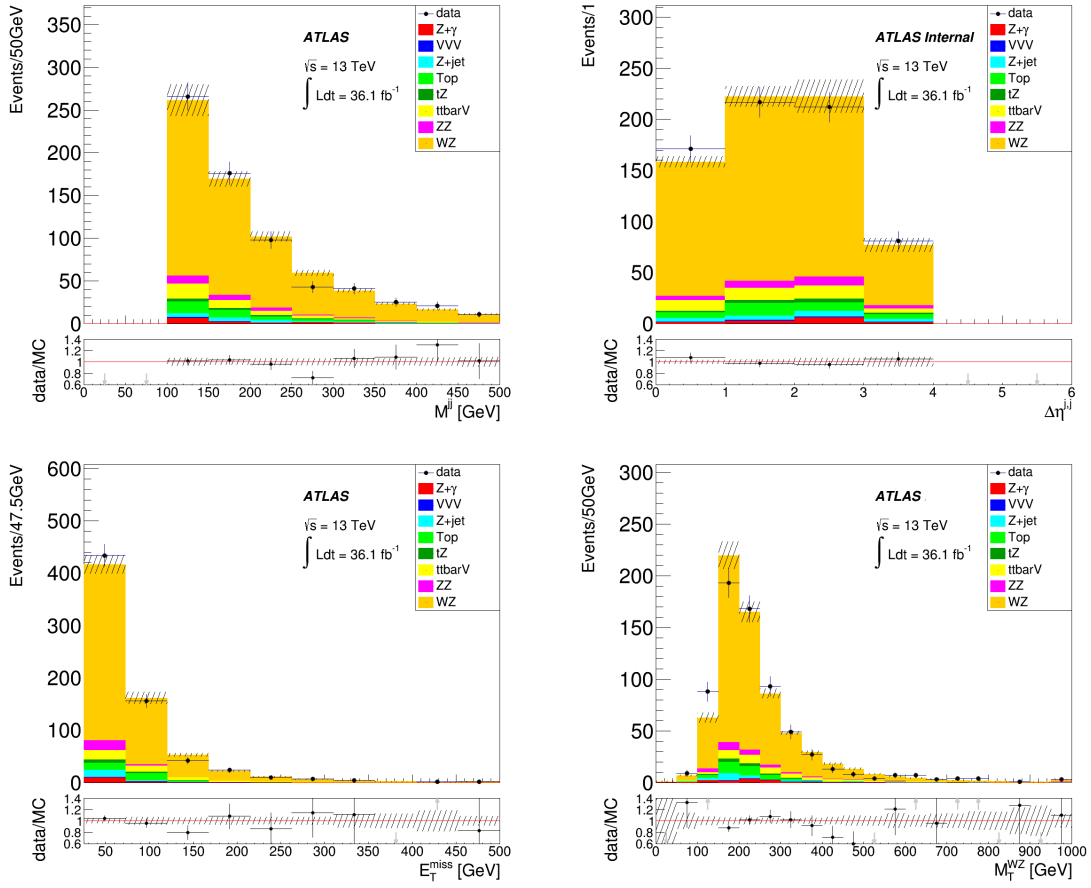


FIGURE 5.27: ***The distributions*** m_{jj}, $\Delta\eta_{jj}$, ***missing transverse energy and*** WZ ***transverse mass in the WZ VBF validation region.***

Results show a good agreement between data and backgrounds prediction with a data/MC ratio close to 1, the WZ-SM background represents 81% while The electroweak process does not contribute significantly in the VBF validation region.

Process	all lepton final states combined
Data	681±26.10
total MC	675.54±31.00
VVV	2.73±0.11
tZ	10.15±0.79
$Z\gamma$	11.28±3.30
Top	30.44±5.83
$t\bar{t}V$	39.28±1.20
ZZ	22.69±3.41
Z+jets	12.02±9.32
WZ	546.95±28.55
Data/MC	1.01±0.06

TABLE 5.16: ***Yields of selected events in 36.1 fb^{-1} of 2015 and 2016 data compared to backgrounds yields from different processes in the VBF validation region.***

After the validation of the WZ-SM backgrounds normalization, the reducible backgrounds are estimated using the matrix method. The fake factors in the signal region are found to be similar to those in the control regions so that no extrapolation is needed. The fake and non-prompt leptons estimated in the VBF signal region are given in Table 5.17.

Channels	$\mu\mu\mu$	$e\mu\mu$	μee	eee
Z+γ	0.0±0.0	0.4±1.0	0.0±0.5	0.5±0.6
Z+jets	0.1±0.6	0.9±0.6	0.9±0.9	0.0±6.5
Top	0.6±1.0	0.9±1.2	1.2±1.1	2.3±1.4
Total MC fake Background	0.7±1.2	2.2±1.7	2.1±1.5	2.8±6.7
Matrix method data	3.0±0.2±1.0	4.3±0.3±1.6	3.4±0.2±0.8	4.7±0.4±1.7

TABLE 5.17: ***Reducible Backgrounds estimation results after VBF signal optimization using the Matrix Method in 36.1 fb^{-1} of 2015 and 2016 data.The statistical and systematics uncertainties are shown for matrix method data.***

To check the results provided by the matrix method in the VBF signal region, the distributions of the WZ transverse mass and the missing transverse energy are presented in Figure 5.28. Once can see that MC distribution match the measured data.

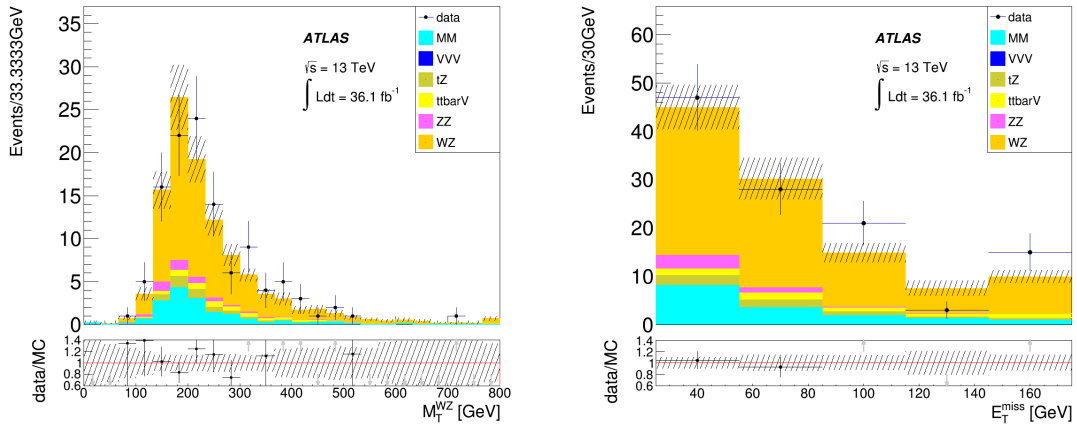


FIGURE 5.28: *WZ transverse mass (left) and missing transverse energy (right) distributions in the VBF signal region, the reducible backgrounds are estimated using the matrix method. The statistical and systematics uncertainties are shown by shaded bands.*

5.6.4 Backgrounds estimation for $q\bar{q}$ category

We did the same calculation as before for the background estimation in the $q\bar{q}$ signal region. The dominant WZ-SM model background normalization is checked in the $q\bar{q}$ validation region defined by inverting the cuts used for the optimization of this category ($p_{\mathrm{T}}^{\mathrm{Z}}/\mathrm{Mass_{WZ}} < 3.5$ or $p_{\mathrm{T}}^{W}/\mathrm{Mass_{WZ}} < 3.5$). The results for the fake backgrounds are summarized in Table 5.18.

Channels	$\mu\mu\mu$	$e\mu\mu$	μee	eee
Z+γ	0±0	2.25±1.2	0±0	1.51±0.50
Z+jets	0.05±1.65	6.05±1.2	2.11±0.50	5.77±1.37
$t\bar{t}$	3.93±1.80	2.24±2.33	1.97±0.91	2.43±2.93
Total MC fake Background	3.98±2.44	10.54±2.88	4.08±1.03	9.71±3.27
Matrix method data	10.1±0.7±0.9	31.2±3.0±5.4	6.3±0.5±1.4	24.6±2.4±4.7

TABLE 5.18: ***Reducible Backgrounds estimation results after $q\bar{q}$ signal optimization using the Matrix Method in 36.1 fb^{-1} of 2015 and 2016 data. The statistical and systematics uncertainties are shown for matrix method data.***

Like before, the background estimation using the matrix method in the $q\bar{q}$ signal region is evaluated by comparing the measured data to the expected backgrounds. The distributions of the WZ transverse mass and the missing transverse energy are presented in Figure 5.29 and show a good agreement between the expected and measured distributions.

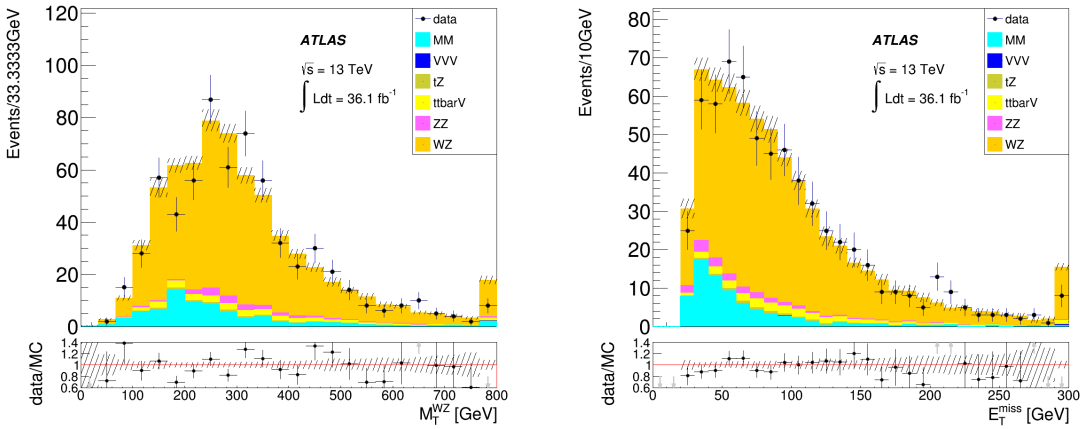


FIGURE 5.29: *WZ transverse mass (left) and missing transverse energy (right) distributions in the $q\bar{q}$ signal region, the reducible backgrounds are estimated using the matrix method. The statistical and systematics uncertainties are shown by shaded bands.*

5.7 Systematic uncertainties

The systematic uncertainties come first from the theoretical modelling, this includes uncertainties on the backgrounds and signal cross-sections as well as on the parton shower models. The second source of the systematic uncertainties are related to the physics object reconstruction, integrated luminosity measurement and pile-up re-weighting. The latter uncertainties are considered as experimental since they originate from the ATLAS detector performance. A detailed description of the various systematic uncertainties considered in this study are discussed in this section.

5.7.1 Theoretical systematic uncertainties

The present section regroups all systematic uncertainties associated to the signal and backgrounds modelling at the generation level, where the uncertainties are estimated from the different parton distribution functions (PDF) sets. thus, the related uncertainties are evaluated for dominant WZ-SM backgrounds.

5.7.1.1 Systematic uncertainties on the $q\bar{q}$ signal

Systematic uncertainties related to the PDF used in the generation of HVT samples are considered in this analysis. They are first taken from the NNPDF LO PDF sets presented in the derivation samples. The standard deviation is taken as an internal variation uncertainty. Afterward, the NNPDFLO sets are compared to CTEQ6L1 and MSTW20081O68CL PDF,

the possible discrepancies are then taken as extra uncertainties. Therefore, the total uncertainties on the HVT $q\bar{q}$ signal modeling are calculated as the quadratic some of both internal PDF variation and the extra uncertainties as described in ref [130]. The relative systematic uncertainty for different HVT masses is found to be between 2% and 5%.

5.7.1.2 Systematic uncertainties on the VBF signal

Systematics associated the the production of HVT and the GM for the VBF signal samples are extracted from its NNPDFLO PDF sets, the standard deviation is taken as an internal uncertainty. Both GM and HVT PDF sets are compared to the CTEQ6L1 and MSTW20081O68CL PDF onces. Any differences are added in quadratic some to the internal PDF variation.

For WZ-SM SHERPA samples, systematic uncertainty on the predicted cross-section are taken from NNPDF30NLOAS0118 PDF sets and compared to CT14NNLO and MMHT2014NLO68CL PDFs sets. Then, the total uncertainties is calculated by adding the maximum differences between PDFs in quadratic with the nominal NNPDF30NLOAS0118. To reach a robust modelisation similar to the VBF and $q\bar{q}$ signal regions, the fiducial selection for each signal category is applied at truth level of the Monte-Carlo samples.

5.7.1.3 Parton shower uncertainties on the WZ background

Since the variations of the parton shower uncertainties are not available in the Sherpa MC samples, the uncertainties associated with the parton shower modeling of the WZ SM backgrounds are computed by comparing different MC samples. Therefore, for the WZ QCD background, POWHEG+PYTHIA8 and POWHEG+HERWIG MC samples have been used to derive possible difference between different parton shower models (see Appendix A). The difference between the distributions provided by these two samples per bin of WZ_{Mass} is added in a quadratic sum to the statistical uncertainty of the POWHEG+HERWIG distribution, then the obtained results are used to calculate the relative uncertainty associated with the POWHEG+HERWIG parton shower. This relative uncertainty is used to construct an uncertainty band centered around SHERPA2.2 distributions. The procedure is shown in Figure 5.30. The obtained parton shower uncertainty band obtained is represented around the SHERPA2.2 predictions by shaded gray band. This uncertainty represents a conservative estimate of the parton shower effect of POWHEG MC.

For WZ EW background, the estimation of the parton shower uncertainties are performed by comparing the WZ EW MADGRAPH and SHERPA2.2.2 generators (see Appendix B). In order to avoid the impact of the large normalization factors in the two MC samples on the calculation of the fragmentation uncertainty, the MADGRAPH distribution is normalized to the Sherpa one. The difference between the two distributions is added quadratically to the

statistical uncertainty of the MadGrap distribution. Therefore, these relative uncertainties are applied to the Sherpa2.2.2 prediction to build a parton shower uncertainty band (Figure 5.31).

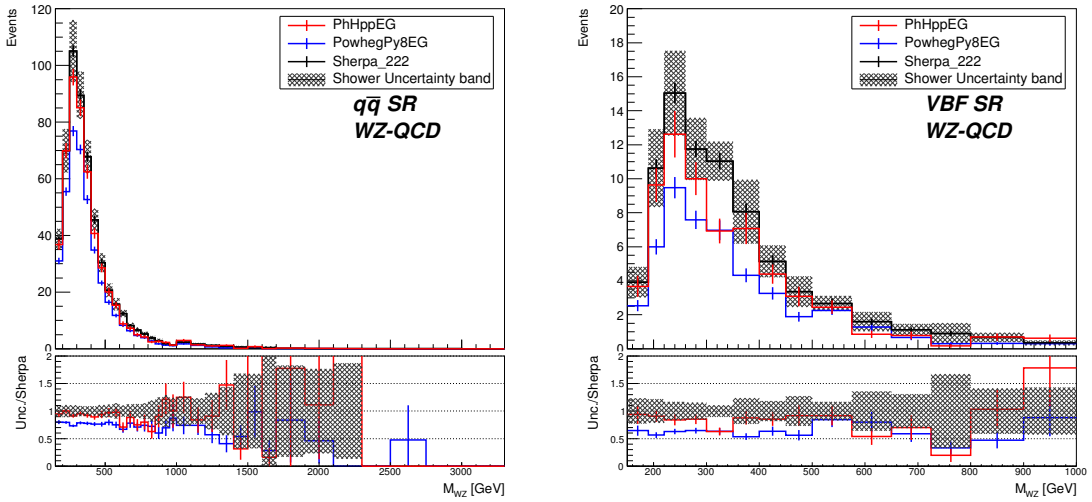


FIGURE 5.30: ***Comparison of the M_{WZ} distribution between Sherpa2.2.2, Powheg+Herwig and Powheg+Pythia8 event generators in VBF SR on the left and $q\bar{q}$ SR in the right. The parton shower uncertainty is shown by shaded gray bands.***

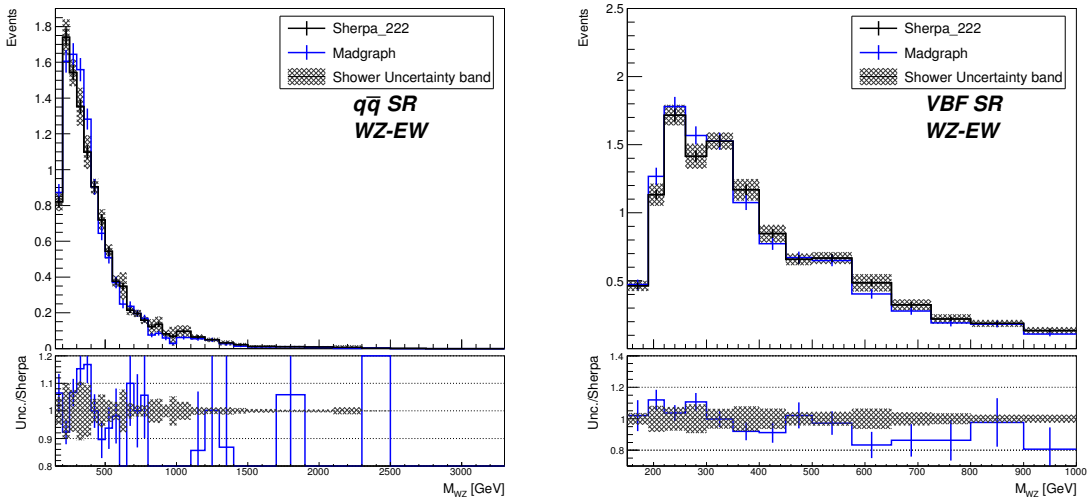


FIGURE 5.31: ***Comparison of the M_{WZ} distribution between Sherpa2.2.2 and MadGraph event generators in VBF SR on the left and $q\bar{q}$ SR in the right. The parton shower uncertainty is shown by shaded gray bands.***

5.7.2 Experimental systematic uncertainties

The systematic uncertainty in the ATLAS measurements is mainly associated with the measurement of the integrated luminosity, the reconstruction and the calibration of physic objects, as well as the effect of pile-up.

5.7.2.1 Integrated luminosity measurement

The systematic uncertainty in the combined 2015 and 2016 integrated luminosity measurement is determined from the calibration of the luminosity scale using the Van Der Meer [110] scans performed in August 2015 and May 2016. The systematic uncertainty on the integrated luminosity is estimated to be 2.1%.

5.7.2.2 Muons

The experimental uncertainties associated to the reconstruction of muons [131] are first estimated from the data-to-simulation efficiency scale factors (SF), by comparing the muon efficiency measurement to that predicted by the simulation ($\epsilon data/\epsilon MC$). Particularly for track-to-vertex-association, trigger, reconstruction and isolation scale factors used to correct the disagreement between data and simulated backgrounds. The total systematic uncertainties related to the scale factors are estimated by varying each SF corrections Up and Down within its uncertainties, then the square root of quadrature sum of the difference between the nominal SF value and its uncertainty is taken as the systematics.

Uncertainties on muon momentum resolution and scale due to the Inner detector and Muon Spectrometer measurements are extracted from data to MC comparison. Systematic uncertainties on the momentum resolution are estimated separately in the ID and MS detectors using $Z \to \mu\mu$ sample, where the reconstructed $m_{\mu\mu}$ invariant mass in the simulation is compared to data in order to extract the scale factor correction. After that, a cuts around Z invariant mass windows and muon transverse momentum are varied within $1 \pm \sigma$ of the $m_{\mu\mu}$ and p_T resolution is applied and the difference in the changes of the SF is then considered as systematic uncertainties. The normalization of the simulated background to data is varied within its uncertainties and the resulting difference on the p_T scale is taken as additional systematics and added in quadrature to the resolution one.

5.7.2.3 Electrons

As for muons, systematic uncertainties affecting electron reconstruction are derived from the electron trigger, identification and isolation scale factor, as well as from the energy scale and resolution [77]. The electron's scale factors of the identification, trigger and isolation are estimated from simulated $Z \to ee$ measurement that to be in agreement with the data. The total scale factor to the reconstruction efficiency is defined as the product of each SF. Its

uncertainty is calculated as a quadrature sum of its individual scale. Then, the uncertainty is evaluated by varying the total scale factor Up and Down within its uncertainties, then the square root of quadrature sum of the difference between the total SF value and its uncertainty is taken as the systematics.

The energy scale and resolution systematic uncertainty for electron is affected by the EM calorimeter pre-sampler calibration and are evaluated in the same way as for muon using $Z \rightarrow ee$.

5.7.2.4 Jets

Jets systematic uncertainties are connected to the jet energy resolution (JER). They are determined from the difference between the measured resolution and the simulated one. This later being corrected with a convenient scale factor. This is done using JERSmearingTool in the JetResolution [132] package. Moreover, jets in the ATLAS detector are calibrated using the jet energy scale. Its related uncertainty is derived from a combination of systematic variations in Monte Carlo simulations and single hadron response measurements performed in situ [133]. The results are provided by JetUncertaintiesTool.

Jets in this analysis are required to pass B-tagging and JVT selection, the systematic uncertainties on these variables estimated using BTaggingEfficiency Tool and JetJvt-Efficiency tool are also applied to the final results.

5.7.2.5 Missing transverse energy

The systematic uncertainty on the reconstruction of the transverse missing energy is extracted from the scale and from the resolution uncertainties of the individual hard terms involved in the calculation of the E_T^{miss}. Electrons, muons and jets and are assumed to be uncorrelated [134]. The uncertainties on the soft term scale and the resolution are also considered for the E_T^{miss}. They are evaluated from data and Monte-Marlo comparison of the p_T balance between the hard and soft terms using several event generator. The procedures are performed with a dedicated framework called METSystematicsTool.

5.7.2.6 Pile-up

The pile-up systematic uncertainty is related to the pileup re-weighting factor used to correct the disagreement between data and MC. Its uncertainty is estimated by varying the nominal pileup scale factor 1.0/1.09 [135] to 1.0 and to 1/1.18 to get the uncertainties bounds. The average number of interactions per bunch crossing $< \mu >$ for data and MC in the inclusive region after W and Z candidate selection can be seen in Figure 5.32

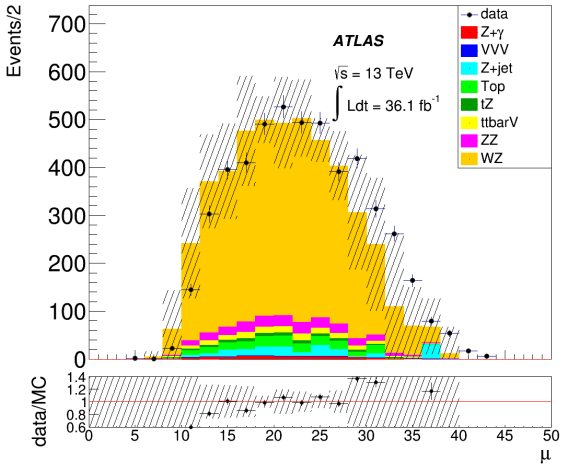


FIGURE 5.32: ***Average number of interactions per bunch crossing after pileup reweighting for data and MC in the inclusive region after selection of the W and Z boson candidates. All MC expectations are scaled to the integrated luminosity of the data using the predicted MC cross sections of each sample.***

5.8 Statistics procedure

The statistical treatment of this analysis uses a combined profile likelihood [136] fit to binned discriminants in all categories simultaneously. The definition of the likelihood and the configuration of the fit in terms of inputs and parameters are defined in this section.

5.8.1 Likelihood definition

The statistical analysis of the data uses a binned likelihood function constructed as the product of Poisson probability terms,

$$\text{Pois}\left(n|\mu S + B\right) = \left[\prod_{b\in\text{bins}}^{n} \frac{\mu\nu_b^{\text{sig}} + \nu_b^{\text{bkg}}}{\mu S + B}\right], \tag{5.20}$$

where μ, a signal strength parameter, multiplies the expected signal yield ν_b^{sig} in each histogram bin b, and ν_b^{bkg} represents the background content for bin b. The dependence of the signal and background predictions on the systematic uncertainties is described by a set of nuisance parameters (NP) θ, which are parameterized by Gaussian or log-normal priors; the latter are used for normalization uncertainties in order to maintain a positive likelihood. The expected numbers of signal and background events in each bin are functions of θ and parameterized such that the rates in each category are log-normally distributed for a normally distributed θ.

The priors act to constrain the NPs to their nominal values within their assigned uncertainties. They are implemented via so-called penalty or auxiliary measurements added to the likelihood which will always increase when any nuisance parameter is shifted from the nominal value. The likelihood function, $\mathcal{L}(\mu, \theta)$, is therefore a function of μ and θ.

The nominal fit result in terms of μ and σ_μ is obtained by maximizing the likelihood function with respect to all parameters. This is referred to as the maximised log-likelihood value, MLL. The statistical test q_μ is then constructed according to the profile likelihood: $q_\mu = 2\ln\Big(\mathcal{L}(\mu, \hat{\hat{\theta}}_\mu)/\mathcal{L}(\hat{\mu}, \hat{\theta})\Big)$, where $\hat{\mu}$ and $\hat{\theta}$ are the parameters that maximise the likelihood (with the constraint $0 \leq \hat{\mu} \leq \mu$), and $\hat{\hat{\theta}}_\mu$ are the nuisance parameter values that maximise the likelihood for a given μ. This test statistic is used to measure the compatibility of the background-only model with the observed data and for exclusion intervals derived with the CL_s method [137]. The limit set on μ is then translated into a limit on the signal cross section times branching ratio, $\sigma \times \mathrm{BR}(HVT \to WZ)$, using the theoretical cross section and branching ratio for the given signal model.

We have performed a binned maximum-likelihood fit to the WZ invariant mass spectrum using histogram templates derived from MC and data driven estimates using the standard package RooStats [138]. The fit is performed including the components for final state: signal, SM WZ, ZZ, $t\bar{t}+V(V=W,Z)$, tZ, VVV and fake lepton background. Electron and muon channels are merged together. The small background contributions background coming from tZ and VVV are added together.
In addition to the experimental uncertainties, the uncertainty on the cross section has been applied to the backgrounds whose estimates are taken directly from MC following ATLAS PHYSICS MODELLING GROUP (PMG) recommendations. The following uncertainties have been applied: 10% for WZ and ZZ, 13% for $t\bar{t}+V(V=W,Z)$, 15% for tZ and 20% for VVV. The fake background is allowed to vary within the uncertainties estimated by the Matrix Method. The shape uncertainties due to the scale and the PDF were applied on the dominant background WZ.

For the dominant background WZ SM, there are the scale and the PDF uncertainty that are to a large amount a normalization uncertainty. In addition, a free normalization for the WZ cross section. This leads unavoidably to to large (anti-)correlations. fixing the scale and PDF uncertainties to one at a low masses and increase the cross section uncertainty, leads to more stabilized fit and makes the results more interpretable. Uncertainties on the normalization are allowed to vary within 20% for $q\bar{q}$ and 40% for VBF (these values are slightly higher than the scale/PDF uncertainties).

5.8.2 Statistical Treatment

The binning is obtained from the expected resolution of the resonance peak with its width estimated from the MC signal. The width of the peak is plotted as a function of the resonance mass and it is fitted with a polynomial function. The obtained polynomial is used to define a variable bin width. In the high mass tail the last bin is enlarged to avoid low MC statistics. Figures 5.34 shows the fitted function for the $q\bar{q}$ and the VBF analyses respectively. These binning is used as baseline in the analysis. Due to the lack of MC statistics for the background samples, a coarser binning is used at high-mass region in the VBF category. The determined binning is: bins = [150, 200, 250, 300, 350, 400, 450, 500, 550, 600, 650, 700, 750, 800, 850, 900, 950, 1000, 1100, 1200, 1300, 1400, 1500, 1600, 1700, 1850, 2100, 2300, 2500, 2750, 3000],for qq-analysis bins =[150,200,250,300,350,400,460,520,580, 650, 720, 800, 900, 1000, 2000] for VBF HVT analysis and bins =[150, 190, 220, 260, 300, 350, 400, 450, 500, 575, 650, 725, 800, 900, 1000] for H_5^+ VBF analysis.

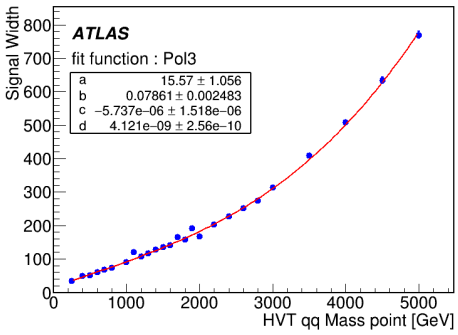


FIGURE 5.33: ***Width of the resonance peak as a function of the resonance mass, for*** $q\bar{q}$***.***

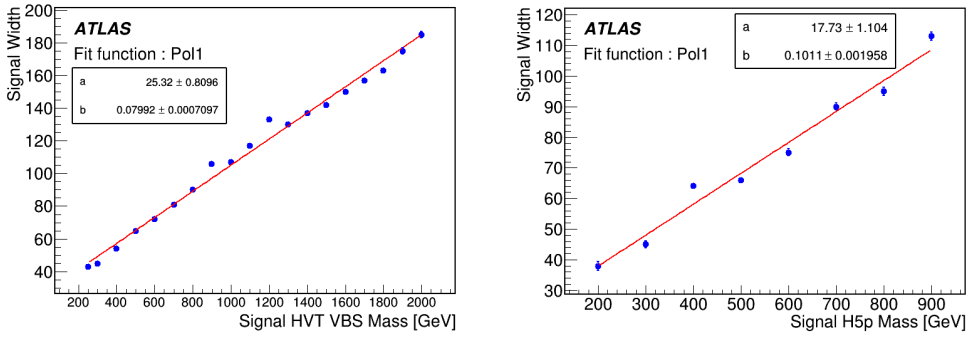


FIGURE 5.34: ***Width of the resonance peak as a function of the resonance mass, for the*** VBF ***analyses.***

5.8.3 Background Modeling

In order to have a smooth background shape across the full mass range, all background contributions are combined together and modelled with a empirical function. The real background contributions coming from WZ, ZZ, tZ and $t\bar{t}V$ are summed up and are taken from the MC. The fake lepton background is treated separately and is estimated using data driven. The WZ continuum is the dominant background across the full mass range. The normalization of the background is estimated directly from MC while its shape is described analytically. The background shapes are described by the same empirical functional form in $q\bar{q}$ and VBF categories with different parameters:

$$f_{q\bar{q}/VBS}(m_{WZ}) = (f_1(m_{WZ}) + f_2(m_{WZ})) \times H(m_{WZ} - m_0) \times C_0 + f_3(m_{WZ}) \times H(m_0 - m_{WZ}), \tag{5.21}$$

where:

$$\begin{aligned} f_1(m_{WZ}) &= \exp(a_1 + a_2 \cdot m_{WZ}), \\ f_2(m_{WZ}) &= (\frac{1}{2} + \frac{1}{2} erf(\frac{m_{WZ} - b_1}{b_2})) \times \frac{1}{1 + \exp\left(\frac{m_{WZ} - b_1}{b_3}\right)}, \\ f_3(m_{WZ}) &= \exp\left(c_1 + c_2 \cdot m_{WZ} + c_3 \cdot m_{WZ}^2 + c_4 \cdot m_{WZ}^{2.7}\right) \\ , C_0 &= \frac{f_3(m_0)}{f_1(m_0) + f_2(m_0)}. \end{aligned} \tag{5.22}$$

The first part of the function f_1 takes care of the flat low mass part of the spectrum, while f_2 models the WZ threshold around the WZ mass and f_3 describes the high mass tail. The transition between low mass and high mass parts is done by the Heaviside step function $H(x)$ around $m_0 = 400$ GeV. Continuity of the function around m_0 is insured by normalization factor C_0 that is applied to the low mass part. a_i, b_i and c_i are shape parameters that will be fixed from MC fit for each category.

Additional systematics on the background shape due to MC statistical errors is taken in to account. This uncertainty is originally given as an error on all the parameters of the background shape described by Equation 5.22. Propagation of such an error to the statistical model of the analysis is quite challenging due to high correlation of the shape parameters. However, the uncertainty can be redefined as an error of a single shape parameter. It can be obtained by refitting the MC distribution with all parameters fixed to their best fit values, but not the one most sensitive to the high mass tail (parameter $c4$ in Equation (5.22)).

5.9 Results

5.9.1 $q\bar{q}$ signal region

Figure 5.35 shows the post-fit WZ invariant mass distribution fo $q\bar{q}$ SR. No significant excesses are observed above the SM expectations. The post-fit background yields are summarized in Table 5.19.The systematic uncertainties on total background are shown in Appendix C.

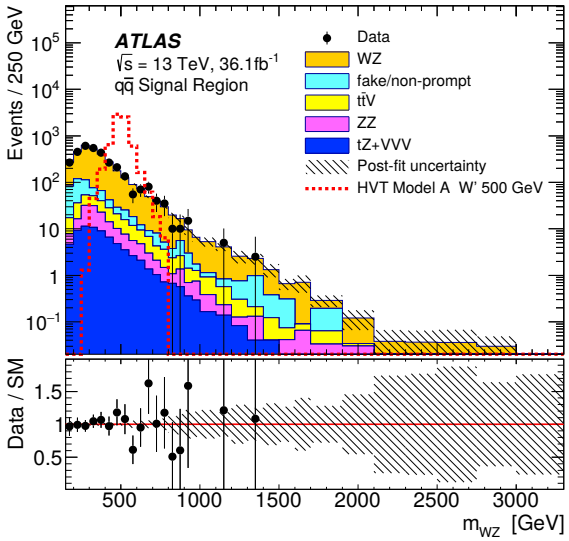


FIGURE 5.35: ***The post-fit WZ invariant mass distribution in $q\bar{q}$ signal region. Pre-fit HVT signal expectation at $m = 500$ GeV is overlaid. The background expectation is shown after the profile likelihood fit to the data. The band denotes the statistical and systematic uncertainty on the background after the fit to the data. The lower panels show the ratio of the observed data to the SM background estimation.***

5.9.2 VBF signal region

Figure 5.36 shows the post-fit WZ invariant mass distribution for VBF SR. A local excess of 3.1σ exceeding the SM expectations around 450 GeV is found for the HVT signal. It corresponds to a global p-value of 0.13 and a significance of 1.6. In the case of GM model, an excess of 2.9σ is observed around 450 GeV with a global p-value of 0.20. The post-fit background yields are summarized in Table 5.20.

	$q\bar{q}$ SR
WZ	533 ± 23
Fakes	64.3 ± 8.1
$t\bar{t}$V	29.4 ± 5.5
ZZ	18.9 ± 4.4
$tZ + VVV$	9.3 ± 3.1
Total Background	654.65 ± 2.62
Observed	650

TABLE 5.19: ***Expected and observed yields in the $q\bar{q}$ signal region. Yields and uncertainties are evaluated after a background-only fit to the data in the $q\bar{q}$ signal region. The uncertainty on the total background estimate can be smaller than the quadratic sum of the individual background contributions due to anti-correlations between the estimates of different background sources.***

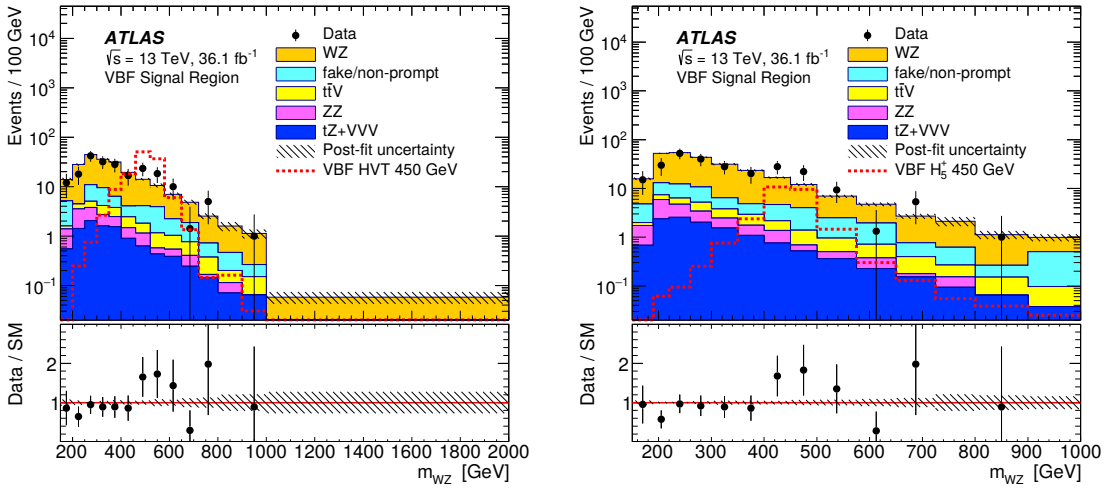


FIGURE 5.36: ***The post-fit WZ invariant mass distribution in VBF signal region. Pre-fit HVT (left) and GM (right) signal expectation at $m = 450$ GeV are overlaid. The background expectation is shown after the profile likelihood fit to the data. The band denotes the statistical and systematic uncertainty on the background after the fit to the data. The lower panels show the ratio of the observed data to the SM background estimation.***

	VBF SR
WZ	87.2 ± 11.9
Fakes	15.36 ± 4.03
$tZ + VVV$	8.1 ± 1.8
$t\bar{t}$V	4.9 ± 0.9
ZZ	4.40 ± 1.01
Total Background	119.9 ± 10.8
Data	114

TABLE 5.20: ***Expected and observed yields in the VBF signal region. Yields and uncertainties are evaluated after a background-only fit to the data in the VBF signal region. The uncertainty on the total background estimate can be smaller than the quadratic sum of the individual background contributions due to anti-correlations between the estimates of different background sources.***

5.10 Upper limit on signal cross section times branching fraction

Due to the absence of significant excesses above the SM expectation, exclusion limits on the cross section times branching fraction of the several signal models are set.

5.10.1 Exclusion limits for qq-analysis

Figure 5.37 presents the expected and the observed upper limits on $\sigma \times \mathrm{BR}(HVT \to WZ)$ signal at 95% C.L for the HVT Model-A; in $q\bar{q}$-enriched category. Masses below 2400 GeV are excluded which is in agreement with the expected limits. Masses below 2600 GeV are excluded for the HVT Model-B.

The largest difference between the observed data and the SM background prediction occurred at 700 GeV with local significance of 1.2 standard deviation.

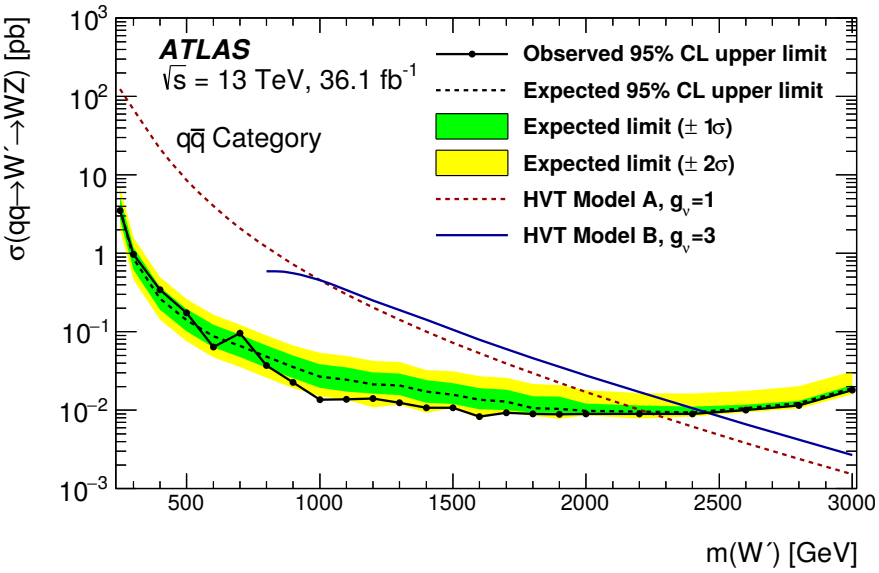


FIGURE 5.37: ***Expected and observed 95% C.L. exclusion upper limits with an integrated luminosity of 36.1 fb^{-1} on the production cross section multiplied by the branching ration $\sigma \times BR(HVT \to WZ)$ in the $q\bar{q}$-enriched category.***

5.10.2 Exclusion limits for VBS-analysis

Expected exclusion limits on $\sigma \times \mathrm{BR}(H_5^+ \to WZ)$ signal at 95% C.L confidence level and on the ratio of vacuum expectation values in the Georgi-Machacek Model as a function of $m_{H_5^+}$ are obtained and shown in Figure 5.38.

In the mass range between 200 and 900 GeV only the 900 GeV mass has a bigger tree-level decay width, here the width Γ is approximately 227 GeV for a value of $sin(\theta_H) = 1$ whereas the experimental resolution is 190 GeV. The width of the new resonance is proportional to the square of $sin(\theta_H)$. Therefore the narrow-width approximation is valid for all mass points and values of $sin(\theta_H)$ except for signal masses above 850 GeV and $sin(\theta_H) > 0.9$.

Expected exclusion limits on $\sigma \times \mathrm{BR}(W' \to WZ)$ signal at 95% C.L confidence level in the VBF HVT model is shown in Figure 5.39. Sensitivity for this model are estimated and masses below 230 GeV can be excluded. A local excess over the Standard Model expectations at a resonance mass of around 450 GeV is obtained.

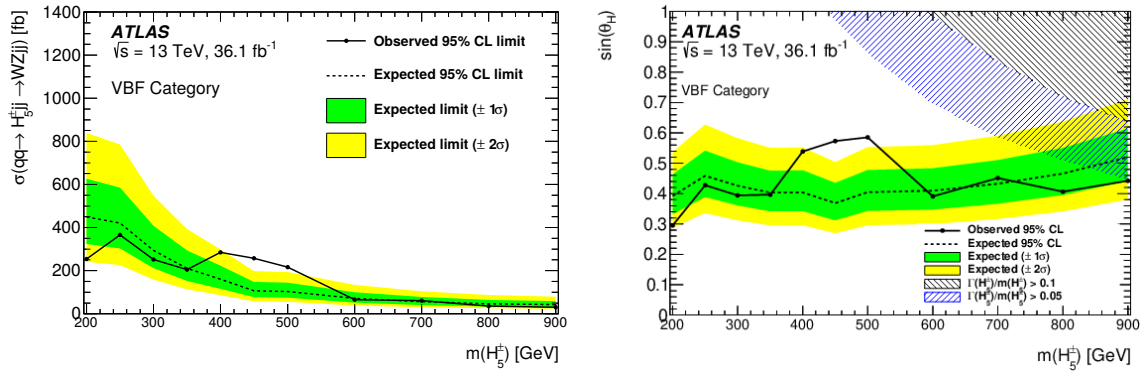


FIGURE 5.38: ***Expected and observed exclusion limits on $\sigma \times BR(H_5^+ \to WZ)$ signal at 95% C.L confidence level and on the ratio of vacuum expectation values in the Georgi-Machacek Model as a function of $m_{H_5^+}$.***

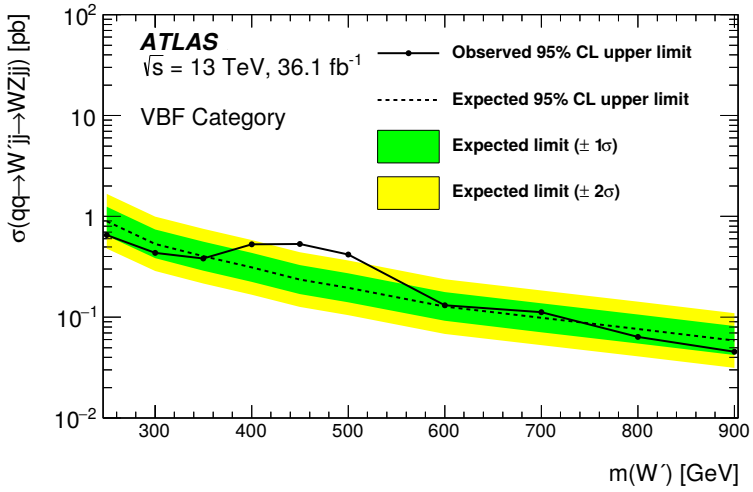


FIGURE 5.39: ***Expected and observed exclusion limits on $\sigma \times BR(W' \to WZ)$ signal at 95% C.L confidence level in the HVT Model as a function of the mass heavy boson mass in the VBF phase space.***

5.11 Previous diboson resonance searches

This section presents the previous results performed by the ATLAS and CMS collaborations during their searches for new heavy bosons decaying to diboson WZ with $\ell\nu\ell'\ell'$, $\ell\ell q\bar{q}$, $\ell\nu q\bar{q}$, JJ, $q\bar{q}q\bar{q}$, $\ell\ell\nu qq$, $\ell\ell qq$, $\ell\nu\ell\nu$, $\ell\ell\nu\nu$, $\ell\nu\ell\ell$, $\ell\ell\ell\ell$, $qqbb$, $\nu\nu bb$, $\nu\nu b\bar{b}$, and $\ell\ell b\bar{b}$ final states using 20.3 fb^{-1} of pp collision data at $\sqrt{s} = 8$ TeV collected in 2012. For both collaboration, no significant deviation over the SM expectation in the invariant mass distribution of the diboson candidates is observed. Moreover, upper limits on the production cross section times branching ratio to WZ di-bosons at the 95% CL are evaluated within heavy vector triplet

models. Results are exposed in Figure 5.40 [139] for ATLAS and in Figure 5.41 [140] for *CMS*.

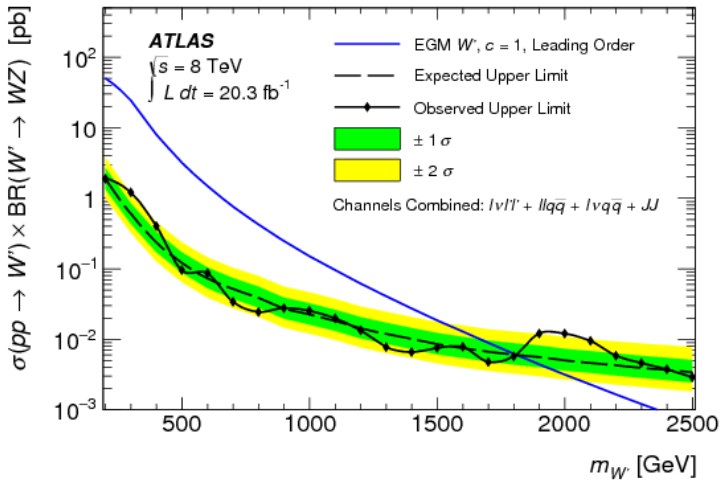


FIGURE 5.40: ***Combined 95% CL limit for diboson WZ with $\ell\nu\ell'\ell'$, $\ell\ell q\bar{q}$, $\ell\nu q\bar{q}$, JJfinal states. The green (yellow) bands representing the 1 σ (2σ) intervals of the expected limit including statistical and systematic uncertainties.***

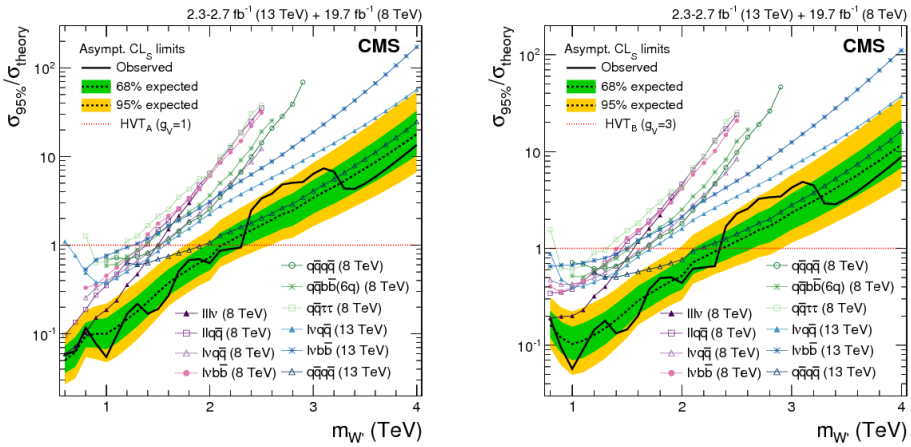


FIGURE 5.41: ***Combined 95% CL limit for diboson WZ with fully-leptonic, semi-leptonic, and all-hadronic final states at $\sqrt{s} = 8$ TeV and 13 TeV (2015) on HVT signal model-A (left) and model-B (right). The green (yellow) bands representing the 1 σ (2σ) intervals of the expected limit including statistical and systematic uncertainties.***

5.12 Combination of recent diboson resonance searches

The ATLAS and CMS collaborations at the Large Hadron Collider (LHC) carried out several analysis searching for diboson VV (V= W, Z) resonance in diverse decay channels with fully-leptonic, semi-leptonic, and all-hadronic final states. No clear deviation from the Standard Model prediction has been observed in both experiments. This section will presents the most significant results sensitive to diboson resonance production via vector-boson fusion at $\sqrt{s} = 13\ TeV$ proton-proton collision collected with ATLAS detector in 2015 and 2016.

5.12.1 Combination of WW and WZ resonance

A search for new resonances decaying into a WW or WZ [141] were performed with the ATLAS collaboration at $\sqrt{s} = 13\ TeV$ proton-proton collision data with an integrated luminosity of 36.1 fb $^{-1}$ via vector-boson fusion, where one W boson decays leptonically ($W \to \ell\nu$ with $\ell = e, \mu$) and the other W/Z boson decays hadronically to quark anti-quark. Results in Figure 5.42 are extracted by performing a simultaneous binned maximum-likelihood fit to the $m(WV)$ distributions in the signal regions. These measurements were found to be in good agreement with the Standard Model predictions, with no significant excess neither at high nor at low mass limits.

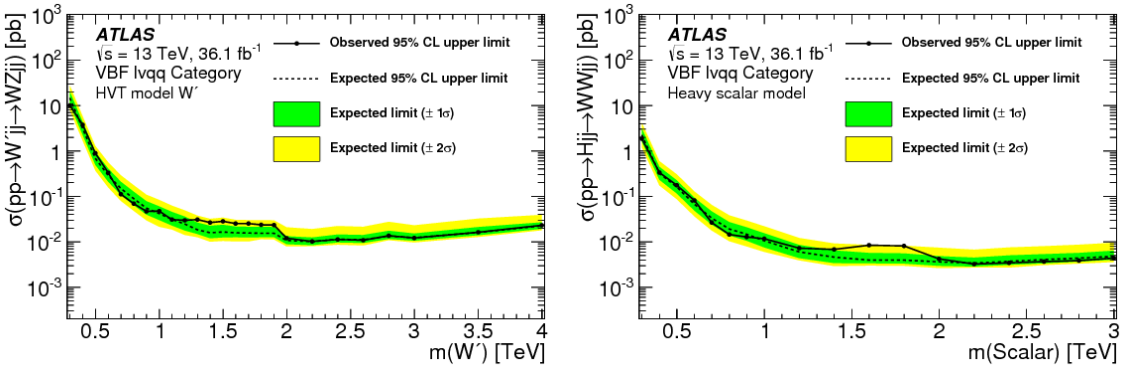


FIGURE 5.42: ***The observed and expected cross-section upper limits at the 95% confidence level for WV production in the VBF category as a function of the resonance mass. The dots in the observed limit curve represent the generated resonance mass values for HVT W' (left) and heavy scalar signals H (right), produced via VBF are shown [141].***

5.12.2 Combination of ZZ and ZW resonance

A searches for heavy ZZ and ZW [142] resonances in the $\ell\ell qq$ and $\nu\nu qq$ final states was performed in the same period with the fully 2015 and 2016 data. Limits in Figure 5.43 are extracted in the same way with binned likelihood function to the observed $m(ZV)$ distributions in the signal regions. These measurements were found consistent with the

Standard Model predictions, with no significant excess. The upper limits on $\sigma \times \mathrm{BR}(W' \to ZW)$ were evaluated for HVT VBF Model with values of 0.98 pb at $m(W') = 300$ GeV and 2.8 fb at $m(W') = 4$ TeV.

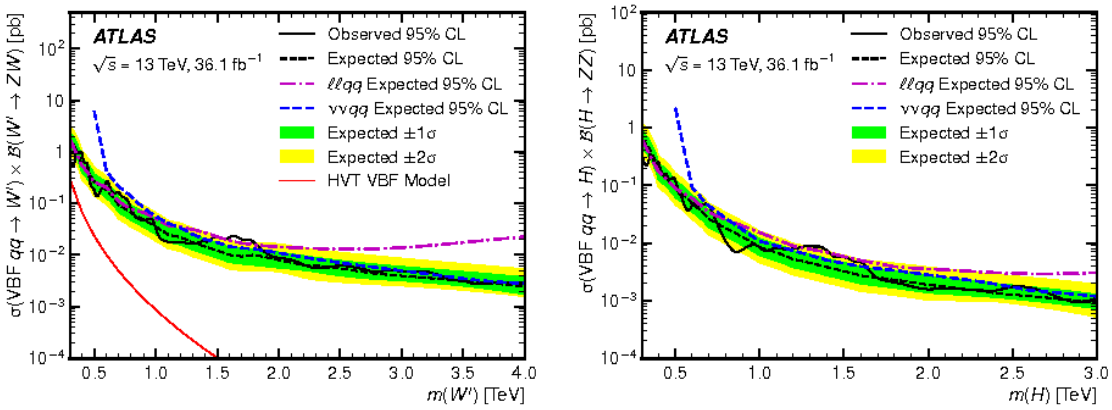


FIGURE 5.43: ***The observed and expected cross-section upper limits at the 95% confidence level for ZV production in the VBF category as a function of the resonance mass. The dots in the observed limit curve represent the generated resonance mass values for HVT W' (left) and heavy scalar signals H (right), produced via VBF are shown [142].***

5.13 Conclusion

A Resonant $WZ \to \ell\nu\ell'\ell'$ search production in fully leptonic final state is performed using 36.1 fb^{-1} of data collected by the ATLAS detector at $\sqrt{\mathbf{s}} = \mathbf{13}\ TeV$ of proton-proton collision at the LHC at 2015-2016 runs. The search is performed for two WZ production mode, namely the quark-anti-quark ($q\bar{q}$) annihilation and vector-boson fusion (VBF).

The data in the $q\bar{q}$ fusion category are found to be consistent with the Standard Model predictions. The results are used to derive upper limits at 95% CL on the cross section times branching ratio of the phenomenological Heavy Vector Triplet benchmark Model A (Model B) with coupling constant $g_V = 1$ ($g_V = 3$) as a function of the resonance mass, with no evidence of heavy resonance production for masses below 2260 (2460) GeV.

In the case of the VBF production processes, limits on the production cross section times branching ratio are obtained as a function of the mass of a charged member of a heavy vector triplet or of the five-plet scalar in the Georgi–Machacek model. The results show a local excess of events over the Standard Model expectations at a resonance mass of around 450 GeV. The local significances for signals of $H_5^{\pm}$ and of a heavy vector W' boson are 2.9 and 3.1 standard deviations respectively. The respective global significances calculated using the Look Elsewhere method are 1.6 and 1.9 standard deviations respectively.

Summary

This study treats two different aspects of The ATLAS detector. The first one is a technical one and concern the upgrade of the ATLAS detector at the projected high luminosity phase II of the large hadron collider. Close to the proton proton interaction point and to the high radioactivity environment, the ATLAS forward calorimeter is one of the most detectors compromised. Two upgrade solutions were proposed by the collaboration. The first one considers the installation of a new mini calorimeter in the front of the FCal while the second proposes a complete replacement of the FCal by a new calorimeter with high granularity, the sFcal. We performed a standalone simulation studies for the FCal and the $sFCal$ in terms of their energy and pointing ϕ resolutions. The results obtained show that the energy resolution for electrons and pions is slightly worst in the sFCal compared to the FCal due to lower sampling fraction that gives an increase of the constant term in the sFCal by a factor of 1.12 for electrons and 1.03 for pions. Results show that the logarithmic weighing provides the best corrections compared to the linear interpolation. Despite of potential improvements in the $sFCal$ performance, the replacement of the $FCal$ was rejected based on the results of the risk analysis. The installation of the new $sFCal$ requires opening of the End-Cap cryostat, and there is a risk that liquid argon will lost through a leak into the vacuum space and destroy the thermal insulation.

The second aspect of this work is a software one dedicated to the WZ resonant search in the fully leptonic final states, produced in quark-anti-quark annihilation and Vector Boson fusion modes, at $s = \sqrt{13}\ TeV$ p-p collision using 36.1 fb^{-1} of data collected by the ATLAS detectors during 2015 and 2016 proton-proton LHC runs. For both production modes, the dominant background is estimated from the ATLAS Monte-Carlo simulation, while backgrounds with one or two fake leptons are evaluated using a matrix method. Data inside WZ event selection are found in good agreement with the simulated backgrounds within its uncertainties for both categories ($q\bar{q}$ and VBF). Results for $q\bar{q}$ category are interpreted in the context of the Heavy Vector Triplet (HVT) Model-A and Model-B, on which the upper limits is extracted at 95% confidential level (CL) on the cross section times branching ratio for the different HVT mass points, no significant deviation from the SM predictions are observed. Thus, Masses below 2260 GeV can be excluded for Model-A and 2460 GeV for Model B. Concerning the VBF production mode, a local excesses over the SM prediction are observed at resonance mass around 450 GeV for both Heavy Vector Triplet, and Georgi-Machacek models, with a local significances standard deviations of 2.9 and 3.1 for $H_5^{\pm}$ and W' signals

respectively.

As perspective for this study, one can continue investigating the search of WZ resonance with the new luminosity delivered by the LHC in 2017 and 2018. More accuracy and many improvements are to be expected with the new collected data and the development of new analysis approaches. This would have important implications for our understanding of the Universe.

Appendix A

Comparison between different WZ QCD MC samples generators

A.1 WZ QCD PowhegPythia8/Sherpa2.2.2 comparison

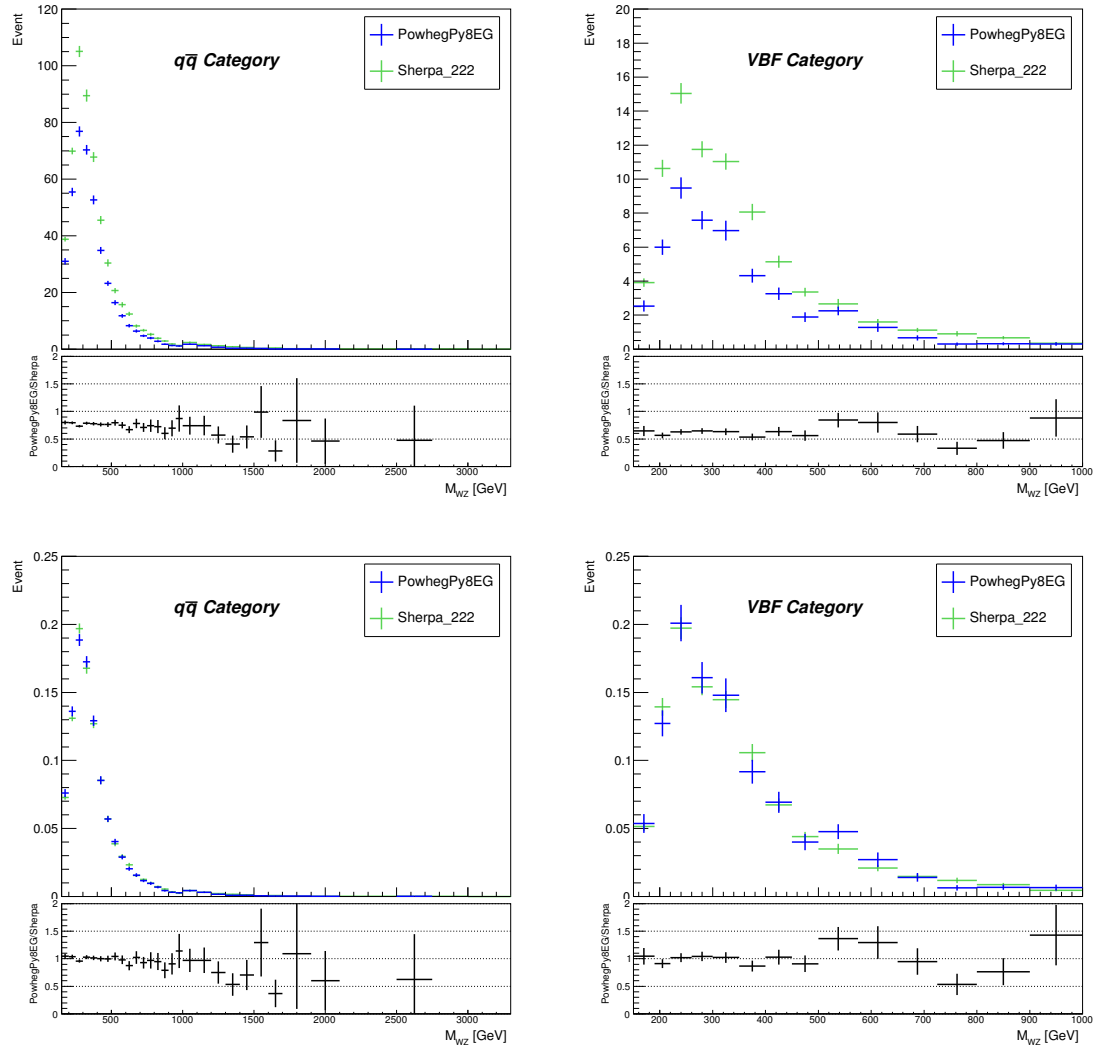


FIGURE A.1: *Comparison of the m_{WZ} distributions normalized to the cross section (top) and to the unit (bottom) in the $q\bar{q}$ SR and VBF SR of the WZ QCD MC samples. Powheg+Pythia8 (Blue) and Sherpa2.2.2 (Green).*

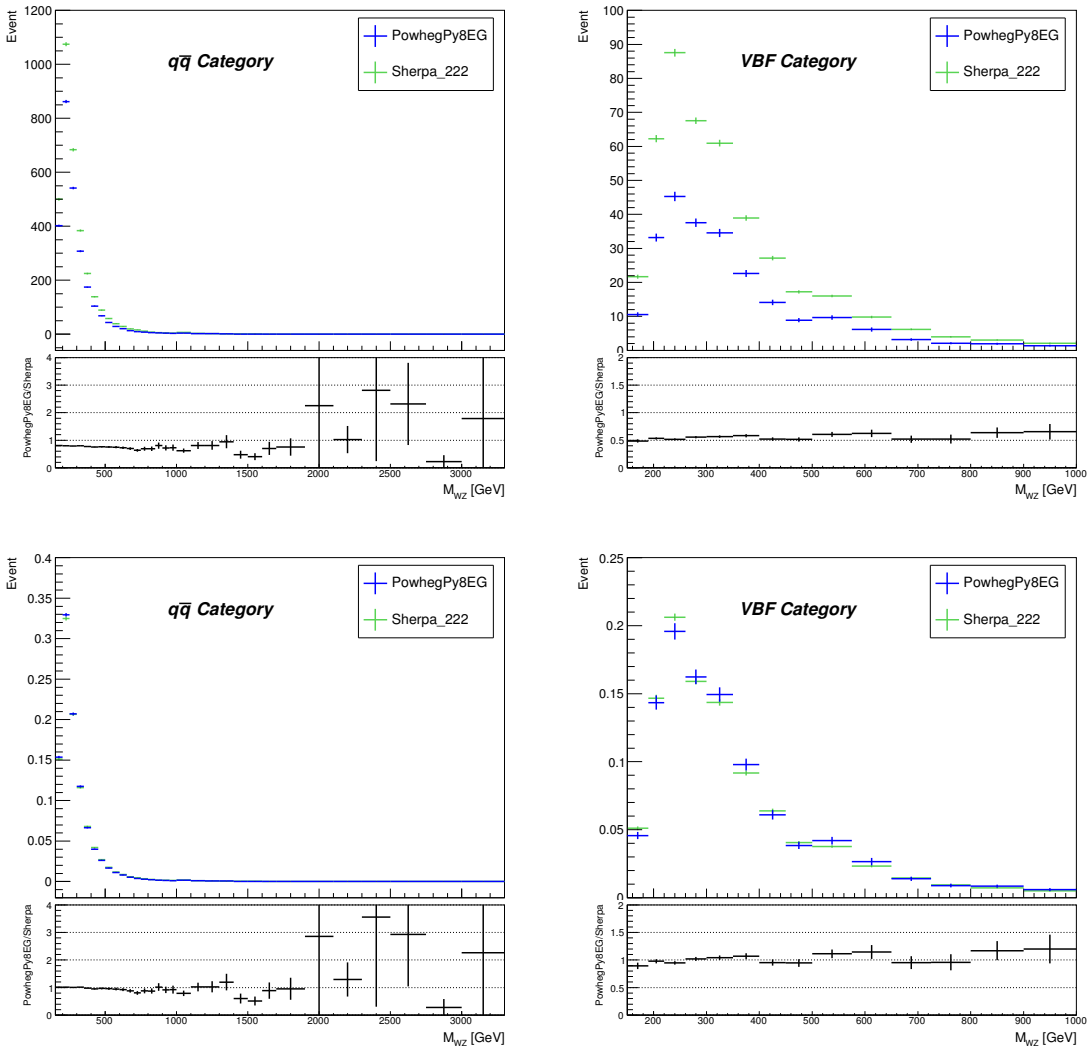


FIGURE A.2: ***Comparison of the m_{WZ} distributions normalized to the cross section (top) and to the unit (bottom) in the $q\bar{q}$ CR and VBF CR of the WZ QCD MC samples. Powheg+Pythia8 (Blue) and Sherpa2.2.2 (Green).***

A.2 WZ QCD PowhegHerwig/Sherpa2.2.2 comparison

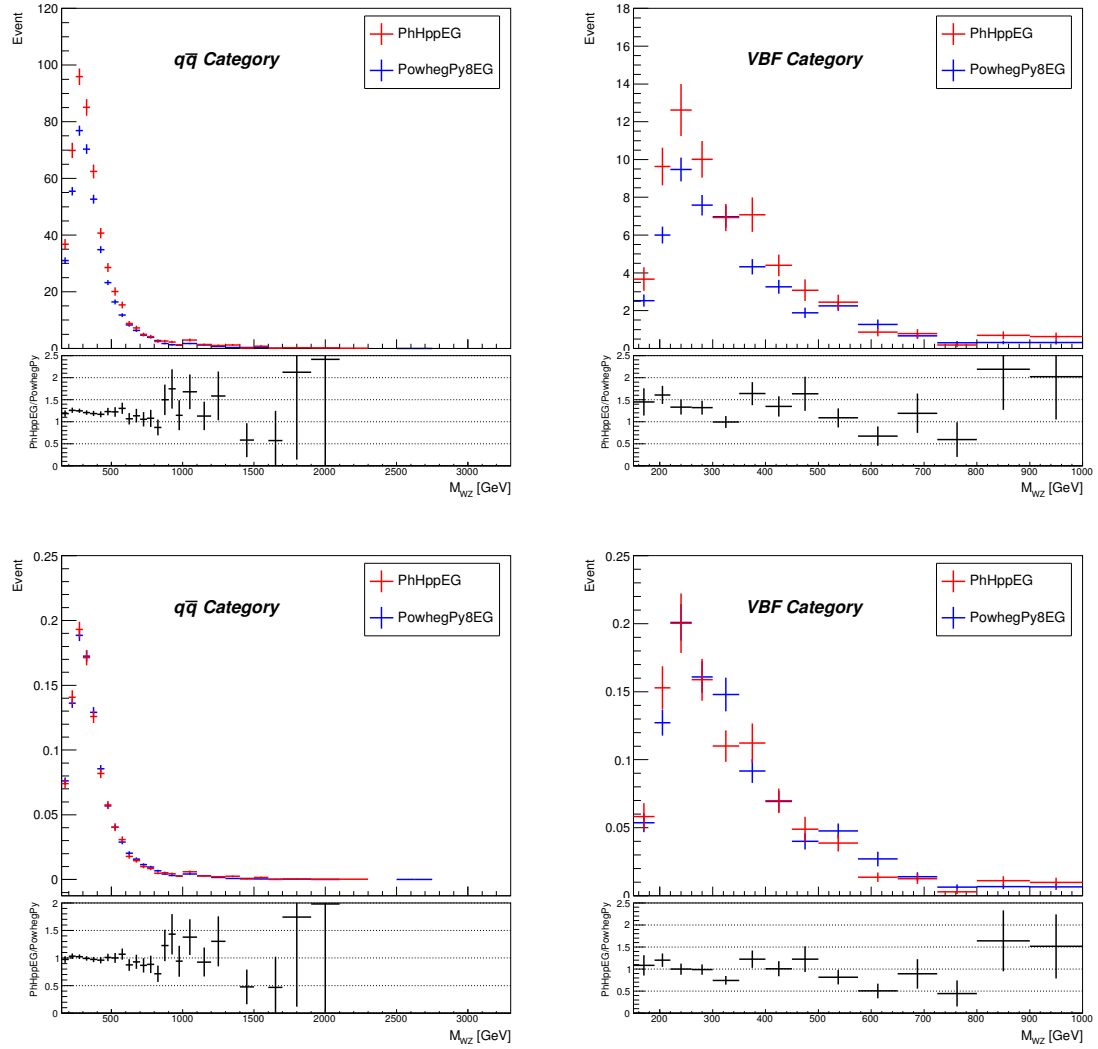


FIGURE A.3: *Comparison of the m_{WZ} distributions normalized to the cross section (top) and to the unit (bottom) in the $q\bar{q}$ SR and VBF SR of the WZ QCD MC samples. Powheg+Pythia8 (Blue) and Powheg+Herwig (Red).*

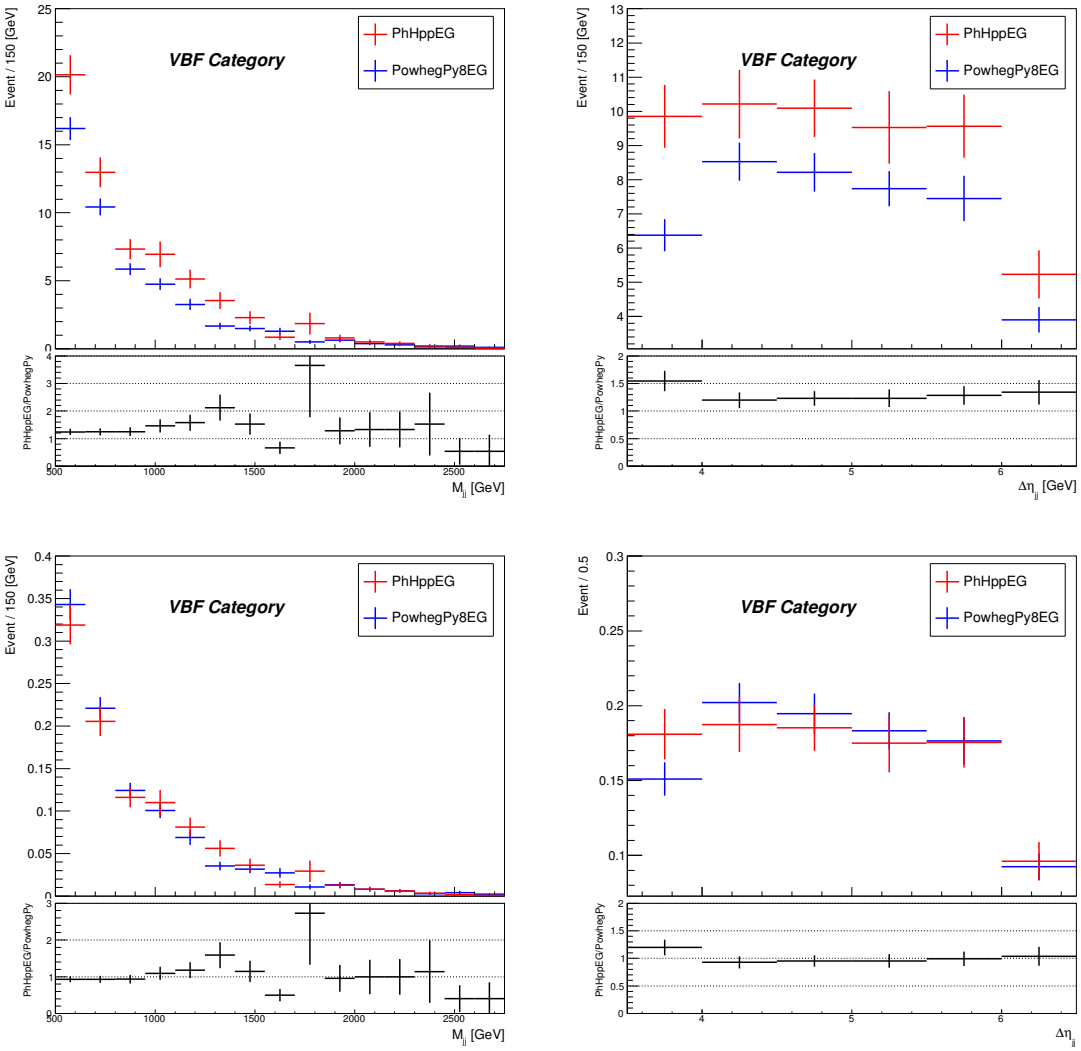


FIGURE A.4: ***Comparison of the m_{jj} and $\Delta\eta_{jj}$ distributions normalized to the cross section (top) and to the unit (bottom) in the VBF SR of the WZ QCD MC samples. Powheg+Pythia8 (Blue) and Powheg+Herwig (Red).***

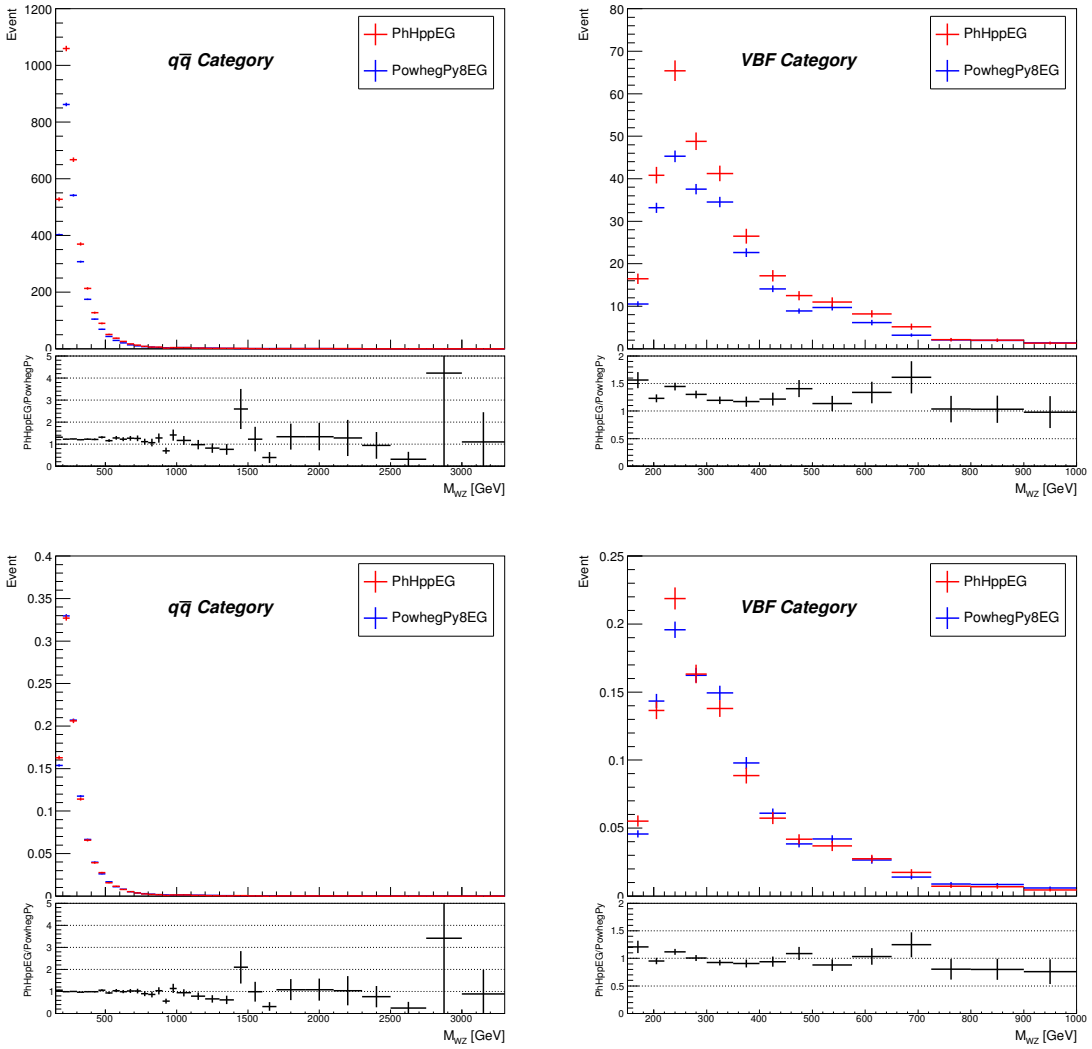


FIGURE A.5: ***Comparison of the m_{WZ} distributions normalized to the cross section (top) and to the unit (bottom) in the $q\bar{q}$ CR and VBF CR of the WZ QCD MC samples. Powheg+Pythia8 (Blue) and Powheg+Herwig (Red).***

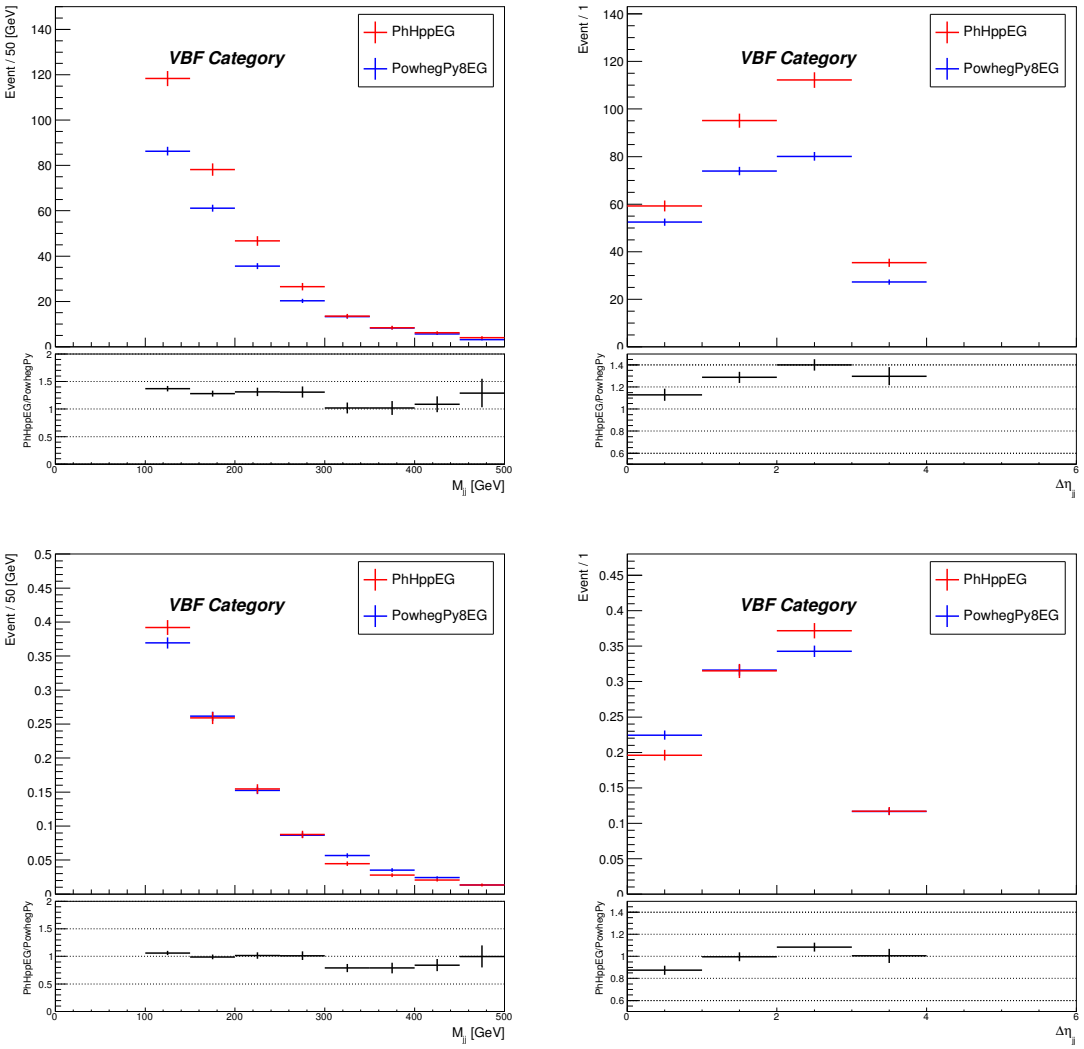


FIGURE A.6: ***Comparison of the m_{jj} and $\Delta\eta_{jj}$ distributions normalized to the cross section (top) and to the unit (bottom) in the VBF CR of the WZ QCD MC samples. Powheg+Pythia8 (Blue) and Powheg+Herwig (Red).***

A.3 WZ QCD PowhegPythia8/PowhegHerwig comparison

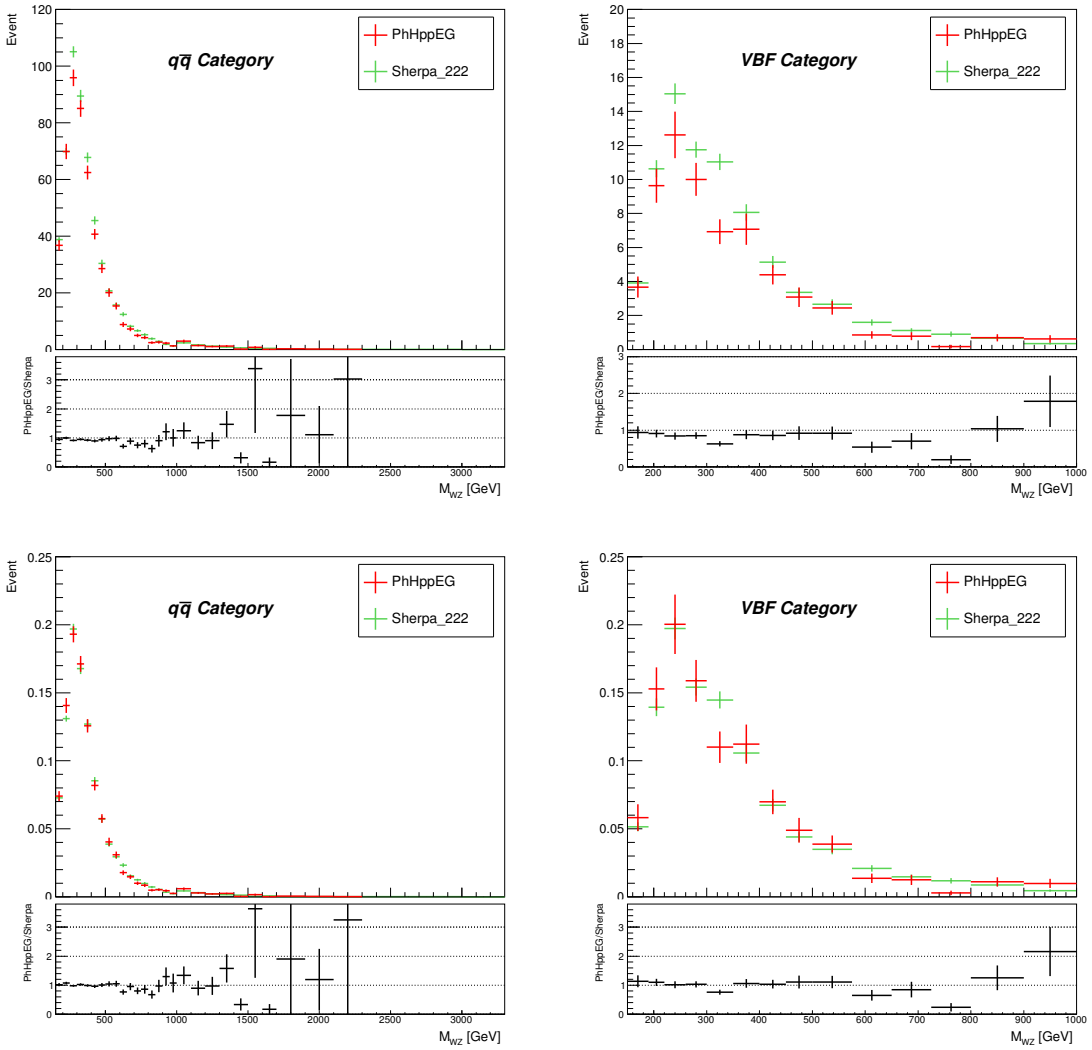


FIGURE A.7: *Comparison of the m_{WZ} distributions normalized to the cross section (top) and to the unit (bottom) in the $q\bar{q}$ SR and VBF SR of the WZ QCD MC samples. Powheg+Herwig (Red) and Sherpa2.2.2 (Green).*

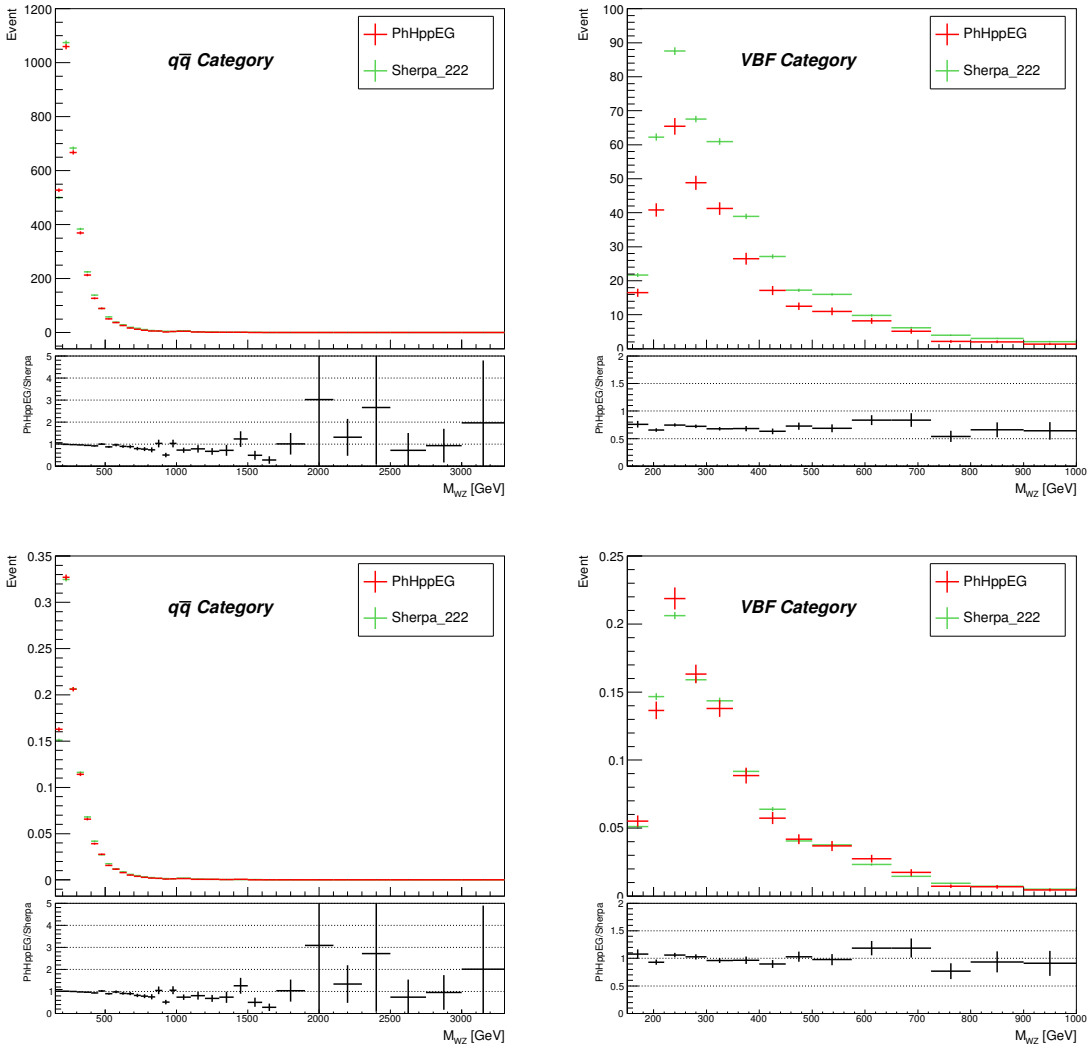


FIGURE A.8: ***Comparison of the m_{WZ} distributions normalized to the cross section (top) and to the unit (bottom) in the $q\bar{q}$ SR and VBF SR of the WZ QCD MC samples. Powheg+Herwig (Red) and Sherpa2.2.2 (Green).***

Appendix B

Comparison between different EW QCD MC samples generators

B.1 WZ QCD PowhegPythia8/Sherpa2.2.2 comparison

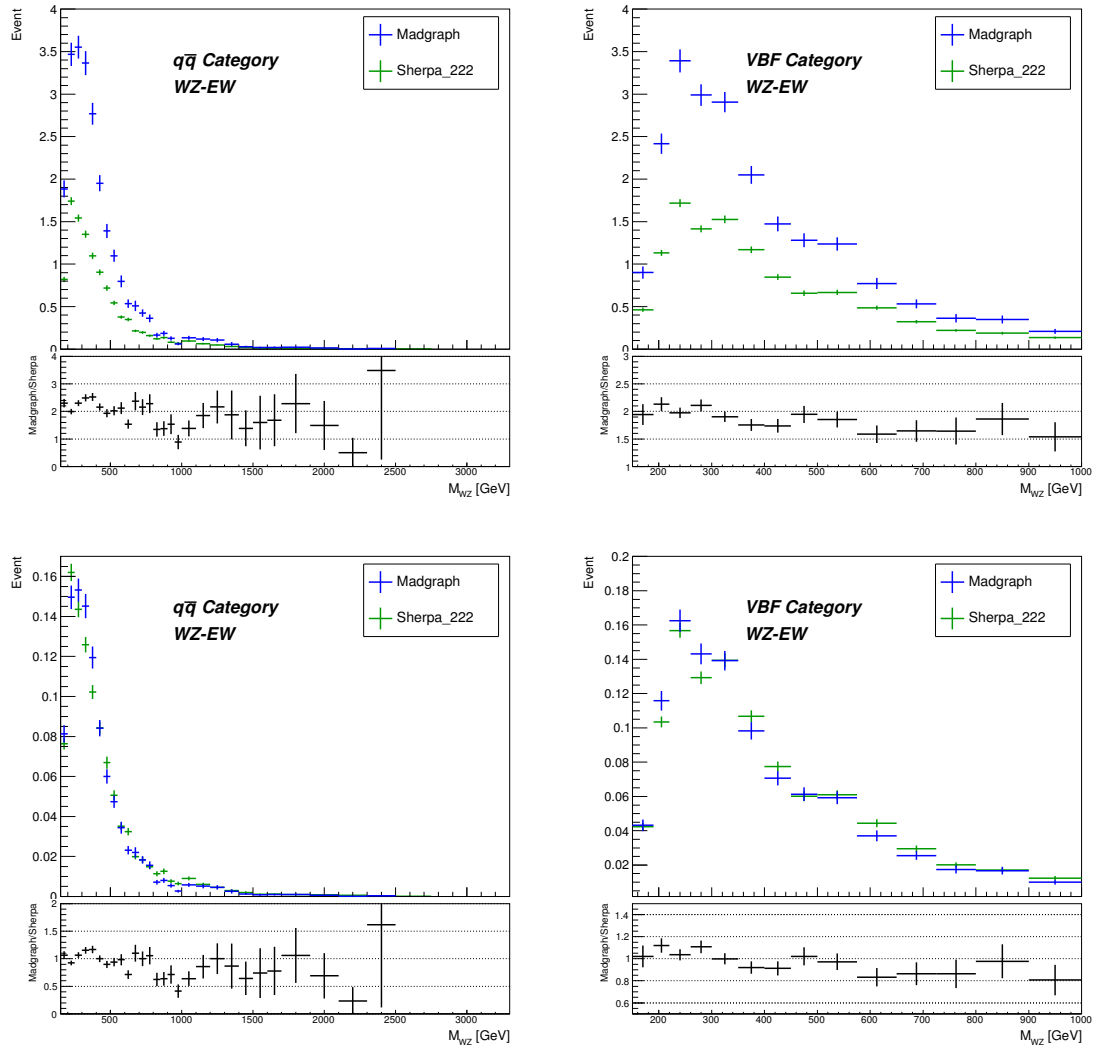


FIGURE B.1: ***Comparison of the m_{WZ} distributions normalized to the cross section (top) and to the unit (bottom) in the $q\bar{q}$ SR and VBF SR of the WZ EW MC samples. MadGraph (Blue) and Sherpa2.2.2 (Green).***

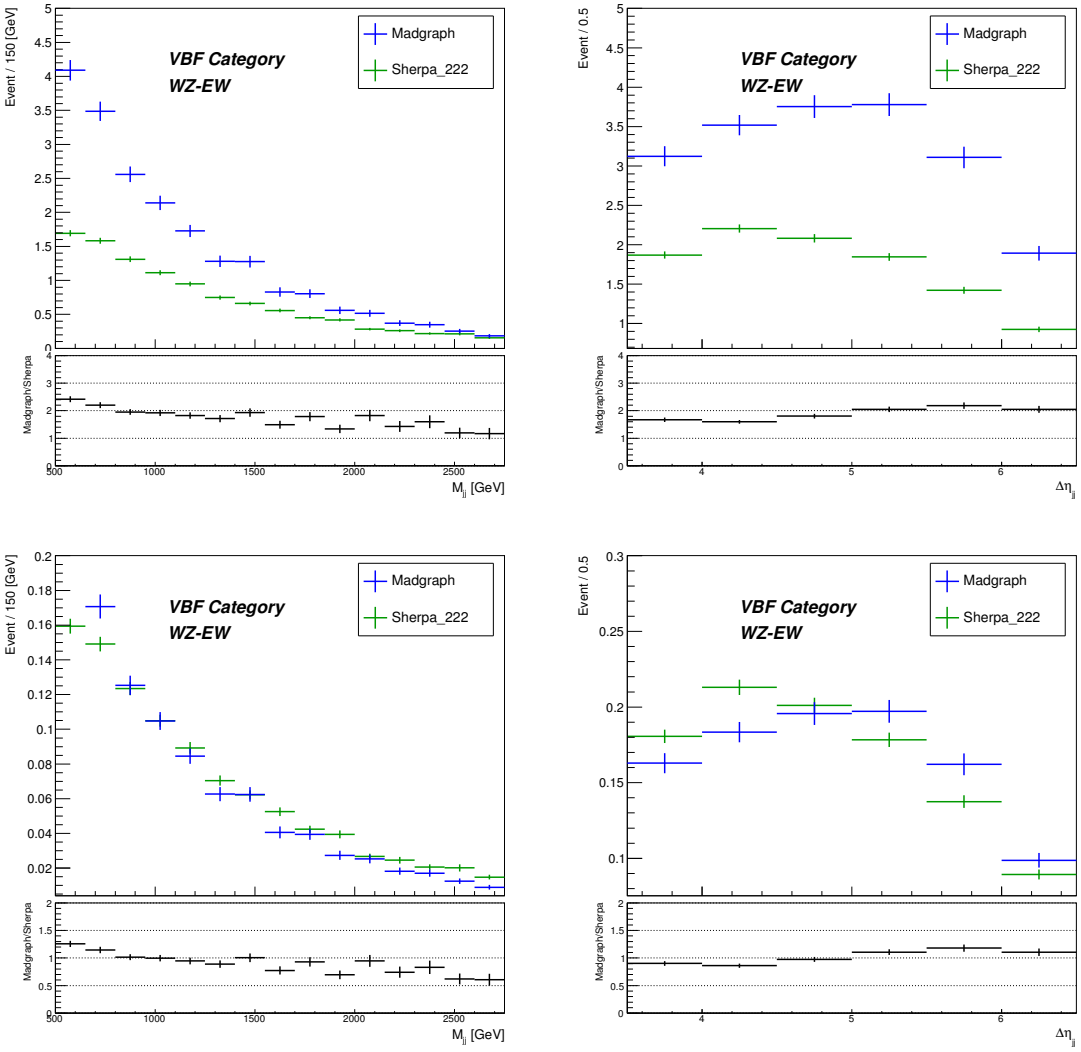


FIGURE B.2: ***Comparison of the m_{jj} and $\Delta\eta_{jj}$ distributions normalized to the cross section (top) and to the unit (bottom) in the VBF SR of the WZ EW MC samples. MadGraph (Blue) and Sherpa2.2.2 (Green).***

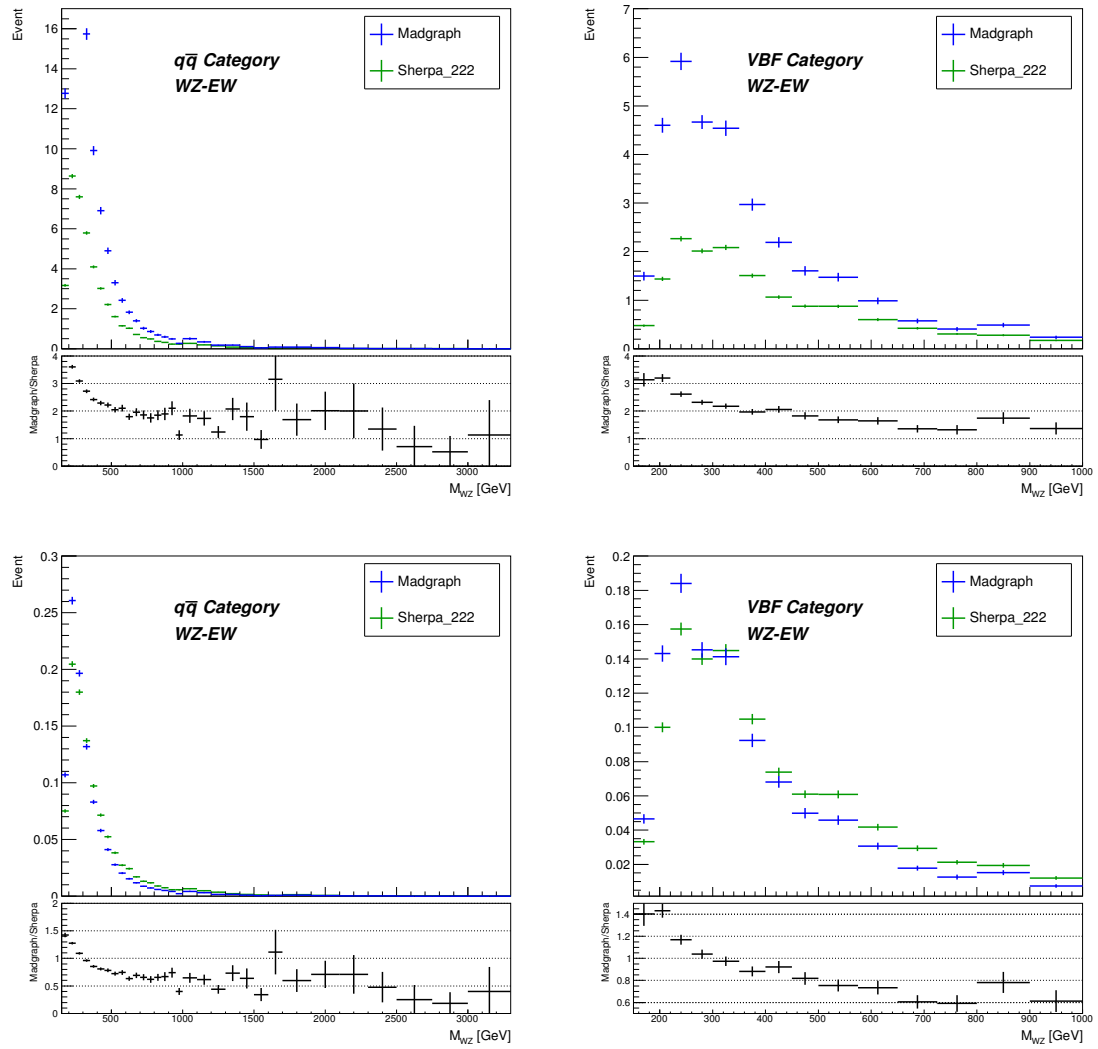


FIGURE B.3: ***Comparison of the m_{WZ} distributions normalized to the cross section (top) and to the unit (bottom) in the $q\bar{q}$ CR and VBF CR of the WZ EW MC samples. MadGraph (Blue) and Sherpa2.2.2 (Green).***

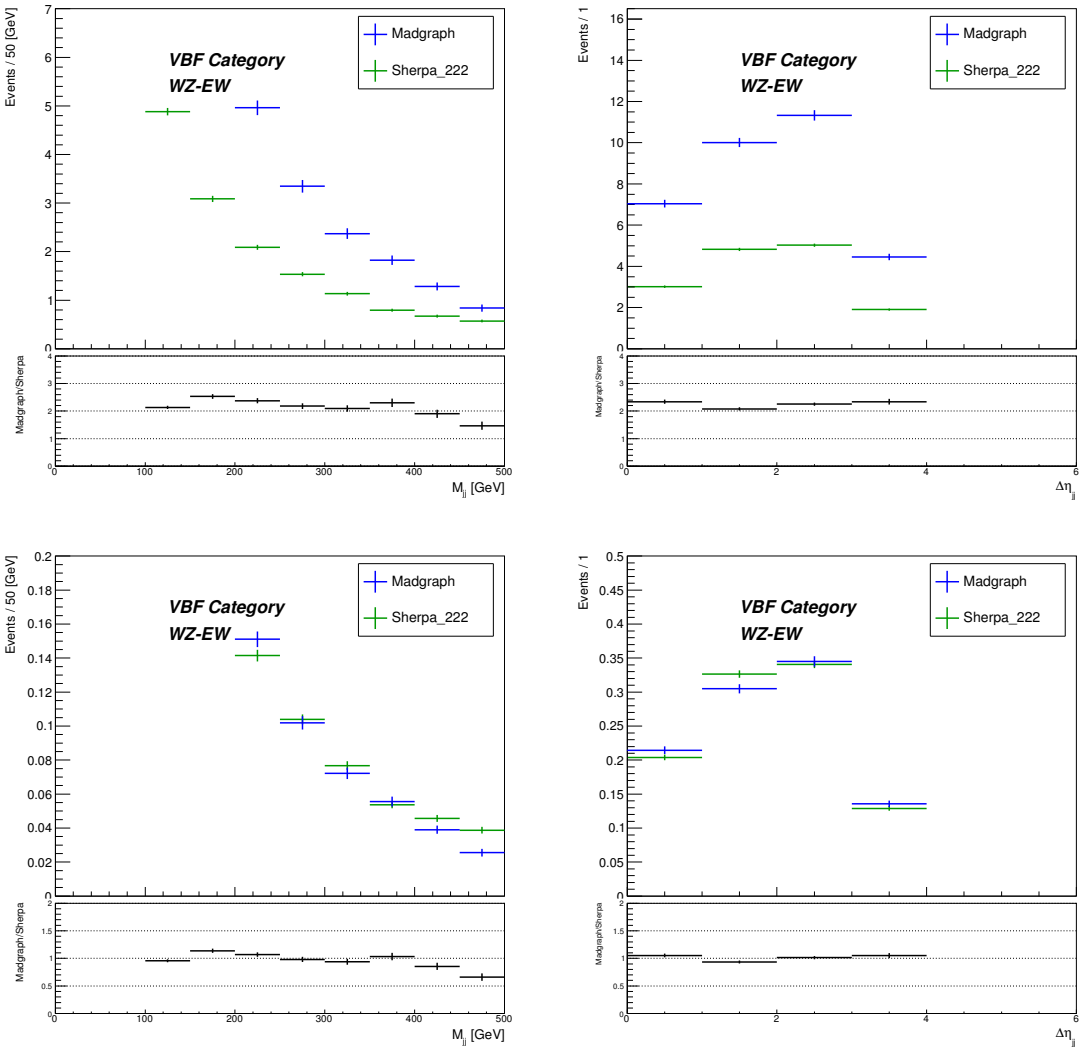


FIGURE B.4: ***Comparison of the m_{jj} and $\Delta\eta_{jj}$ distributions normalized to the cross section (top) and to the unit (bottom) in the VBF CR of the WZ EW MC samples. MadGraph (Blue) and Sherpa2.2.2 (Green).***

Appendix C

Systematic uncertainties for the total background for $q\bar{q}$ SR

Figures C.2, C.3, C.4, C.5, C.6, and C.1, show muons, electrons, missing energy, jets and pile-up reweighing systematic uncertainties from the workspace for the total background for $q\bar{q}$ SR.

C.1 Pileup Systematic uncertainties

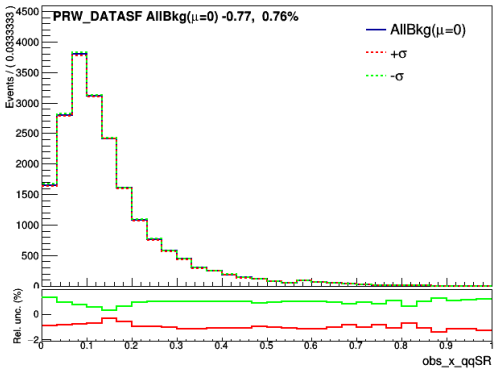


FIGURE C.1: ***Pileup systematic uncertainties from the workspace for the total background for $q\bar{q}$ SR.***

C.2 Muon Systematic uncertainties

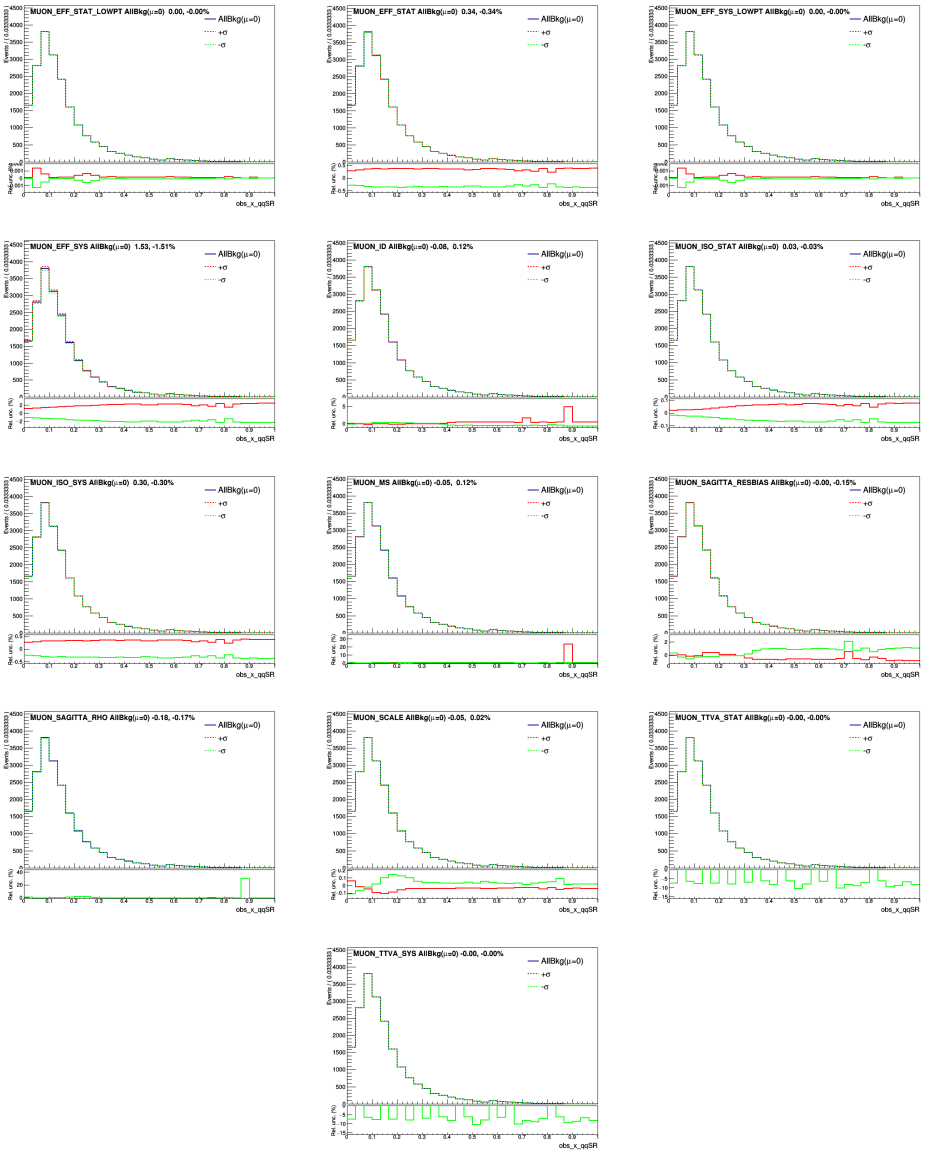


FIGURE C.2: ***Muons systematic uncertainties from the workspace for the total background for $q\bar{q}$ SR.***

C.3 Electron Systematic uncertainties

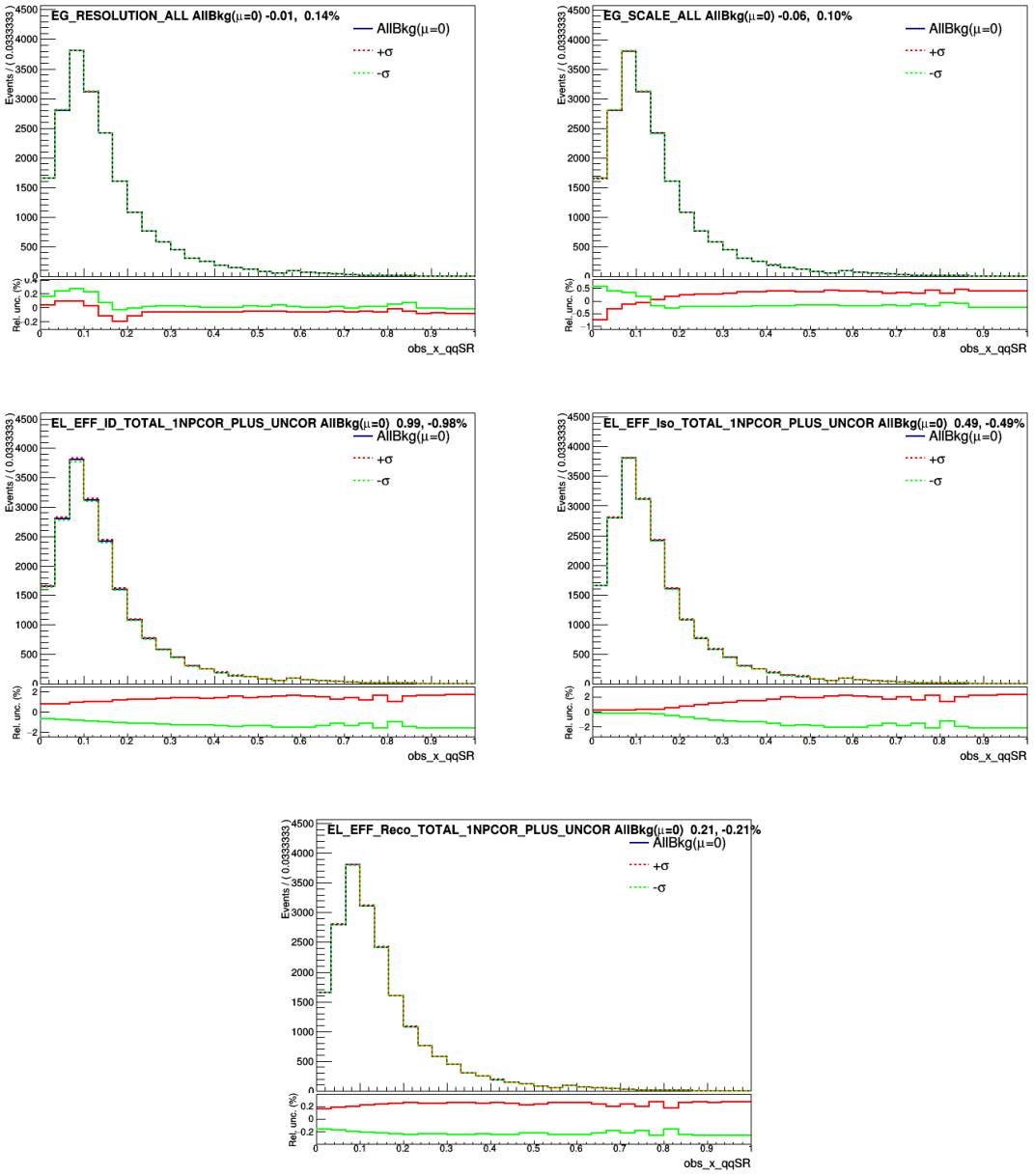


FIGURE C.3: ***Electrons systematic uncertainties from the workspace for the total background for $q\bar{q}$ SR.***

C.4 Jet Systematic uncertainties

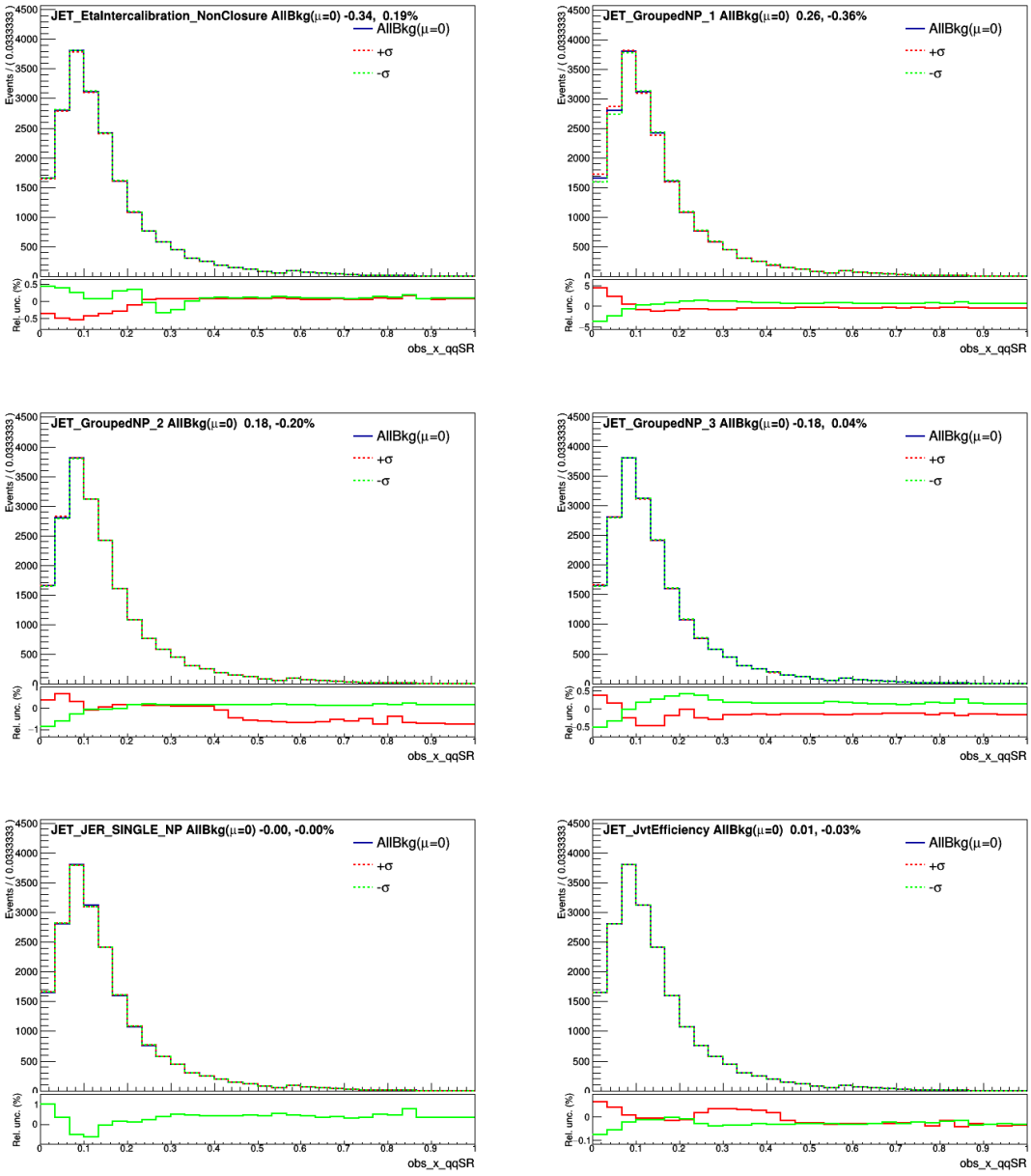


FIGURE C.4: ***Jets systematic uncertainties from the workspace for the total background for $q\bar{q}$ SR.***

C.5 Missing transverse energy Systematic uncertainties

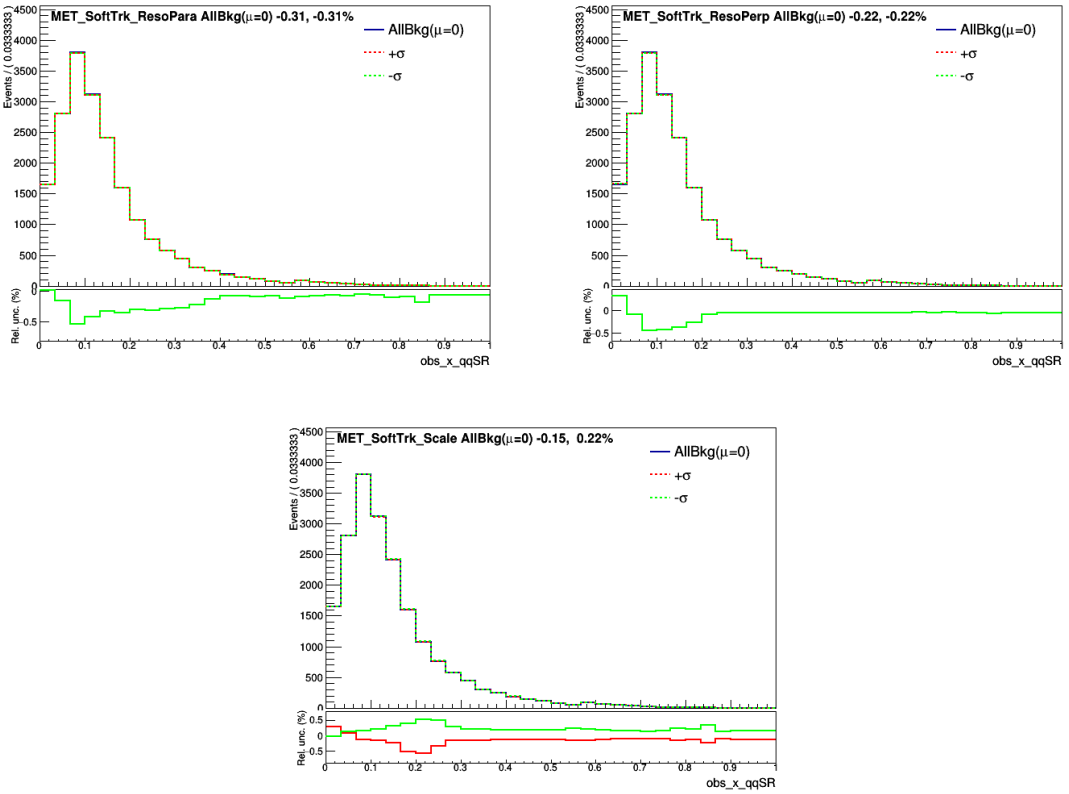
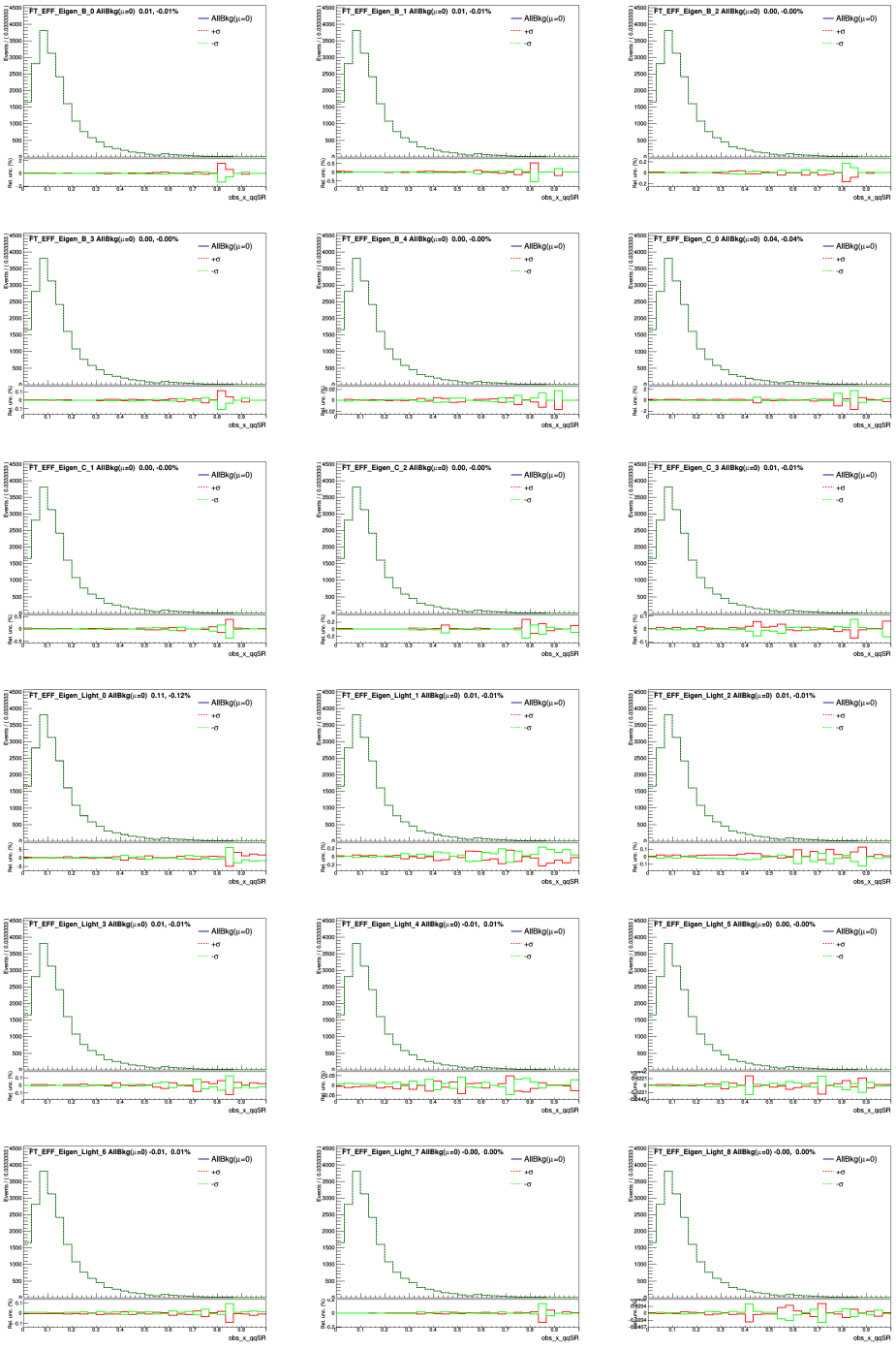


FIGURE C.5: ***MET systematic uncertainties from the workspace for the total background for $q\bar{q}$ SR..***

C.6 B-tagging Systematic uncertainties



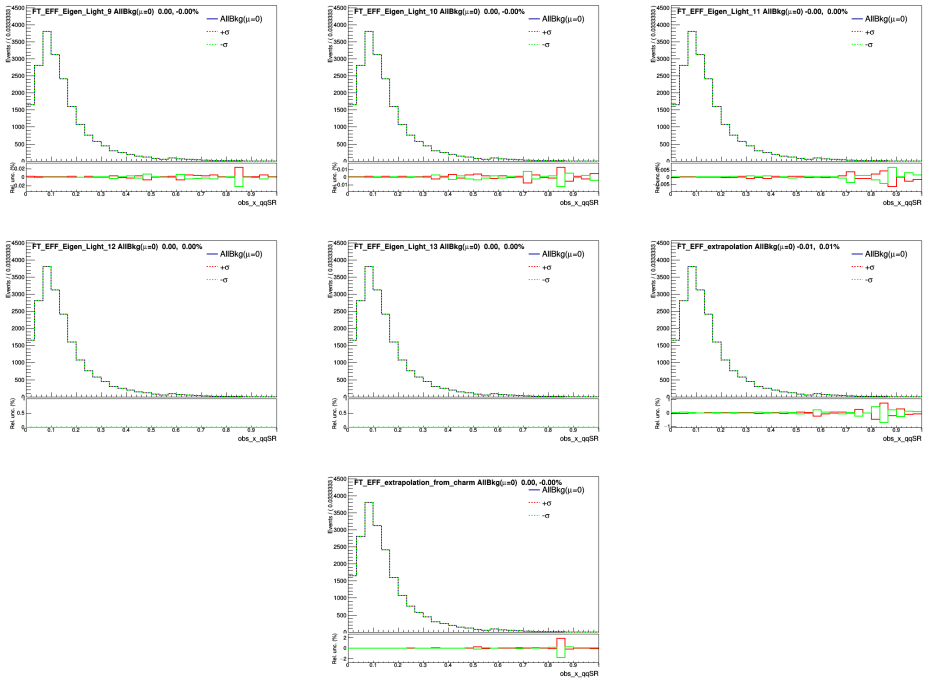


FIGURE C.6: ***b-tagging systematic uncertainties from the workspace for the total background for $q\bar{q}$ SR.***

Résumé détaillé

Le grand collisionneur d'hadrons (LHC) est la machine la plus puissante jamais construite par l'humanité pour explorer les forces fondamentales de la nature. Après des années de conception et de construction, le LHC a commencé ses premières collisions proton-proton à très haute énergie depuis 2009. Les données collectées ont permis aux collaborations ATLAS et CMS de réaliser en 2012 un triomphe historique. Ces deux collaborations ont annoncé la découverte du boson de Higgs à 125 GeV à partir de ses désintégrations en paires de photons, Z et W. Cette découverte complète le modèle standard de la physique des particules et justifie le prix Nobel 2013 décerné à Peter Higgs et à François Englert pour la découverte théorique d'un mécanisme qui contribue à notre compréhension de l'origine de la masse des particules élémentaires.

Malgré son énorme succès, le modèle standard laisse de nombreuses questions fondamentales sans réponse. Parmi ces questions, l'interaction gravitationnelle, ignorée par le modèle standard dans la description des interactions fondamentales. Toutefois, ce modèle n'est pas une théorie unifiée pour les trois interactions décrites. Un autre problème majeur lié à l'origine de la matière noire et de l'énergie sombre, constituant près de 95% de la densité énergétique de l'Univers, reste totalement inexplicable par le modèle standard des particules.

De nombreux arguments suggèrent que ce modèle n'est qu'une théorie spécifique d'un modèle plus fondamental se manifestant à une énergie plus élevée. Face à ces lacunes, de nombreuses théories ont été développées pour étendre le modèle standard et proposer une explication théorique à ces phénomènes. Parmi ces théories, certaines prédisent de nouvelles résonances de particules vecteurs fortement couplées aux paires de bosons WZ. Jusqu'à présent, aucune de ces théories n'a encore été confirmée, c'est dans ce contexte que le LHC a été conçu. En mettant en collision des protons à une énergie élevée avec une haute luminosité, cet accélérateur puissant permet de sonder la matière à de nouvelles échelles et de tester de manière approfondie le modèle standard.

Le travail présenté dans cette thèse a été réalisé dans le cadre de la collaboration ATLAS et porte sur deux thèmes principaux. Le premier concerne une mise à niveau du calorimètre à l'avant (FCal) d'ATLAS à haute luminosité prévue pour le HL-LHC. La seconde est entièrement dédiée à la recherche des résonances des paires WZ se désintégrant dans les canaux leptoniques.

Concernant la première partie, pour le programme de la mise à niveau du FCal, afin de réduire l'impact de la luminosité instantanée très élevée au LHC de phase-II, un nouveau calorimètre (sFCal) a été étudié et caractérisé par une granularité fine due à l'étroitesse de ses cellules de détection. Le chauffage du FCal par l'irradiation élevée pourrait entraîner la formation de bulles d'argon dans le détecteur et le taux d'ionisation entraînerait des effets de charges d'espace réduisant le signal, ce qui se traduirait par une chute de tension dans les résistances. En collaboration avec le groupe de physique des particules de l'institut royal de technologie de Stockholm, nous avons effectué l'étude du super-Calorimètre à l'avant (sFCal) en tant que proposition de remplacement du FCal à haute luminosité du LHC. En se basant sur la simulation de FCal et sFCal, l'impact d'une granularité de lecture plus fine sur la résolution en énergie et spatiale dans la région de *eta* élevé est évalué pour les électrons et les pions.

La seconde partie de cette thèse est réalisée en collaboration avec le groupe ATLAS du CEA de Saclay en cherchant des résonances se désintégrant en paires de bosons WZ dans les canaux leptoniques. L'étude a été évaluée en utilisant des données collectées par l'expérience ATLAS au CERN au cours des périodes 2015-2016 avec une luminosité intégrée de 36,1 fb $^{-1}$ correspondant à des collisions proton-proton à $s =$ *sqrt*13 TeV d'énergie de centre de masse. Des limites supérieures du rapport de section efficace de la production de WZ multiplié par le taux d'embranchement d'une particule vecteur lourde produite soit par fusion entre quark et antiquark (*q barq*), soit par fusion entre bosons vecteurs (VBF) ont été calculées. Des contraintes sont également obtenues sur la masse et les couplages d'un boson de Higgs chargé dans le modèle théorique de textsc Georgi-Machacek, produit par fusion des bosons vecteurs. Ces limites sont compétitives pour les faibles masses par rapport aux autres analyses sur les recherches des résonances dans la voie bosonique.

Cette thèse est composée de cinq chapitres. Le premier chapitre traite le modèle standard de la physique des particules, en se focalisant sur l'interaction électrofaible mettant l'accent sur la brisure spontanée de la symétrie et du mécanisme de *Higgs* générant la masse des bosons de W et de Z impliqués dans cette analyse. Les modes de production de WZ dans le LHC ainsi que les modèles de la physique au-delà du modèle standard utilisés pour interpréter les résultats sont également exposés dans ce chapitre. Le deuxième chapitre décrit brièvement le grand collisionneur d'hadrons et l'expérience ATLAS avec ses sous-détecteurs ainsi que le centre de calcul d'ATLAS. Le troisième chapitre est consacré à l'étude des performances du super calorimètre à l'avant ($sFCal$) simulé en tant que proposition pour le remplacement du calorimètre à l'avant d'ATLAS (FCal) à haute luminosité, en examinant deux méthodes différentes pour corriger la résolution spatial. La reconstruction des objets physiques impliqués dans cette analyse est présentée dans le quatrième chapitre, elle comprend des critères de sélection et l'identification des électrons, des muons, des jets et de l'énergie transverse manquante associée aux neutrinos. Finalement, les résultats de la

recherche des résonances qui se désintègrent en paire de bosons WZ sont présentés dans le dernier chapitre

Les résultats obtenus montrent que la résolution en énergie pour les électrons et les pions est légèrement dégradée dans le sFCal que dans le FCal en raison de la fraction d'échantillonnage qui donne une augmentation du terme constant dans le sFCal d'un facteur de 1,12 pour les électrons et de 1,03 pour les pions. De plus, les résultats montrent que la méthode logarithmique fournit les meilleures corrections par rapport à l'interpolation linéaire en termes de la résolution en position pour les deux calorimètres, on outre le sFCal dispose d'une résolution spatiale plus fine. Malgré les améliorations potentielles de la performance du $sFCal$, le remplacement du $FCal$ a été rejeté sur la base des résultats de l'analyse de risque, due à l'installation du nouveau $sFCal$ nécessitant l'ouverture du cryostat qui risque de perdre de l'argon liquide en cas de fuite dans l'espace sous vide, conduisant à la destruction de l'isolation thermique.

Le deuxième aspect de ce travail est dédié à la recherche des résonances WZ dont les états finaux sont entièrement leptoniques, et produits dans les modes de l'annulation de quark antiquark et la fusion des Bosons vecteurs. Pour les deux modes de production, le bruit de fond dominant est estimé à partir de la simulation du détecteur ATLAS en utilisant Monte-Carlo, tandis que les bruit de fonds comportant un ou deux faux leptons sont évalués à l'aide d'une méthode matricielle nommée Matrix Méthode. Les données collectées par le détecteur ATLAS passant la sélection d'événements dans cette analyse sont en bon accord avec les données simulées à l'intérieure de leurs incertitudes pour les deux catégories ($q\,barq$ et VBF). Les résultats pour $q\,barq$ annulation sont interprétés dans le contexte du modèle A et du modèle B des vecteurs triplets lourds (HVT), sur lesquels la limite supérieure est extraite dans un intervalle de confiance de 95%. Aucune déviation significative par rapport aux prévisions du modèle standard n'était observée. Les masses inférieures à 2260 GeV peuvent être exclues pour le modèle A et 2460 GeV pour le modèle B. En ce qui concerne le mode de production VBF, des excès locaux par rapport à la prédiction du SM sont observés à une masse de résonance autour de 450 GeV pour les deux modèles théoriques HVT, et Georgi-Machacek, avec des écarts-types locaux de 2.9 et 3.1 pour les signaux ${H_5}^{pm}$ et W' respectivement.

Comme perspective pour cette étude, on peut continuer à étudier la recherche de résonance WZ avec la nouvelle luminosité fournie par le LHC en 2017 et 2018 avec plus de précision. De nombreuses améliorations sont à prévoir pour les nouvelles données collectées avec des approches d'analyse plus développées, cela aurait des implications importantes pour notre compréhension de l'univers.

Bibliography

[1] Howard Georgi and Marie Machacek. "DOUBLY CHARGED HIGGS BOSONS". In: *Nucl. Phys.* B262 (1985), pp. 463–477. DOI: 10.1016/0550-3213(85)90325-6.

[2] Michael S. Chanowitz and Mitchell Golden. "Higgs Boson Triplets With M (W) = M (Z) cos $\theta\omega$". In: *Phys. Lett.* B165 (1985), pp. 105–108. DOI: 10.1016/0370-2693(85)90700-2.

[3] J. de Blas, J. M. Lizana, and M. Perez-Victoria. "Combining searches of Z' and W' bosons". In: *JHEP* 01 (2013), p. 166. DOI: 10.1007/JHEP01(2013)166. arXiv: 1211.2229 [hep-ph].

[4] Duccio Pappadopulo et al. "Heavy Vector Triplets: Bridging Theory and Data". In: (2014). arXiv: 1402.4431 [hep-ph].

[5] Isobel Falconer. "J J Thomson and the discovery of the electron". In: *Physics Education* 32.4 (1997), p. 226. URL: http://stacks.iop.org/0031-9120/32/i=4/a=015.

[6] Professor E. Rutherford F.R.S. "LXXIX. The scattering of α and β particles by matter and the structure of the atom". In: *The London, Edinburgh, and Dublin Philosophical Magazine and Journal of Science* 21.125 (1911), pp. 669–688. DOI: 10.1080/14786440508637080. eprint: https://doi.org/10.1080/14786440508637080. URL: https://doi.org/10.1080/14786440508637080.

[7] Jean Alexandre et al. "Gauge invariance and the Englert-Brout-Higgs mechanism in non-Hermitian field theories". In: (2018). arXiv: 1808.00944 [hep-th].

[8] Samoil M. Bilenky and J. Hosek. "GLASHOW-WEINBERG-SALAM THEORY OF ELECTROWEAK INTERACTIONS AND THE NEUTRAL CURRENTS". In: *Phys. Rept.* 90 (1982), pp. 73–157. DOI: 10.1016/0370-1573(82)90016-3.

[9] Maria J. Herrero and Ester Ruiz Morales. "The electroweak chiral lagrangian for the standard model with a heavy Higgs". In: *Nuclear Physics B* 418.3 (1994), pp. 431–455. ISSN: 0550-3213. DOI: https://doi.org/10.1016/0550-3213(94)90525-8. URL: http://www.sciencedirect.com/science/article/pii/0550321394905258.

[10] Joseph Kouneiher and Burra G. Sidharth. "Mass Generation Without the Higgs Mechanism". In: *Int. J. Theor. Phys.* 54.9 (2015), pp. 3044–3082. DOI: 10.1007/s10773-015-2542-1.

[11] John Ellis. "Higgs Physics". In: arXiv:1312.5672. KCL-PH-TH-2013-49. LCTS-2013-36. CERN-PH-TH-2013-315 (2013). 52 pages, 45 figures, Lectures presented at the ESHEP 2013 School of High-Energy Physics, to appear as part of the proceedings in a CERN Yellow Report, 117–168. 52 p. URL: https://cds.cern.ch/record/1638469.

[12] *Measurement of the effective leptonic weak mixing angle using electron and muon pairs from Z-boson decay in the ATLAS experiment at* $\sqrt{s} = 8$ *TeV*. Tech. rep. ATLAS-CONF-2018-037. Geneva: CERN, 2018. URL: http://cds.cern.ch/record/2630340.

[13] Georges Aad et al. "Observation of a new particle in the search for the Standard Model Higgs boson with the ATLAS detector at the LHC". In: *Phys. Lett.* B716 (2012), pp. 1–29. DOI: 10.1016/j.physletb.2012.08.020. arXiv: 1207.7214 [hep-ex].

[14] Serguei Chatrchyan et al. "Observation of a new boson at a mass of 125 GeV with the CMS experiment at the LHC". In: *Phys. Lett.* B716 (2012), pp. 30–61. DOI: 10.1016/j.physletb.2012.08.021. arXiv: 1207.7235 [hep-ex].

[15] *Measurement of* $W^{\pm}Z$ *production cross sections and gauge boson polarisation in pp collisions at* $\sqrt{s} = 13$ *TeV with the ATLAS detector*. Tech. rep. ATLAS-CONF-2018-034. Geneva: CERN, 2018. URL: https://cds.cern.ch/record/2630187.

[16] *Measurements of the* pp $\rightarrow$ WZ *inclusive and differential production cross section and constraints on charged anomalous triple gauge couplings at* $\sqrt{s} = 13$ TeV. Tech. rep. CMS-PAS-SMP-18-002. Geneva: CERN, 2018. URL: https://cds.cern.ch/record/2628761.

[17] Barry R. Holstein. "Graviton Physics". In: *Am. J. Phys.* 74 (2006), pp. 1002–1011. DOI: 10.1119/1.2338547. arXiv: gr-qc/0607045 [gr-qc].

[18] Thomas Grégoire, Heather E. Logan, and Bob McElrath. "Little Higgs models". In: *Workshop on CP Studies and Non-Standard Higgs Physics*. CERN. CERN, 2006, pp. 297–348. DOI: 10.5170/CERN-2006-009.297.

[19] Duccio Pappadopulo et al. "Heavy vector triplets: bridging theory and data". In: *Journal of High Energy Physics* 2014.9 (2014), p. 60. ISSN: 1029-8479. DOI: 10.1007/JHEP09(2014)060. URL: https://doi.org/10.1007/JHEP09(2014)060.

[20] Howard Georgi and Marie Machacek. "Doubly charged Higgs bosons". In: *Nuclear Physics B* 262.3 (1985), pp. 463 –477. ISSN: 0550-3213. DOI: https://doi.org/10.1016/0550-3213(85)90325-6. URL: http://www.sciencedirect.com/science/article/pii/0550321385903256.

[21] Oliver S. Bruning et al. "LHC Design Report Vol.1: The LHC Main Ring". In: (2004).

[22] The ATLAS Collaboration. "The ATLAS Experiment at the CERN Large Hadron Collider". In: *Journal of Instrumentation* 3.08 (2008), S08003. URL: http://stacks.iop.org/1748-0221/3/i=08/a=S08003.

[23] The ALICE Collaboration et al. "The ALICE experiment at the CERN LHC". In: *Journal of Instrumentation* 3.08 (2008), S08002. URL: http://stacks.iop.org/1748-0221/3/i=08/a=S08002.

[24] The CMS Collaboration et al. "The CMS experiment at the CERN LHC". In: *Journal of Instrumentation* 3.08 (2008), S08004. URL: http://stacks.iop.org/1748-0221/3/i=08/a=S08004.

[25] The LHCb Collaboration et al. "The LHCb Detector at the LHC". In: *Journal of Instrumentation* 3.08 (2008), S08005. URL: http://stacks.iop.org/1748-0221/3/i=08/a=S08005.

[26] "Linear accelerator 2". In: (2012). URL: https://cds.cern.ch/record/1997427.

[27] "The Proton Synchrotron Booster". In: (2012). URL: https://cds.cern.ch/record/1997372.

[28] "The Proton Synchrotron". In: (2012). URL: https://cds.cern.ch/record/1997189.

[29] "The Super Proton Synchrotron". In: (2012). URL: https://cds.cern.ch/record/1997188.

[30] Christiane Lefèvre. "The CERN accelerator complex. Complexe des accélérateurs du CERN". 2008. URL: https://cds.cern.ch/record/1260465.

[31] M Bajko et al. *Report of the Task Force on the Incident of 19th September 2008 at the LHC*. Tech. rep. LHC-PROJECT-Report-1168. CERN-LHC-PROJECT-Report-1168. Geneva: CERN, 2009. URL: http://cds.cern.ch/record/1168025.

[32] Lyndon Evans and Philip Bryant. "LHC Machine". In: *Journal of Instrumentation* 3.08 (2008), S08001. URL: http://stacks.iop.org/1748-0221/3/i=08/a=S08001.

[33] R. Bruce et al. "Reaching record-low β^* at the CERN Large Hadron Collider using a novel scheme of collimator settings and optics". In: *Nuclear Instruments and Methods in Physics Research Section A: Accelerators, Spectrometers, Detectors and Associated Equipment* 848 (2017), pp. 19 –30. ISSN: 0168-9002. DOI: https://doi.org/10.1016/j.nima.2016.12.039. URL: http://www.sciencedirect.com/science/article/pii/S0168900216313092.

[34] by Rende Steerenberg and Anais Schaeffer. "LHC Report: Running towards a production break". In: (2018). URL: http://cds.cern.ch/record/2621210.

[35] G. Aad et al. "The ATLAS Simulation Infrastructure. The ATLAS Simulation Infrastructure". In: *Eur. Phys. J. C* 70.arXiv:1005.4568. CERN-PH-EP-2010-044 (2010). Submitted to Eur. Phys. J. C, 823–874. 53 p. URL: https://cds.cern.ch/record/1267853.

[36] S Haywood et al. *ATLAS inner detector: Technical Design Report, 2*. Technical Design Report ATLAS. Geneva: CERN, 1997. URL: https://cds.cern.ch/record/331064.

[37] In: ().

[38] A Vogel. *ATLAS Transition Radiation Tracker (TRT): Straw Tube Gaseous Detectors at High Rates*. Tech. rep. ATL-INDET-PROC-2013-005. Geneva: CERN, 2013. URL: https://cds.cern.ch/record/1537991.

[39] Francesco Poppi. "The Colliderscope: a real-time show. Le Colliderscope, spectacle en temps réel". In: BUL-NA-2010-010. 04/2010 (2010), p. 7. URL: https://cds.cern.ch/record/1234569.

[40] Norbert Wermes and G Hallewel. *ATLAS pixel detector: Technical Design Report*. Technical Design Report ATLAS. Geneva: CERN, 1998. URL: https://cds.cern.ch/record/381263.

[41] *ATLAS Insertable B-Layer Technical Design Report Addendum*. Tech. rep. CERN-LHCC-2012-009. ATLAS-TDR-19-ADD-1. Addendum to CERN-LHCC-2010-013, ATLAS-TDR-019. 2012. URL: https://cds.cern.ch/record/1451888.

[42] The ATLAS collaboration. "Operation and performance of the ATLAS semiconductor tracker". In: *Journal of Instrumentation* 9.08 (2014), P08009. URL: http://stacks.iop.org/1748-0221/9/i=08/a=P08009.

[43] Marija Marjanovic. *ATLAS Tile calorimeter calibration and monitoring systems*. Tech. rep. arXiv:1806.09156. 8 pages, 21 figures, IEEE Real Time 2018 proceedings. 2018. URL: https://cds.cern.ch/record/2629424.

[44] *ATLAS liquid-argon calorimeter: Technical Design Report*. Technical Design Report ATLAS. Geneva: CERN, 1996. URL: http://cds.cern.ch/record/331061.

[45] In: ().

[46] *ATLAS muon spectrometer: Technical Design Report*. Technical Design Report ATLAS. Geneva: CERN, 1997. URL: https://cds.cern.ch/record/331068.

[47] F. Bauer et al. "Construction and Test of MDT Chambers for the ATLAS Muon Spectrometer". In: *Nucl. Instrum. Meth.* A461 (2001), pp. 17–20. DOI: 10.1016/S0168-9002(00)01156-6. arXiv: 1604.02000 [physics.ins-det].

[48] Theodoros Argyropoulos et al. "Cathode strip chambers in ATLAS: Installation, commissioning and in situ performance". In: *IEEE Trans. Nucl. Sci.* 56 (2009), pp. 1568–1574. DOI: 10.1109/TNS.2009.2020861.

[49] G. Aad et al. "Commissioning of the ATLAS Muon Spectrometer with Cosmic Rays. Commissioning of the ATLAS Muon Spectrometer with Cosmic Rays". In: *Eur. Phys. J. C* 70.arXiv:1006.4384. CERN-PH-EP-2010-045 (2010), 875–916. 58 p. URL: https://cds.cern.ch/record/1275998.

[50] G Cattani. "Performance of the ATLAS Resistive Plate Chambers". In: (2010). URL: http://cds.cern.ch/record/1243766.

[51] Koichi Nagai. "Thin gap chambers in ATLAS". In: *Nuclear Instruments and Methods in Physics Research Section A: Accelerators, Spectrometers, Detectors and Associated Equipment* 384.1 (1996). BEAUTY '96, pp. 219 –221. ISSN: 0168-9002. DOI: https://doi.org/10.1016/S0168-9002(96)01065-0. URL: http://www.sciencedirect.com/science/article/pii/S0168900296010650.

[52] *ATLAS magnet system: Technical Design Report, 1*. Technical Design Report ATLAS. Geneva: CERN, 1997. URL: https://cds.cern.ch/record/338080.

[53] Aranzazu Ruiz-Martinez and ATLAS Collaboration. *The Run-2 ATLAS Trigger System*. Tech. rep. ATL-DAQ-PROC-2016-003. Geneva: CERN, 2016. URL: https://cds.cern.ch/record/2133909.

[54] Thomas Schoerner-Sadenius. "The Trigger of the ATLAS Experiment. The trigger of the ATLAS experiment." In: *Mod. Phys. Lett. A* 18.hep-ex/0307078 (2003). Comments: 21 pages, 11 figures, submitted to Mod. Phys. Lett. A, 2149–2168. 21 p. URL: http://cds.cern.ch/record/630658.

[55] Fernando Harald Barreiro Megino et al. "Operation of the ATLAS distributed computing". In: (2018). URL: https://cds.cern.ch/record/2626049.

[56] Jamie Shiers. "The Worldwide LHC Computing Grid (worldwide LCG)". In: *Computer Physics Communications* 177.1 (2007). Proceedings of the Conference on Computational Physics 2006, pp. 219 –223. ISSN: 0010-4655. DOI: https://doi.org/10.1016/j.cpc.2007.02.021. URL: http://www.sciencedirect.com/science/article/pii/S001046550700077X.

[57] P Nilsson et al. "The ATLAS PanDA Pilot in Operation". In: *Journal of Physics: Conference Series* 331.6 (2011), p. 062040. DOI: 10.1088/1742-6596/331/6/062040.

[58] V Garonne et al. "Rucio – The next generation of large scale distributed system for ATLAS Data Management". In: *Journal of Physics: Conference Series* 513.4 (2014), p. 042021. DOI: 10.1088/1742-6596/513/4/042021.

[59] R. Brun and F. Rademakers. "ROOT: An object oriented data analysis framework". In: *Nucl. Instrum. Meth.* A389 (1997), pp. 81–86. DOI: 10.1016/S0168-9002(97)00048-X.

[60] Andreas J Peters and Lukasz Janyst. "Exabyte Scale Storage at CERN". In: *Journal of Physics: Conference Series* 331.5 (2011), p. 052015. DOI: 10.1088/1742-6596/331/5/052015.

[61] E Martelli and S Stancu. "LHCOPN and LHCONE: Status and Future Evolution". In: *Journal of Physics: Conference Series* 664.5 (2015), p. 052025. DOI: 10.1088/1742-6596/664/5/052025.

[62] Derek Weitzel et al. "Accessing Data Federations with CVMFS". In: *Journal of Physics: Conference Series* 898 (2017), p. 062044. DOI: 10.1088/1742-6596/898/6/062044.

[63] A Buckley et al. "Implementation of the ATLAS Run 2 event data model". In: *Journal of Physics: Conference Series* 664.7 (2015), p. 072045. DOI: 10.1088/1742-6596/664/7/072045.

[64] *ATLAS Phase-II Upgrade Scoping Document*. Tech. rep. CERN-LHCC-2015-020. LHCC-G-166. Geneva: CERN, 2015. URL: https://cds.cern.ch/record/2055248.

[65] *ATLAS liquid-argon calorimeter: Technical Design Report*. Technical Design Report ATLAS. Geneva: CERN, 1996. URL: http://cds.cern.ch/record/331061.

[66] J P Archambault et al. "Energy calibration of the ATLAS Liquid Argon Forward Calorimeter". In: *Journal of Instrumentation* 3.02 (2008), P02002. URL: http://stacks.iop.org/1748-0221/3/i=02/a=P02002.

[67] A. Artamonov et al. "The ATLAS forward calorimeters". In: *JINST* 3 (2008), P02010. DOI: 10.1088/1748-0221/3/02/P02010.

[68] S. Agostinelli et al. S. Agostinelli GEANT4 collaboration. "Geant4- a simulation toolkit". In: *Nuclear Instruments and Methods in Physics Research Section A: Accelerators, Spectrometers, Detectors and Associated Equipment* 506.3 (2003), pp. 250 –303. ISSN: 0168-9002. DOI: http://dx.doi.org/10.1016/S0168-9002(03)01368-8. URL: http://www.sciencedirect.com/science/article/pii/S0168900203013688.

[69] Rene Brun and Fons Rademakers. "ROOT- An object oriented data analysis framework". In: *Nuclear Instruments and Methods in Physics Research Section A: Accelerators, Spectrometers, Detectors and Associated Equipment* 389.1 (1997). New Computing Techniques in Physics Research V, pp. 81 –86. ISSN: 0168-9002. DOI: http://dx.doi.org/10.1016/S0168-9002(97)00048-X. URL: http://www.sciencedirect.com/science/article/pii/S016890029700048X.

[70] J P Archambault et al. "Performance of the ATLAS liquid argon forward calorimeter in beam tests". In: *Journal of Instrumentation* 8.05 (2013), P05006. URL: http://stacks.iop.org/1748-0221/8/i=05/a=P05006.

[71] R Sacco. *Position resolution of an ATLAS electromagnetic calorimeter module*. Tech. rep. ATL-LARG-2003-008. Geneva: CERN, 2003. URL: http://cds.cern.ch/record/685537.

[72] W Lampl et al. *Calorimeter Clustering Algorithms: Description and Performance*. Tech. rep. ATL-LARG-PUB-2008-002. ATL-COM-LARG-2008-003. Geneva: CERN, 2008. URL: http://cds.cern.ch/record/1099735.

[73] W. Lampl et al. "Calorimeter clustering algorithms: Description and performance". In: (2008).

[74] *Improved electron reconstruction in ATLAS using the Gaussian Sum Filter-based model for bremsstrahlung*. Tech. rep. ATLAS-CONF-2012-047. Geneva: CERN, 2012. URL: http://cds.cern.ch/record/1449796.

[75] *Electron efficiency measurements with the ATLAS detector using the 2015 LHC proton-proton collision data*. Tech. rep. ATLAS-CONF-2016-024. Geneva: CERN, 2016. URL: https://cds.cern.ch/record/2157687.

[76] M. Aaboud et al. "Jet energy scale measurements and their systematic uncertainties in proton-proton collisions at $\sqrt{s} = 13$ TeV with the ATLAS detector". In: *Phys. Rev.* D96.7 (2017), p. 072002. DOI: 10.1103/PhysRevD.96.072002. arXiv: 1703.09665 [hep-ex].

[77] M. Aaboud et al. "Electron efficiency measurements with the ATLAS detector using 2012 LHC proton–proton collision data". In: *The European Physical Journal C* 77.3 (2017), p. 195. ISSN: 1434-6052. DOI: 10.1140/epjc/s10052-017-4756-2. URL: https://doi.org/10.1140/epjc/s10052-017-4756-2.

[78] S. Hassani et al. "A muon identification and combined reconstruction procedure for the ATLAS detector at the LHC using the (MUONBOY, STACO, MuTag) reconstruction packages". In: *Nucl. Instrum. Meth.* A572 (2007), pp. 77–79. DOI: 10.1016/j.nima.2006.10.340.

[79] B Resende. *Muon identification algorithms in ATLAS*. Tech. rep. ATL-PHYS-PROC-2009-113. Geneva: CERN, 2009. URL: https://cds.cern.ch/record/1209632.

[80] S. Hassani et al. "A muon identification and combined reconstruction procedure for the ATLAS detector at the LHC using the (MUONBOY, STACO, MuTag) reconstruction packages". In: *Nuclear Instruments and Methods in Physics Research Section A: Accelerators, Spectrometers, Detectors and Associated Equipment* 572.1 (2007). Frontier Detectors for Frontier Physics, pp. 77 –79. ISSN: 0168-9002. DOI: https:

//doi.org/10.1016/j.nima.2006.10.340. URL: http://www.sciencedirect.com/science/article/pii/S0168900206019863.

[81] Luigi Marchese. *Muon reconstruction performance of the ATLAS detector in 2016*. Tech. rep. ATL-PHYS-PROC-2017-246. Geneva: CERN, 2017. URL: http://cds.cern.ch/record/2292925.

[82] Arthur Lesage. *Muon reconstruction performance in ATLAS at Run 2*. Tech. rep. ATL-PHYS-PROC-2015-157. Geneva: CERN, 2015. URL: https://cds.cern.ch/record/2108896.

[83] Matteo Cacciari, Gavin P. Salam, and Gregory Soyez. "The anti- k t jet clustering algorithm". In: *Journal of High Energy Physics* 2008.04 (2008), p. 063. URL: http://stacks.iop.org/1126-6708/2008/i=04/a=063.

[84] G. Aad et al. "Topological cell clustering in the ATLAS calorimeters and its performance in LHC Run 1". In: *The European Physical Journal C* 77.7 (2017), p. 490. ISSN: 1434-6052. DOI: 10.1140/epjc/s10052-017-5004-5. URL: https://doi.org/10.1140/epjc/s10052-017-5004-5.

[85] Tancredi Carli, Klaus Rabbertz, and Steffen Schumann. "Studies of Quantum Chromodynamics at the LHC". In: *The Large Hadron Collider: Harvest of Run 1*. Ed. by Thomas Schörner-Sadenius. 2015, pp. 139–194. DOI: 10.1007/978-3-319-15001-7_5. arXiv: 1506.03239 [hep-ex]. URL: http://inspirehep.net/record/1375494/files/arXiv:1506.03239.pdf.

[86] *Jet-Based Event Cleaning*. URL: https://twiki.cern.ch/twiki/bin/view/AtlasProtected/HowToCleanJets2017.

[87] *Tagging and suppression of pileup jets with the ATLAS detector*. Tech. rep. ATLAS-CONF-2014-018. Geneva: CERN, 2014. URL: https://cds.cern.ch/record/1700870.

[88] *JVTCalibration*. URL: https://twiki.cern.ch/twiki/bin/viewauth/AtlasProtected/JVTCalibration.

[89] *Optimisation of the ATLAS b-tagging performance for the 2016 LHC Run*. Tech. rep. ATL-PHYS-PUB-2016-012. Geneva: CERN, 2016. URL: http://cds.cern.ch/record/2160731.

[90] Morad Aaboud et al. "Measurements of b-jet tagging efficiency with the ATLAS detector using $t\bar{t}$ events at $\sqrt{s} = 13$ TeV". In: (2018). arXiv: 1805.01845 [hep-ex].

[91] G. Aad et al. "Performance of algorithms that reconstruct missing transverse momentum in $\sqrt{s} = 8$ TeV proton-proton collisions in the ATLAS detector". In: *Eur. Phys. J.* C77.4 (2017), p. 241. DOI: 10.1140/epjc/s10052-017-4780-2. arXiv: 1609.09324 [hep-ex].

[92] *Usage of Missing ET in analyses: rebuilding and systematics.*

[93] Morad Aaboud et al. "Identification and rejection of pile-up jets at high pseudorapidity with the ATLAS detector". In: *Eur. Phys. J.* C77.9 (2017). [Erratum: Eur. Phys. J.C77,no.10,712(2017)], p. 580. DOI: 10.1140/epjc/s10052-017-5081-5,10.1140/epjc/s10052-017-5245-3. arXiv: 1705.02211 [hep-ex].

[94] D Adams et al. *Recommendations of the Physics Objects and Analysis Harmonisation Study Groups 2014*. Tech. rep. ATL-PHYS-INT-2014-018. Geneva: CERN, 2014. URL: https://cds.cern.ch/record/1743654.

[95] Paul Langacker, Richard W. Robinett, and Jonathan L. Rosner. "New Heavy Gauge Bosons in p p and p anti-p Collisions". In: *Phys. Rev.* D30 (1984), p. 1470. DOI: 10.1103/PhysRevD.30.1470.

[96] Christopher T. Hill and Elizabeth H. Simmons. "Strong dynamics and electroweak symmetry breaking". In: *Phys.Rept.* 381 (2003). erratum: ibid,390 (2004),553, pp. 235–402. DOI: 10.1016/S0370-1573(03)00140-6,10.1016/S0370-1573(03)00140-6. arXiv: hep-ph/0203079 [hep-ph].

[97] N. Arkani-Hamed et al. "The littlest Higgs". In: *JHEP* 07 (2002), p. 034. arXiv: hep-ph/0206021.

[98] Kenneth Lane and Stephen Mrenna. "The Collider phenomenology of technihadrons in the technicolor straw man model". In: *Phys. Rev.* D67 (2003), p. 115011. DOI: 10.1103/PhysRevD.67.115011. arXiv: hep-ph/0210299.

[99] Estia Eichten and Kenneth Lane. "Low-scale technicolor at the Tevatron and LHC". In: *Phys.Lett.* B669 (2008), pp. 235–238. DOI: 10.1016/j.physletb.2008.09.047. arXiv: 0706.2339 [hep-ph].

[100] Francesco Sannino and Kimmo Tuominen. "Orientifold theory dynamics and symmetry breaking". In: *Phys.Rev.* D71 (2005), p. 051901. DOI: 10.1103/PhysRevD.71.051901. arXiv: hep-ph/0405209 [hep-ph].

[101] Alexander Belyaev et al. "Technicolor Walks at the LHC". In: *Phys. Rev.* D79 (2009), p. 035006. DOI: 10.1103/PhysRevD.79.035006. arXiv: 0809.0793 [hep-ph].

[102] Kaustubh Agashe, Roberto Contino, and Alex Pomarol. "The Minimal composite Higgs model". In: *Nucl.Phys.* B719 (2005), pp. 165–187. DOI: 10.1016/j.nuclphysb.2005.04.035. arXiv: hep-ph/0412089 [hep-ph].

[103] G.F. Giudice et al. "The Strongly-Interacting Light Higgs". In: *JHEP* 0706 (2007), p. 045. DOI: 10.1088/1126-6708/2007/06/045. arXiv: hep-ph/0703164 [hep-ph].

[104] Lisa Randall and Raman Sundrum. "A large mass hierarchy from a small extra dimension". In: *Phys. Rev. Lett.* 83 (1999), pp. 3370–3373. DOI: 10.1103/PhysRevLett.83.3370. arXiv: hep-ph/9905221.

[105] H. Davoudiasl, J. L. Hewett, and T. G. Rizzo. "Bulk gauge fields in the Randall-Sundrum model". In: *Phys. Lett.* B473 (2000), pp. 43–49. DOI: 10.1016/S0370-2693(99)01430-6. arXiv: hep-ph/9911262.

[106] Csaba Csaki et al. "Gauge theories on an interval: Unitarity without a Higgs". In: *Phys.Rev.* D69 (2004), p. 055006. DOI: 10.1103/PhysRevD.69.055006. arXiv: hep-ph/0305237 [hep-ph].

[107] G. Aad et al. "The ATLAS Simulation Infrastructure". In: *The European Physical Journal C* 70.3 (2010), pp. 823–874. ISSN: 1434-6052. DOI: 10.1140/epjc/s10052-010-1429-9. URL: https://doi.org/10.1140/epjc/s10052-010-1429-9.

[108] PJ Laycock et al. "ATLAS data preparation in run 2". In: *Journal of Physics: Conference Series* 898.4 (2017), p. 042050. URL: http://stacks.iop.org/1742-6596/898/i=4/a=042050.

[109] URL: https://atlas-lumicalc.cern.ch/.

[110] Morad Aaboud et al. "Luminosity determination in pp collisions at $\sqrt{s} = 8$ TeV using the ATLAS detector at the LHC". In: *Eur. Phys. J.* C76.12 (2016), p. 653. DOI: 10.1140/epjc/s10052-016-4466-1. arXiv: 1608.03953 [hep-ex].

[111] Samuel David Jones. *The ATLAS Electron and Photon Trigger*. Tech. rep. ATL-DAQ-PROC-2017-040. Geneva: CERN, 2017. URL: https://cds.cern.ch/record/2290123.

[112] *Luminosity Public Results Run2*. URL: https://twiki.cern.ch/twiki/bin/view/AtlasPublic/LuminosityPublicResultsRun2.

[113] J. Alwall et al. "The automated computation of tree-level and next-to-leading order differential cross sections, and their matching to parton shower simulations". In: *Journal of High Energy Physics* 2014.7 (2014), p. 79. ISSN: 1029-8479. DOI: 10.1007/JHEP07(2014)079. URL: https://doi.org/10.1007/JHEP07(2014)079.

[114] Torbjörn Sjöstrand, Stephen Mrenna, and Peter Skands. "A brief introduction to PYTHIA 8.1". In: *Computer Physics Communications* 178.11 (2008), pp. 852 –867. ISSN: 0010-4655. DOI: https://doi.org/10.1016/j.cpc.2008.01.036. URL: http://www.sciencedirect.com/science/article/pii/S0010465508000441.

[115] Katy Hartling, Kunal Kumar, and Heather E. Logan. "GMCALC: a calculator for the Georgi-Machacek model". In: (2014). arXiv: 1412.7387 [hep-ph].

[116] Marco Zaro and Heather Logan. "Recommendations for the interpretation of LHC searches for H_5^0, $H_5^\pm$, and $H_5^{\pm\pm}$ in vector boson fusion with decays to vector boson pairs". In: (2015). URL: http://cds.cern.ch/record/2002500.

[117] D. de Florian et al. "Handbook of LHC Higgs Cross Sections: 4. Deciphering the Nature of the Higgs Sector". In: (2016). DOI: 10.23731/CYRM-2017-002. arXiv: 1610.07922 [hep-ph].

[118] T. Gleisberg et al. "Event generation with SHERPA 1.1". In: *Journal of High Energy Physics* 2009.02 (2009), p. 007. URL: http://stacks.iop.org/1126-6708/2009/i=02/a=007.

[119] Simone Alioli et al. "A general framework for implementing NLO calculations in shower Monte Carlo programs: the POWHEG BOX". In: *Journal of High Energy Physics* 2010.6 (2010), p. 43. ISSN: 1029-8479. DOI: 10.1007/JHEP06(2010)043. URL: https://doi.org/10.1007/JHEP06(2010)043.

[120] Mathias Brucherseifer, Fabrizio Caola, and Kirill Melnikov. "On the NNLO QCD corrections to single-top production at the LHC". In: *Physics Letters B* 736 (2014), pp. 58 –63. ISSN: 0370-2693. DOI: https://doi.org/10.1016/j.physletb.2014.06.075. URL: http://www.sciencedirect.com/science/article/pii/S0370269314004808.

[121] Jun Gao et al. "CT10 next-to-next-to-leading order global analysis of QCD". In: *Phys. Rev. D* 89 (3 2014), p. 033009. DOI: 10.1103/PhysRevD.89.033009. URL: https://link.aps.org/doi/10.1103/PhysRevD.89.033009.

[122] Torbjörn Sjöstrand, Stephen Mrenna, and Peter Skands. "PYTHIA 6.4 physics and manual". In: *Journal of High Energy Physics* 2006.05 (2006), p. 026. URL: http://stacks.iop.org/1126-6708/2006/i=05/a=026.

[123] Y Rozen. *Data-driven background estimation in ATLAS*. Tech. rep. ATL-PHYS-PROC-2013-023. Geneva: CERN, 2013. URL: http://cds.cern.ch/record/1510523.

[124] *Tile Trip Reader*. URL: https://twiki.cern.ch/twiki/bin/viewauth/Atlas/TileTripReader.

[125] The ATLAS collaboration. "Monitoring and data quality assessment of the ATLAS liquid argon calorimeter". In: *Journal of Instrumentation* 9.07 (2014), P07024. URL: http://stacks.iop.org/1748-0221/9/i=07/a=P07024.

[126] A Dafinca, J Henderson, and A R Weidberg. *Single Event Upset Studies Using the ATLAS SCT*. Tech. rep. ATL-COM-INDET-2013-064. TWEPP proceedings deadline is 1/11/13. Geneva: CERN, 2013. URL: https://cds.cern.ch/record/1607080.

[127] Kathryn Grimm et al. *Primary vertex reconstruction at the ATLAS experiment*. Tech. rep. ATL-SOFT-PROC-2017-051. 4. Geneva: CERN, 2017. URL: http://cds.cern.ch/record/2253428.

[128] G. Aad et al. "Search for WZ resonances in the fully leptonic channel using pp collisions at s=8 TeV with the ATLAS detector". In: *Physics Letters B* 737 (2014), pp. 223 –243. ISSN: 0370-2693. DOI: https://doi.org/10.1016/j.physletb.2014.08.039. URL: http://www.sciencedirect.com/science/article/pii/S0370269314006066.

[129] G. Aad et al. "Measurements of $W^{\pm}Z$ production cross sections in pp collisions at $\sqrt{s} = 8$ TeV with the ATLAS detector and limits on anomalous gauge boson self-couplings". In: *Phys. Rev. D* 93 (9 2016), p. 092004. DOI: 10.1103/PhysRevD.93.092004. URL: https://link.aps.org/doi/10.1103/PhysRevD.93.092004.

[130] Michiel Botje et al. "The PDF4LHC Working Group Interim Recommendations". In: (2011). arXiv: 1101.0538 [hep-ph].

[131] ATLAS Collaboration. "Muon reconstruction performance of the ATLAS detector in proton–proton collision data at $\sqrt{s}$=13 TeV. Muon reconstruction performance of the ATLAS detector in proton–proton collision data at $\sqrt{s}$=13 TeV". In: *Eur. Phys. J. C* 76.CERN-EP-2016-033. CERN-EP-2016-033 (2016), 292. 45 p. URL: https://cds.cern.ch/record/2139897.

[132] *JET RESOLUTION*. URL: https://twiki.cern.ch/twiki/bin/viewauth/AtlasProtected/JetResolution2015Prerecom.

[133] Lucy Kogan. "Determining the Jet Energy Scale uncertainty in the ATLAS detector". In: *Nuclear Instruments and Methods in Physics Research Section A: Accelerators, Spectrometers, Detectors and Associated Equipment* 718 (2013). Proceedings of the 12th Pisa Meeting on Advanced Detectors, pp. 86 –87. ISSN: 0168-9002. DOI: https://doi.org/10.1016/j.nima.2012.11.048. URL: http://www.sciencedirect.com/science/article/pii/S016890021201385X.

[134] *Performance of missing transverse momentum reconstruction for the ATLAS detector in the first proton-proton collisions at at $\sqrt{s}$= 13 TeV*. Tech. rep. ATL-PHYS-PUB-2015-027. Geneva: CERN, 2015. URL: https://cds.cern.ch/record/2037904.

[135] *Extended Pileup Reweighting*. URL: https://twiki.cern.ch/twiki/bin/viewauth/AtlasProtected/ExtendedPileupReweighting.

[136] Michele Pinamonti and Christopher Neu. "Statistical methods". In: (2018). URL: https://cds.cern.ch/record/2642098.

[137] Alexander L. Read. "Presentation of search results: The CL(s) technique". In: *J. Phys.* G28 (2002), pp. 2693–2704. DOI: 10.1088/0954-3899/28/10/313.

[138] L. Moneta et al. "The RooStats Project". In: *Proceedings of the 13th International Workshop on Advanced Computing and Analysis Techniques in Physics Research, ACAT2010*. Proceedings of Science. 2010. arXiv: 1009.1003.

[139] ATLAS Collaboration. "Combination of searches for WW, WZ, and ZZ resonances in pp collisions at $\sqrt{s} = 8$ TeV with the ATLAS detector. Combination of searches for WW, WZ, and ZZ resonances in pp collisions at $\sqrt{s} = 8$ TeV with the ATLAS detector". In: *Phys. Lett. B* 755.CERN-PH-EP-2015-269. CERN-PH-EP-2015-269 (2015). 20 pages plus author list + cover pages (37 pages total), 4 figures, 5 tables, submitted to PLB, All figures including auxiliary figures are available at https://atlas.web.cern.ch/Atlas/GROUPS/PHYSICS/PAPERS/EXOT-2014-18, 285–305. 21 p. URL: https://cds.cern.ch/record/2115337.

[140] CMS Collaboration. "Combination of searches for heavy resonances decaying to WW, WZ, ZZ, WH, and ZH boson pairs in proton–proton collisions at $\sqrt{s} = 8$ and 13 TeV. Combination of searches for heavy resonances decaying to WW, WZ, ZZ, WH, and ZH boson pairs in proton-proton collisions at $\sqrt{(s)} = 8$ and 13 TeV". In: *Phys. Lett. B* 774.CMS-B2G-16-007. CMS-B2G-16-007-003 (2017), 533–558. 26 p. URL: http://cds.cern.ch/record/2265922.

[141] ATLAS Collaboration. "Search for WW/WZ resonance production in $\ell\nu qq$ final states in pp collisions at $\sqrt{s} = 13$ TeV with the ATLAS detector. Search for WW/WZ resonance production in $\ell\nu qq$ final states in pp collisions at $\sqrt{s} = 13$ TeV with the ATLAS detector". In: *JHEP* 03.CERN-EP-2017-223 (2017), 042. 44 p. URL: https://cds.cern.ch/record/2289945.

[142] ATLAS Collaboration. "Searches for heavy ZZ and ZW resonances in the $\ell\ell qq$ and $\nu\nu qq$ final states in pp collisions at $\sqrt{s} = 13$ TeV with the ATLAS detector". In: *JHEP* 03.CERN-EP-2017-146 (2017), 009. 52 p. URL: https://cds.cern.ch/record/2281501.